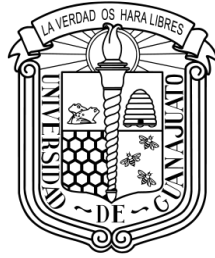Universidad de Guanajuato

Campus Leon

Science and Engineering Division

# Design and Development of Cable-in-Conduit superconductor technology for the Magnets of the Future Electron-Ion Collider

A thesis presented by

## Daniel Chávez Valenzuela

Submitted to the
Department of Physics
in partial fulfillment of the requirements for the degree of

Doctor of Science

in

Physics

León, Guanajuato, December 2018

# Universidad de Guanajuato

Campus Leon
Science and Engineering Division

The committee members, certify that have read the thesis presented by Daniel Chávez Valenzuela and that it is entirely adequate in scope and quality as a partial requirement for the degree of Doctor of Science in Physics.

_____

Dr. Peter M. McIntyre
Texas A&M University
Principal Advisor

_____

Dr. Mauro Napsuciale Mendivil
Universidad de Guanajuato
Secondary Advisor

_____

Dr. José Luis Lucio Martínez
Universidad de Guanajuato
Committee Member

_____

Dr. Georfrey Humberto Israel Maury Cuna
Universidad de Guanajuato
Committee Member

_____

Dr. Modesto Antonio Sosa Aquino
Universidad de Guanajuato
Committee Member

_____

Dr. Cristhian Alfonso Valerio Lizarraga
Universidad Autónoma de Sinaloa
Committee Member

_____

Dr. Carlos Hernandez
Universidad Autonoma de Sinaloa
Committee Member

i

# Declaration of Authorship

I, Daniel Chávez Valenzuela, declare that this thesis titled, "Design and Development of Cable-in-Conduit superconductor technology for the Magnets of the Future Electron-Ion Collider" and the work presented in it are my own. I confirm that:

- This work was done wholly or mainly while in candidature for a research degree at this University.

- Where any part of this thesis has previously been submitted for a degree or any other qualification at this University or any other institution, this has been clearly stated.

- Where I have consulted the published work of others, this is always clearly attributed.

- Where I have quoted from the work of others, the source is given. With the exception of such quotations, this dissertation is entirely my work.

- I have acknowledged all the main sources of help.

- Where the thesis is based on work done by myself jointly with others, I have made clear exactly what was done by others and what I have contributed.

<div align="right">

_____

Daniel Chávez Valenzuela

León, Guanajuato, December, 2018

</div>

I dedicate this work to my parents that always been there, and to my beloved family, Oliver, and Paola.

# Acknowledgments

Being part of a Ph.D. program in physics has been so far, the most exciting and challenging journey I have ever taken. Many people have been part of this adventure including friends, family, and colleges; I thank all of them for feedback and constant support.

In particular, I would like to thank to my mentors:

# Design and Development of Cable-in-Conduit superconductor technology for the Magnets of the Future Electron-Ion Collider

by

Daniel Chávez Valenzuela

## Abstract

The development of superconducting magnets strongly depends on the superconductor, its critical surface, its winding method (Wind-and-react or react-and-wind), and its ability to be formed into complex bends. The majority of the current superconductors (NbTi, $Nb_3Sn$, Bi2212, $MgB_2$, among others) follow the so-called "Rutherford topology." The latter is a geometrical arrangement of superconducting wires, that has been successfully applied to develop most of the superconducting dipoles (Cos $\theta$) worldwide. Two significant drawbacks are inherited in this topology: 1. The anisotropy for bending the cable, which limits its forming capabilities in the azimuthal direction, leading to more elaborated magnet designs. 2. The governing heat transfer mechanism is the heat conduction in solids. Unfortunately, this mechanism is not coolant-superconductor, but coolant-metal-epoxy-superconductor.

In this work, Is presented an alternative topology for the arrangement of superconducting wires: The Cable-In-Conduit superconductor technology (CIC). In this topology, the superconductors (NbTi, $Nb_3Sn$, Bi2212, $MgB_2$) arranged in a spiral around a coolant channel, allows the superconductors to be fixed and locked in a position avoiding instabilities. The channel enables the coolant to bathe the superconductors proving thermal stability. The heat conduction mechanism is by direct contact between the coolant and the superconductor. Furthermore, in this technology, the CIC posses an inherit isotropy for small-radius bending, which facilitates and potentiates the magnet design. The use of this technology has proven to be a success for developing the superferric magnets for the future Electron-Ion Collider of the Thomas Jefferson National Laboratory (JLEIC).

In the following chapters, is presented the design and development of the CIC superconducting technology. The research begins with introducing the conceptual design of the CIC conductor, followed by analytically models, simulations, and experiments that lead us to produced optimized CIC conductors for specific applications; This includes the methods for fabricating small length of CIC superconductor and the techniques for validating zero current degradation's are described. The development of the associated technology required for producing the CIC conductor and forming it into complex bends is presented, along with the methods for extrapolating small-length production to long-length production of CIC conductors.

The research incorporates an overview of the 3 T superferric CIC dipoles, designed for the Ion-Ring of the JLEIC. A first muck-up winding on a 1.2 m long model, is used to validate the winding strategy, and to analyze the relationship with the multipole content is and the errors in the winding.

The last part of the dissertation shows the current efforts for developing magnet technology for Mexican projects. In particular, describes the analytical, thermal, mechanical and magnetic studies for a low gradient normal-conducting quadrupole. Incorporates the current efforts for the developing and characterization of a first full-scale quadruple.

# List of Figures

# List of Tables

# Contents

# List of Publications

1. Pogue, N. J., **Chavez, D.**, Kellams, J., McIntyre, P. M., & Sattarov, A. I. (2015). Strong focusing cyclotron and its applications. **IEEE Transactions on Applied Superconductivity, 25(3), 1-4.**

2. Breitschopf, J., Elliot, T., Garrison, R., Gerity, J., Kellams, J., McIntyre, P., ... & **Chavez, D.**. (2016). Sperferric Arc Dipoles for the ION Ring and Booster of OF JLEIC. **Bulletin of the American Physical Society, 61.**

3. Sattarov, A., McIntyre, P., Breitschopf, J., **Chavez, D.**, Gerity, J., & Kellams, J. (2017). New magnet technology for a 1.5 T open-MRI breast imager. **IEEE Transactions on Applied Superconductivity, 27(4), 1-4.**

4. Assadi, S., Breitschopf, J., **Chavez, D.**, Gerity, J., Kellams, J., McIntyre, P., & Shores, K. (2017). Cable-in-conduit dipoles to enable a future hadron collider. **IEEE Transactions on Applied Superconductivity, 27(4), 1-5.**

5. McIntyre, P., Assadi, S.,**Chavez, D.**, Gerity, J., Pogue, N., Sattarov, A., ... & Mann, T. (2015). Magnet Design and Synchrotron Damping Considerations for a 100 TeV Hadron Collider (No. IPAC-2015-THPF134, p. THPF134).

6. McIntyre, P. M., Assadi, S., Bannert, S., Breitschopf, J., Gerity, J., Kellams, J. N., **Chavez, D.** & Pogue, N. (2017, January). Collider in the sea: vision for a 500 TeV world laboratory. In **North American Particle Accelerator Conf.(NAPAC'16)**, Chicago, IL, USA, October 9-14, 2016 (pp. 13-16). JACOW, Geneva, Switzerland.

7. McIntyre, P., Assadi, S., **Chavez, D.**, Collins, C., Gerity, J., Kellams, J., ... & Smit, K. 100 TeV Hadron Collider for a World Laboratory.

8. Breitschopf, J., **Chavez, D.**, Albosta, R., Elliot, T., Garrison, R., Kellams, J., ... & Sattarov, A. (2017, December). Fabrication of long-length cable-in-conduit for superconducting magnets. In **IOP Conference Series: Materials Science and Engineering (Vol. 279, No. 1, p. 012036). IOP Publishing.**

9. Chavez, D., & McIntyre, P. (2015). A NbTi Cable-in-Conduit conductor for the Medium-energy Electron-Ion Collider (MEIC) magnets and for ultimate-energy hadron colliders. **Bulletin of the American Physical Society, 60**

10. McIntyre, P., Breitschopf, J.,**Chavez, D.**, Gerity, J., Kellams, J., Sattarov, A., & Tomsic, M. (2018). Block-Coil High-Field Dipoles Using Superconducting Cable-in-Conduit. **IEEE Transactions on Applied Superconductivity, 28(3), 1-7.**

11. Breitschopf, J., **Chavez, D.**, McIntyre, P (2015). Construction of Next Generation Dipole Magnets. **Bulletin of the American Physical Society, 60.**

12. Breitschopf, J., **Chavez, D.** Elliot, T., Garrison, R., Gerity, J., Kellams, J., McIntyre, P. Superferric arc dipoles for the Ion Ring anda the Booste of the JLEIC. **Proceedings of NAPAC2016.**

13. McIntyre, P. M., Breitschopf, J., **Chavez, D.**, Gerity, J., Kellams, J., Sattarov, A., & Tomsic, M. (2018). Stealth Superconducting Magnet Technology for Collider IR and Injector Requirements. **IEEE Transactions on Applied Superconductivity, 28(3), 1-6.**

14. Valerio-Lizarraga, C. A., Yee-Rendon, B., Duarte-Galvan, C., Guillermo Cantn, G., Medina, L., **Chavez, D.**, ... & Maury Cuna, G. H. I. (2018). Study of the first Mexican RF linear accelerator. **Rev. Mex. Fis., 64, 116.**

15. Lizarraga, C. V., Loaeza, A. C., Cantn, G. G., Duarte, C.,**Chavez, D.**, Chahn, K. H., ... & Garca, A. V. (2016, October). Science and Technology of Accelerators. In **Journal of Physics: Conference Series (Vol. 761, No. 1, p. 012005). IOP Publishing.**

16. P. McIntyre, Jeff Breitschopf, **Daniel Chavez**, Tim Elliott, Raymond Garrison1, James Gerity, Joshua Kellams, and Akhdiyor Sattarov. Cable in Conduit dipoles for the Ion Ring of the JLEIC. In **IEEE Transactions on Applied Superconductivity 2018. Manuscript submitted for publication.**

17. P. K. Ghoshal, **D. Chavez**, R. Fair, S. Gopinath, D. Kashy, P. McIntyre, T. Michalski, R. Rajput-Ghoshal, A. Sattarov. Quench Protection Study of 3T Super-Ferric Booster Magnet using CICC for Future Electron-Ion Collider at Jefferson Laboratory. In **IEEE Transactions on Applied Superconductivity 2018. Manuscript submitted for publication.**

18. **D. Chavez**, J. Breitschopf, T. Elliot, R. Garrison, J. Gerity, J. Kellams P. McIntyre, K. OQuinn and A. Sattarov. 3 Tesla superferric cable-in-conduit dipole for the Ion Ring of the JLEIC collider. In **IEEE Transactions on Applied Superconductivity Manuscript submitted for publication.**

19. **D. Chavez**, J. Breitschopt, J.N. Kellams, P. McIntyre, M. Rindfleish, A. Sattarov, and M. Tomsic. Cable-in-Conduit using $MgB_2$, $Nb_3Sn$ and Bi-2212 for wind-and-react coils. **IEEE Transactions on Applied Superconductivity 2018. Manuscript submitted for publication.**

20. **Chavez, D.**, Maury, G. H. I., Napsuciale, M., Ortiz, C. B., Pea, J., Galvan-Duarte, C., ... & Sattarov, A. I. (2017, October). Status Report on the R&D of a 5 T/m Normal Conducting Quadrupole Magnet for the 10-MeV Beam Line of the Electron Linac of the Mexican Particle Accelerator Community. In **Journal of Physics: Conference Series (Vol. 912, No. 1, p. 012038). IOP Publishing**.

21. **Chavez, D.**, Cuna, G. M., Napsuciale, M., Basilio, J. C., Yee-Rendon, B., Valerio-Lizarraga, C. A., ... & Sattarov, A. I. (2018, September). Field and Cost Optimization of a 5 T/m Normal

Conducting quadrupole for the 10-MeV Beam Line of the Electron Linac of the Mexican Particle Accelerator Community. In **International Particle Accelerator Conference 2018. Journal of Physics: Conference Series (Vol. 1067, No. 8, p. 082014). IOP Publishing**.

22. P. McIntyre, **Chavez, D.** and Sattarov, A. I. 6 T cable-in-conduit dipole to double the ion energy for JLEIC. **Preparing for submission**.

23. **Chavez, D.**, J. Basilio, G.H.I. Maury Cuna, M.C. Garcia Castaneda, M. Rios, K. Cantun and V. Cruz. Magnet Technology Development in Mexico Towards a Future In-House Production ofParticle Accelerators. **Preparing for submission**.

# Intellectual Property

1. McIntyre, P., Sattarov, A., Mann, T., Gerity, J., Smit, K., **Chavez, D.** & Tomsic, M. (2018). "Quench protected structured superconducting cable". U.S. Patent Application No 15/899,840. **Patent granted 16 Agost 2018**

2. **Chavez, D.** & P. McIntyre. (2018). "Real-Time Echo Breaking Detection and Monitoring system, for CIC manufacturing and bending process". U.S. Patent in tramit.

3. **Chavez, D.**, G.H.I. Maury & M. Napsuciale. (2018). "Mecanismo supresor de grados de libertad para el ensamble de polos magnticos en magnetos multipolares." Instituto Mexicano de la Propiedad Intelectual. MX. Patent in tramit.

4. **Chavez, D.**, Basilio, J., Cantun-Avila, K.B., Castaneda M.C., Cruz-Delgado, V.J., Maury-Cuna G.H.I. & Rios, M. Instituto Mexicano de la Propiedad Intelectual. MX. Patent in tramit.

# Awards



Figure 1: Applied Superconductivity Conference 2018. Award for Best Student Paper in Large-Scale-First Place.

# Chapter 1

# Introduction

## 1.1 Motivation

Scientific breakthroughs made in physics in the last two centuries, both regarding theory and experiments, have expanded at an unprecedented rate our understanding of Nature and its composition. In a few years, we moved from Dalton's atomic model, that considered the atoms as solid spheres with a measurable mass [1], to the atomic model of Bohr [2], which recognizes the atom as an entity composed of a nucleus, where the most of the mass is located and constitutes a positive charge. In this model, the electrons (negatively charged) are revolving around the nucleus in definite circular paths called orbits or shells. This model encapsulates the modern understanding of the atom structure, represents the beginning of nuclear science which inspired the scientific community to study the constitution of the nucleus, its dynamics and the laws governing its behavior.

The development of state of the art machines known as particle accelerators has been critical for boosting the nuclear science, in both senses:

- Experimentally, by developing high-end machines, that made possible the discovery of a zoo of new elementary particles, whether they were proposed by a theoretical model, or were accidentally discovered.

- And theoretically, by developing beam dynamics theories that describe the particles trajectories as they are moving through the different components of the machines. Which allows determining specific parameters for the accelerator components (magnets, cavities, collision angles, field qualities, collision velocities, among others), to produce the conditions that lead to the detection or discovery a new particle, or properties of the particles.

The development of this technology is critical for a deeper understanding of Nature. Unfortunately, developing accelerator technology is a very complex task, that requires substantial capital and a large group of scientist, technicians, and engineers working together towards a common goal. Two projects drive my motivation, and in both the development of cost-effective accelerator technology is

involved: The first, is the development of a new superconducting cable that allows producing cost-effective superferric dipoles, for the future Electron-Ion collider for the Thomas Jefferson National Laboratory. The second is the development of magnet technology for Mexican project in accelerator physics. The latter constitutes a marvelous opportunity that comes with a huge responsibility; it will be the first time magnet technology is developed in Mexico.

**Motivation:Cost-effective magnets for the future Electron-Ion Collider**

As of today, the scientific community is still pursuing a nuclear theory that explains the origin of nucleons, its composition, and how their components interact and affect the global properties of the nucleon. Thanks to the titanic effort of many scientist, technician and engineers, we now know that the nucleons are themselves composed of more basic particles, known as quarks, that moves with relativistic speeds inside the nucleon radius [3], and are bonded together by the exchange of other basic particles known as gluons, responsible for carrying the strong nuclear force, as proposed by the Quantum Chromodynamics [4]. The QCD is a complex, exciting and a relatively new theory, that has rapidly gained recognition and acceptance among the scientific community, and provides within its limits, the most recent description of the nuclear world. In this theory, the confinement of quarks inside the nucleon is due to the color charge property of gluons, a concept analogous to that of electric charge. The fact that the gluons carry color charge causes that the gluons interact with each other, having a considerable contribution to the nucleon mass [5, 6], leading to a little-explored regime of matter where abundant gluons dominate its behavior [7].

Understanding these interactions is a fundamental and imperative goal of nuclear science, that potentially could lead to new frontiers, new science and the development of new technological break-throughs. Exploring this regime of Nature requires a new experimental facility: An Electron-Ion Collider (EIC) [8, 9, 10].

Two designs have been proposed, and supported by the Department of Energy (DOE) of the United States of America, through the Nuclear Science Advisory Committee. In both designs, the magnetic requirements of beam rigidity, field quality, field uniformity, and relatively large magnet aperture, set a challenge for the development of reliable and cost-effective superconducting magnets.

The complexity and production cost of the magnet depends on the type of superconductor and its topology. Conventionally, the majority of the practical superconductors (NbTi, Nb3Sn, Bi2212, MgB2, among others) follow the so-called Rutherford topology. The latter is a geometrical arrangement of superconducting wires, that posses two inherent drawbacks: 1.The anisotropy for bending the cable, which limits its forming capabilities in the azimuthal direction, leading to more elaborated magnet designs. 2. The governing heat transfer mechanism is the heat conduction in solids. Unfortunately, this mechanism is not coolant-superconductor, but coolant-metal-epoxy-superconductor.

The use of a superconducting cable with a novel and more effective topology could facilitate and expedite the magnet design and construction, therefore reducing the overall price of the machine. The latter motivates us to develop an alternative topology for the arrangement of superconducting wires: The Cable-In-Conduit superconductor technology (CIC). In this topology, the superconductors (NbTi,

Nb3Sn, Bi2212, MgB2) arranged in a spiral around a coolant channel, allows the superconductors to be fixed and locked in a position avoiding instabilities. The channel enables the coolant to bathe the superconductors proving thermal stability. The heat conduction mechanism is by direct contact between the coolant and the superconductor.

Furthermore, in this technology, the CIC posses an inherit isotropy for small bending radius, which facilitates and potentiates the magnet design. This technology will produce the superferric dipoles of the future Electron-Ion Collider of the Thomas Jefferson National Laboratory (JLEIC). Furthermore, this technology has been proposed to be used in the fast ramping dipole magnets of the boost ring, and for the high gradient quadrupoles of the interaction region.

**Motivation: Development of magnet technology for Mexican Projects**

Mexico interest in experimental particle physics started in the early 1980s, when Leon Lederman, former director of Fermilab and Nobel prize of physics (1988), initiated a program to encourage experimental high-energy physics in Latin America [11]. From this, a successful first generation of Mexican experimental particle-physicist was born, this inspired Mexican Universities for the continuous formation of human resources. After three decades, research groups in experimental high energy physics have been consolidated at eight Mexican Universities. This groups actively collaborate with international institutes, developing experimental high-energy physics [12]. Nevertheless, it worth to clarify, that these collaborations are not targeting in-house development of particle accelerators. The first attempt to develop accelerator science and technology in Mexico was conceived at the Institute of Physics of Universidad de Guanajuato in 1986, as a collaboration with Fermilab. Unfortunately, this project did not succeed, in 1992 the accelerator project was closed, and new groups working on other topics started a new era of this Institute [13].

In early 2006, with the proposition of developing the first national synchrotron radiation facility in Mexico, a new era began, boosting the formation of human resources in different areas of particle accelerator physics. Since then, Dr. Mauro Napsuciale from the Physics Department at Universidad de Guanajuato, took the enormous responsibility of preparing specialized Ph.D. Students, targeting critical areas required for developing accelerator technology in Mexico.

After a decade, Dr. Mauro Napsuciale consolidated the first group of trained Ph.D. student and scientist and proposed the development of the first Mexican electron-Linear Accelerator (eLINAC). The project constitutes the first (founded) attempt to develop accelerator technology in Mexico. For this reason, this project represents a significant challenge and a big opportunity, for me to contribute to the development of accelerator technology in Mexico, through the design, modeling, and development of the low-gradient normal conducting quadrupoles, required by the eLINAC.

## 1.2   Electron-Ion Collider (EIC)

The future Electron-Ion Collider is a proposed facility specially designed to provide insight into fundamental question concerning the basic structure of hadronic matter, i.e., its meant to address the

fundamental issues of quantum chromodynamics. The NSAC has summarized this questions in three branches [14]:

1. How are the sea quarks and gluons, and their spins, distributed in space and momentum inside the nucleon?

2. Where does the saturation of gluon densities set in?

3. How does the nuclear environment affect the distribution of quarks and gluons and their interactions in nuclei?

"The complexity of the machine is distinguished from all past, current and contemplated facilities around the world by being at the intensity frontier with a versatile range of kinematics and beam polarizations, as well as beam species, allowing the above questions to be tackled at one facility" [8].

## 1.2.1   Electron Ion Collider projects worldwide

The international community of nuclear science is highly interested in developing Electron-Ion Colliders. Five different institutions have developed a research plan. From those, two are American Institutions competing for support from DEO: The Thomas Jefferson National Laboratory (JLEIC), and the Brookhaven National Laboratory (eRHIC). A German institution: The Gesellschaft fr Schwerionenforschung Laboratory (GSI). A Chinese Institution, the Institute of Modern Physics (HIAF), and the CERN (LHeC). Table 1.1 taken from Brüuning et at. summarizes the main parameters from such facilities [15].

|                | Ring-Ring      |                | Linac-Ring    |               |               |
| -------------- | -------------- | -------------- | ------------- | ------------- | ------------- |
|                | ENC            | JLEIC          | LHeC RR       | LHeC LR       | eRHIC         |
| CM energy, GeV | 14             | 15-70 (140)    | 1300          | 1300 (2000)   | 30-70 (175)   |
| Based at       | HESR FAIR (GSI) | CEBAF (JLAB)   | LHC (CERN)    | LHC (CERN)    | RHIC (BNL)    |

Table 1.1: Electron-Ion Colliders world wide.

## 1.2.2   JLEIC: The ion ring and dipole requirements

The conceptual design of the JLEIC is characterized by its figure-8 layout using the CEBAF as the electron injector and the RF systems using both normal conducting (NC) and superconducting (SC) technology for electron and ions acceleration. In this facility, highly polarized beams of ions and electrons would be collided at energies up to 100 GeV/u for ions and 20 GeV for electrons [17]. Each of the two rings is configured as a figure 8, so that the polarization is intrinsically preserved, see figure 1.2, [18].

The Ion Ring is described in and shown in figure 1.2. The arc lattice contains a total of 62 half-cells, and each half-cell contains a total dipole bending angle of 4.2°. The bend angle would produce an unacceptable sagitta (8 cm) if the bending were done in a single straight-body dipole. The bending

| | HERA | | ENC | | MEIC 1ST Stage | | MEIC 2nd Stage | | eRHIC 1st Stage | | eRHIC | | LHeC linac-ring | | LHeC ring-ring | |
|---|---|---|---|---|---|---|---|---|---|---|---|---|---|---|---|---|
| | P | e | P | e | | e | P | e | P | e | P | e | P | e | P | e |
| Energy, Gev | 920 | 27.5 | 15 | 3 | 60 | 5 | 250 | 10 | 250 | 5 | 250 | 20 | 7000 | 60 | 7000 | 60 |
| Bunch frequency [MHz] | 10.4 | | 52 (104) | | 750 | | 750 | | 14.1 | | 14.1 | | 20 | | 40 | |
| Bunch Intensity [$10^{11}$] | 0.72 | 0.29 | 0.54 (0.36) | 2.3 | 0.04 | 0.25 | 0.04 | 0.25 | 2 | 0.22 | 4 | 0.2 | 1.7 | 0.02 | 1.7 | 0.2 |
| Beam current [A] | 0.1 | 0.04 | 0.45 (0.6) | 1.9 | 0.5 | 3 | 0.5 | 3 | 0.42 | 0.05 | 0.83 | 0.1 | 0.43 | 0.006 | 0.86 | 0.1 |
| Norm. rms emittance x/y [$\mu m$] | 5 | 1100 /180 | 2.3 /0.8 | 930 /320 | 0.35 /0.07 | 54 /11 | 0.45 /0.02 | 32 /13 | 0.18 | 6.5 | 0.18 | 26 | 3.75 | 50 | 3.75 | 580 /290 |
| $\beta^*$ x/y [cm] | 245 /18 | 63 /26 | 30 (10) | 30 | 4 /0.8 | 4 /0.8 | 16 /0.8 | 16 /0.8 | 5 | 5 | 5 | 5 | 10 | 12 | 180 /50 | 18 /10 |
| Beam size at IP. x/y [$\mu m$] | 112/30 | | 200/120 | | 15/3 | | 15/3 | | 6/6 | | 6/6 | | 7/7 | | 30/16 | |
| Bunch length [cm] | 19 | 1 | 30 (20) | 8 | 1 | 0.75 | 1 | 0.75 | 8 | 0.4 | 5 | 0.2 | 8 | 0.03 | 8 | 1 |
| Polarization [%] | 0 | 45 | 80 | 70 | 80 | 80 | 70 | 80 | 70 | 70 | 70 | 80 | 0 | 90 | 0 | 40 |
| Peal luminosity $10^{33} cm^{-2} s^{-1}$ | 0.04 | | 0.2 (0.6) | | 14.2 | | 52 | | 11 | | 27 | | 1 | | 1.8 | |

Figure 1.1: The main beam parameters and luminosities of future EICs and the past HERA collider. Source: Abeyratne aet.. [16]
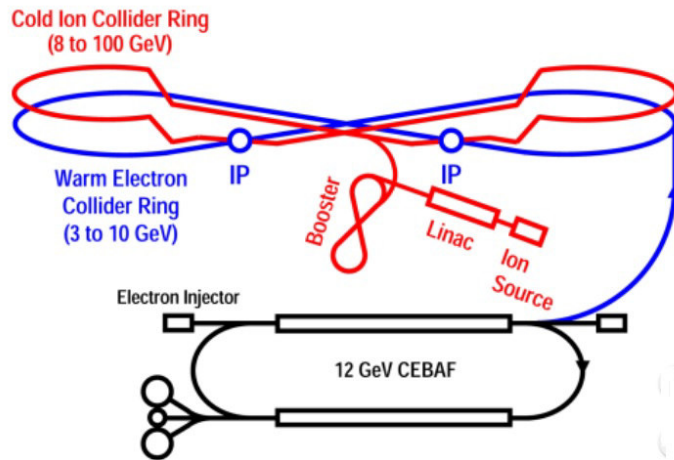


Figure 1.2: JLEIC machine overview.

is therefore split into two dipoles, and a short sextupole is located between them. Neuffer [19] showed that a sextupole located in the center of the bends of a half-cell is effective in nulling the effects of body sextupole in the dipoles. We use that provision to good effect, as discussed below.

In developing a design for the arc dipoles, the JLEIC team expressed several priorities:

1. The minimum operating dipole field must be 3 T; higher field capability would be desirable.

2. Minimum construction cost

3. Field quality for long-lifetime collisions over a wide range of ion energies $30 \to 100$ GeV.

4. Injection at 6 GeV.

5. The dipole aperture explored by the circulating beam is 10 cm horizontal x 6 cm vertical.

The horizontal aperture poses a significant challenge for dipole design [20], even with the reduction of sagitta by splitting the dipole within each half-cell. If the beam is positioned to symmetrize the aperture requirement, it will follow an arc that enters the dipole at a position x= -1 cm, traverses to a position x = +1 cm at the center, and then exits at x= -1 cm. The beam thus explores a wide-aspect-ratio aperture, which makes a particular challenge for homogeneity.

The two most challenging requirements for the dipole are the large aperture (10 cm x 6 cm) that is covered by the stored beam, and the requirement for flared ends that clear the same aperture. Two dipole design options were explored to meet the above requirements: $\cos\theta$ vs. block coil geometry, Rutherford cable vs. cable-in-conduit conductor. These comparisons are described in length in chapter 3 and 4, where it can be seen that The CIC conductor provides a basis for a manufacturable dipole that meets the JLEIC requirements [21]. An external panel reviewed the design on 6/4/2015.

## 1.3 Magnetic Field in accelerator magnets

Particle accelerators demand the use of electromagnetic fields, off specific characteristics and complexity, to provide acceleration, guidance, and focusing on the charged particle's beam.

The development of magnet technology (normal o superconducting) that allows us to create and shape magnetic fields in a region inside the beam pipe, is based on the classical electromagnetic theory, and therefore, is governed by Maxwell's equations [22]. To provide a basic analytic description of the magnetic field, its multipole content and its errors, in the aperture of the magnets, let's make the following observations:

- The length of the accelerator magnets is, in general, several times larger than the aperture radius, i.e., end effects are negligible at the body of the magnet,

- The axis of the magnet, for reference purposes, is located at the center of the aperture, and runs parallel to the charged particle's beam,

- The wires (normal or superconductor) at the body of the magnet, run parallel to the beam, and therefore the current is parallel (or anti-parallel) to the beam,

- The aperture of the magnet is considered empty space, free of magnetized materials and currents,

- The magnets developed and presented in this work, are DC magnets. Therefore, the time variation of the magnetic fields is considered negligible, restricting the analysis to the magneto-static case[a].

Under this considerations, we can derive a 2d model of the fields in the aperture, valid along the body of the magnet and until a few apertures away from the end of the magnet, where edge effects are no longer negligible, as it can be seen in section *"Magnet design"* on Chapter 2 and in chapter 6. The following derivation is based on the work of Mess [23], Tanabe [24], Fisher [25] and Gupta [26], and its meant to provide an outline of the formalism needed to assess the field quality in the aperture of the magnet i.e. the field harmonics.

The above considerations imply, that the flux density field $\vec{B}$ , at the aperture of the magnets must satisfy:

$$\nabla \cdot \vec{B} = 0 \tag{1.1}$$

$$\nabla \times \vec{B} = 0 \tag{1.2}$$

The functional form of equations 1.1) and 1.2), allows us to define the flux density field $\vec{B}$ in two different ways, in terms of a curl of a *vector field*, and in terms of the gradient of a *scalar field*. Both definitions, are representations of the same flux density field $\vec{B}$, and therefore, must satisfy the non-trivial solution of the system of equations.

If the flux density field $\vec{B}$, is defined in terms of an auxiliary vector field $\vec{A}$, through the gauge transformation[b]:

$$\vec{B} = \nabla \times \vec{A} \tag{1.3}$$

where $\vec{A}(r')$, is the vector potential, defined as[c]:

$$\vec{A}(r') = \frac{\mu\mu_0}{4\pi} \int_\nu \frac{\vec{J}(\vec{r'})}{\mid \vec{r} - \vec{r'} \mid} d\nu \tag{1.4}$$

then, the vector potential $\vec{A}(r')$ is parallel to current density vector $\vec{J}(r)$, and therefore runs parallel to the particles beam, with no components other than $A_z$. Inserting this result into Eqn.1.3:

---

[a]For a basic analytic description, the effects on the magnetic field due to this time variation, are considered negligible. In reality, When the accelerator is "turn on", the magnets ramp from zero to its operational field. In this process, a time-varying magnetic field is induced, creating "eddy currents" in the iron yoke and in adjacent conductors. If the magnet is superconducting, the "eddy currents" will freeze in the conductor, affecting the field quality

[b]A gauge transformation explodes the symmetry of a vector field under a given arbitrary function, in such a way that, when applied, leaves the vector field -$\vec{B}$ in this case- unaffected.

[c]Where $\vec{J}$ is the current density; $\mu$ and $\mu_0$ correspond to the magnetic permeabilities of the medium and the vacuum, $r$ and $r'$ correspond to the position vector from the coordinate origin to the current distribution, and from the origin to the point of observation, and $d\nu$ is the volumetric differential.

$$\vec{B} = \nabla \times \vec{A} = \begin{vmatrix} \hat{i} & \hat{j} & \hat{k} \\ \partial x & \partial y & \partial z \\ 0 & 0 & A_z \end{vmatrix} = \frac{\partial A_z}{\partial y}\hat{i} - \frac{\partial A_z}{\partial x}\hat{j} \qquad (1.5)$$

the resulting flux density field $\vec{B}$, is now expressed in terms of a single scalar quantity "Az", with no component in the Z direction $(B_x, B_y, 0)$, as required by a 2d approximation. This field naturally satisfies Eqn. 1.1, as it can be seen if the Schwarz's theorem[d] of the symmetry of second derivatives is applied, and the inner product is solved:

$$\nabla \cdot \left( \nabla \times \vec{A} \right) = \nabla \cdot \left[ \left( \frac{\partial A_z}{\partial y} - \frac{\partial A_y}{\partial z} \right)\hat{i} + \left( \frac{\partial A_x}{\partial z} - \frac{\partial A_z}{\partial x} \right)\hat{j} + \left( \frac{\partial A_y}{\partial x} - \frac{\partial A_x}{\partial y} \right)\hat{k} \right] = 0 \quad (1.6)$$

Applying Eqn.1.5 into Eqn.1.2, and applying *the Coulomb Gauge* $(\nabla \cdot \vec{A} = 0)$, leads to the Laplace Equation:

$$\nabla \times \left( \nabla \times \vec{A} \right) = \nabla(\nabla \cdot \vec{A}) - (\nabla \cdot \nabla)\vec{A} = \nabla^2 A = 0 \qquad (1.7)$$

On the other hand, if the flux density field $\vec{B}$ is defined in terms of an scalar potential $\phi$ in the 2d plane:

$$\vec{B} = -\nabla\phi = -\left( \frac{\partial \phi}{\partial x}\hat{i} + \frac{\partial \phi}{\partial y}\hat{j} \right) \qquad (1.8)$$

it naturally satisfies Eqn.1.2, which can be seen if Schwarz's Theorem is applied:

$$\nabla \times (-\nabla\phi) = \begin{vmatrix} \hat{i} & \hat{j} & \hat{k} \\ \partial x & \partial y & \partial z \\ -\frac{\partial \phi}{\partial x} & -\frac{\partial \phi}{\partial y} & -\frac{\partial \phi}{\partial z} \end{vmatrix} = \hat{i}\left( -\frac{\partial^2 \phi}{\partial y \partial z} + \frac{\partial^2 \phi}{\partial z \partial y} \right) + \hat{j}\left( \frac{\partial^2 \phi}{\partial x \partial z} - \frac{\partial^2 \phi}{\partial z \partial x} \right)$$
$$+ \hat{k}\left( -\frac{\partial^2 \phi}{\partial x \partial y} + \frac{\partial^2 \phi}{\partial y \partial x} \right) = 0 \qquad (1.9)$$

and, if applied to Eqn.1.1, it lead to the Laplace Equation:

$$\nabla \cdot (-\nabla\phi) = -\nabla\phi = 0 \qquad (1.10)$$

Both definitions of the flux density field $\vec{B}$ , Eqn. 1.5 and Eqn. 1.8, must be compatible, this implies that the components of the vector field must be equal:

---

[d]If a function "$f : R^n \rightarrow R$", has continuous second derivatives at a given point "$R^n$", lets say $(a_1, a_2, ..., a_n)$, then $\forall i, j \in \{1, 2, ..., n\}$, the partial differentiation of this function are commutative at this point: $\frac{\partial^2 f}{\partial x_i \partial x_j}(a_1, a_2, ...a_n) = \frac{\partial^2 f}{\partial x_j \partial x_i}(a_1, a_2, ...a_n)$.

$$B_x = \frac{\partial A_z}{\partial y} = -\frac{\partial \phi}{\partial x}$$
$$B_y = -\frac{\partial A_z}{\partial x} = -\frac{\partial \phi}{\partial y}$$

(1.11)

This result resembles the familiar "Cauchy-Riemann conditions" for the derivability of an analytic function in complex variable: if $\widetilde{A}(z)$, is an analytic complex function, such that $z = x + iy$, then the function can be rewritten in terms of a sum of two real functions $A_z(x,y)$ and $\phi(x,y)$:

$$\widetilde{A}(x,y) = A_z(x,y) + i\phi(x,y)$$

(1.12)

such that, when derived relative to any of its components, satisfies:

$$\widetilde{A}'(x,y) = \partial_x A_z(x,y) + i\partial_x \phi(x,y) = \partial_y \phi(x,y) - i\partial_y A_z(x,y)$$

(1.13)

Naturally, this is an analytic function in complex variable, which implies that it can be expressed in terms of a power series:

$$\widetilde{A}(x,y) = \sum_{n=0}^{\infty} C_n(x + iy)^n = \sum_{0}^{\infty} C_n Z^n$$

(1.14)

where $C_n$ are the complex coefficients, that correspond to a *pure* multipolar field. In the American notation, the expansion series begins with n=0,1,2... and corresponds to the dipole, quadrupole, sextupole, while on the European notation, the expansion begins with n=1,2,3,... and correspond to a dipole, quadrupole, sextupole and so on.

This is a beneficial and powerful result; it *describes* the multipole content of the flux density field $\vec{B}$ inside the magnet's aperture[e]. Although this formalism so far, has not yet "directly" provided any information or guidance, of where to place the conductors or the amount of current needed to create the "desired" magnetic field inside the aperture, it can be further developed to describe the angular distribution of currents that could create, within certain allowed errors, pure multipole fields . Its primarily meant to provide a mechanism to asses the field quality, by describing how much of non-desirable multipoles, actually exist in the aperture. One of the requirements for accelerator magnets is to produce "uniform" magnetic fields whose main multipole is several orders of magnitude larger than the secondary multipoles, which are usually kept within $10^{-4}$ parts per million.

From Eqn. 1.13 and 1.14, it can be seen that if the partial derivative of the function $\widetilde{A}(x,y)$ is taken, with respect to any of its variables, then the multipole expansion for the components of the flux density field $\vec{B}(x,y)$ is obtained. Equation 1.14, represents a general expansion which includes multipole fields of any order. In practical accelerators, "pure" fields are required to either focus, bend or

---

[e]This expression convergence within the largest circle that contains no currents or magnetized materials [23]. If the region of space contains currents, then the magnetic field cannot be expressed in terms of the gradient of a scalar function, since it would have to be non zero, which would break the functional form of the Cauchy-Riemann equations.

correct Chromatism. The magnet technology is restricted to pair multipoles. The letter "n" represents half of the poles, with $n = 1, 2, 3, ...$, being $n = 1$ a dipole, $n = 2$ a quadrupole, $n = 3$ a sextupole, and so on.

There is a similar expression to this equation (Eqn. 1.15) that explicitly describes the multipole content in terms of the normal and skew multipoles [26], both formulations are used and widely known.

$$B_y + iB_z = 10^{-4}B_{Ro} \sum_{0}^{\infty}[b_n + ia_n]\left[Cos(n\theta) + iSin(n\theta)\right]\left(\frac{r}{R_0}\right)^n \tag{1.15}$$

where $B_x$ and $B_y$ are the horizontal and vertical components of the magnetic field at (r,$\theta$), $R_O$ is the normalization radius, and $i = \sqrt{-1}$ is the imaginary number. The previously defined harmonics $(a_n; b_n; c_n)$ are all dimensionless coefficients.

Two notations are used by different laboratories around the world. American notation begins with $n = 0$, while in European laboratories the summation begins with $n = 1$ [27]. Both notations are related by:

$$
\begin{aligned}
(a_{n+1})_{Europe} &= -10^{-4}(a_n)_{US} \\
(b_{n+1})_{Europe} &= 10^{-4}(b_n)_{US}
\end{aligned}
\tag{1.16}
$$

The design of normal and superconducting magnets, its aimed to produced very specific magnetic fields in small regions of space. The fields by design restrict the undesired multipoles below certain values [28]. The values of the undesired components of the magnetic field are chosen based on the beam dynamics requirements. When the magnets are developed, their main goal is to achieve the design performance. Nevertheless, a spectrum of parameters may interfere with this: winding errors, iron yoke misalignment, superconductor irregularities, movement of superconductor when cooled to cryogenic temperatures, differential thermal expansion between different materials, epoxy cracking, etc. These errors contribute to the magnetic field multipole content [29]. This undesired multipoles have a different impact on the beam dynamics according to the machine: Circular accelerators, or linear accelerators. In the first, the particles travel several times for the same magnets, having a built-up effect on the dynamics, while for the latter, the particles only travel once. This effect must be evaluated to establish the main parameters for a superconducting magnet. In practice, a beam dynamics group is responsible for proving the specifications on the field quality to the magnet design group.

# Chapter 2

# Cable-In-Conduit Superconductor

## 2.1 Introduction to Superconductivity

The discovery of superconductivity is one of the most exciting phenomena in physics. Its implementation has a significant impact on basic science: The design of superconducting wires allowed the design and operation of superconducting magnets, capable of reaching high magnetic fields and boosting the experimental particle physics. In medicine, its implementation on Magnetic Resonance Imagining is critical for achieving high-resolution images of cross-sectional planes of different parts of the body.
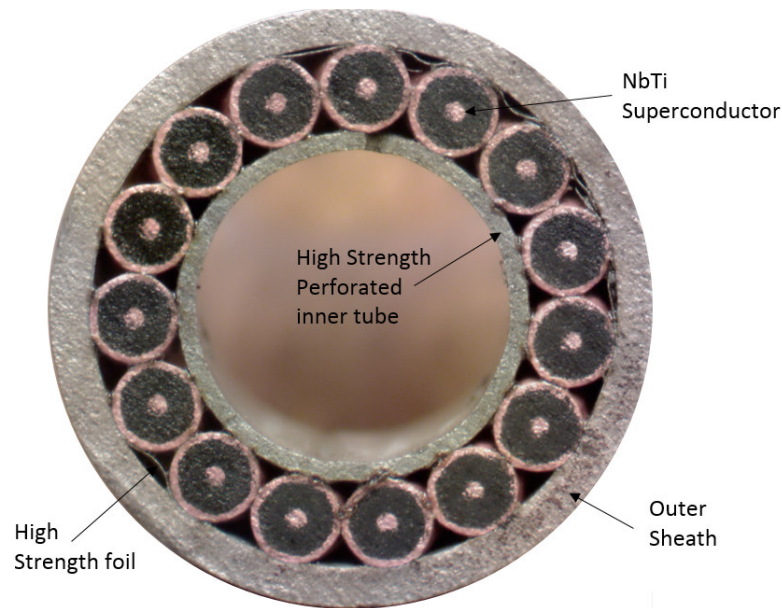


Figure 2.1: Critical surface for NbTi superconductor.

The superconductivity was discovered by the great Dutch physicist Heike Kamerlingh Onnes (1853-1926) on July 10, 1908. After 25 years of hard work on building his cryogenic laboratory at Leiden University, he was able to liquefied helium, reaching a record on the lowest temperature achieved in a laboratory, and opening a new field in physics. Consequently, this discovery pushed the

development of new low-temperature thermometers, and cryogenic vessels capable of maintaining such low temperature. With this, Kamerlingh Oness performed experiments on determining the resistance of several materials at LHe temperatures. From those materials, he notices that mercury exhibited "practically zero" resistance [30]. With this discovery, the superconductivity was born. It offers the possibility of conducting current without power dissipation.

As kamerlingh later discovered, there are some limitations with the superconductivity. Three parameters are required to achieved superconductivity: A critical current density $J_c$, a critical temperature $T_c$ and a critical magnetic field $Bc$, this parameters live in a 3D surface known as the critical surface, as depicted in figure 2.1.

In the following subsections, the basic properties of superconductivity, the type of superconductors, the practical superconductors and the main theories describing superconductivity are described.

## 2.1.1 Basic concepts for practical superconductivity

In this subsection, the critical parameters: Critical current density Jc, Critical magnetic field Bc, and Critical temperature Tc will be studied. The understanding of these properties is of significant importance for magnet designers and must be considered to establish the safe operational values, which will determine the performance of the magnet.

### Critical temperature

The Critical temperature Tc is the first property associated with the superconducting state. At the early days where Kamerlingh Onnes studied the resistance of different materials under cryogenic temperatures, this was the only known requirement for the superconducting materials to achieve the superconducting state, was the low temperature. [31]

When the temperature of a superconducting material is lower than the critical temperature $T_c$, the transition to the superconducting state happens suddenly, and the resistance of the material vanishes to zero. Figure 2.2 shows the experimental results obtained by kamerlingh Onnes, in 1911 [31]. The sudden transition behaves like a phase transition to a different state of matter.

### Critical field

The second property associated with the superconducting state is the applied critical field. It a superconductor is kept below the critical temperature, but the applied field exceeds the critical field, then the materials brake the superconducting phase, returning to the resistive state.

### Critical current density

The third condition to reach the superconducting state is to limit the current that is sent through the superconductor. If the current exceeds the critical value, even when the temperature or field are maintained below its critical parameters, then the superconducting state is violated.
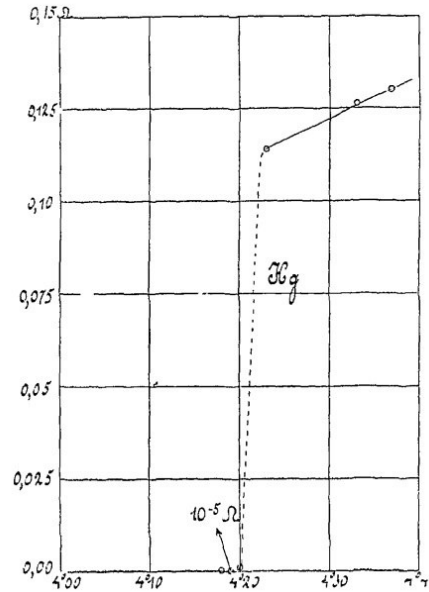
Figure 2.2: Experimental measurement of the resistance of solid mercury obtained by Kamerlingh Onnes in 1911.

All three main parameters must be contained below the critical values. This set of parameters is different for each superconductor.

## 2.1.2 Basic theories for superconductivity

In 1952, Bardeen, Cooper and Shrieffer, proposed that the superconducting state is characterized by the condensation of the conduction electrons of metal, into a state of lower energy. This theory was baptized as the *BCS theory of superconductivity*, and it was awarded with the Nobel prize in 1972.
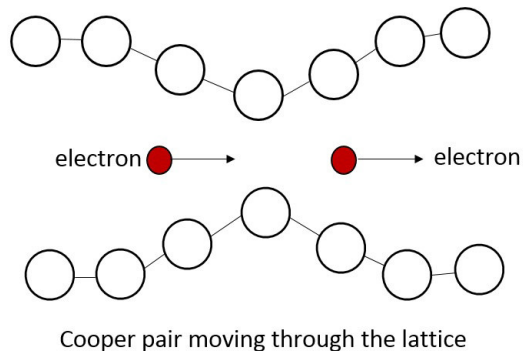


Figure 2.3: Cooper pair moving through the lattice of a superconductor.

In this theory, the authors suggest that the condensation state may be caused by "an attractive force between a pair of electrons (see figure 2.3), which is transmitted via lattice vibrations in the crystal (phonons)" [32]. This pairs of electrons are responsible for the supercurrent and share a single

quantum state, known as *BCS ground state*, which happen to be different from the single-electron state. Both states are separated by an energy gap of $2\Delta(T)$. This shows the intimate relationship between the critical temperature $T_c$ and the energy gap [23]. The theory also predicts that the magnetic flux through a superconducting ring is quantized, the smallest unit of flux being the elementary flux quantum, also known as fluxoid, which is given by [33, 23]:

Although this is a fascinating theory, we should not pursue it further.

$$\Phi_0 = \frac{h}{2e} = 2.07x10^{-15}Vs \tag{2.1}$$

where $h = 6.626x10^{-34}$Js is the plank constant, and $e = 1.602x10^{-19}$C, the fundamental unit of charge. A broader discussion on the specifics of the BCS theory, can be found at [34, 35, 36].

## Meissner - Ochsenfeld effect

In 1933, Walter Meissner and Robert Ochsenfeld discovered a magnetic phenomenon that showed that superconductors are not just perfect conductors [37]. In the Meissner effect, when a superconductor (Type I) is cooled below the critical temperature, and an external magnetic field is applied, the magnetic field is expelled out of the bulk of the superconductor. The same result is obtained, if a different path is chosen i.e., if the superconductor is now exposed to an external magnetic field, and then cooled down below the critical temperature, the magnetic field will also be expelled .

This is possible thanks to the zero-resistance of the superconductor. When the external field is applied, a non-vanishing current is induced, which in turns, produces an opposite magnetic field, which cancels the external field. This can't be explained in terms of the law of induction, because the magnetic field is kept constant.
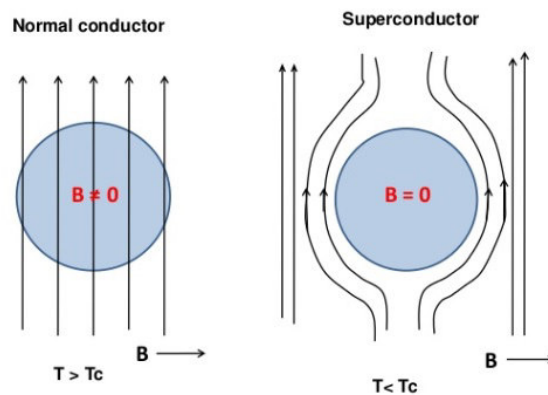


Figure 2.4: Meissner-Ochsenfeld effect. At left, a superconductor is exposed to an external magnetic field B. Immediately after, its temperature decreased below the critical temperature. The non-vanishing induced current produces a magnetic field that cancels the external magnetic field, as depicted in the figure at right.

The fact that the magnetic field could be expelled by two different paths, is a key element that differentiates a superconductor with a metal of perfect conductivity. The first path will still be truth i.e.,

cooling the perfect metal and then exposing it to an external field will induce an opposing magnetic field (Lenz rule). But the second path will not hold. The cooling will have no effect at all [38].

**London penetration depth**

In the last subsection, the Meissner effect was described. It was show that induced current was responsible for creating an opposite magnetic field that canceled the applied external magnetic field. The London penetration theory, provides a classical description of the penetration of the current, responsible for expelling the external field.

In 1935, the London brothers explained the Meissner effect, by assuming that the supercurrent is carried by a fraction of the electron in the metal. In their model, they estimate the penetration depth of the current in surface of the superconductor. The typical penetration lengths range between 20-50 nm. Its important to mention that type I superconductor are governed by Meissner effect, and therefore interior currents are forbidden [23].

## 2.1.3  Type of superconductors

There are two types of superconductors in nature: Type-I and Type-II. Different physical phenomenon govern each type, and they are classified according to their behavior in a magnetic field.

**Type-I superconductors**

The first superconductors discovered by Kamerlingh Onnes were tin, lead and mercury. This superconductors have something in common, they are single elements. This is one of the characteristics of the type-I superconductors, examples of this superconductors are: Zr, Ir, Sn, Al, Pa, Th, Pb, Hg, Ta, Cd, Zn, Ga, Mo, etc. One of the physical properties that characterizes this type of superconductors, is their low critical-field, usually a couple of hundreds of militesla. The Meissner effect governs this type of superconductors.

**Type-II superconductors**

Superconductivity in Type-II is more complex than Type-I, see figure 2.5 a). This superconductors are not completely described by the Meissner effect, instead, they are characterized by the formation of magnetic vortices in an applied magnetic field (see figure 2.5 b, [39]). This occurs above a certain critical field strength $B_{C1}(T)$. The vortex density increases with increasing field strength. At a higher critical field $B_{C2}(T)$, superconductivity is destroyed.

Type-II superconductors are usually alloys, and cover both: the low-temperature superconductors (LTS) and some of the high-temperature superconductors (HTS). Examples of LTS are: NbTi, MgB2 and Nb3Sn, while examples of HTS are: Bi2212, Bi2213, YBCO and REBCO.
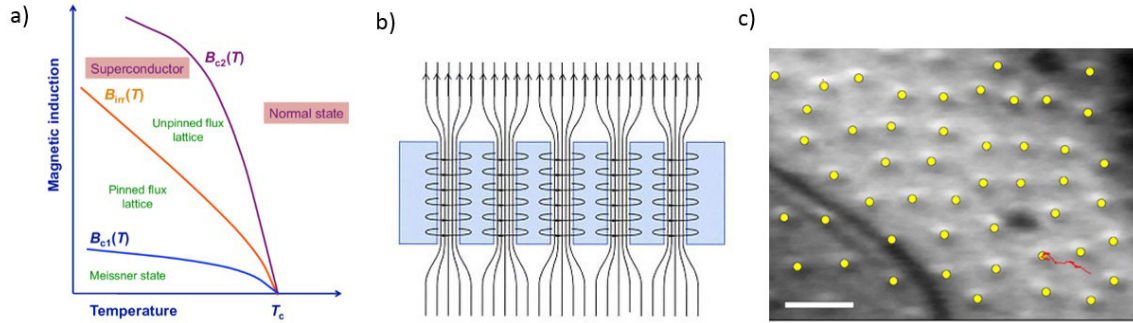
Figure 2.5: Type-II superconductors. On figure a), the critical surface for type-II superconductors is shown. As it can be seen, there is two critical fields instead of one. In the first, the Meissner effect is the governing effect. If the external field increases beyond this point ($B_{C1}$), the Meissner effect is no longer valid, and the magnetic field penetrates the bulk of the superconductor through discrete vortexes, as shown in figure b). Figure c) shows a Lorentz microscope image of flux line distribution in an Nb thin film at 4.5 K, image taken from Sow et al

### 2.1.4 Practical superconductors

As of 2018, the list of confirmed superconducting materials is exceeds one thousand [40, 41, 42, 43], every year material science, chemist and engineers, share their discoveries to the scientific community. The list is large and it keeps growing, nevertheless, this do not implies that all of them could be use for practical applications, where the material should satisfy the following minimum requirements:

- The material should be able to be produced in wires, tapes or cable form.

- The material should be able to be produced in long-lengths.

- If heat treatments are required, the temperatures and pressures should be reasonable in order to be used in coils.

- The critical parameters should be large enough, in order to be of practical use.

- The manufacture procedure should be reliable and reproducible.

- The production cost should be reasonable.

This requirements sets a boundary, that only a few materials satisfy, namely NbTi, $MgB_2$, $Nb_3Sn$, Bi2212, Bi2223, YBCO and REBCO. The National High Magnetic Field Laboratory, at Florida State University, actively researches the performance and characteristics of superconducting materials. The figure 2.6 [44], shows the lattes results obtained on the characterization of the practical superconductors. The graph shows the $J_C$ vs B for different wires and tapes.

## 2.2 Superconducting cables

After Kamerlinh Onnes discovered the superconductivity, he planned to used superconducting wires to power magnets. Unfortunately, the superconducting wires he used, was made of Pb [45], a type I
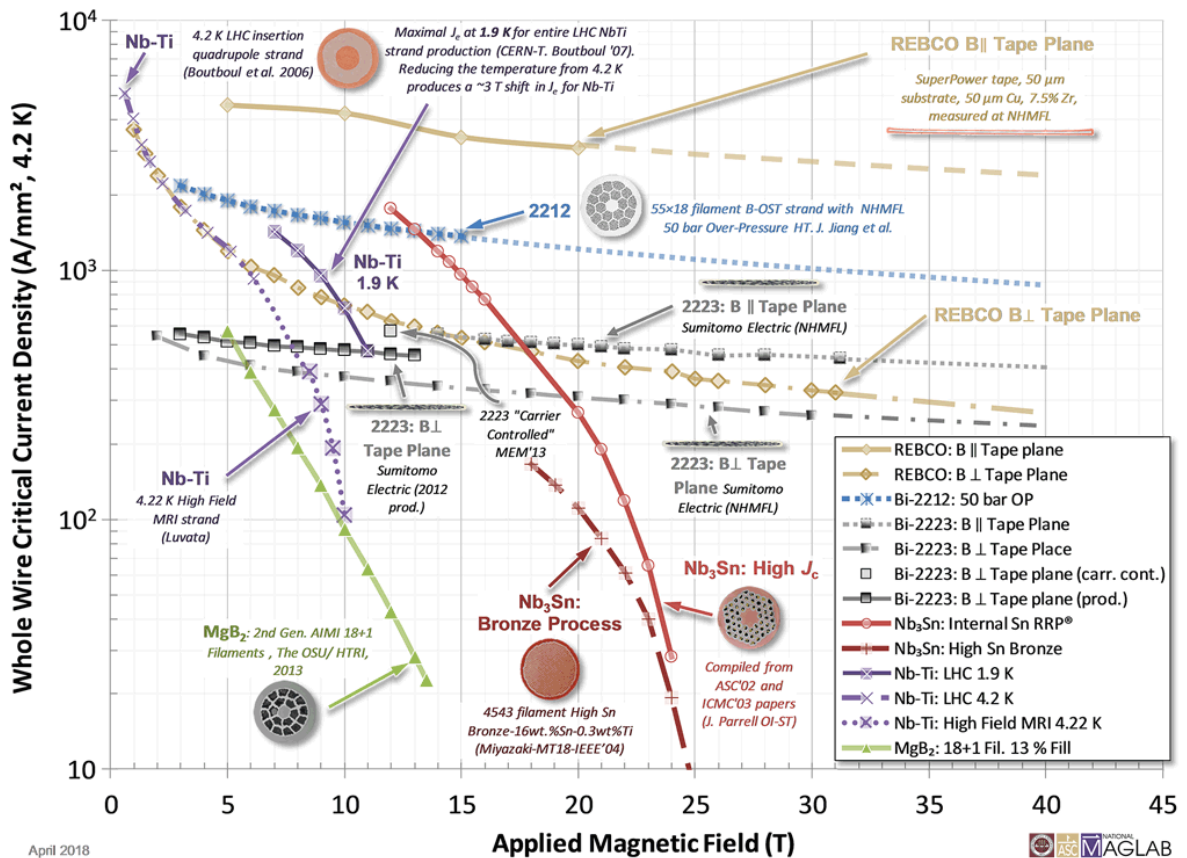
Figure 2.6: Critical current densities for practical superconductors.New data, April 2018.

superconductor characterized by having a very small critical magnetic field (60 mT [30]), which make it impossible to compete with standard copper wires.

With this mind, a new revolution in material science began. In late 1950s, the first superconducting wires for magnet construction were produced in industry. Short after, the first magnets were produced using NbZr wires [46]. Short after, superconducting wires made of $Nb_3Sn$, an inter-metallic allow, were produced. In 1965, with the accidental discovery of Niobium-titanium wires, a new era began, leading to the research and discovery of different materials targeting superconducting wires. In the following sections, the principal requirements for superconducting wires for magnet applications, and the different types of cables are described.

## 2.2.1    Single wires

As it was discussed on the previous section, from the long list of superconductors, only a few can be used for practical applications: NbTi, Nb3Sn, MgB2 and Bi2212[a]. From this group: NbTi, Nb3Sn, MgB2 and Bi2212 can be produced in wire form and in relatively long-lengths (2-3 km). While YBCO can only be produced in tape form. The fact that the superconductors can be produced in wires, spans

---

[a]The HTS technology has improved in recent years, the recent top current densities achieved by round Bi2212/Ag wire are over 550 $A/mm^2$ at 4.2 K and a field of 15 T [47, 48, 49]

their application, even with the mechanical limitations of the superconductor itself. This wires, are not made exclusively of pure superconductor, they make use of a thermal stabilization materials, usually copper[b].

The use of pure superconducting wires in superconducting magnet is forbidden. The wires would experience flux flow resistance, i.e., if a current flows through an ideal type II superconductor which is exposed to a magnetic field (from the neighboring wires in the coil), heat is generated as a response to the flux jumps. The current density ($\vec{j}$) exerts a Lorentz force on the flux lines ($\vec{B}$), and causes them to move away from their pinning centers ($\vec{\nu}$) and across the superconductor. The motion is perpendicular to the current and to the field, and is described as a viscous motion that leads to heat dissipation [50, 51, 52], even when the current flows without resistance. The heat dissipated may increase the temperature of the superconductor beyond the critical temperature, since the resistivity of most of the superconductors in their normal state is relatively high (It's actually larger than copper resistivity), it would end in a quench. Figure 2.7, shows the flow resistance mechanism.
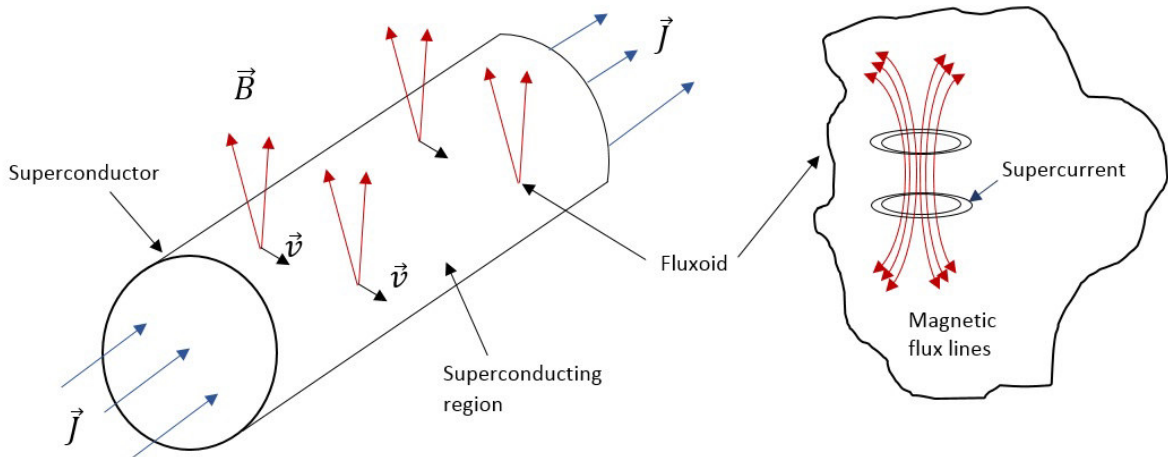


Figure 2.7: Flux flow resistance in a hypothetical pure superconducting wire.

As the motion of the fluxoids is related with heat dissipation, we could capture the fluxoids into pinning centers and avoid the flux flow resistance. In practice, and depending on the superconductor, this usually done by adding impurities to the Crystal structure. For the NbTi superconductor, impurities and Ti precipitates in the $\alpha$-phase are the two major pinning centers [23], while for Nb3Sn, the pinning could be created artificially by using highly energetic radiation, or nano-inclusions [53, 54, 55]. On HTS, the most important pinning center are strong layering and structural defects such as dislocations and grain boundaries [56].

Swartz et. al., [57] showed that, only thin superconductor filaments are stables against flux jumps. For the NbTi superconductors, the suggested diameter has to be less than 100 $\mu$m [32]. The NbTi wires that will be used for making the CIC for the JLEIC dipole, are composed of 7400 filaments, 9 $\mu$m each.

[b]For superconductors like MgB2, a Monel 400 sheath may be used, along with a copper core for thermal stabilization.

## 2.2.2 Rutherford cable

The Rutherford cable is a 2D geometrical arrangement of superconductors, either NbTi or Nb3Sn, used to generate magnetic fields on superconducting magnets. It is used in most of the superconducting magnets of the major particle accelerator laboratories around the world [58, 59, 60]. The topology of the cable is based on twisting and compressing the wires into a flat two-layer cable [61]. It was design to be permeable to liquid helium, although in practical applications the wires are required to be fixed in position by applying an epoxy layer, this restricts the wires to be in direct contact with the coolant, forcing the heat transfer mechanism to be conduction cooling through the epoxy: helium-epoxy-Rutherford. This topology was originally designed to target "$Cos(\theta)$" magnets, where the block coils are meant to be trapezoidal to properly approximate the azimuthal subdivision of the current shells in the magnet [62]. This topology has very high performance on this type of magnets, this is precisely at the same time its drawback.
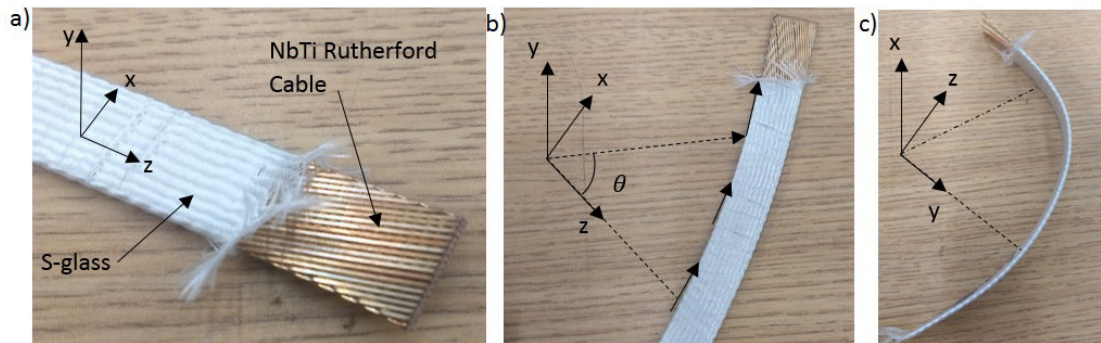


Figure 2.8: Rutherford cable and common bends. On figure a) a straight section of NbTi Rutherford cable covered with S-glass fiber. In the figure, the cable lies on the XZ coordinate plane. Figure b) shows the natural limitations for the Rutherford cable to bend on the XZ plane. On the other hand, figure c) shows that the cable can be bend easily on the ZY plane.

Figure 2.8 shows a normal condition NbTi Rutherford cable protected by S-glass fiber. As it can be seen in figure, the cable does not allows the same bending radius on different bend directions. The minimum bend radius of a bend in the plane XZ (figure 2.8b) at which the registration of the wires is avoided, is considerably larger than a bend along the normal plane of the cable, plane ZY, figure 2.8c) . For applications where complex wind forms are required, a different cable topology is recommended. In such case, the requirements and limitations of a given application will have determine which cable topology is convenient.

## 2.2.3 Cable-in-conduit

The Cable-in-Conduit conductor, is a type of superconducting cable used to generate high-strength magnetic fields for applications such, fusion magnets [63], wind generators [64], MRI [65], power transmission lines [66], superconducting magnetic energy storage devices [67], etc.

This technology, offers a different approach to the conventional Rutherford cable. Two main

properties mark the difference: 1) In the CIC conductor, the superconducting wires are inserted into a tube that transports coolant and provides thermal stability, i.e, the CIC is its own cryogenic vessel [68]. While in the Rutherford cable, the wires are not in direct contact with the coolant. 2) The geometrical distribution of the wires on the Rutherford cable, naturally limits its degrees of freedom for bending the cable in any direction other than the planar, producing instabilities of the wires [69], see figure 2.9.The geometrical distribution of the superconducting wires in the CIC conductors, naturally avoids this issue, increasing the allowed degrees of freedom during winding operation [70]. In the following section, the CIC conceptual design and general procedure for its development will be thoroughly described .

| Description | Rutherford cable behavior | Instability |
|---|---|---|
| Hard-bending | | Opening |
| Twist favourable direction | | Tightening |
| Twist unfavourable direction | | Decabling |
| Soft-bending | | Strand pop-out |

Figure 2.9: Rutherford cable instabilities for winding. Source: Image taken from Pulikowski et al. [69].

## 2.3 CIC conductor technology

Since Cable-In-Conduit conductor was proposed by Morpurgo *et*. *al*. in 1975 [71], to be used in superconducting magnets for particle accelerators, many designs have been proposed, and others developed and applied. Different groups around the world focused on different applications. In each design, different geometries, materials and superconductors were used. This are some of the successful development cases, and their major issues:

- The WENDELSTEIN 7-X Technical group, developed a 16 kA NbTi aluminum jacket CIC, for the magnets of the stellarator system. One of the limits of this design, is the relative large "minimum bending radius" capabilities, of 0.2 m. The manufacture procedure to produce the CIC, involved a co-extrusion of the superconductor and the aluminum jacket, and a heat treatment at relative high temperatures. As a consequence, they experience a current degradation of 10%, as compared with virgin strand measurements [72].

- Bottura *et. al.* developed a 13kA fast-ramping CIC for targeting SIS-100 magnets of the International Accelerator Facility at GSI and . In their design, the CIC is composed of a single-layer of coated-insulated superconductors (NbTi Or Nb3Sn), cabled around a spiral tube [73]. A drawback of this design is that the coating in between the strands, limits the current sharing in a quench scenario . When taken to practice, the Nb3Sn CIC showed formation of micro-cracks, leading to irreversible degradation of the current carrying capabilities.

- Fisher *et. al.* developed a version of CIC (without jacket), to be used in the SIS-100 dipoles for the FAIR project [74].In this design, the CIC does not have an outer jacket, losing the built-in capabilities of a cryogenic vessel, and exposing the superconductors to damage during winding operation. Other drawback of this design is large current degradation (up to 30%) in the cable due to induced eddy currents.

- Bruzzone *et. al.* developed a 40kA Nb3Sn CIC prototype cable for the toroidal field coils for the tokamak nuclear reactor. The cable make use of austenitic steel jacket, and packed multi-filamentary sub-cables arrangements [Bruzzone]. In practice, the manufacturing process associated with the cabling of the wires, produced a current degradation of about 15% [75]. Although they observed no relevant current degradation during operation, the bulk geometry of the conductor and the large thickness of the jacket limits its capability for small bending radius.

- Similarly, Takahashi *et.al.* developed a Nb3Sn CIC for ITER toroidal field coils. In their design, they recognize that there is a persistent current degradation associated with the manufacturing process, in which due to the lack of symmetry and confinement of the superconducting wires, they periodically experience strand bending, leading to current degradation [76].

From the latter, we can conclude that some of the main factors that could compromise the CIC integrity or its performance are:

- Mechanical deformations on the strands produced during manufacture procedures.

- Dangerous thermal treatments experienced by the superconductor post and during cable fabrication.

- Lack of proper support to the superconductors allows movement and deformation during operation.

- Election of materials for the jacket plays a role for the overall mechanical properties of the CIC.

- An uneven surface for the superconductors to lay, if a multi-layer CIC is needed.

- A large bending radius limits the CIC capabilities and range of use for other applications.

- A lack of outer jacket not only suppresses the self-contain cryogenic vessel property of most of the CIC, but opens a possibility for damage during winding.

With this in mind, the Accelerator Research Lab (ARL) at Texas A&M University, has developed a new CIC technology for high-performance superferric magnets, that provides a cost-effective basis for fabrication of the arc dipoles for the ion ring of the proposed Jefferson Lab Electron-Ion Collider (JLEIC) facility [77, 78, 79]. The CIC-conductor is the central element of the JLEIC dipoles design, its unique benefits make it suitable for a large number of practical applications, including high ramping magnetic fields [80].

In the following subsections the development of CIC conductor will be fully described, starting from:

1. A general conceptual design,

2. An analytical model for developing optimum CIC conductors for a given application,

3. An experimental quest for determining the effects of different materials on CIC prototypes,

4. And the short-length sample preparation procedure and testing.

From this, a quality control procedure was developed and implemented to assess the performance of the CIC conductor and its components, after manufacture, during operation and after bends. Moreover, a mechanical characterization to determine the spring-back effect and the required force for drawing is presented. The latter constitutes the so-called standard procedure for testing our CIC conductor and has become a crucial part for the development of long lengths of CIC conductor.

## 2.3.1 Conceptual design

Four basic components integrate the CIC technology developed at Texas A&M University: 1) The superconductor[c]. 2) The high strength, thin wall, non-reactive, inner tube made of perforated 316L Stainless Steel. 3) The stainless steel thin foil wrap, that acts as a slip plane for the conductors, and 4) The high strength outer tube, that provides protection and support to the superconductors, see figure 2.10.

To form the CIC conductor, the superconducting wires are spiral-cabled around the thin-wall high-strength perforated inner tube, keeping a constant and uniform twist-pitch. In this process, the superconductors are always in touch with the inner tube, and a space (or gap) is led in between neighboring wires azimuthally. A thin stainless steel foil is wrapped around the wires without overlap. We will refer from now on the assembly composed of the inner tube, the superconducting wires and the foil, as the *core*. Once the core is ready, is inserted into a high-strength outer tube that protects the superconductors, adds mechanical support, and constitutes the outermost wall of the self-confined cryogenic vessel. To finalize the CIC cable, the gap in between the superconducting wires has to be closed, in order to provide shoulder-to-shoulder contact between neighboring wires. This is a critical

---

[c]Either NbTi, MgB2, Nb3Sn or Bi2212 wires. The superconductors is selected based on the field requirements
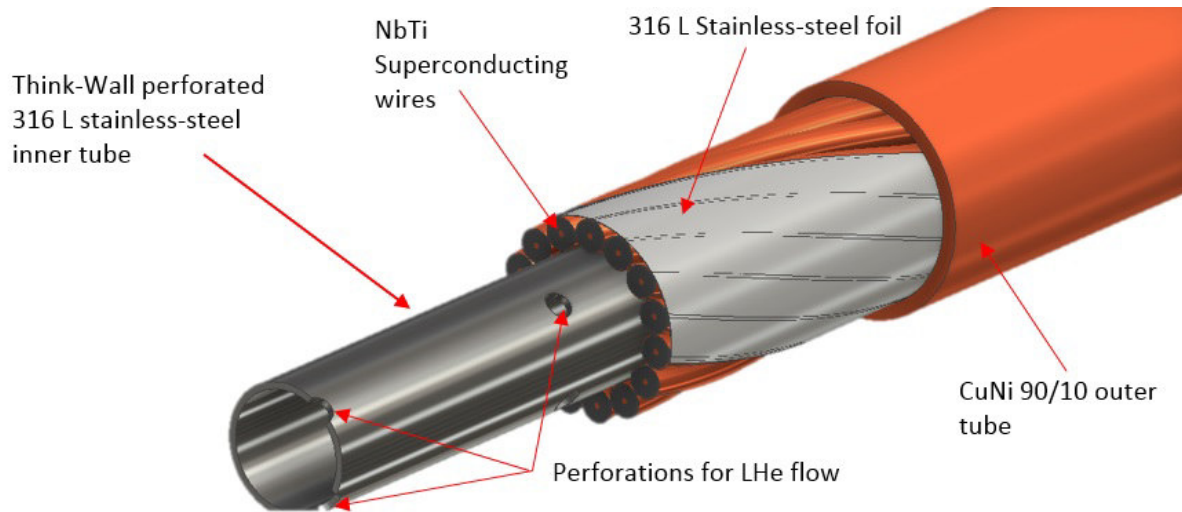
Figure 2.10: Sketch of a NbTi Cable-in-Conduit conductor for the JLEIC dipoles.

requirement to allow for current sharing if a quench event is developed. To close the gap, the outer tube containing the core has to be drawn. The final dimension of the CIC conductor is specified by the required drawn factor.

This technology, allows the superconductors to be formed in complex windings at a relatively small bending radius (25 mm), provides direct contact between wires, facilitating current sharing in case of a quench event is developed, and it provides mechanical support to conductors while serving as its own cryogenic vessel.

## 2.3.2 Structural materials for CIC conductor

Once the CIC conductor global dimensions have been specified, and the superconductor its been selected in order to meet the field requirements for a given application, the following step is to specified the proper materials for the inner tube, the slip plane foil, and the outer tube. The selected materials must fulfill the following requirements:

- Must be non-reactive and ought to be strong enough to provide proper support to the superconductors.

- Must be ductile, and preserve its form during small radius bending.

- Must perform at cryogenic temperatures without cracking or collapsing.

- Must be cost-effective

- Must support high pressures that could be developed in case of a quench event happens.

- Must be corrosion resistant

| Material | wall thickness (in) | Ultimate tensile strength ($N/mm^2$) | Hardness (HB) |
|---|---|---|---|
| Brass C260 | 0.006 | 275 | 77 |
| | 0.010 | 275 | 77 |
| Stainless-Steel 316L | 0.020 | 483 | 217 |
| | 0.010 | | |
| Monel 400 | 0.020 | 482 | 215 |
| Copper Nickel 90/10 | 0.020 | 280 | 70 |
| Copper | 0.020 | 210 | 35 |

Table 2.1: Candidate materials for the inner and outer tube of CIC conductors

With this in mind, there are a couple of candidate materials for the inner and outer tube. It is mandatory to experimentally determine the performance of the CIC using this materials.

In the following experiments, the integrity and overall mechanical performance of the CIC conductor will be studied, considering Brass c260 as the material for the inner tube. The wall thickness of the inner brass tube and OD of the cable were varied to evaluate two important engineering features of CIC cables: indentation and shoulder-shoulder contact between the wires in the cable. Silicon bronze wire was used as a substitute for NbTi wire in some cases to save some cost as silicon bronze wire is a good mechanical substitute for deformation studies.

Several tests were done combining four different drawing dies (.2583, .256, .254 and .252) with cables designed with a brass inner tube with two different wall thickness (0.006 and 0.010), leaving the rest of the CIC variables constant, e.g.,. number of wires, material of the wires, cabling twist pitch and SS-foil wrapping angle.

For each drawing die, two CIC cables (4 feet long each) were drawn, one per each wall thickness, 0.006" and 0.010". Each CIC was cut in 4 samples, 9" long each. Three were bent 180° (+20° over-bend at a 1.75" radius and an angular velocity of 150°/min); the forth sample (remaining straight) was transversely cut using EDM. Table 1 describes the results of each 9" long sample.

| ID | Drawing Die (in) | Wall Thickness (in) | Test | Results |
|---|---|---|---|---|
| 1 | 0.2583 (0.8% CC) | 0.006 | Straight (EDM) | No visible damage of wires, SS foil or Inner tube 50% of wires show azimuthal contact Low wire indentation into the inner tube Inner tube did not collapse |
| 2 | 0.2583 (0.8%) | 0.006 | Bend (Dissect) | No visible damage of wires, SS foil or inner tube SS foil spread at the bend (2 mm) small indentation from wires into inner tube Inner tube did not collapse Azimuthal gap between strands still open |
| | | | | Continued on next page |

**Table 2.2 – continued from previous page**

| ID | Drawing Die (in) | Wall Thickness (in) | Test | Results |
|---|---|---|---|---|
| 3 | 0.2583 (0.8% CC) | 0.006 (Dissect) | Bend | No visible damage of wires, SS foil or inner tube<br>The SS foil did no spread<br>Errors during bending technique damage the wires<br>Poor indentation at the inner tube<br>Inner tube did not collapse |
| 4 | 0.2583 (0.8% CC) | 0.006 | Bend (Dissect) | No visible damage of wires, SS foil or inner tube<br>The SS foil wrapping did not spread<br>Poor indentation at the inner tube<br>Inner tube did not collapse |
| 5 | 0.256 (1.63% CC) | 0.006 | Straight (EDM) | No visible damage of wires, SS foil or inner tube<br>Wire azimuthal contact is in 90% of the wires<br>Better indentation at the inner tube<br>Inner tube did not collapse |
| 6 | 0.256 (1.63% CC) | 0.006 | Bend (Dissect) | No visible damage of wires, SS foil or inner tube<br>The SS foil wrapping spreads at the bend<br>Better indentation at the inner tube<br>Inner tube did not collapse |
| 7 | 0.256 (1.63% CC) | 0.006 | Bend (EDM) | No visible damage of wires, SS foil or inner tube<br>Debris caught in the cable damage the sample<br>Better indentation at the inner tube<br>Inner tube did not collapse |
| 8 | 0.256 (1.63% CC) | 0.006 | Bend (Dissect) | No visible damage of wires, SS foil or inner tube<br>The SS foil wrapping spreads at the bend<br>Better indentation at the inner tube<br>Inner tube did not collapse |
| 9 | 0.254 (2.4% CC) | 0.006 | Straight (EDM) | No visible damage of wires, SS foil or inner tube<br>One wire penetrate into the inner tube<br>Wire azimuthal contact compromised<br>Wire indentation compromised<br>Inner tube did not collapse |
| 10 | 0.254 (2.4% CC) | 0.006 | Bend (Dissect) | No visible damage of wires, SS foil or inner tube<br>One wire penetrate into the inner tube<br>Wire azimuthal contact compromised<br>Wire indentation compromised<br>Inner tube did not collapse |
| 11 | 0.254 (2.4% CC) | 0.006 | Bend (EDM) | No visible damage of wires, SS foil or inner tube<br>One wire penetrate into the inner tube<br>Wire azimuthal contact compromised<br>Wire indentation compromised<br>Inner tube did not collapse |

**Table 2.2 – continued from previous page**

| ID | Drawing Die (in) | Wall Thickness (in) | Test | Results |
|---|---|---|---|---|
| 12 | 0.252 (3.17% CC) | 0.006 | Straight (EDM) | No visible damage of wires, SS foil or inner tube<br>Azimutal contact present in 100% of wires<br>Much better indentation<br>Inner tube did not collapse |
| 13 | 0.252 (3.17% CC) | 0.006 | Bend (EDM) | No visible damage of wires, SS foil or inner tube<br>One wire penetrate into the inner tube<br>Inner tube compromised<br>Inner tube did not collapse |
| 13 | 0.252 (3.17% CC) | 0.006 | Bend (EDM) | No visible damage of wires, SS foil or inner tube<br>One wire penetrate into the inner tube<br>Inner tube compromised<br>Inner tube did not collapse |
| 14 | 0.252 (3.17% CC) | 0.006 | Bend (Dissect) | No visible damage of wires, SS foil or inner tube<br>One wire penetrate into the inner tube<br>The inner tube compromised<br>Inner tube did not collapse |
| 15 | 0.256 (1.63% CC) | 0.010 | Straight (Dissect) | No visible damage of wires, SS foil or inner tube<br>Much better indentation<br>The SS foil spreads at the bend<br>Inner tube did not collapse |
| 16 | 0.256 (1.63% CC) | 0.010 | Straight (EDM) | No visible damage of wires, SS foil or inner tube<br>Azimuthal contact present in 100% of wires<br>Slight indentation at the inner tube<br>Inner tube did not collapse, but it ovals |
| 17 | 0.256 (1.63% CC) | 0.010 | Bend (Dissect) | No visible damage of wires, SS foil or inner tube<br>Slight indentation at the inner tube<br>Slight oval deformation on the inner tube<br>Inner tube did not collapse, but it ovals |
| 18 | 0.256 (1.63% CC) | 0.010 | Bend (Dissect) | No visible damage of wires, SS foil or inner tube<br>The SS foil wrapping spread at the bend<br>Slight indentation at the inner tube<br>Inner tube did not collapse, but it ovals |
| 19 | 0.256 (1.63% CC) | 0.010 | Bend (EDM) | No visible damage of wires, SS foil or inner tube<br>One of the wires penetrate into the inner tube<br>Slight indentation at the inner tube<br>Inner tube did not collapse, but it ovals |
| 20 | 0.254 (2.4% CC) | 0.010 | Straight (EDM) | No visible damage of wires, SS foil or inner tube<br>Azimuthal contact present in 100% of wires<br>Slight indentation at the inner tube<br>Inner tube did not collapse, but it ovals |

**Table 2.2 – continued from previous page**

| ID | Drawing Die (in) | Wall Thickness (in) | Test | Results |
|---|---|---|---|---|
| 21 | 0.254 (2.4% CC) | 0.010 | Bend (Dissect) | No visible damage of wires, SS foil or inner tube<br>Azimuthal contact present in 100% of wires<br>Slight indentation at the inner tube<br>Inner tube did not collapse, but it ovals |
| 22 | 0.254 (2.4% CC) | 0.010 | Bend (Dissect) | No visible damage of wires, SS foil or inner tube<br>Azimuthal contact present in 100% of wires<br>Slight indentation at the inner tube<br>Inner tube did not collapse, but it ovals |
| 23 | 0.254 (2.4% CC) | 0.010 | Bend (Dissect) | No visible damage of wires, SS foil or inner tube<br>Azimuthal contact present in 100% of wires<br>Slight indentation at the inner tube<br>Inner tube did not collapse, but it ovals |
| 24 | 0.252 (3.17% CC) | 0.010 | Bend (Dissect) | No visible damage of wires, SS foil or inner tube<br>Brass and metal debris caught damage the tube<br>Azimuthal contact present in 100% wires<br>Inner tube did not collapse, but it ovals |
| 25 | 0.252 (3.17% CC) | 0.010 | Bend (Dissect) | No visible damage of wires, SS foil or inner tube<br>Larger indentation<br>Azimuthal contact present in 100% wires<br>Inner tube did not collapse, but it ovals |

Table 2.2: Test results on CIC with two different size for the inner tube, and drawn to various sizes with different drawing dies.

Optical analysis indicated that most of the .006 samples suffered some kind of damage since the thinner wall makes the brass tube more susceptible for undesired deformation. Even with the smallest compaction factor (.8%), two out of four samples suffered irreparable damage of the inner tube. The two other samples had poor indentation of the wires (against the inner tube) and poor shoulder-shoulder contact, which makes the combination 0.006-0.2583 not a good choice. Drawing to 0.256 and 0.252 appeared to greatly improve the shoulder-shoulder contact (90% for the 0.256 wire draw pass and 100% for 0.252). Theses samples also showed very good indentation, but deformation was seen to be always present in cables with the 0.006 brass tube.

On the other hand, the 0.010 brass wall thickness appeared to be more robust and less susceptible to deformation. Only one sample suffered wire penetration which was caused by brass and steel debris between wires that caused a localized deformation that behaved totally different from the 0.006 wires penetration case. This shows the importance of maintaining a clean environment while cabling, since small metallic debris can jeopardize the entire cable.

The robustness nature of the 0.010 brass wall, which makes it the best candidate, also affects its ability to be indented by the wires, at least with the available drawing dies used. The indentation plays an important role for avoiding transverse slippage of the wires causing heat and eventually driving a

quench.

From this work we concluded the 0.010 brass wall thickness is a better candidate than the 0.006 wall thickness and recommended the use of the 0.254 and 0.252 drawing dies, as both of them offered optimum shoulder-shoulder contact between wires and decent indentation.
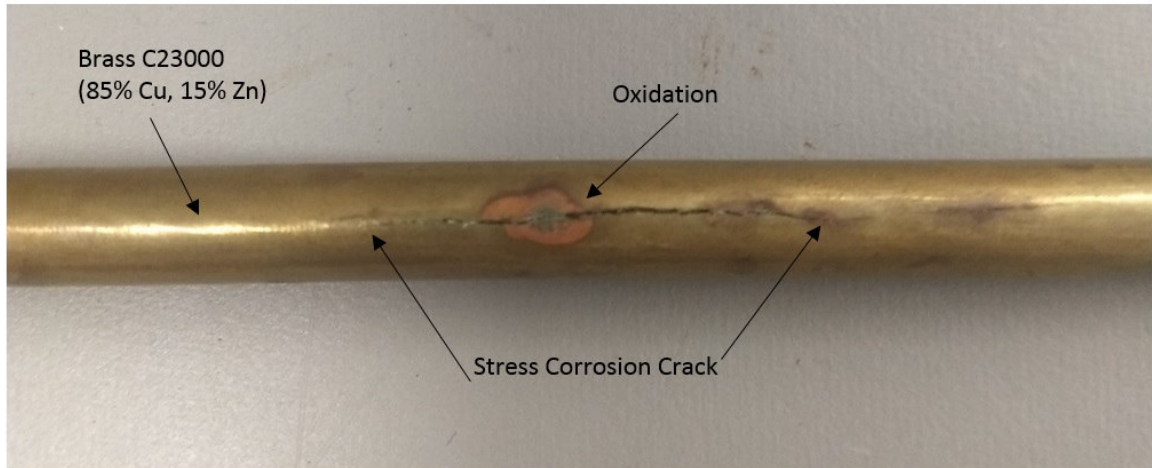


Figure 2.11: Stress corrosion cracking on Brass C23000 Sheath for CIC.

### 2.3.3 Stress corrosion cracking

Unfortunately, metals are subject to corrosion [d]. Corrosion can take many forms; the form that concerns us here is the interaction of corrosion and mechanical stress to produce a failure by cracking.

The Stress corrosion cracking (SCC) is the cracking induced from the combined influence of tensile stress and a corrosive environment. The impact of SCC on a material usually falls between dry cracking and the fatigue threshold of that material. This type of stress corrosion cracking is present in samples that used Brass C23000 sheath, and have been storage for a year [81].

The most effective means of preventing SCC are: 1) storage properly with the right materials and environment; 2) reduce stresses, a stress-relieve process is often recommended; 3) remove critical environmental species such as hydroxides, chlorides, and oxygen; 4) and avoid stagnant areas and crevices in heat ex changers where chloride and hydroxide might become concentrated. Low alloy steels are less susceptible than high alloy steels, but they are subject to SCC in water containing chloride ions.

Chloride stress corrosion is a type of inter-granular corrosion and occurs in austenitic stainless steel under tensile stress in the presence of oxygen, chloride ions, and high temperature [82]. This type of corrosion could affect the inner tube, therefore, the CIC has to be stored in a chloride-free location.

---

[d]The noble metals, such as gold and platinum are an exception to this, but they are rather too rare for common use

## 2.3.4 Manufacturing procedure for short-Sample development

The main purpose of the short-sample development is to provide a set procedures that will lead to current-degradation-free CIC conductors. For this, a number of point must be address:

1. The manufacturing procedure must be easily to extrapolated into long-length production, while preserving the CIC components integrity i.e., a model that will serve as a guide for making reproducible sections of CIC conductor.

2. A quality control procedure must be developed to assess the performance of the CIC conductor at various possible failures scenarios, i.e., a set of measurement that will provide feedback on the integrity of the superconductor, inner tube and outer tube.

3. It must provide a full description of the mechanical behavior. What phenomenons takes place during drawing and bending procedures. What is the required drawing force for a given CIC conductor? What is required torque for bending the CIC? What major effects take place during bending? How big is the the spring-back effect and how it can be corrected?

4. The development and characterization of special tools is required to form the CIC into complex bend, maintaining high tolerances and reproducibility.

### Cabling procedure

The cabling procedure for research purposes is characterize by producing short-segments of CIC conductors. This offers two possibilities, it reduces the equipment for large operations, and provide insights of what would it be in long-lengths. The short-length production make use of a hand-stranding machine, especially designed to make up to 2 m long segments, a swagger machine, and a drawing bench, as depicted in figure 2.12.

In the development process, a 1 m long hand-stranding device containing 15 channels, was developed to guide the superconductors around the inner the tube, see figure 2.12 a). In this process, once the superconductors are attached to the inner tube, a 5 cm section is solder to fix the superconductors on place. The superconductors are then hand-cabled, meaning that the device is pulled-and-twisted manually, maintaining a 3 in twist-pitch. The process is repeated for the length of the cable. At the end, the wires are secured and soldered. A protective layer of high-strength stainless-steel is wrapped around the cabled wires maintaining a quarter millimeter gap between turns. Once the core is finished, is inserted into a high strength straight outer tube. To reduce the gap between the core and the outer tube, and to lock the superconductors, the cable is swagged in a hammer-swagger machine, as shown in figure 2.12 c). In this process, two things limit the long-length production:

- The hand-cabling process lacks of accuracy for long-length production, and it requires a long straight section.

- An automatic drawing and spooling system is required for the desired lenght. The maximum length that could be drawn in the draw-bench is 14 m.

### Cable-In-Conduit drawing

Tube drawing is the last step in the CIC production line. In this process, the outer sheath of the CIC conductor is uniformly reduced by means of a drawing die, see figure 2.13. In this process, the
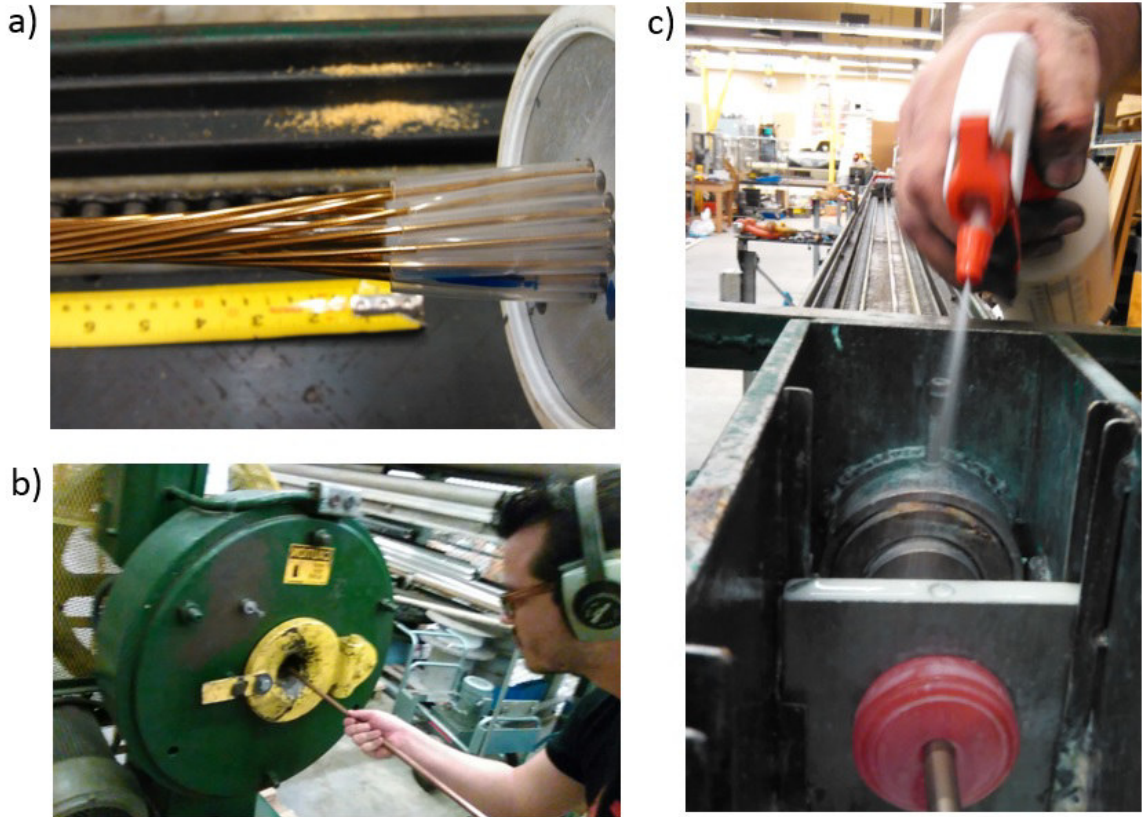
Figure 2.12: CIC conductor short-sample development process. On a), a hand-stranding machine for cable the superconductors around the inner tube. On b) a hammer-swagging machine used to point the CIC conductor, prior drawing process. On c) a two-stage drawing box drawing the CIC conductor.

thickness of the tube is not affected [83]. Volume conservation implies an increase in the lenght of the outer tube. In this process, the amount of reduction depends on the material and its manufacturing process. For our purposes, drawing reductions greater than 12% will be avoided, and if needed, a stress-relieve treatment will be applied between drawings.

The amount of reduction is a key element that must be computed properly, on one hand, the amount of reduction affects the mechanical properties of the tube [84], adding strains and stresses [85] that could lead to the collapse or cracking of the tube. On the other hand, the amount of compaction, locally deforms the superconductors. If the amount of reduction is large, the spring-back properties of the CIC and the torque required for bending the samples will change dramatically. This, in turn, could affect the forming capabilities of the robotic benders, by exceeding the values for the operational torque in the stepper motors.

## 2.3.5 Mechanical characterization

The previously described manufacturing procedure, is meant to be extrapolated to long-lenght production. In both cases, the CIC conductor will be the same i.e., it will be described in terms of the same mechanical properties. Two major phenomenons govern the mechanical behavior of the CIC: the first, is the spring-back effect that the cable experienced when is bend in small bend radius. The second,
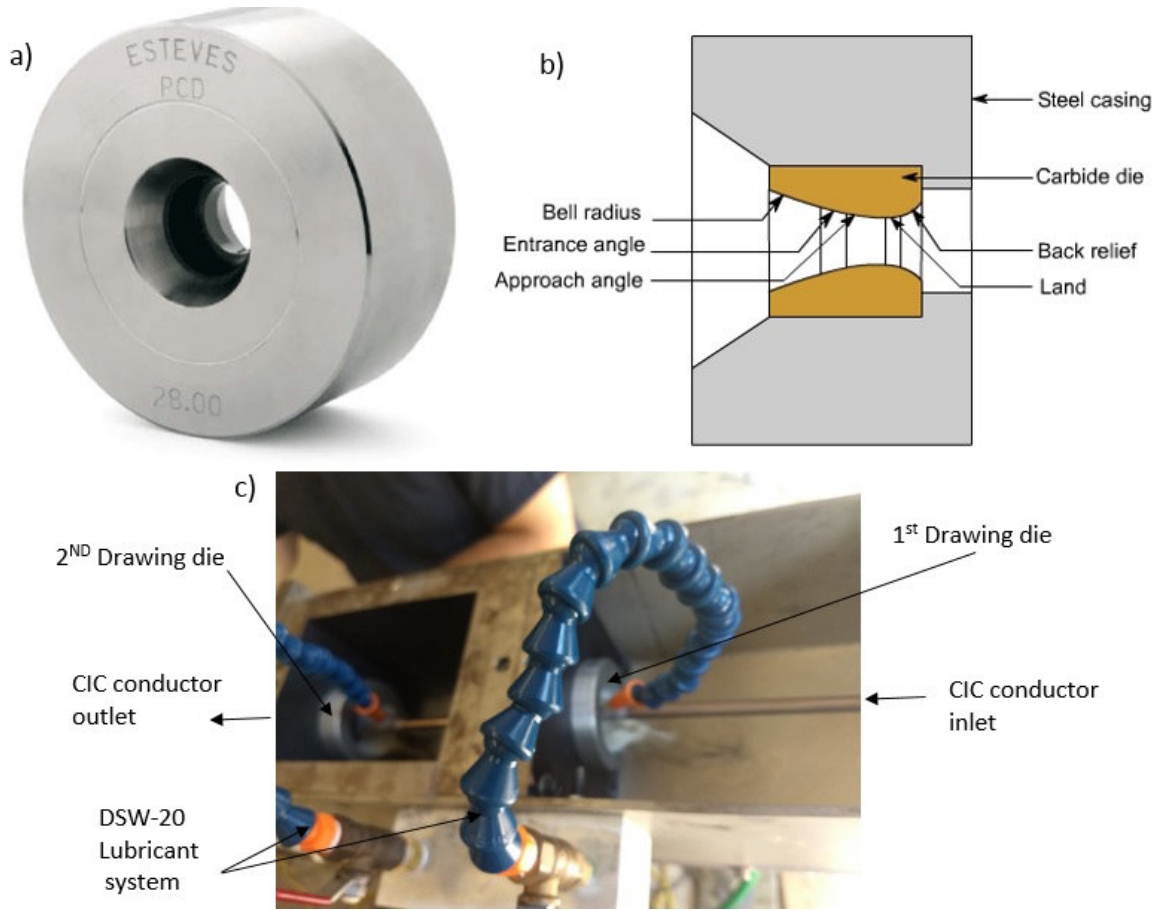
Figure 2.13: Drawing process for Cable-in-conduit conductor.

is related with the manufacturing procedure it self, and its determining the force required to draw the cable to the desired final dimensions. Both effects will be addressed shortly.

**Spring back effect**

In order to correct the un-desired spring back effect, a series of samples containing "dummy wires" with the right dimensions i.e,. 1.2mm OD were done. The dummy material used is Silicon-Bronze weld wire, which happened to have a very close tensile strength as the NbTi wire at room temperature [86, 87] . The inner tube use in this experiments is 0.1875" OD brass 0.010" wall thickness. The wire is cable using the usual 3" twist pitch and after is cable the SS foil is wrapped around. The samples were bend in a 1.75" bend radius die, at 150°/min, in the 180-200°region. By means of a open source software the spring back angle was measure relative to the direction of the left leg of each sample. Picture shows the amount of spring back after adding 10°over bend increments. A 20°over bend happen to be close but not enough to produce an effective 180°bend.

Besides the spring back angle, the bending radius on each sample was measure manually by means of a protractor tracing perpendicular lines along the arc. The measurement revealed that the bending radius of the bending die has to be change. An interpolation based on different measurements using a 2", 1.75" and 1.25" bending radius die, predicts that the bending radius needed to produce a 2" bend is 1.833". The experiment was repeated extending the bending range from 180 to 215. In the
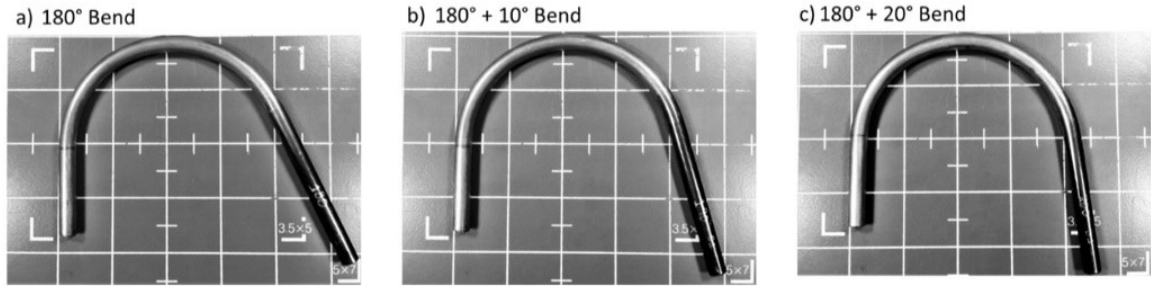
Figure 2.14: Spring-back effect on NbTi CIC conductor. Figure a,b and c) show the level of spring-back base on the over-bend applied to a 180° bend.

experiment Silicon-Bronze wire was replace by actual NbTi superconductor that was post heat treated to reduce stresses.

**Spring-back cause**

In order to identify which element was the main responsible of the spring back or if its a more global collective effect, a sample of CIC using real superconductor was bend using the recommended configuration i.e 1.833" bending die, 150°/min angular velocity at bend and 31.25°(30°works better) over bend. The following picture describe the contribution of the spring back due to individual elements, in the present picture a (-) indicates that the bend opens out, and a (+) indicate the contrary. Figure 2.14 a) shows in the initial state of the CIC.
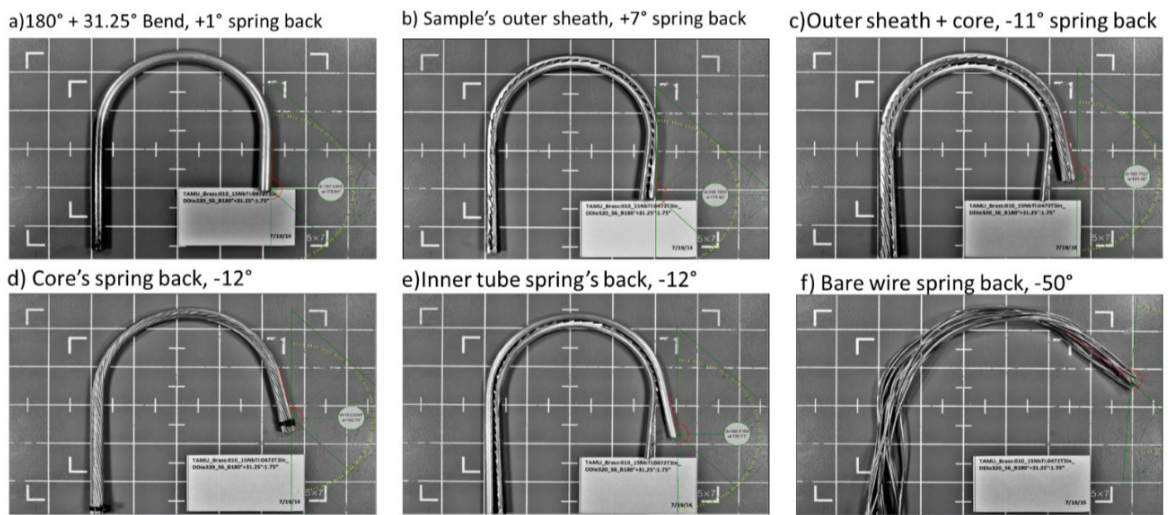


Figure 2.15: Discerning the spring-back effect. Figures a to f, shows the contribution on the spring back, from different components of the CIC conductor. As its shown, the higher contribution comes from the superconductor itself.

The spring back angle was measure revealing +1 spring in. This is not surprising, the sample was over bend 31.25 instead of 30°, confirming the effectiveness of the prediction. In figures 2.14 b), c) and d) a radial dissection was performed on the CIC, in which the outer tube was completely removed,

the spring back angle was measure on the core (CIC without outer tube) revealing that without the outer tube the sample spring backs 12°, so outer tube holds the sample on place, this implies that there is an element pushing out the whole assembly. The spring back angle measure on the dissected outer tube without the core, shows that actually after the 31.25° over bend the tube "springs in" 7°.

In order to determine which element is the responsible of the spring out, the core was dismantle, figure 2.14 e) shows the contribution of the inner tube, (brass 3/16" 0.010" wall), as it can be seen the inner tube springs out 12°, this shows that the mechanical properties of the inner tube have an important contribution to the spring back.
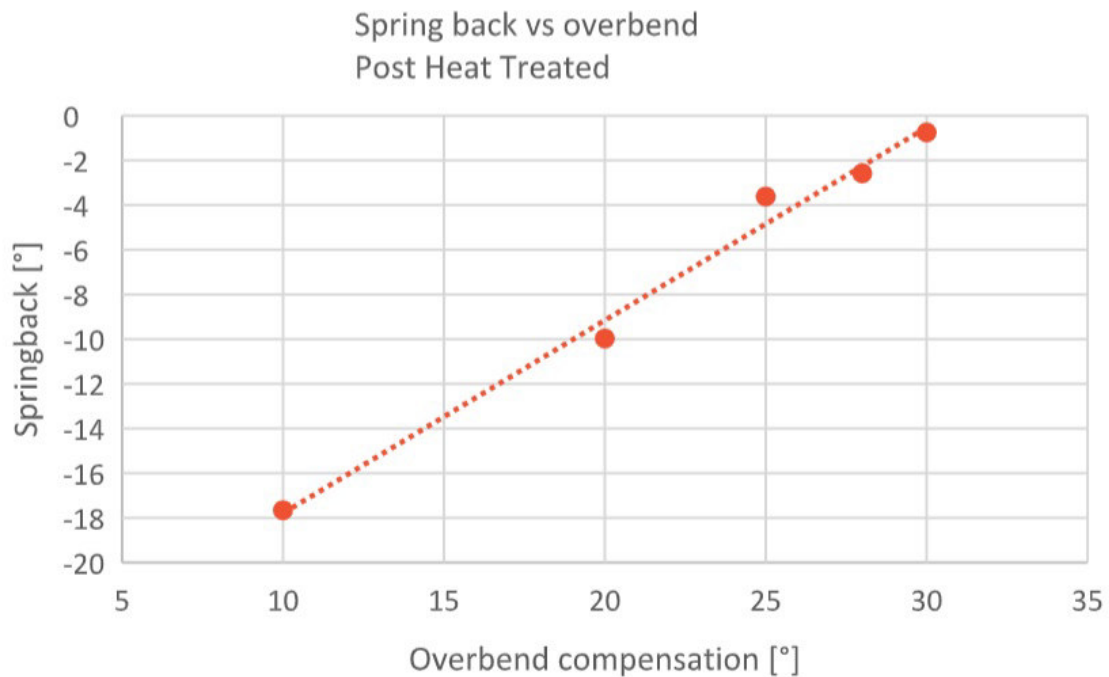


Figure 2.16: Spring-back compensation for a CIC using post-heat treated NbTi wires.

Finally, figure 2.14 f) shows that actually, the element that has the biggest contribution to the spring back is the superconductor. It was found that not annealed wire springs back upto 70°, while post heat treated springs backs little less, 50°. So, the heat treatment is important on the spring back. From now on, we choose NbTi post heat treated.Figure 2.16 shows the spring back vs over bend compensation, for the samples describe above, the experiment predicts that a over bend of 30°(210°total) is needed to provide desire 180°bend. The measurement of the bending radius reveal that the 1.833" prediction actually take us to the desire 2°bend.

## CIC drawing force

The short-sample production, serves to provide a general understanding of the basic phenomenons laying the CIC development. In general, every application would require a costumed made CIC conductor, this implies that the set of defining parameters will be different: Each one would require specific dimensions, different number of superconductors, different twist-pitch, etc. In general, every CIC would make use of a different set of materials, which would affect its mechanical behavior. This matter has to be consider when long-length production is foreseen. An important parameter common

to any of the CIC conductors, is the amount of compaction factor. As it would be seen in further sections, the compaction factor plays a very important role in the performance of the conductor, affecting directly the amount of torque needed to bend the CIC, and deforming the superconductor, which if chosen improperly, could degraded the current or damage the strands. In this subsection, a study of the drawing force is described.
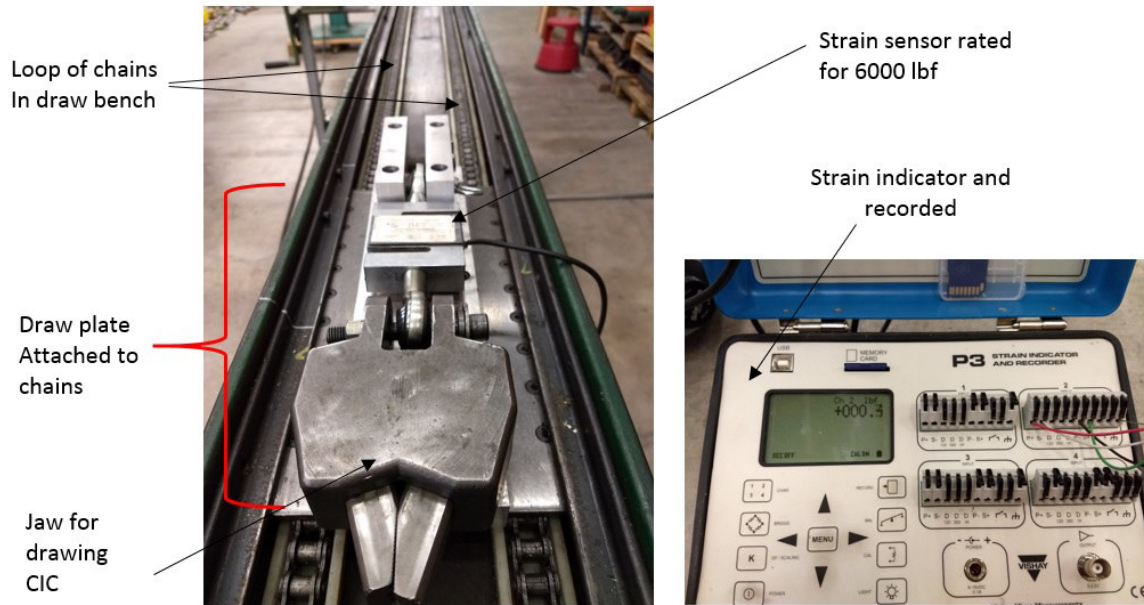


Figure 2.17: Drawing force experiment.

To get useful information that could be extrapolated to any CIC conductor, an experiment varying the compaction factor and determining its corresponding average drawing force is presented. In the experiment, as depicted in figure 3.2, a CIC core is inserted into a oversized outer tube, leaving a radial gap between them. The CIC is then inserted into the drawing box and a draw bench pulls the CIC through the drawing dies. At this point, a large set of drawing dies was used to gradually close the gap until a given compaction is achieved. In this process, the draw bench accommodate a stain gauge connected to a strain indicator and recorder.

The data collected in the experiment, is presented in figure 2.18. In the figure, the amount of drawing force per drawing die i.e., compaction factor, is shown. As it can be seen, for the firs 4 data points, there is zero percent compaction factor, meaning that when those drawing dies where used, there was a gap between the outer tube and the core. Nevertheless, this does not imply that there must be zero drawing force. As in matter of fact, the drawing force for the firs three points, represent the amount of force required to draw the outer tube. Notice that, for the fourth data point, there is actually a considerably larger drawing force. This, may be caused by small variations on the dimensions of wires, the inner tube or the outer tube. In the last 6 reductions, there is a constant reduction of 0.002" in diameter. For the last three points, there is an active compaction from the outer tube against the inner tube. As the compaction increases, different phenomenons takes place, first, the wires move radially towards the inner tube, if the azimuthal spacing becomes zero, a portion of the the drawing force will be used to deformed the wires azimuthally, while the other fraction will keep deforming them radially. The combined and complex effect ends with the wires digging into the inner tube, locking them in place and guaranteeing full azimuthal contact. The latest, is a key matter for the current-sharing [88].
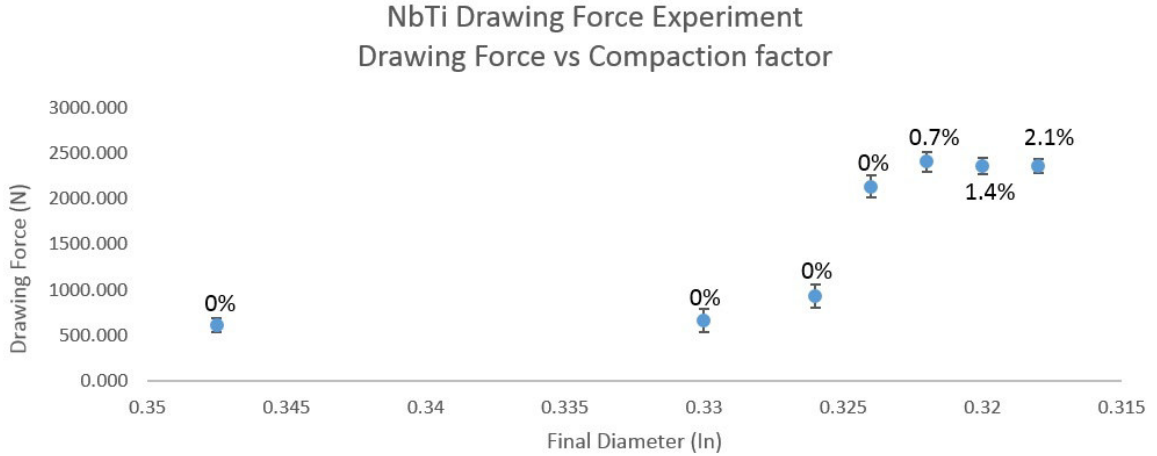
Figure 2.18: Drawing force for incremental drawing of NbTi post-heat treated CIC conductor. The data points represent the amount of drawing force required per used drawing die, i.e., per compaction factor.

For the CIC that would be use for the 3 T superferric dipole, the required drawing force its about 3000 N.

### 2.3.6 Current degradation measurements for JLEIC CIC

The quality control procedure developed for the CIC conductor, considers three steps, as described in previous section. The most relevant test is the actual measurement of the performance of the supercon-ductor. For this matter, a U-bend CIC conductor is dissected, i.e., the outer sheath is removed without damaging the superconductors. The strands are then extracted and tested at cryogenic temperatures and in presence of an increasing background magnetic field. A detailed description of the Current degradation is presented in section "2.7.4 Current degradation measurements".

The samples were measured on a probe that can hold three coiled wires simultaneously, each with a distance of 575mm between voltage taps. Measurements were taken with the wires submerged in liquid helium at approximately 4.2K.

## 2.4 Analytical model for optimum development of CIC conductor

A large number of parameters are required to fully specified a particular CIC conductor, see eqn. 2.2). The values of those parameters, boost or affect, the overall performance of the CIC conductor. If cho-sen improperly, the integrity of the superconductor and/or the CIC components may be compromised. Then, it's of vital importance to understand the interaction between the parameters, and from there develop a relationship between them and the CIC requirements for a given application.

$$CIC = CIC(R_w; N_w; f_{tp}; CuSc; R_t; t_w, T_p; R_b; CIC_{OD}, ) \qquad (2.2)$$

where, $R_w$ is the radius of the wire, $N_w$ is the optimum number of wires per cable, $f_{tp}$ is the
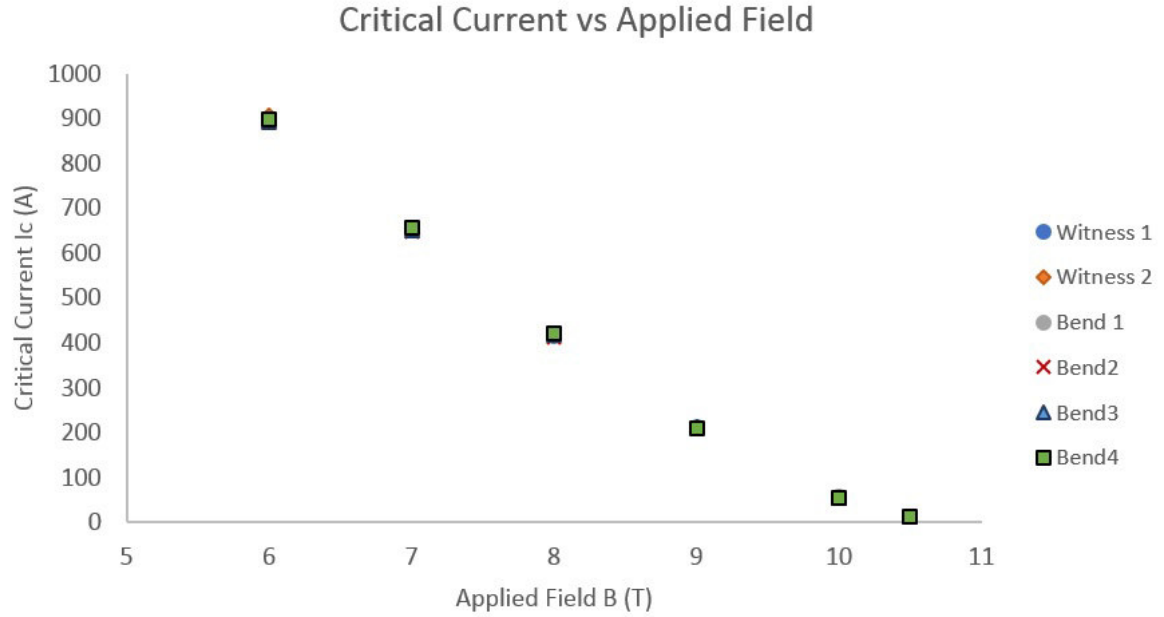
Figure 2.19: Current degradation measurement on extracted strands from CIC conductor.

internal superconducting filament's twist-pitch[e], $CuSc$ is the copper to superconductor ratio of the wires, $R_t$ is the radius of the inner tube, $t_w$ is the wall thickness of the inner tube , $T_p$ is the twist-pitch of the wires around the inner tube, $R_b$ is the bending radius of the CIC conductor and $CIC_{OD}$ is the CIC outer diameter, directly related with the compaction factor of the wires.

From the list of parameters, three constitute the basis for developing an analytical model: 1.-The wire radius, 2.-The inner tube radius, and 3.-The bend radius. This model will help us to determine the optimum conditions for producing the most favorable CIC conductor i.e., it can provide the optimum number of superconductors of a given dimension, cabled around an inner tube of certain diameter, with the optimum twist-pitch designed to match the required bend radius and produce zero net strain, which is known to be associated with current degradation on superconductors [89]. The first part of the model, is to define the twist-pitch.

### 2.4.1 The impact of the Twist-Pitch on the current degradation

The election of the twist-pitch is crucial for defining the integrity of the conductor, and as it will be shown, this parameters is design to match half of the arc lenght for a given bend of radius $R_t$, see figure 2.20. If this condition is not satisfied, non-vanishing strains could be developed, resulting in current degradation of the strains [89, 90], or in the worst case scenario, the superconducting strands could be tared.

Figure 2.20 shows a single wire cabled around the inner tube, with a twist-pitch that matches the arc lenght for a 90°bend.

The curve that describes the superconductor around the inner tube is a helix, see figure 2.20 c).

---

[e]The parameters associated with the superconducting wire, like the internal twist-pitch of the filaments, the wire diameter and the copper to superconductor ratio, become crucial when AC losses are studied, see section 2.8
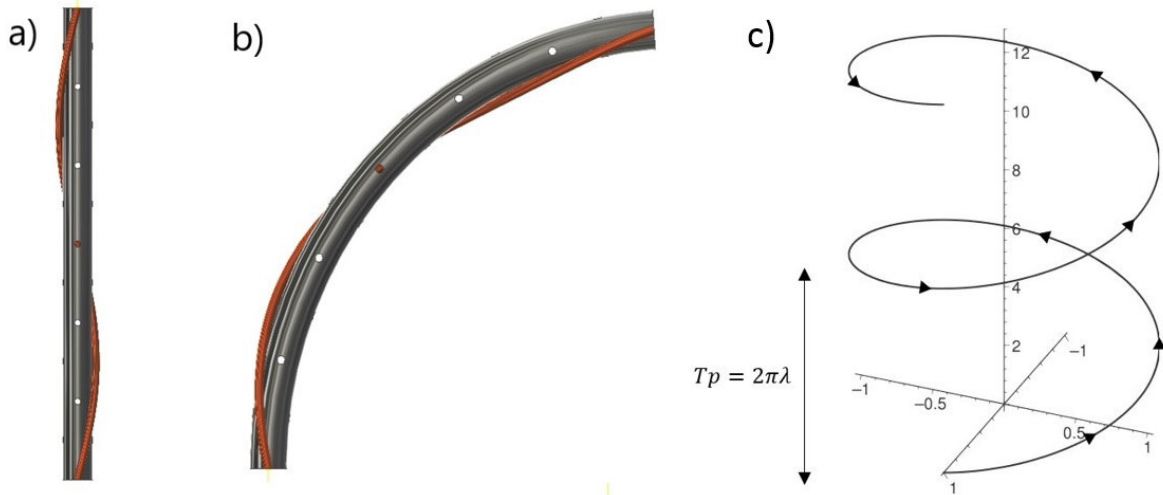
Figure 2.20: Superconducting strand cabled around an inner tube. On figure a), the strand is cabled around a straight inner tube, with a 3" twist-pitch. On figure b), the CIC is bent 90°with a 1.833" radius.

To estimate the strain ($\epsilon$) produced by bending the CIC in a arc or radius ($R_t$), its necessary to estimate the arc lenght $L$ of the helix prior and after bending. According to the strain definition [91]:

$$\epsilon = \frac{elongation}{original\ \ length} = \frac{\delta L}{L_0} \tag{2.3}$$

To estimate the length, the following the parametric equation for a circular helix of radius $R$, defined as $R = R_w + R_t$, and slope $\lambda/R$ is used:

$$\vec{r}(s) = \begin{pmatrix} x(s) = Rcos\left(\dfrac{s}{\lambda}\right) \\ y(s) = Rsin\left(\dfrac{s}{\lambda}\right) \\ z(s) = s \end{pmatrix} \tag{2.4}$$

where $s$ is the length of CIC associated with the ellipse, and it can take values in the range of $[0, 2\pi\lambda)$. While $\lambda$, is a constant associated with the advance in $\hat{z}$ direction used to define the twist-pitch, if multiply by $T_p = 2\pi\lambda$. This parametric equations can be used to estimate, the differential arc length of the curve $dl$:

$$\vec{r}'(s) = \left[ -\frac{R}{\lambda}sin\left(\frac{s}{\lambda}\right) ; \frac{R}{\lambda}cos\left(\frac{s}{\lambda}\right) ; 1 \right]$$

$$\parallel \vec{r}'(s) \parallel = \sqrt{\frac{R^2}{\lambda^2} + 1}ds \tag{2.5}$$

if integrated along the range of values of $s$, it provides the initial length of the helix $L_0$. Now to estimate the length of the superconductor when the CIC is bend in a radius $R_b$, its necessary to transform the parametric equations along the arc:

$$\vec{r}(s)_{bend} = \begin{pmatrix} x(s) = R cos\left(\frac{s}{\lambda}\right) \\ y(s) = \left[R_b + R sin\left(\frac{s}{\lambda}\right)\right] cos\left(\frac{s}{R_b}\right) \\ z(s) = \left[R_b + R sin\left(\frac{s}{\lambda}\right)\right] sin\left(\frac{s}{R_b}\right) \end{pmatrix} \tag{2.6}$$

the former parameters define the position vector, for a given point on the curved helix. Taking the derivative with respect to $s$, for each of his components gives:

$$\vec{r'}(s)_{bend} = \begin{pmatrix} \hat{i}\left(-\frac{R}{\lambda}sin\left(\frac{s}{\lambda}\right)\right) ds \\ \hat{j}\left(-sin\left(\frac{s}{R_b}\right) + \frac{R}{\lambda}cos\left(\frac{s}{\lambda}\right) cos\left(\frac{s}{R_b}\right) - \frac{R}{R_b}sin\left(\frac{s}{\lambda}\right) sin\left(\frac{s}{R_b}\right)\right) ds \\ \hat{k}\left(cos\left(\frac{s}{R_b}\right) + \frac{R}{\lambda}cos\left(\frac{s}{\lambda}\right) sin\left(\frac{s}{R_b}\right) + \frac{R}{Rb}sin\left(\frac{s}{\lambda}\right) cos\left(\frac{s}{R_b}\right)\right) ds \end{pmatrix} \tag{2.7}$$

taking the norm of the vector, and solving the cumbersome algebra results in:

$$\| \vec{r'}(s) \|_{bend} = \sqrt{1 + 2\frac{R}{R_b}sin\left(\frac{s}{\lambda}\right) + \frac{R^2}{\lambda}cos\left(\frac{s}{\lambda}\right) + \frac{R^2}{R_b^2}sin\left(\frac{s}{\lambda}\right)} ds \tag{2.8}$$

In the extreme case, when the bend radius tends to infinity ($R_b \to \infty$), one recovers the arc length for the straight case:

$$\| \vec{r'}(s) \|_{bend} = \sqrt{\frac{R^2}{\lambda^2} + 1} ds = \| \vec{r'}(s) \| \tag{2.9}$$

With this result, the strain on the bend can be computed as a function of the twist-pitch. If the twist-pitch does not matches half-arc lenght of the bend, the cable experience strain, as shown in figure 2.21 a), and as described by equation 2.10:

$$\epsilon = \frac{\| \vec{r'}(s) \|_{bend} - \| \vec{r'}(s) \|}{\| \vec{r'}(s) \|} \tag{2.10}$$

Understanding the level of strain developed during manufacturing process, is a key element for producing zero current degradation CIC conductors. Experiments performed by Eikin et al. [92, 91], shows that there is a straight relationship between the current degradation and the strain applied to the superconductor. As it can be seen in figure 2.21 b), the current degradation on NbTi superconducting wires is less than 2% when the strain in the superconductor is 0.5%. Fortunately for us, the cabling procedure guarantees small enough deviations on the applied twist-pitch, such that a less than 2% current degradation is guarantee (by the manufacturing process).
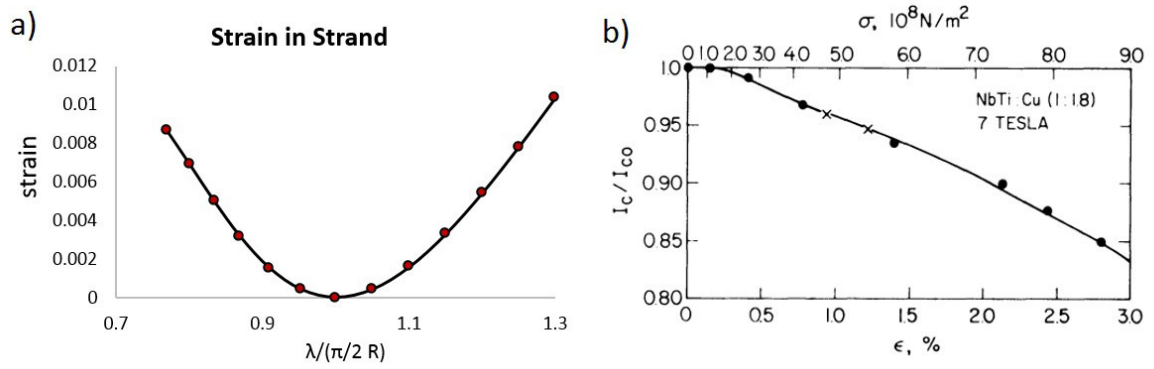
Figure 2.21: Strain in superconductor.[92, 91]

## 2.4.2   Analytical model for producing optimum CIC conductors

Lets define the twist-pitch in terms of a half arc lenght:
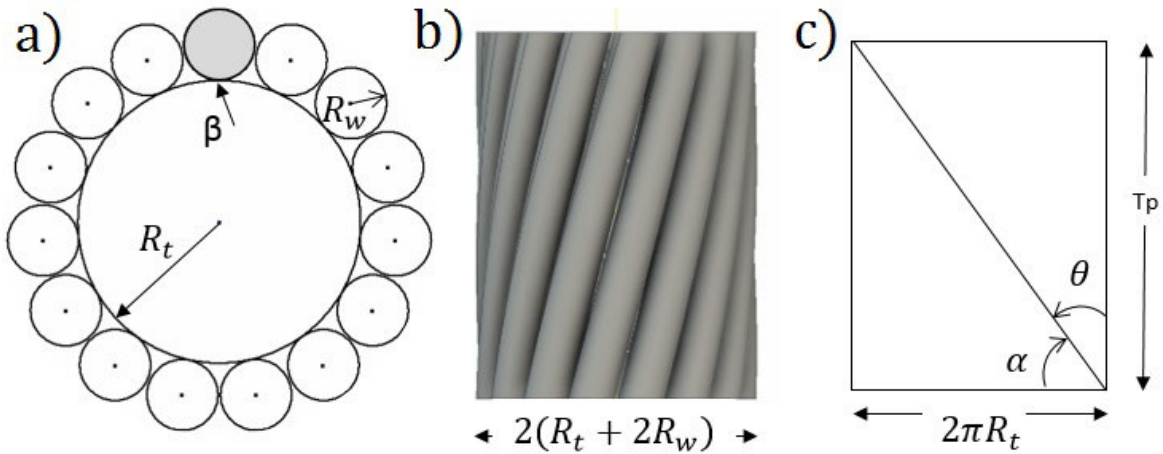


Figure 2.22: Geometrical construction of a Cable-in-Conduit conductor. Figure a) shows a cross-section of the CIC conductor and some of its main parameters: the radius of the wire $R_w$ , and the radius of the inner tube $R_t$. Notice that the wires are in touch with the inner tube, at the point $\beta$. Figure b) shows a lateral view of a CIC, the wire is cabled around the inner tube with a given twist-pitch $T_p$. Figure c) shows an unfolded model of the CIC, the point contact of any of the wires $\beta$ with the inner tube, becomes a line that runs across the rectangle formed by the twist-pitch and the unfolded perimeter of the inner tube. The angle $\theta$ represents the cabling angle, while $\alpha$ is its complementary.

Let's compute the relationship between the twist-pitch $T_p$, the radius of the inner tube $R_t$, the radius of the wires $R_w$, and the bending radius $R_b$. The relation between this parameters can be derived from a cross-section cut of a CIC conductor, see figure 2.22. In the figure, the cross-section is mapped into an unfolded space, where the point contact of the wires with the inner tube $\beta$ becomes a line, and the cylindrical tube, becomes a rectangle with the based defined in terms of the perimeter of the inner tube, and the lenght defined in terms of the twist pitch[f]. For avoiding stress accumulation during bending, we will define the twist-pitch for a $180°$ bend, as half of the arc lenght:

------

[f]Upto this point, the lenght of the twist-pitch is arbitrary, nevertheless, there is an important constrain relating this quantity and the bending radius. Such a relation will be explained at the end of the section.

$$T_p = \pi \frac{R_b}{2} \tag{2.11}$$

the cabling angle as established by the twist-pitch is:

$$\alpha = \arctan\left(\frac{R_b}{4R_t}\right) \tag{2.12}$$

When the wires are cabled and a cross-section is taken, the round wires become ellipses of minor axis $R_w$ and major axis $R_e$. From the cabling angle we can compute the major axis of the ellipses, see figure 2.23 and 2.24:
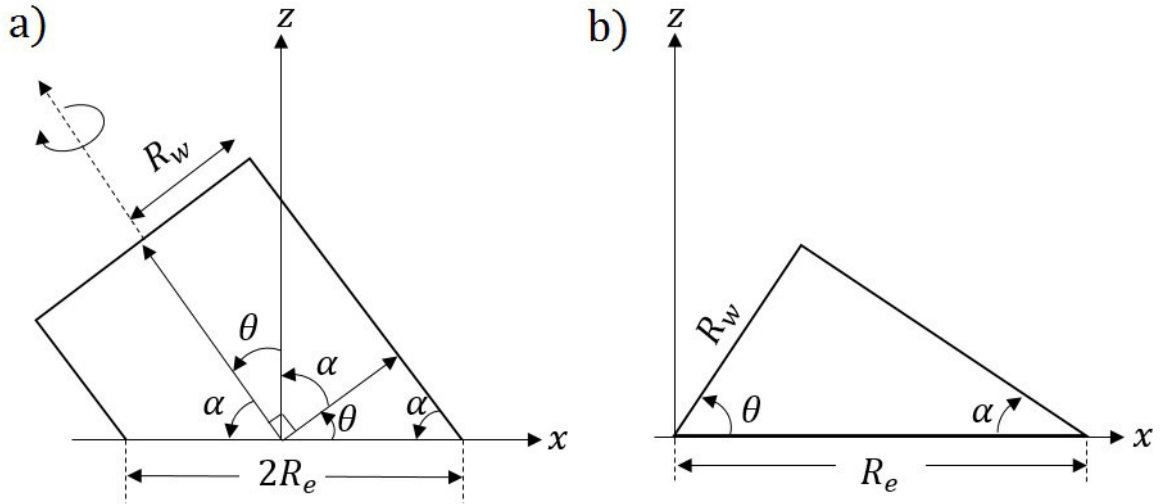


Figure 2.23: Geometrical construction for a superconducting wire of radius $R_w$, cabled around an inner tube of radius $R_t$, with a twist-pitch $T_p$. Figure a) reveals the geometrical relation between the wires and the cross-section of the CIC in the plane $XY$. In this plane, the wires become ellipses of minor axis $R_w$ and major axis $R_e$. Figure b) shows the relation between the ellipse major axis's, and the twist-pitch angle $\theta$.

$$R_e = \frac{R_w}{\cos(\theta)} = \frac{R_w}{\cos\left[\arctan\left(\frac{R_b}{4R_t}\right)\right]} \tag{2.13}$$

To compute the number of wires (ellipses) that can be wound around the inner tube, we can estimate the portion of arc that each wire requires, see figure 2.25. To do so, we will intersect the circles from the origin to the center of the wires, i.e, a circle of radius $R = R_t + R_w$, eqn. 2.14), with the equation of the ellipse, with center $R$ 2.15 Eqn. 2.15:

$$x^2 + y^2 = R^2 \tag{2.14}$$

$$\frac{y^2}{R_e^2} + \frac{(x-R)^2}{R_w^2} = 1 \tag{2.15}$$

by solving this system of equations one can compute the distance from the origin to the point of intersection $x$, as described in figure 2.25:
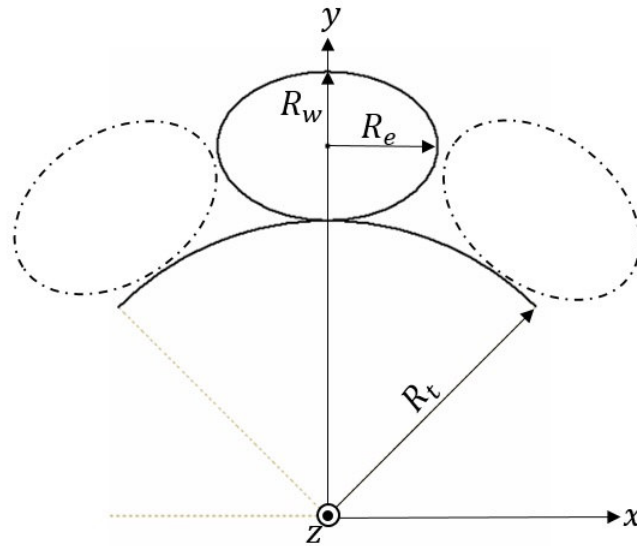
Figure 2.24: Representation of the elliptical wires in the cross-section of the CIC conductor.
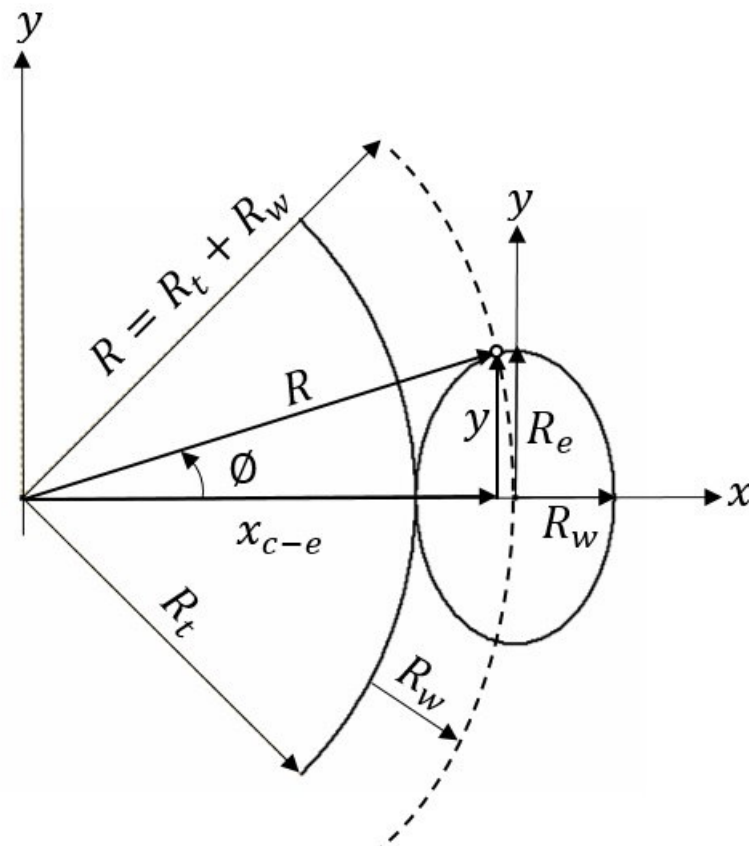


Figure 2.25: Geometrical construction for determining the arc length of an elliptical wire in the cross-section of a CIC conductor. The length $R$ is defined as the distance from the center of the CIC to the center of the superconducting wire. The angle $\phi$ represents the angular distance for half arc length.

$$x_{c-e} = \frac{2RR_e^2 \pm 2R_w\sqrt{R_e^4 - R_w^2(R_e^2 - R^2)}}{2(R_e^2 - R_w^2)} \qquad (2.16)$$

from this equation, one can estimate the corresponding angle of arc produced by one wire:

$$\phi = \arccos\frac{x_{c-e}}{R} \qquad (2.17)$$

the number of wires is given in terms of the ratio of the arc of an individual wire, to the total arc lenght of the circle with radius $R$, Eqn.2.18:

$$N_w = \frac{2\pi R}{2R\phi} = \frac{\pi}{\arccos\left(\frac{x_{c-e}}{R}\right)} \qquad (2.18)$$

this, is an initial value, that depends on the spacing available within wires, this value holds only if the spacing withing wires is greater than zero, if not, the new value has to be corrected by decreasing one wire. To estimate this gap,

$$\varphi = \frac{2\pi}{\lfloor N_w\rfloor} \qquad (2.19)$$



Figure 2.26: Geometrical construction for determining the gap ($G$) between neighboring elliptical wires, when cabled with a given twist-pitch. The length $X_{e-l}$ represents the collision point between the line that connects the center of the elliptical wires ($P_0$ and $P_1$), and the ellipse of center $P_1$. The distance between the collision point and the center of the ellipse ($l$) is symmetrical for both wires. The length $D$ represents the separation between neighboring wires and can be written in terms of the length $l$ and the gap $G$.

where the points $P_1$ and $P_2$ are $[R, 0]$ and $[RCos(\varphi), RSin(\varphi)]$ respectively. From this points, one can find the intersection point between the line (Eqn. 2.20) that connects them, and the ellipse (Eqn. 2.15). The distance between this point and the center of the ellipse, is related with the real gap

between wires when cabled with a given twist-pitch.

$$m = \frac{Sin(\varphi)}{(Cos(\varphi) - 1)}$$
$$y = m\,(x - R) \tag{2.20}$$

Solving the system of equations given by 2.20 and 2.15, results in the *x* point:

$$x_{e-l} = R \pm \frac{1}{2}\sqrt{\frac{4R_w^2 R_e^2 (Cos(\varphi) - 1)^2}{R_w^2 Sin^2(\varphi) + R_e^2 (Cos(\varphi) - 1)^2}} \tag{2.21}$$

Notice that this point lays shorter than the intersection point between the circle of radius $R$ and the ellipse $X_{c-e}$. This implies, that the actual point of contact between wires, is precisely along the line given by Eqn. 2.21.

$$D = 2RSin(\varphi)$$
$$G = D - 2X_{e-t} \tag{2.22}$$

**Model predictions and restrictions**

The previous mathematical model, set the fundamentals for developing Cable-in-conduit cables, it allows to make predictions and estimates for determining the values of the parameters that will lead to producing current degradation free cable-in-conduit cables. Some of the parameters that can be estimated are:

1. The optimum twist pitch for a given application, based on the dimensions of the wires and the inner tube.

2. The optimum number of wires that could safely be wound into the cable without casing deformation on the wires.

3. Allows to compute the value of all the parameters to achieve any desire azimuthal gap between strands.

4. The optimum drawing factor for the CIC.

5. The optimum foil thickness.

6. And, in general the optimum conditions for a double-layer CIC, their azimuthal spacing in each layer and the optimum amount of compaction.

## 2.5 CIC development by the Continuous Tube Forming and Filling route

Cable-in-Conduit Conductors could be produced in long-lengths by two different paths, the former was previously described, and requires the use of seamless tubing. Considering the current setup,

the long-length production is bound to lengths of the order of 150 m, provisions could be made to triple this value. Production of several kilometers is a challenge, which would require a re-engineering of the manufacturing process. Nevertheless, there is an alternative path to produce long-lengths of superconductor, namely the Continuous Tube Forming and Filling procedure (CTFF), a technique developed for producing long-lengths of superconductor produced by the PIT procedure.

## 2.5.1   CTFF Procedure

The CTFF technique is applied to form and weld the Copper Nickel outer sheath around the cores of NbTi superconductor. In this process, long-lengths of superconductors are cabled and secured around a perforated inner tube. After the stainless steel foil is applied, the CIC core is then fed into a CTFF machine, which forms a strip of Copper Nickel around the inner tube and welds it, as depicted in figure 2.27. In this process, a high power laser, performs a full penetration, without damaging the superconductor.
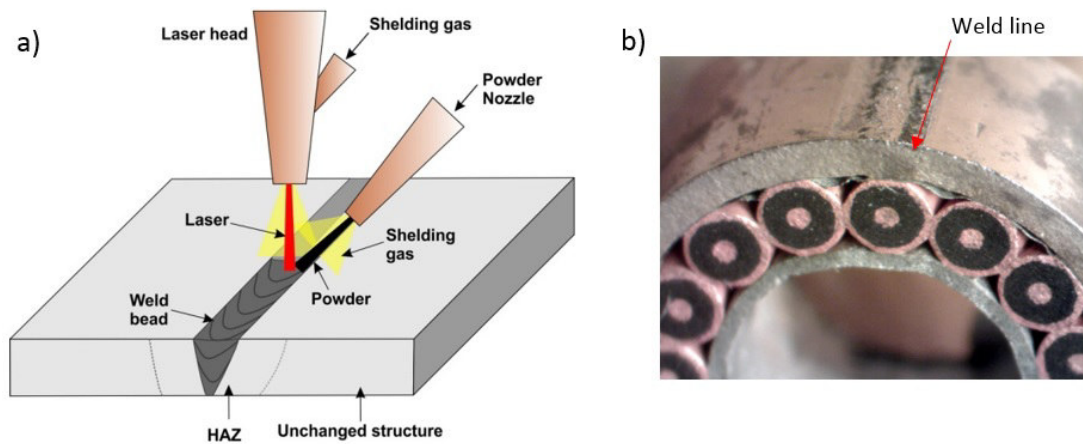


Figure 2.27: In figure a), a representation of the continuous tube forming and filling procedure "CTFF" for producing long-lengths of Cable-in-Conduit conductor. On figure b), a cross-section of a NbTi CIC conductor produced via CTFF technique.

This is a complex procedure, the integrity of the weld must remain unaffected and survive extreme conditions: forming into complex bends with small bend radius, cryogenic temperatures, and furthermore it most survive the high pressures that could be developed during a quench event.

## 2.5.2   The standard Procedure

To assess the integrity of the weld line, and detect if any cracks are developed during the CTFF procedure, drawing, bending, or after the cables are exposed to normal operating conditions, a quality control procedure was developed and applied, see figure 2.28:

1. Helium Leak Test (HLT) the weld line of CIC conductors after the CTFF procedure

2. HLT the CIC conductors after bent $180°$.

3. HLT the CIC after high pressurized at 600 PSI (40 atm) at 300 K for 10 min.

4. HLT the CIC after thermal shocked from 300 to 77 K for 10 min.
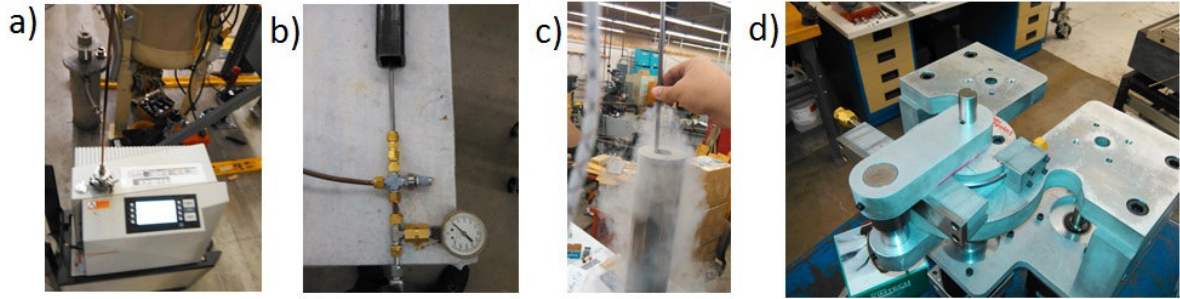


Figure 2.28: Standard procedure for assessing the integrity of the weld line for CTFF CIC conductor. On a), a high-resolution helium leak detector. On b), a high pressure (600 psi) test on CIC produced through the CTFF procedure. On c), a thermal sock test performed in liquid nitrogen. On d), a robotic bender forms the CIC conductor into a U-bend.

## 2.6    CIC long length production

In August 2018, the ARL and ATC joint collaboration completed the development of a CIC long-length production facility, capable of mass producing 130m-long sections of NbTi CIC conductor [93]. Three main components were used to produce the CIC conductors: 1) a high-speed planetary stranding machine, responsible for applying the spiral wrap of the superconductors around the perforated inner tube; 2) the taping head unit, responsible for adding the protective layer of thin foil stainless steel tape, and 3) a set of two caterpillars, one responsible for providing active insertion of the cables into the rigid outer tube and the other responsible for drawing the CIC into the required dimensions, see Figure 1.

### 2.6.1    Manufacturing procedure: Planetary stranding machine

The production process of long sections of CIC conductor is divided into three stages. First, a long spool of perforated stainless steel tube feeds the planetary stranding machine, which contains 15 spools of 1.2 mm OD NbTi wires. Then, the superconductors are fixed across the joint of the ending portion of the inner tube and the initial portion of a galvanized cable, which is used merely to initiate the cabling process by providing a lead end to pull from the caterpillar. The previous assembly is sent through a compactor die, which avoids wire overlapping, ensuring a uniform cable and of the right dimensions (Figure 1a). The angular rotation of the spools in the stranding machine, is linked by a system of mechanical gears, to the linear motion of the rubber band clamp in the caterpillar (Figure 1b). The synchronized motion of both systems, is configured to match the desired twist-pitch of the JLEIC CIC conductor, for instance, 73.13mm [3]. The taping head unit is located in between the compactor die and the caterpillar and is responsible for applying a constant wrap of stainless steel tape. For the JLEIC CIC conductor, a no-spaced wrap is applied. Nevertheless, the unit offers the possibility to adjust the spacing if needed, Figure 1c.
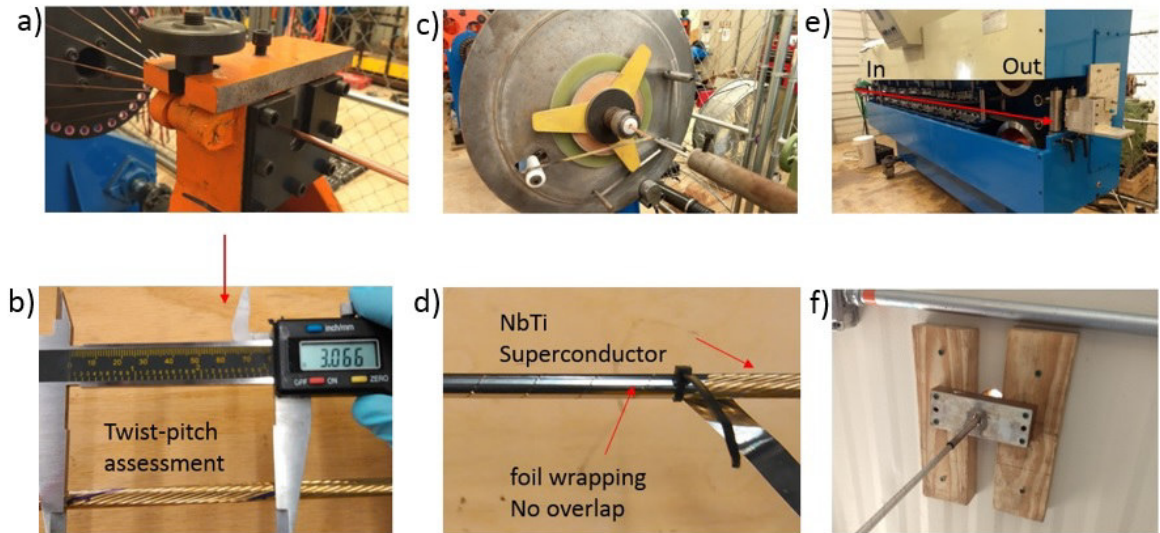
Figure 2.29: Manufacturing procedure for Cable-in-conduit conductor.

The second stage of the procedure involves inserting the product coming from the caterpillar (CIC core) to a pre-straightened long section of high strength outer tube. In this process, the galvanized a) b) c) cable is used again to ease the insertion of the CIC core to the long-length of the outer tube and avoids friction accumulation. The pulling force is provided by a powered take-up spool unit. Once the CIC core is fully inserted into the outer tube, the CIC is obtained. The third stage involves the drawing of the CIC. To produce an operational CIC, a two-step drawing process is required. The first drawing eliminates the gap between the outer tube and the CIC core, while the second, compacts the wires onto the inner tube, immobilizing them, and providing direct contact between neighboring wires. This, is a critical property for current sharing. For the NbTi wires inside the JLEIC CIC conductor, the contact region takes 12% of the surface of the wires. The latter is a general procedure that allows the CIC production facility at ATC, to span the development of CIC conductors. It covers a wide range of possibilities for development of CIC conductors for diverse applications, which may include the fabrication of multilayer CIC conductors, which could be used to produce D-shape toroidal coils for nuclear fission reactors.

## 2.6.2 CTFF Long length production

The long length production process of CIC conductors is divided into three stages: First, the high strength perforated tube is feed into the cabling machine, which contains the required number of spools of superconductor. After that, the wires are fixed and cabled around the inner tube, with the desired twist-pitch, figure 2a). The angular rotation of the spools in the cabling machine, is mechanically linked to the linear motion of the caterpillar, which provides the pulling in the cabling process. The synchronized motion of both systems is configured to match the desired twist-pitch of the CIC. Provision have been made to control and avoid wire overlapping, ensuring a uniform cable of the right dimensions, see figure 2b) and 2c). Second, a taping head unit, located at the exit of the cabling machine, provides a uniform wrapping of high strength foil around the cabled superconductor, figure 2c). Third, once the foil is applied, the cable is inserted into the outer sheath, and the drawing process take place. Two different paths can lead to the long length production of CIC: The first, make use of

seamless sheath, and the process was described above. In the second, the Continuous Tube Forming and Filling (CTFF) procedure is applied to form and weld a strip of outer sheath around the cable. The CTFF procedure has been validated for short lengths, in which no cur-rent degradation has been observed.

## 2.7 CIC Splice Joint

The CIC technology requires the development of a low-resistance splice-joint system that allows testing, operate, and power the magnets prior to and during operation at the ion ring of the JLEIC facility, and for any other application. The ARL group has developed a reliable and easy-to-operate design of a splice-joint system, for the CIC conductor of the JLEIC Super-ferric magnets. Provisions have been made to confine the superconductors in narrow channels allowing for liquid helium to flow and provide thermal stabilization. The use of adequate materials and solder allows the splice joint to be reusable. To detach the joint, a set of high-power heat cartridges, embedded at the back of the splice joint, provides the required heat to rapidly melt the solder, allowing for an easy detachment of both halves of the splice joint. Simulation of current flow in the CIC splice predict a low resistance ¡ 2 nΩ joint. LHe flow is routed through the joint and provision is made to provide supply-return flow connections at each joint.
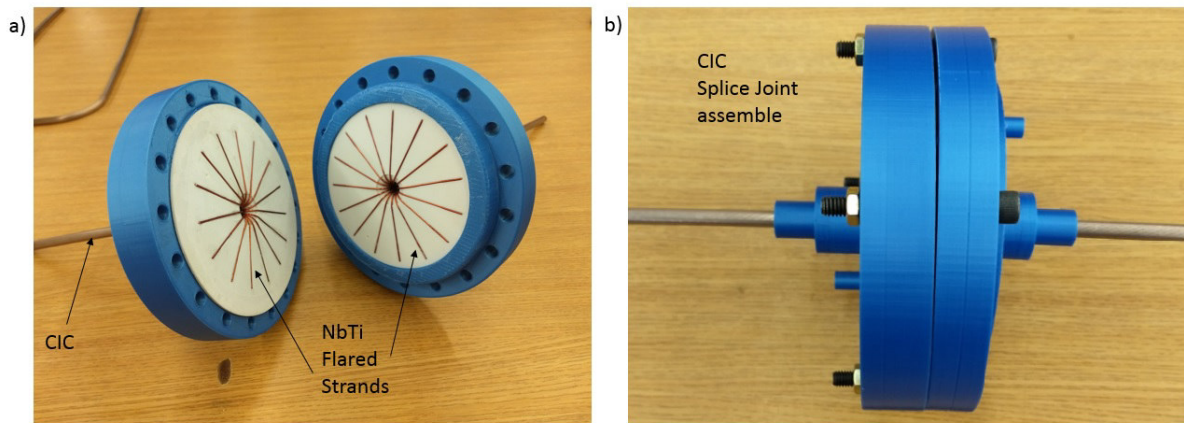


Figure 2.30: Splice Joint design.

## 2.8 Exotic CIC: Nb3Sn, MgB2 and Bi2212

The flexibility and robustness of the Cable-In-Conduit technology, make it desirable for a large number of applications, which may include the use of Nb3Sn, MgB2 and Bi2212 superconductors [94]. To extend this technology to embrace the reaction bake superconductors, a full research plan was conducted.

In this section, the development of long-lengths of Nb3Sn and MgB2 CIC through the CTFF technology is described in lenght. The research is divided in three main topics:

- **CIC components and its manufacture process: Drawing and bending**. This firs section, includes the search for suitable materials for the CIC components, such that the reaction bake process doesn't compromise its performance at normal and extreme conditions.

- **CTFF Welded CIC and the Standard procedure**. In this second section, the performance of the CIC weld line under stresses and strains inherit from manufacture (Cabling, drawing and bending procedures) is studied, including possible failure scenarios, for instance, a quench event[g].

- **Stress relieve and annealing process: MgB2 and Nb3Sn CIC**. The third, studies the performance of MgB2 and Nb3Sn strands at various bending radius and how a proper heat treatment of the CIC components impact on the strain seen by the superconductors.

At each section, a brief description of the goals is given, followed by a detailed description of the experiments. Discussion and conclusions are presented at the end of each subsection. At the end of the study, the measurements of the current degradation, for the case of MgB2 and Nb3Sn extracted strands is presented.

## 2.8.1 Components and its manufacture process: Drawing and bending

The Nb3Sn and MgB2 CIC specific design parameters follow the requirements established by a preliminary design of a model dipole and quadrupole for the interaction region of the future Electron-Ion Collider. The model dipole requires an 18-MgB2 (0.8mm OD), 0.256 OD CIC capable of bending at a minimum bending radius of 2.00. The quadrupole requires an 18-Nb3Sn (0.8mm OD), 0.256 OD CIC capable of bending at a minimum bending radius of 1.14. See chapter 3 for specifics on the magnet design.

### Section Goals

As it was mentioned, the main goal is the production of long-lengths of Nb3Sn and MgB2 CIC, through the CTFF process. In this section, our primary goal is to find the proper set of materials, suitable for the reaction bake process, such that the CIC withstands the stresses and strains developed during manufacture.

### Experimental setup

One of the essential elements of both CIC designs, is the high strength inner tube. Considering the high temperatures developed during the reaction bake process, of either superconductor, a suitable candidate material is the perforated 316L stainless-steel.

Unfortunately, due to strong technical limitations from the suppliers on their capability to produce costumed-made 5/32 OD, 0.010 wall, perforated 316 L Stainless-Steel, we had to perform a drawing process to reduce the diameter of the available inner tube (5mm OD) to the desired outer diameter. The effect of the drawing process on the perforations, and the overall performance of the inner tube is studied and presented in table 2.3.

---

[g]At cryogenic temperatures, High pressures could be produced in the CIC due to a quench scenario, a model described by [95] estimates a value of 600 psi

To guarantee the correct performance of the perforated tube during drawing and bending, a set of test samples were produced. The samples were manufacture following the requirements of the magnets. In this test, dummy strands (Silicon-Bronze, 0.031 OD wires) of similar mechanical properties and dimensions were used. The samples were bend at various radius and a dissection was performed to assess their performance.

To find the proper drawing size that will produce optimum shoulder-shoulder contact between wires, we will refer to the results obtained from TAMU-Hypertech NbTi CIC Phase I [96], in which several tests were done combining four different drawing dies (0.2583, 0.256, 0.254 and 0.252) with two different wall thickness for the brass inner tube, leaving the rest of the CIC variables fix i.e. number of wires, material of the wires, cabling twist-pitch and SS-foil wrapping angle. That research concluded that a wall thickness of 0.010 of either brass or Stainless-steel is needed to support the internal structure at bends. The research also concluded that the drawing dies of 0.256 and 0.254 provide proper shoulder-to-shoulder contact between superconductors, therefore we will start the experiments based on those results. Table 2.3 describes the first series of experiments needed to find out the optimum CIC components configuration and bending recommendations.

The following table presents the most relevant results of the set of twenty experiments, labeled from S1 to S20, in which three different bend radius were used, 0.75", 1.00" and 1.470".
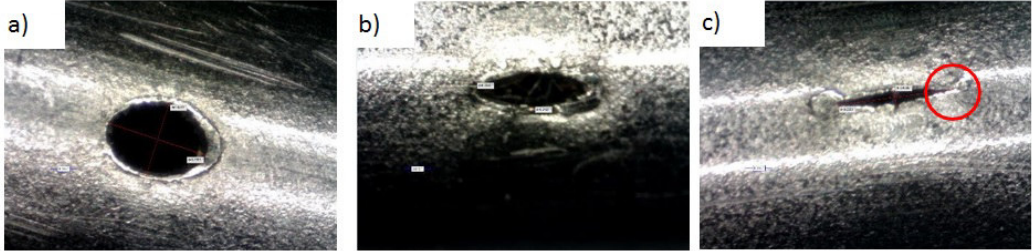
| ID | Description | Results |
|---|---|---|
| S1 | A .1875 thin wall (0.010) Stainless-steel perforated tube, was drawn to .1562 OD in a two-step process: starting at .1875 and having an intermediate draw at .1675 (10% reduction), and ending at .1562 (6.7% reduction). The goal is to evaluate and analyze its performance at every step. | As it can be seen on figure below, the tube survived the drawing process, there is no evidence of damage to the weld, although the holes suffer a substantial deformation. This deformation could compromise the CIC manufacturing process, especially at bending in a close radius. Two more experiments were done to get a further understanding of the tube performance. Bends on pure inner tube, revealed that there is no cracking at the bends. |



a)  b)  c)

Continued on next page

**Table 2.3 – continued from previous page**

| ID | Description | Results |
|---|---|---|
| S2 | The goal of this experiment is to develop a reliable 18- Nb3Sn CIC (using Stainless Steel perforated tube) and study its performance while bending it around a small radius .75 paying special attention to the integrity of the perforated tube. The CIC was made of a .1875 OD Stainless Steel thin wall (0.010) perforated inner tube, drawn to size in a three-step drawing process: .1875 OD to .1775 (5.3% reduction), .1775 OD to .1675 OD (5.6% reduction), and .1675 OD to .1562 (6.7% reduction). 18 Silicon-Bronze 0.808mm OD wires were cable around the inner tube with a constant twist pitch of 3 inches. A 0.001 thick Stainless-Steel foil was wrapped around the cable without overlap. The whole assembly (core) was then inserted into a .325 OD Copper-Nickel thin wall (0.020) outer tube. The CIC was then drawn to size in a single step process, from .325 to .256. In this process, the outer tube suffered a 21.2% reduction, although only 1.5% acted as core-compaction, the rest was free drawing in which the outer tube does not touches the core. | Sample S2 was bend in a .75 radius at a constant speed using a tube bending machine. **While bending, the outer tube tore at two locations, 30 and 150 degrees**. The inner tube behaves as expected, there Is no collapse of the inner tube bending nor uncontrolled rupture of perforated holes. Dissection shows that the amount of strain experienced by the wires is too high, resulting in a 30% of the broken strands. The figure below shows the evident outer damage on the CIC sample, a dissection revealed that the wires tore at two locations. A zoom on the broken wires, agrees with the assumption of high strains. The wires experience bottle necking, characteristic of ductile fractures. The experiment was repeated to discard any possible effect from the tube bending machine. |

**Table 2.3 – continued from previous page**
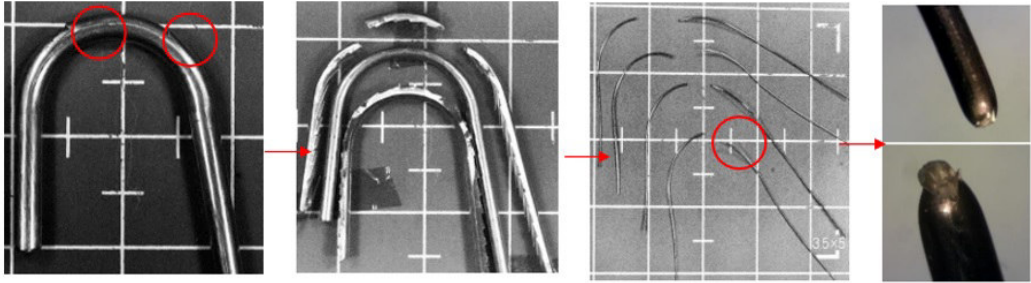
| ID | Description | Results |
|---|---|---|
| |  | |
| S3 | The goal of this experiment is to develop a reliable Nb3Sn and MgB2 CIC (using Stainless-Steel perforated tube) with high performance at small bending radius .75. The CIC was made of a .1875 OD Stainless-Steel thin wall (0.010) perforated inner tube, drawn to size in a three-step drawing process: .1875 OD to .1775 (5.3% reduction) .1775 OD to .1675 OD (5.6% reduction), and .1675 OD to .1562 (6.7% reduction). 18 Silicon-Bronze 0.808mm OD wires were cable around the inner tube with a constant twist pitch of 3 inches. A 0.001 thick Stainless-Steel foil was wrapped around the cable without overlap. The whole assembly (core) was then inserted into a .325 OD Copper-Nickel thin wall (0.020) outer tube. The CIC was then drawn to size in a single step process, from .325 to .256. In this process, the outer tube suffered a 21.2% reduction, although only 1.5% acted as core-compaction, the rest was free drawing in which the outer tube does not touches the core. The sample was bent in a .75 radius at a constant speed using a tube bending machine. While bending, the outer tube tore at 30deg, consistent with samples S1 and S2. | As it can be seen in figure below. The failure is consistent with samples S1 and S2, as a matter of fact, in this particular case, the fracture is more evident on the outer sheath. Its time to change parameters, the current configuration has probed to be incorrect. Either the outer tube must increase its strain at failure or we must use varied materials. In the following samples, the experiment was repeated changing the outer tube for different materials, including pure copper, Monel 400 and Stainless-Steel. Experiment |

Continued on next page

**Table 2.3 – continued from previous page**
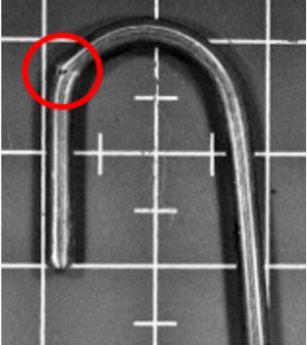
| ID | Description | Results |
|---|---|---|
| |  | |
| S4 | The goal of this experiment is to develop a reliable Nb3Sn and MgB2 CIC (using Stainless Steel perforated tube) with high performance at small bending radius .75. The CIC was made of a .1875 OD Brass thin wall (0.010) inner tube. 18 Silicon-Bronze5 0.808mm OD wires were cable around the inner tube with a constant twist pitch of 3 inches. A 0.001 thick Stainless-Steel foil was wrapped around the cable without overlap. The whole assembly (core) was then inserted into a .300 OD pure Copper thin wall (0.020) outer tube. The CIC was then drawn to size in a single step process, from .300 to .256. In this process, the outer tube suffered a 14.6% reduction, although only 1.5% acted as core-compaction, the rest was free drawing in which the outer tube does not touches the core. The sample was bent in a .75 radius at a constant speed using a tube bending machine. | In this case, the pure copper outer tube suffered less deformation as the initial OD is .300 not .320 as in samples S1-S3. Although strain seen by the CIC is less than previous samples, the result is the same. The sample tore at two locations 30 and 70. The deformation did not cause the wires to tear, but a visible kink arises at 80% of the wires, which may cause current degradation after wind and react. Similar results were obtained when Monel 400, and Stainless-Steel outer tube were used. This experiments correspond to samples S6 to S16 and include test at different bend radius( 1.00"). In this experiments, a deformation of the outer tube and the wires was always present. A larger bend radius test was done (1.470"), using the same configuration as samples S1-S4, to understand the effects of the high-strain developed during the bends. The results are presented on samples S5. |
| | | |
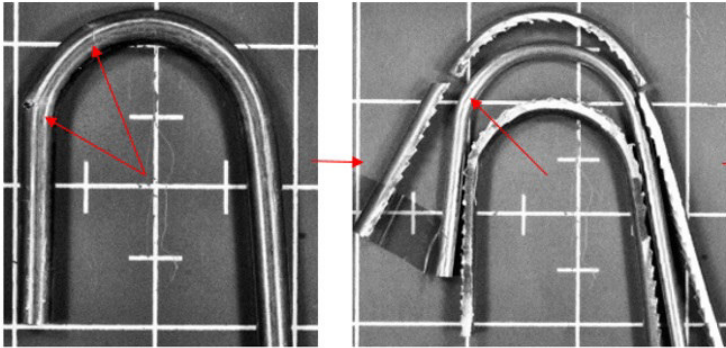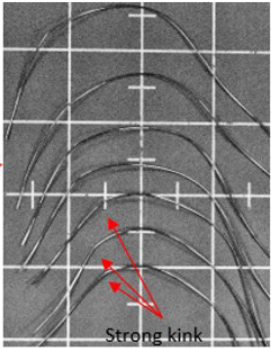
**Table 2.3 – continued from previous page**

| ID | Description | Results |
|----|-------------|---------|
|  | | |

**Table 2.3 – continued from previous page**

| ID | Description | Results |
|----|-------------|---------|
| S5 | The goal of this experiment is to develop an 18-Nb3Sn CIC (using Stainless Steel perforated tube) and study its performance while bending it around a bigger bending radius 1.470. The CIC was made of a .1875 OD Stainless Steel thin wall (0.010) perforated inner tube, drawn to size in a three-step drawing process: .1875 OD to .1775 (5.3% reduction), .1775 OD to .1675 OD (5.6% reduction), and .1675 OD to .1562 (6.7% reduction). 18 Silicon-Bronze7 0.808mm OD wires were cable around the inner tube with a constant twist pitch of 3 inches. A 0.001 thick Stainless-Steel foil was wrapped around the cable without overlap. The whole assembly (core) was then inserted into a .325 OD Copper-Nickel thin wall (0.020) outer tube. The CIC was then drawn to size in a single step process, from .325 to .256. In this process, the outer tube suffered a 21.2% reduction, although only 1.5% acted as core-compaction, the rest was free drawing in which the outer tube does not touches the core. The sample was bent in a 1.470 radius at a constant speed using a motorized bending machine. There is no evidence of damage to the outer tube. Dissection probe there is no collapse of the inner tube or tear of wires. | As it can be seen in figure below. The sample behaved as expected, the amount of strain is not enough to compromise CIC integrity. No signs of deformation to the outer tube or the wires was observed. So far, we've found that small bend radius compromise the integrity of the superconductor and the outer tube. In samples S17-S20, We annealed the outer tube to decrease the hardness and increase ductility during bend. The results are presented on next sample. |

**Table 2.3 – continued from previous page**
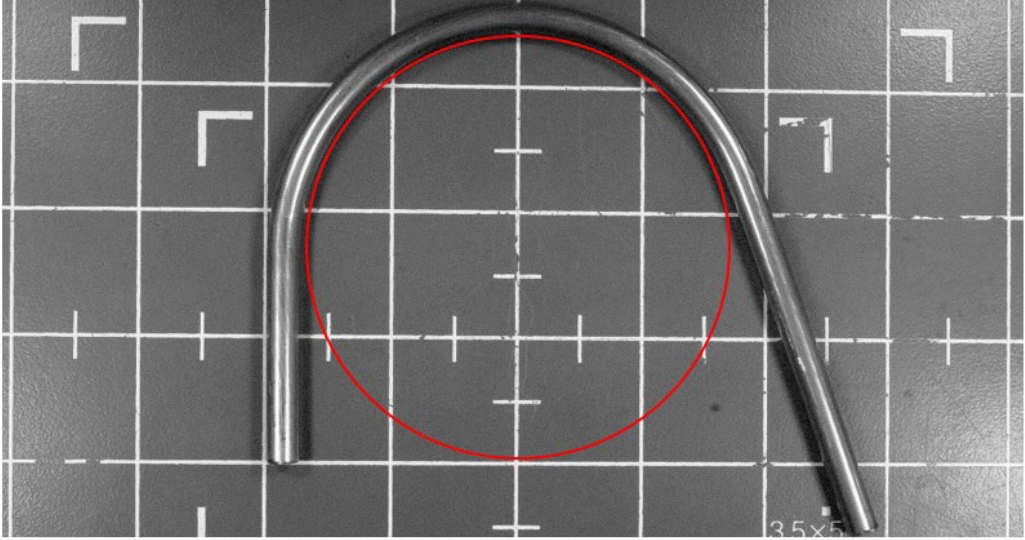
| ID | Description | Results |
|----|-------------|---------|
|  | | |
| | | Continued on next page |

**Table 2.3 – continued from previous page**

| ID | Description | Results |
|---|---|---|
| S17 | The goal of this experiment is to develop an 18-Nb3Sn CIC (using Stainless Steel perforated tube) using a recycle sample from Tamu-Hypertech NbTi CIC Phase I which uses Monel 400 as outer tube and study its performance while bending it around a small radius .75. This recycle sample belong to the batch in which the CTFF technique was improved and reliable. The CIC was made of a .1875 OD Brass thin wall (0.010) inner tube. 18 Silicon-Bronze18 0.808mm OD wires were cable around the inner tube with a constant twist pitch of 3 inches. A 0.001 thick Stainless-Steel foil was wrapped around the cable without overlap. The whole assembly (core) was then inserted into a .300 OD Monel 400 thin wall (0.020) outer tube. The CIC was then drawn to size in a single step process, from .300 to .256. In this process, the outer tube suffered a 14.6% reduction, although only 1.5% acted as core-compaction, the rest was free drawing in which the outer tube does not touches the core. The sample was uniformly annealed using a hand torch for 3 minutes and then it was bent in a .75 radius at a constant speed using a tube bending machine. | The sample was uniformly annealed. A careful inspection revealed no crack lines or bottle neck lines at the outer tube. A dissection showed no deformation or kinks to the Si- Bronze wires. We conclude that a proper annealing has to be done on the the inner and outer tube, to increase ductility. A detailed study of the heat treatment and its mechanical characterization is presented on section " Stress relieve and annealing process: MgB2 and Nb3Sn CIC". |

**Table 2.3 – continued from previous page**
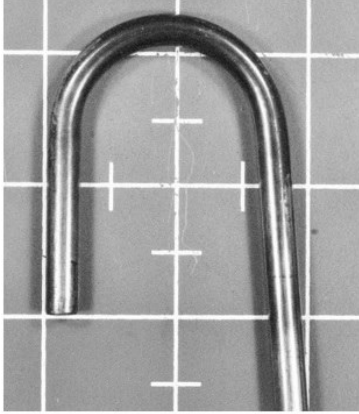
| ID | Description | Results |
|----|-------------|---------|
|    |  |         |

Table 2.3: Summary of the most relevant results on the MgB2 and Nb3Sn bending test.

As it can be seen from table 2.3. There is a positive effect on applying a heat treatment on the CIC components to reduce the strain after drawing.

**Experiment remarks**

1. Drawing the 316L perforated tube using path 1 or 2 (Experiments 1 and 2), do not compromise weld line integrity. There is little to non-difference between the two drawing paths. In both scenarios, the holes are deformed substantially without tearing. A different result may arise if the inner tube gets a stress relief treatment in between drawing process, this may have a positive impact for current-sharing while drawing.

2. To evaluate the impact of the Stainless-Steel inner tube on the dummy samples, many CIC-dummy samples were tested using standard tube bending machine at the different bending radius (Experiments 3,4 5, 8 and 9). Experiment 3 to 9 concluded:

   (a) The use of non-robotic bending tools probed to be deficient. They do not provide proper support of the CIC while bending (holding die is not costumed-made to the actual .256" OD CIC), and bending speed cannot be controlled accurately.

   (b) The .75 bending radius of the standard tube bending machine is considerably lower than the target bending radius (1.14"). This excess bending leads to a substantial increase in the total strain seen by the outer tube (Drawing + bending), which compromises its performance.

   (c) Experiments #3, #4 and #5 show consistent results (failure). In all of them, the outer tube and 30% of the strands tore while preserving inner tube integrity. Points A and B suggest that the amount of strain (.75" bending radius) is the leading case of failure.

(d) Experiments #8 and #9 proved that if the bending radius increases by an inch, from .75 to 1.75 (reducing the strains), then the tearing and bottle-necking effect wont appear on the outer tube or strands. This result is consistent with the results obtained at TAMU-Hypertech NbTi CIC Phase I [96]].

3. Previous conclusions lead us to suspect that the main cause of tearing (on the outer tube and strands) might be the over-strain produce at the small bending radius. However, another possibility is the "harness" of the inner tube and its poor indentation capabilities after drawing. If the spring tube do not deform allowing the strands to re-arrange and be in full contact while bending, then it contributes to the strains on the strands.

4. To test this hypothesis, Experiments #6 and #7 tested the response of CIC made of softer inner tubes, such brass, and different outer tubes, such pure copper (Experiment #6) and Monel400 (Experiment #7) while being bent under same conditions as experiments #3, #4, #5, #8 and #9. The results agree that the strain due to bending its the principal cause of tearing. It also suggests that a "friction lock" effect may be happening at the strands due to the sandwich effect of Stainless Steel Tube-Superconductor-Stainless Steel foil or Superconductor-Stainless steel foil-Outer tube.

5. In order to test the effects of a lower strain scenario, which is more realistic to our needs (1.14" bending radius for the Nb3Sn CIC), we let Experiments #10, #11 and #14 to test bend samples using a 1 inch bending radius. Unfortunately, when we performed this test we did not have a costumed-made die, and the holding region of the 1 bending die was larger than .256. Because of the lack of proper holding, both samples slipped and kinked.

6. A heat treatment to stress relieve the samples after drawing may reduce the net strain. To test the idea, in Experiment #18 we decided to perform a "stress relieve test. Unfortunately, the stress relieve process wasn't uniform, leaving harder zones which tented to kink.

7. In Experiments #19 and #20, the stress relieving process was uniform. The test was successful, even at .75" bending radius there were no broken strands and the outer tube did not show bottle-necking effect. This is a remarkable result, it tells us that we could actually achieve the desired bending radius (.75, smaller than our target bending radius) by reducing the net strain of CIC individual components through a thermal process (stress relieve or annealing) done prior the bending test, such that the thermal process does not interfere with the reaction bake process of the superconductor (As it will be seen in section 3, the stress relieve and annealing process of 316 L Stainless Steel is greater than the reaction bake temperature of Nb3Sn or MgB2).

8. In experiments S21-S25 we explore the possibility of replacing the Monel 400 outer sheath for another material with a higher elongation at failure. Unfortunately, the material that we used was considerably larger in diameter than the target OD after drawing. The tube was heat treated using a hand torch, the results are comparable with those of Monel l400 (Stress relieved).

9. Experiments S26-S32, pretend to reproduce experiments described previously, without the need of a heat treatment. The results are not conclusive. We opted to step aside from this idea and go back with the Monel 400 (using the improved welding technique) and thermal treatment on the inner tube.

## 2.8.2   CTFF Weld CIC and standard procedure

The results from the previous section gave us hints of how to deal with over-strained CIC individual components while preserving its performance at small bending radius. In this section, we will apply such recommendations, and study the actual performance of CIC made with real superconductor i.e., Nb3Sn and MgB2. We will focus our efforts on providing a reliable a 1" bending radius Nb3Sn-CIC, and a 1.75" bending radius MgB2-CIC, for a quadrupole and dipole magnets respectively. We will also study the performance of both superconductors at smaller radius to understand their actual limitations.

TAMU manufactured 2 6-foot long CIC cores, one using 18 0.786 mm OD MgB2 wires (21% MgB2) and one using 18 0.786 mm OD Nb3Sn wires. In both cases, a 0.254 mm wall thickness (0.010) and 3.96 mm OD (5/32) 316 L Stainless-Steel perforated inner tube was used as a support structure for cabling the superconductors. Three main goals drive the test:

1. The examination of the CTFF Monel 400 outer sheath at every stage of the standard procedure

   - Helium Leak Test (HLT) after CTFF.

   - HLT after bent 180°in a 1.75" radius.

   - HLT after high pressurized at 600 PSI (40 atm) at 300 K for 10 min.

   - HLT after thermal shocked from 300 to 77 K for 10 min.

2. The determination of the spring back compensation needed to provide a complete 180°bent

3. The assessment of the superconductor after bending at the small bending radius.

Before entering into the specifics of the experiment, a description of the superconductor and their capabilities will be addressed.

### MgB2-CIC: Enhanced superconductor

The MgB2 superconducting wires we use in the following experiments were provided by HyperTech Research Inc. The superconductors are part of an intensive research plan, in which the current density was substantially enhanced. This property mark a breakthrough in the MgB2 performance at high fields, and it constitutes a 2nd generation in MgB2 production. Figure 2.31 compares the Jc performance of 1st generation and (non-optimized) 2nd generation MgB2 wires, with 2nd generation Jc over 1000 $A/mm^2$ at 4 K, 12 T.

According to theoretical calculation made by the MgB2 manufacturer[h], the optimized 2nd generation could increase the critical current in a factor of three, in this case the current densities could reach as high as 30,000 $A/mm^2$ at 5 T 4 K; 20,000 $A/mm^2$ at 5 T 10 K; 3000 $A/mm^2$ at 12 T 4 K; and 2000 $A/mm^2$ at 12 T 10 K (which would be close to Nb3Sn's Jc at 4 K). This breakthrough potentially brings about Nb3Sn type magnets at NbTi type pricing, with clear and dramatic impact on the whole Nuclear Physics, fusion, HEP, MRI [97] and NMR communities.

### MgB2-CIC: Performance at a 1.75" bend radius

The test samples consist of 18 MgB2 superconductors, cabled around a 3.96 mm OD inner tube, with a 76.2 mm twist-pitch. During the cabling procedure, we find that one of the wires had a damage spot.

---

[h]Mike Tomsic, private communications.
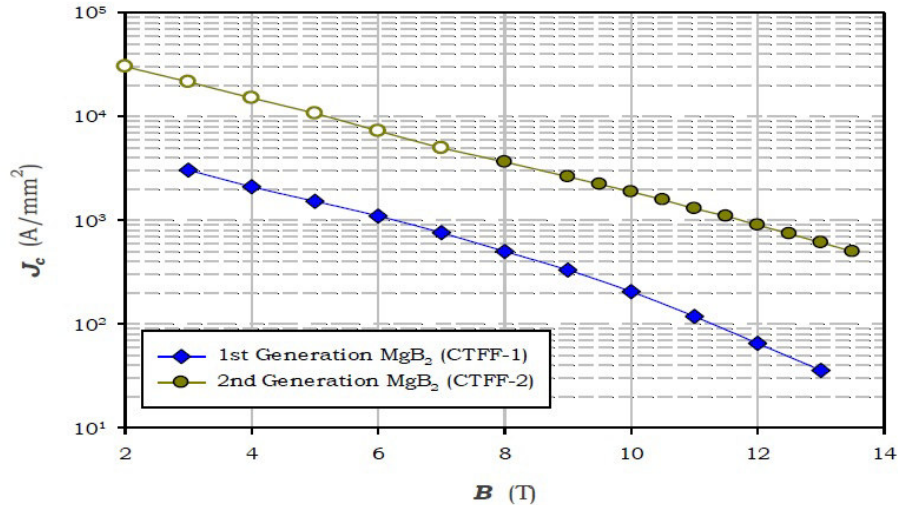
Figure 2.31: Jc comparison at 4.2 K of 2nd generation MgB2 superconductors with todays commercial 1st generation MgB2 conductors. Image courtesy of HyperTech Research Inc.

After inspecting it at the microscope we suspect that "something was dragged" leaving a "hole", See figure 2.32, probably during drawing the wire.
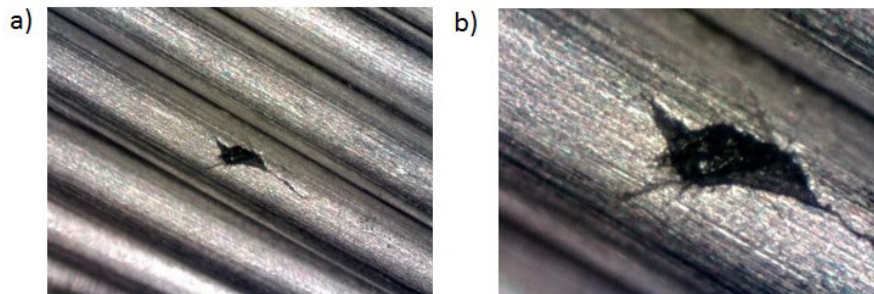


Figure 2.32: The picture at left shows the hole + crack found at one of the 18 MgB2 strands used for the first MgB2 CIC using Strand #3359. The shape and the depth of the deformation suggested that something was pulled and dragged from the strand.

After inspecting the remaining strands already cabled, no more visible (up to magnifying glass level) damage spot were identified. We proceed with the CTFF procedure. Having this type of defects could provide precise information of the evolution of the deformation, and the mechanical behavior of strands during CTFF procedure and after bending. The location of the hole at the damaged strand was tracked along the CTFF procedure.

**CTFF Weld assessment and Spring back measurements**

Hypertech performed the CTFF on both CIC (MgB2 and Nb3Sn) and shipped both CIC back to us. The MgB2 CIC was tested for leaks in a Helium Leak detector. No leaks were found within the accuracy of $1.0x10^-12$ atm*cc/s leak rate at a pressure of $< 2x10^-3$ torr. The CIC was then divided into five samples, 254 mm (10.5) long each. The samples were bent in a 1.75" radius robotic bender at

an angular speed of 150°/min. To figure out the spring back compensation, samples 1 to 3 bent adding in gradual over-bend starting at zero i.e. 0°, +10°and +15°. The samples were examined using the commercial software MB-Ruler to measure the spring back angle, see figure 2.33. By interpolation of
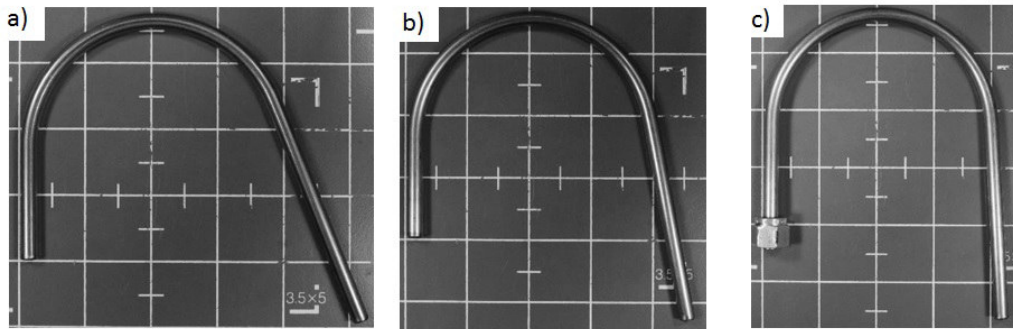


Figure 2.33: MgB2 CIC. 18 strands 0.778 mm OD of MgB2 cabled around a 3.96 mm OD stainless steel inner tube with a 76.2 mm twist pitch. Sample A) was bent 180°in a 1.75 radius without over-bending. The measured spring back is -27.19°. Sample B) was bent 180°in a 1.75 radius with 10°over-bend. The measured spring back is -11.06°. Sample C) was bent 180°in a 1.75 radius with 15°over-bend. The measured spring back is -7.00°.

data shown in figure 2.33, we estimated the required over-bend to suppress the spring back effect, to be 19°. Sample 4 was bend using the predicted value and the data of its spring back was incorporated to figure 2.34 to re-adjust spring back calculations. The adjusted value, colored in red, was 21.4°. Sample 5 was bend using the new predicted value, its spring back data matched the red point i.e. its spring back is less than 1-degree.
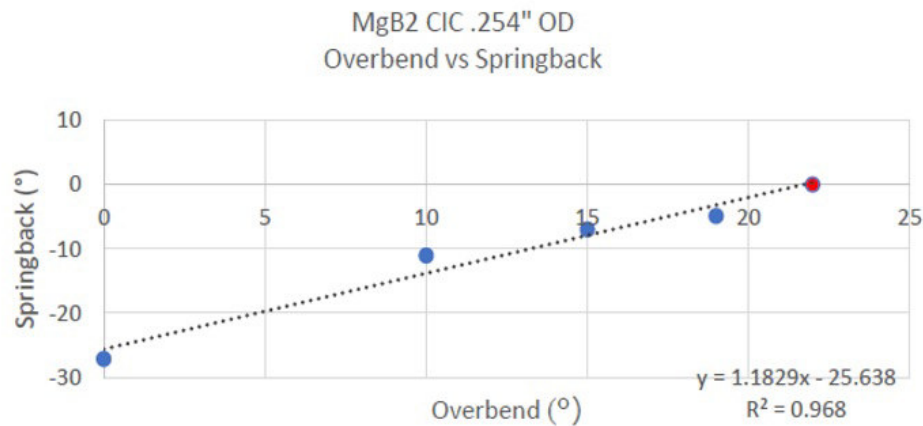


Figure 2.34: Spring back vs. over-bend in three MgB2 samples bent with progressive over-bend. The estimated value needed to suppress spring back was 19°. The predicted over-bend was applied to sample 4, and its spring back data was used to re-estimate the spring back interpolation. The adjusted value, colored in red predicts an over-bend of 21.4°. Sample 5 was over-bent using this corrected value and the measured spring back was within a 1-degree of accuracy.

**Standard procedure on the weld**

Each of the 5 samples were subjected to the standard procedure, early described. The results of the test are shown in Table 2.4. After careful inspection, the standard test reveals no damage to the outer

sheath in any of the test. The original plan was to extract MgB2 strands form sample 5 and have them test for Ic. While dissecting sample 5 (and the rest of the samples), it was found that :

1. For sample 5, there was a MgB2 leak (burst) before the bend (at the straight section), where it was grabbed by the holding die. 12 wires were torn at $30°$. The sample was over bent $21.4°$.

2. For sample 4, 14 wires were torn, the sample was over bent $19°$.

3. We proceed by dissecting the remaining samples 1,2 and 3. Sample 1 was bent 180 without over-bend, and no broken strands were found.

4. Sample 2 bent $180°$ adding a $10°$ over-bend, there was one broken strand.

5. Sample 3 was the one that had the damage strand. That was the only broken strand.

| ID | HLC as received | Over bend (°) | Weld line | HLC after bend | HLC after pressurizing at 600 Psi | HLC after thermal shock from 300-77 K | # Broken strands | Angular distribution |
|---|---|---|---|---|---|---|---|---|
| MgB2-s1 | ✓ | 0.0 | C | ✓ | ✓ | ✓ | 0 | — |
| MgB2-s2 | ✓ | 10.0 | D | ✓ | ✓ | ✓ | 1 | 150° |
| MgB2-s3 | ✓ | 15.0 | U | ✓ | ✓ | ✓ | 1 | 90° |
| MgB2-s4 | ✓ | 19.0 | C | ✓ | ✓ | ✓ | 14 | 150° |
| MgB2-s5 | ✓ | 21.4 | E | ✓ | ✓ | ✓ | 12 | 150° |

Notes: S3 is the sample that had the damage strand.

E- Weld line facing the expansion side of the bend.

C- Weld line facing the compaction side of the bend.

U- Weld line facing the Upward top side of the bend.

D- Weld line facing the Downward side of the bend.

Table 2.4: Heat treatment study on 316 L Perforated SS inner tube and superconductor performance at 1 bending radius.

As it can be seen, data suggest that there is a strong correlation between the over-bend and the number of broken strands. Which is related with the total strain seen by the superconductor, the larger the arc, the larger the strain. Sample S3 is exempt of this supposition. In this case, the deformations

(hole) noted on the wire, weakens the strand prior the bending, figure 2.32. To confirm this, sample S3 was dissected and the strand was isolated and inspected under the microscope, see figure 2.35. The strain seen by the strand during bending, was enough to tear it.

This unfortunate finding, lead us to perform routinely inspection of the superconductor prior cabling. Two possible scenarios could lead to deformations on the wire:

- Debris caught in the drawing die, or contamination on the drawing fluid.

- Debris caught during cabling procedure.

To discard the first, we will inspect random sections taken directly from the spool of superconducting wire, and carefully inspect them.



Figure 2.35: Dissection of cable sample 3. The tear shown occurs after the outer sheath welding process and the bending tests, most likely due to the strain at the bend. Figure at left shows the breaking point of the strand. The image at right shows a close-up image of the tear.

## Superconductor Assessment

To figure out which part of the process damage the superconductor, we performed three different experiments (labeled as Experiment D#) to determine if by changing the drawing parameters, the inner tube or the metal foil, we could avoid having breaking strands.

The strands used in the samples were examined by microscope prior inserting into the cabling device. All the strands had some visible mysterious dots running in straight lines along the axis of the wires, located at random locations around the wires, and randomly spread along the wires, see figure 2.36. The depth of the deformations is not comparable to the one seen in figure 20.

By inspecting the remaining wires, all of them show shallow stripes (or scratches) along the wires. Similar lines are present when contaminated drawing lubricant is used and/or when the material is reaching its drawing limit. NOTE: For comparison purposes, a careful inspection of MgB2 30-mono filaments (Hypertech Inc) was done, the outer surface did not show scratches or perforations, although the OD it's slightly larger (1 mm OD) as well as the wall thickness.

In Experiment D1, we keep the same configuration as previous samples i.e. Perforated Stainless Steel tube, 18 MgB2 strands, SS foil and Monel 400 outer sheath (Hypertech Provided already CTFF tubing dated as 11/15/16), 1.75 bending radius, but we increased the drawing factor from .254 to .256. Table 2.5 shows the results after dissection of the 3 samples.

Findings: Note that the amount of over-bending is practically the same as the one used in samples S1 to S5, 21°, the only thing that changed was the OD by 2 mils in diameter.

1. The straight section, ED1.3, it doesn't have any broken strand. This may imply that the cabling + drawing procedure does not contribute to worsening the damage of the strands, or the added damage is not big enough to cause a tear.
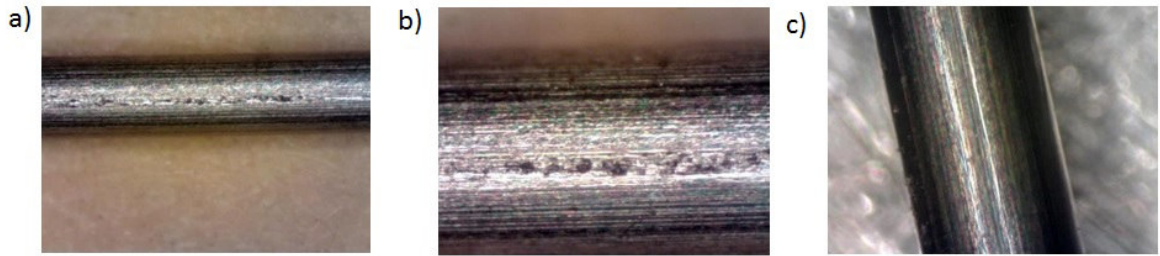
Figure 2.36: Mysterious dots at the surface of most of the strands used for experiments D1, D2 and D3. The dots are not scratches; they may be caused by imperfections of the drawing die or the use of improper lubricant. The parallel thin stripes along the surface of the strand suggest that the wire drawing pushed the wire to its drawing limit.

| ID | Bend (°) | Over-bend (°) | #Broken Strands | Angular position |
|---|---|---|---|---|
| ED1.1 | 180 | 21 | 0 | — |
| ED1.2 | 180 | 21 | 0 | 150° |
| ED1.3 | straight | — | 0 | — |

Table 2.5: Experiment D1: Decreasing compaction factor.

2. Samples E1.1 and ED1.2 experience a 21°over-bend. Sample ED1.2 has nine broken strands.

3. For some reason Sample ED1.1. does not have any broken strands even when it was subjected to same conditions as ED1.2.

In Experiment D2, we keep the same configuration as previous samples i.e., 18 MgB2 strands, SS foil and Monel 400 outer sheath, 1.75 bending radius; We added two changes, we increased the drawing factor from .254 to .256 and we replaced the 5/32 OD Stainless Steel Perforated Inner tube by a Brass tube of same dimensions. We did so bearing in mind that the indentation effect of wires into the brass could allow the strands to rearrange at the bend, which may be beneficial for the strand integrity. Table 2.6 shows the results.

| ID | Bend (°) | Over-bend (°) | #Broken Strands | Angular position |
|---|---|---|---|---|
| ED2.1 | 180 | 21 | 15 | 150° |
| ED2.2 | 180 | 21 | 1 | 150° |
| ED2.3 | 180 | 21 | 0 | — |

Table 2.6: Experiment D2: Drawing factor + Brass inner tube replacement

Findings: Sample ED2.1 was bend using the wrong bending die, instead of using 1.75 radius, a

1 radius was used. Surprisingly, the outer tube did not collapse or tore, this may be beneficial for the future test at the smaller bending radius.

1. Sample ED2.1 had 15 broken strands. The three remaining strands had some holes located at the straight section preceding the bend. See figure 2.37.

2. Sample ED2.2 was bent using 21°over-bend, and it has only one broken strand, same results as experiment ED1.2.

3. Sample ED2.3 was bent using 21°over-bend, and it has only one broken strand, same results as experiment ED1.1.

4. It seems that aside from sample ED2.1, we obtained the same results as Experiment#1.
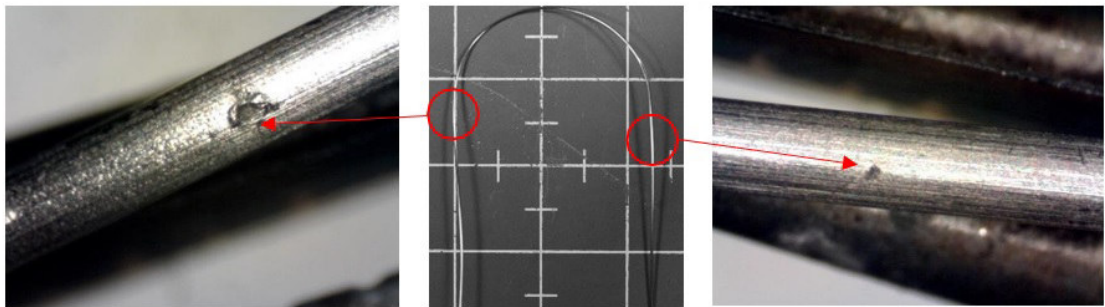


Figure 2.37: One of the three MgB2 strands that survived the 1-inch bending radius, sample ED2.1. The deformation is observed to be deep (picture A) and is in the straight section before the bend. A second defect (picture C) was found in the right leg of the MgB2 strand; the deformation is smaller than the one found at the left leg but is visible and its also located at the straight section of the bend.

In Experiment D3 the same configuration is used, as in previous samples i.e. Perforated Stainless Steel tube, 18 MgB2 strands and Monel 400 outer sheath, 1.75 bending radius; The drawing factor was increased from .254 to .256, the Stainless-Steel foil was replaced by Copper foil, thinking that this could relax a possible friction lock effect of the Stainless Steel - Monel 400 - Stainless Steel tandem of the Inner Tube  Superconductor  Foil assembly. Table 2.7 shows results of the experiment.

| ID | Bend (°) | Over-bend (°) | #Broken Strands | Angular position |
|---|---|---|---|---|
| ED3.1 | 180 | 21 | 1 | 180° |
| ED3.2 | 180 | 21 | 0 | — |
| ED3.3 | straight | 0 | 0 | — |

Table 2.7: Experiment D3: Drawing factor + Copper foil replacement

Findings:

1. Sample ED3.1 experienced a 21 over-bend and has only one broken strand.

2. Sample ED3.2 was under same conditions as of Samples ED3.1 and has no broken strands.

3. The straight sample ED3.3 has zero broken strands.

The experiments ED1, ED2 and ED3 probed:

- If the strands have some deformation/damage previous bend, the deformations will survive the drawing process (Samples ED1.1. and ED3.3 probed that).

- If the deformation is long enough (S3) it will tear.

- If the deformation is not too long and its located in a bend-free region, it may survive the drawing + bending process (ED2.1).

- If the strands are damage free, they can survive even after small radius (1) bends (ED2.1)

Apparently, increasing the drawing factor, changing the inner tube and the foil may have a positive impact on the integrity of the superconductor. To provide evidence, we need to use well inspected and damage free superconductors.

## Experiment remarks

1. 2 6-foot long CIC's cores were manufacture using real superconductor, the first used 18 0.786 mm OD MgB2 strands (21% MgB2) and the other used 18 0.786 mm OD Nb3Sn strands. In both cases, a 0.254 mm wall thickness (0.010) and 3.96 mm OD (5/32) 316 L Stainless-Steel perforated inner tube was used as a support structure for cabling the superconductors.

2. While cabling the 18 MgB2 strands around the Stainless Steel inner tube, we find that one of the strands had a damage spot. After inspecting it at the microscope we suspect that something was dragged leaving a hole. We decided to proceed and CTFF the sample with the contingency of accurately tracking the damaged area.

3. The CIC was divided into 5 samples 8 inches long each. The samples were bent in a robotic bending machine using a costumed-made 1.75 bending radius die (according to dipole requirements). Gradual over-bend was applied to each of the samples to perform interpolation and predict the over-bend need to compensate spring back effect. The interpolation predicted an over-bend of 21.4 degrees.

4. The standard procedure applied to the five samples resulted in a success. No evidence of bottle-necking, cracking or leaking was found at any of the samples. It worth to mention that during the bend test the weld line was placed facing different direction at every test i.e. In sample #1 the weld line faced the compaction side of the bend, while in sample #2 it faced the downward side of the bend. In sample #3 it faced the upward side of the bend, in sample #4 it faced the compaction side again, and finally, in sample #5, it faced the expansion side.

5. After dissection on samples 1 to 5, in which a gradual over-bend was applied, reveal that the only sample in which no broken strands were detected was the one without over-bend. The test suggested that there is a direct proportionality between the over-bend and the number of broken strands.

6. To understand which part of the process damaged the superconductor, we performed three different experiments (labeled as Experiment D#) to determine if by changing the drawing parameters, the inner tube or the metal foil (friction lock effect), we could avoid having breaking strands.

   - In Experiment D1 we keep the same configuration as previous samples i.e. Perforated Stainless Steel tube, 18 MgB2 strands, SS foil and Monel 400 outer sheath (Hypertech Provided already CTFF tubing dated as 11/15/16), but we changed the drawing factor by increasing the OD from .254 to .256. We probed that the drawing process without bending does not cause brake of the strands. The bending test is inconclusive, in one sample 9 strands tore, while in the other (which was done under same conditions and configurations) there is none.

   - In Experiment D2, we changed the drawing factor from .254 to .256 and we replace the 5/32 OD Stainless Steel Perforated Inner tube by a Brass tube of same dimensions. We though that a softer material would allow larger indentations after drawing, reducing the strain seen by the strands. The strands are not damaged in the straight sample. The bend samples tore, this suggests two things, 1. The amount of OD increase wasn't large enough to reduce significantly the strain, and 2. That it may be combined with other contribution that leads to a larger strain reduction.

   - In Experiment D3, we changed the drawing factor from .254 to .256 and we replaced the Stainless-Steel foil for a Copper foil, thinking that this could relax a possible friction-lock effect of the Stainless Steel - Monel 400-Stainless Steel tandem of the Inner Tube Superconductor Foil ensemble. Again, the straight sample is not related to damage strands. The bend test is no conclusive, one show one broken strand while the other test didn't, both were done under same conditions.

7. Inconclusive results taken from experiments D1, D2 and D3 suggest that there must be another reason why the strands are braking. The damaged spot located at one of the strands of the already cabled MgB2 CIC, and the lack of inspection of individual strands prior cabling, opens the possibility of the existence of other damaged spots that could have been hidden along the cabled strands. This motivates us to inspect 5 random samples, 10-inch-long of MgB2 wire and seek for other deformations.

8. Five 10-inch-long virgin MgB2 strands were taken directly from the spool and examined under the microscope. A careful Inspection revealed that all the samples suffered microscopical deformations located along and around the strands. Among the deformations, crack lines, gauges, and non-superficial scratches were found. The deformation represents potential failure areas and it may be the cause of the tearing seen in previous experiments.

9. A new batch of MgB2 strands will be manufactured, in the meantime, we will perform a reproducible study on the heat treatment of the 316L SS perforated tube. Then, we will explore different options for the outer sheath of the MgB2, 1.-Annealing at cold temperatures to increase the ductility of the MgB2 outer sheath, 2.- MgB2 with lubricant, 3.- MgB2 without lubricant + stress relieved and, 4.- Glidcop as outer sheath instead of Monel 400.

### 2.8.3 Stress relieve and annealing process: MgB2 and Nb3Sn CIC

Hyper Tech is commercializing this superconductor, supplying wires to companies that are selling 12-16T research magnets. The non-Cu Jc values for 217 sub-element Tube-Type strands have reached 2500 $A/mm^2$ at 12 T, as shown in figure 2.38. These types of wires can be made with small filaments so they are stable at low fields.
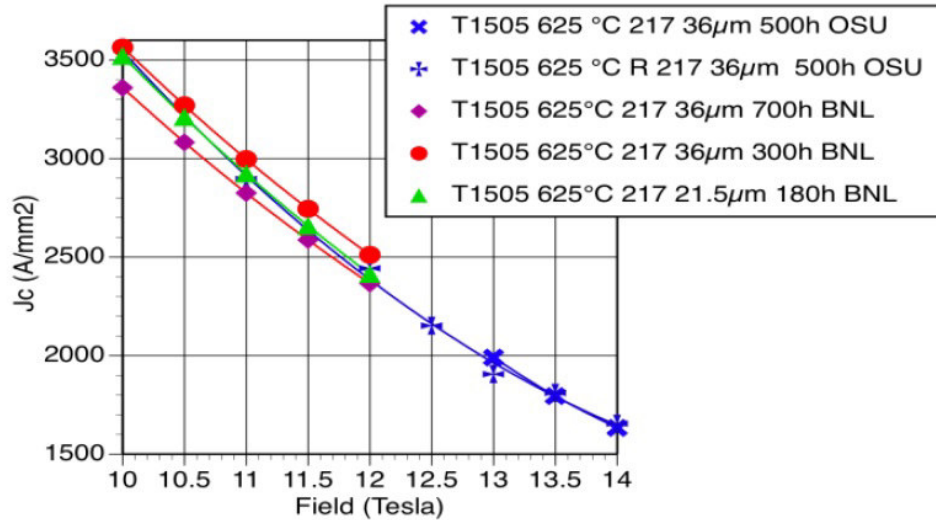


Figure 2.38: non-Cu Jc of a 217 re-stack strand at 0.7 mm (35 $\mu$m sub-element). Image courtesy of HyperTech Research Inc.

There is the desire to see Nb3Sn wires improve at high fields. For the first time in a bulk wire, Hyper Tech has demonstrated the potential for artificial pinning in a Nb3Sn binary wire. We all know typical ternary Nb3Sn (both Nb(Ta)3Sn or Nb(Ti)3Sn) have layer Jc's at 12T,4K around 5000-5500 $A/mm^2$ at 12T, 4K) which has been the limit for the improving the wire properties. Hyper Tech and OSU have reported preliminary work that demonstrates the fact that we reacted a Nb(1Zr)3Sn sub-element and oxidized the Zr throughout the sub-element. For the sub-element wire we achieved a layer Jc of 9600 $A/mm^2$ at 12T, 4K. The grain size was tremendously reduced compared to Nb3Sn without the ZrO2. Grain size reduced from about 100 nm to 40-50 nm , and the layer Jc in the Nb3Sn area was doubled compared to traditional Nb3Sn high Jc wires with Ta or Ti additions. This is a big achievement. Plus in the future there is the potential to also introduce Ta or Ti additions to even further improve the layer Jc. Even after 60 years of Nb3Sn R&D there is still considerable room for further improvement.

A new batch of MgB2 strands will be manufactured to correct the errors on the surface of the superconductor. We will repeat previous experiments applying a thermal process on the CIC inner. We will conduct a study to identify the appropriate heat treatment on the 316L SS perforated tube. We will follow the American Society for Metals (ASM) heat treatment procedures for the stainless-steel alloys. The perforated inner tube is made of 316L Stainless Steel (AISI/UNS S31603), and according to its grain structure is cataloged as an austenitic alloy; To identify the proper heat treatment, we need to understand the effects of the cold drawing on the grain structure. In the drawing process, the outer diameter was reduced from 3/16 (4.76mm) to 5/32 (3.96mm), causing a severe plastic deformation (SDP). According to [98], SDP of an austenitic promotes the formation of sub-microcrystalline (SMC)
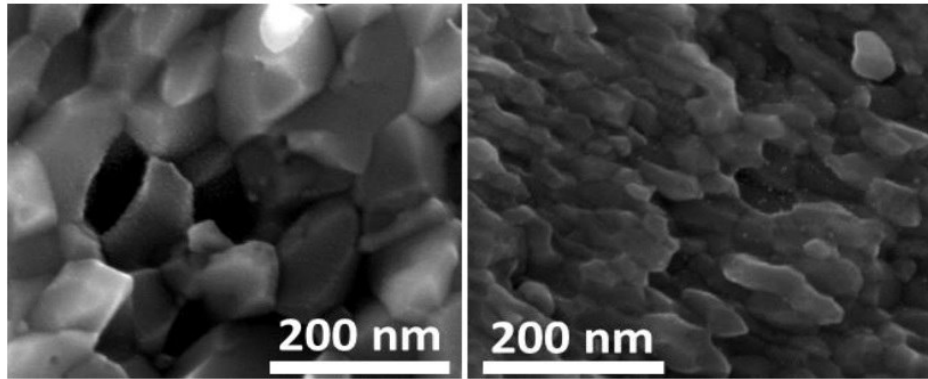
Figure 2.39: Nb3Sn grains with and without pinning; grain sizes reduced in half with ZrO2 pinning compared to Nb3Sn with no ZrO2 pinning. Image courtesy of HyperTech Research Inc.

and/or nanocrystalline (NC) structures, which in return increases significantly the strength properties.

To get rid of the accumulated stresses while preserving the spring effect on the inner tube, two thermal procedures will be explored [99], 1.-Removing the peak stress and 2.- Stress Reliving between forming operations. In the first, the samples will be heat treated at 480 C in an air atmosphere, and then slow cooled; For the second, the sample will be stress relieved at 900 C, in air atmosphere, and then slow cooled. The soaking times for both procedures depend on the thickness of the tube. Data taken from [100] was used to extrapolate the soaking time for the 316L SS 0.020 wall thickness tube, see table 2.8 and figure 2.40.
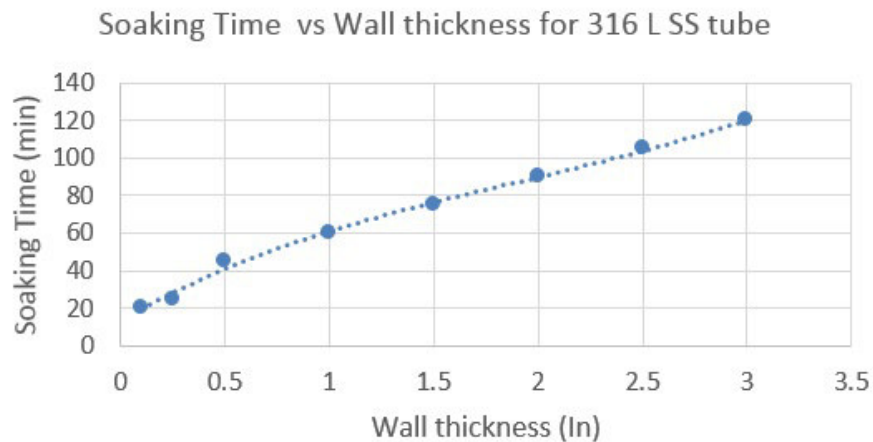


Figure 2.40: Soaking time extrapolation for 316 L SS 0.020 wall thickness tube.

For practical purposes, and making use of the available equipment, we will perform the stress relieve at the box furnace using air atmosphere. Two inner tubes, 20 long each were heat treated. One for the removing the peak stress, and the other for stress reliving between formation operations. The first tube was divided into two sections, and it was used to produce two samples, S52 and S53, see table 12. Both made use of 18 dummy strands (Silicon-Bronze AWS 5.7/ ErCuSi-A), 2 twist pitch,0.001 SS foil, and stress relieved CuNi 90/10 outer tube (We used the ASM stress relieve recommendation for

CuNi 90/10 alloy, [100]). Deep inspection (dissection) of samples S52 and S53 proved that removing the peak stress is not enough to soften the inner tube, therefore the strands are not able to rearrange and to indent deep enough into the inner tube, which leads to 6 and 4 broken strands for the first and second samples. The outer tube at both samples showed evidence of bottlenecking, a full annealing process will be explored in future. The second tube, was also divided into two sections, and they were used to produced two samples, S54 and S55, see table 12. Both samples also made use 18 dummy strands (Silicon-Bronze AWS 5.7/ErCuSi-A), 2 twist pitch, SS foil, and stress relieved CuNi 90/10 outer tube (Stress relieved according to ASM recommendations). No broken strands were found at both samples. This suggests that the 900 C stress relieved heat treatment softens enough the inner tube, such that the strands are capable to indent and slightly deform the inner tube during drawing process, in fact, the heat treated inner tube suffers a reduction of about 5mil on the OD after the CIC is drawn.

| ID | Inner tube thermal process | Drawing process | Strand Material | Outer tube thermal process | Overbend | Broken strands | Comments |
|----|----------------------------|-----------------|-----------------|----------------------------|----------|----------------|----------|
| 1 | Stress Relieve at 480 C 15 min soaking time air atmosphere | 0.1875 0.1675 0.1562 | Silicone-Bronze (AWS 5.7/ERCuSi-A) | CuNi 90/10 (Annealed at 480 C for 20 min soaking time, air atmosphere) | 22 | 4 | CuNi outer tube survived. Bottlenecking effect is present. 4 Broken Strands. |

Table 2.8: Heat treatment study on 316 L Perforated SS inner tube and superconductor performance at 1 bending radius.

Based on the latter results, we will use the Stress relieve between formation operations, as the preferred heat treatment for 316 L SS perforated tube. As it can be seen in Figure 32, the heat treatment relaxes local and overall stresses on the inner tube.

### Nano indenter: Harness measurement on several 316L SS samples vs heat treatment

To achieve the desired final dimension on the 316 L Stainless-Steel inner tube, the tube must be drawn from 5mm to 3.96mm, in this process, the thin wall remains unchanged 0.010 (.254 mm), and the tube gains harness. After the heat treatment, the stress relieve process relaxes the material and it becomes softer. To characterize the level of hardness and the relevant mechanical properties of the tubes, prior and after heat treatment, we will make use of a Nano-indenter. Nanoindentation has become the preferred technique for measuring and testing small volumes, it allows to record small loads and displacements with high accuracy, and use the displacement to estimate material properties as harness, modulus of elasticity and reduced modulus, among others [101].

For this study, we will focus on measuring the harness for two groups of samples of 316 L SS, at various stages of the drawing process, with and without stress relieve treatment. 1. The first group, is associated with a first batch of costumed made perforated Stainless-Steel tube. In this group, the original outer diameter of tube was 5mm. A three-drawing process was applied, and the harness was measured experimentally at 5, 4.7 and 3.96 mm, with and without stress relieve. 2. In the second group, the SS tube was drawn to the final size. We measured the samples with and without heat treatment, and we compared with the samples of first group.
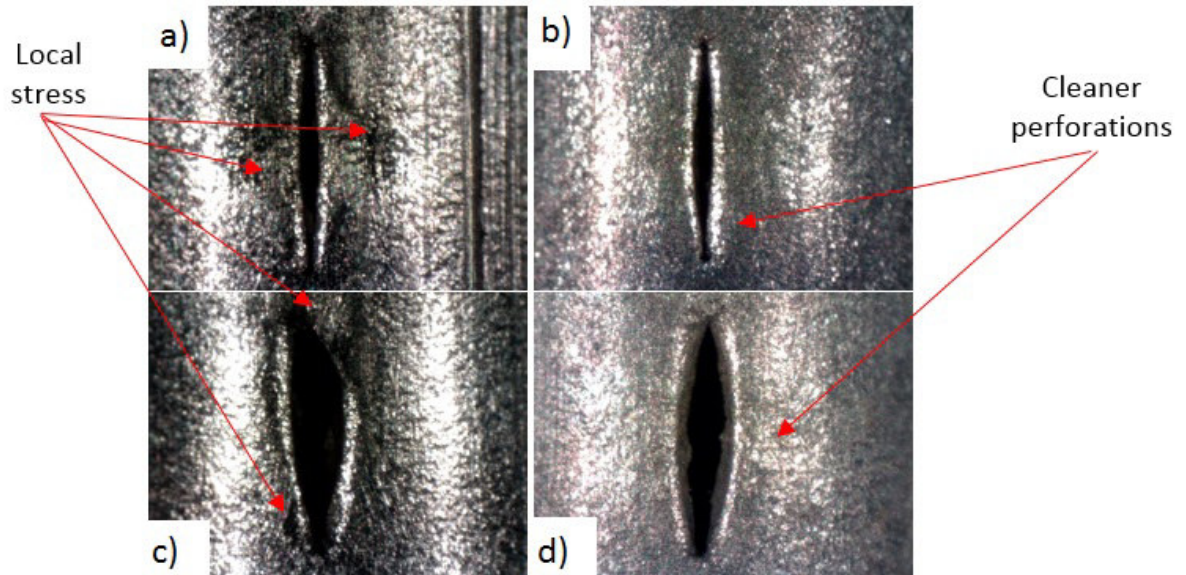
Figure 2.41: Effect on the stress relieving vs. no heat treatment on a 0.020 wall thickness, 316L SS perforated tube. Figures A and C show the initial condition of samples belonging to the first and second batch respectively. Figures B and D show the effect of the heat treatment applied to samples belonging to the first and second batch respectively. Samples heat treated show no marks of stress and the debris around perforations disappear.

## Sample Preparation

The experimental measurement was done using a 3-sided pyramid Berkovich indenter. To prepare the samples, the tubes were flattened in a press and then heat treated, see figure 34. After treatment, an EDM was used to cut 3x3mm squares. The samples were clean using acetone and isopropyl alcohol prior inserting them into the Nanoindenter.
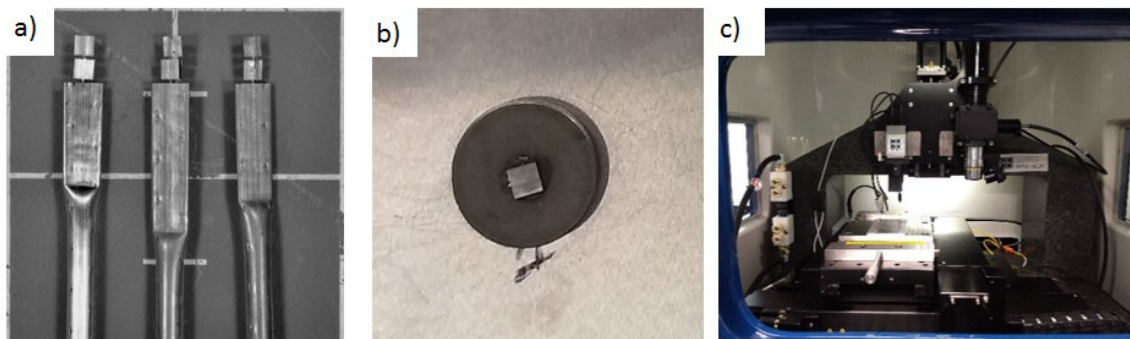


Figure 2.42: Sample preparation for hardness measurement using TI 950 Triboindenter by Hysitron. EDM cuts for samples after heat treatment (figure A). A 3x3mm flat sample glued to the sample holder (figure B). Samples deposited on the Nanoindenter prior to measurement (figure C).

To validate the measurement and the proper use of the Berkovich tip, the nanoindenter was calibrated on air [102] and a determination of the roughness of the sample was done. The indentation test done on the samples, complies with the with requirement of having at least 3x the roughness of the samples, represented with a topography map, see figure 34 B.

For each sample, two groups of 9 indentations were done. The samples were subjected to a load

of 10 000 N, with a holding time of 2 seconds (to avoid creep effect). After the load is applied, the Berkovich tip is removed, and the displacement is measured. The smooth curvature corresponding to the loading is characteristic of the Berkovich 3 sided-pyramid, and it represents an elastoplastic material, see figure 34.A). The response of the material is measured at initial stages of the unloading portion, in which plastic and stain energies are being released. In that region, the material response is considered as a pure plastic deformation, and the slope of the curve is related to hardness of the sample [8].
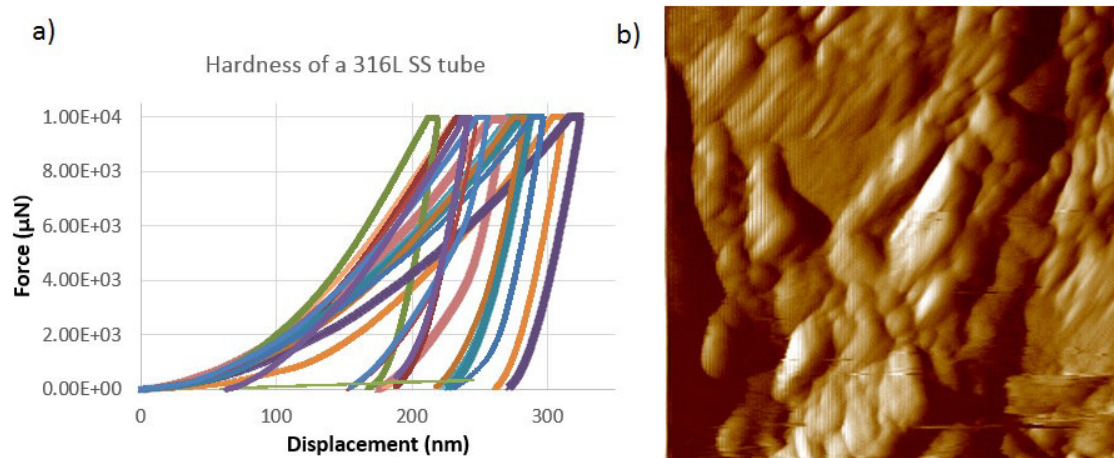


Figure 2.43: Nanoindentation done on a 316L SS perforated tube. In each sample, two groups of 9 measurements were taken, and their response is presented by the colored curves on figure A. To validate the use of the Berkovich tip, a comparison between the displacement of a test indentation and the roughness of the sample was determined. The net displacement complies with the requirement of being at least 3x the roughness of the sample. The roughness was determined using an atomic force microscope (figure B).

On table 13, the average and standard deviation of the computed harness for each of the samples is presented. For each sample, three measurements were done. The first, labeled as Raw represents a measurement of sample prior heat treatment. The tag Plain represents a measurement on a sample after is being heat treated at 900 C for 15 min. The sample do not have the weld line on it. On Column Weld the measurement was done on a sample that was heat treated at 900 C for 15 min, and it has the weld line of the tube on it.

As it can be seen on table 13, after performing nanoindentation on sample IN#0, we concluded that the sample was annealed at the 5 mm OD, there is no reduction of the hardness after the heat treatment. On the other hand, there is clear reduction on the harness after stress relieving sample IN#3, which probes that the sample was not heat treated at the 5/32 OD (as received). Sample IN#1 Raw remains practically unchanged in comparison with sample IN#0 Raw, the drawing process on sample IN#1 represents a 4.8% reduction, small to be detected. On the other hand, in sample IN#2 Raw, the drawing factor, compare to the dimension of sample IN#0, is 20.8%. This relatively large cold drawing process, may have induced microcrystalline grain growth, causing a 2GPa increment on the Hardness. A comparison between the harness of all the plain samples which includes different drawing processes, proves that the stress relieve treatment relaxes the material; the data stabilizes around 3GPa, which a number that will be using to characterize the effectiveness of the heat treatment.

**Experiments remarks**

1. Different heat treatment process on the 316 L perforated SS were study, with the aim to soften the tube and allow some deformation while preserving support structure.

2. We follow the ASM recommendations for stress reliving and removing peak stress on austenitic alloy. Removing the peak stress does not allow enough deformation of the inner tube, and is still associated with broken filaments.

3. A stress relieves after formation heat treatment, at 900 C for 15 min relaxes the material and allows a proper cabling. We decided to use this as the preferred heat treatment for the inner tube.

4. A consequence of the heat treatment on the 316 L SS tube, is that removes the stresses around the perforation, and cleans the debris of the stamp process.

5. A material characterization on the heat-treated samples was done using a Nano indenter. A good indicator of a properly done heat treated after the samples were drawn is 3 GPa.[15]

## 2.8.4 Current degradation measurements

The superconducting systems are extremely complex, a large number of phenomenons are involved, in fact, is a multi physics and engineering problem. The development of magnet systems is not the exception. When the magnets are design, precautions are taken to estimate the tolerances on the machining of parts, and the placement of the superconducting cables. The superconducting cable itself are tested prior the winding process to understand the actual performance at their virgin state. One of the most important and frequently useful test is the current degradation test i.e., is the determination of the $J_C$ as a function of the B at a given temperature, usually 4.2K (LN2 temperature). Usually this test is done in a small section of superconductor taken from the ends or beginnings of a new spool. The assumption is that, the small section should represent the overall performance of the entire spool of wire.This is usually a standard procedure prior winding a magnet. In our case, we measure the $J_c$ prior developing sections of CIC. In this subsection, the experimental procedure for measuring current degradation is explained, nevertheless, it must remain clear that the Accelerator Research lab at Texas A&M University, presently does not have capabilities for testing current degradation. The equipment necessary is costly and special installations are required. Nevertheless the procedure will be given and described in lenght.

**Sample preparation**

The development of CIC, as it was described in previous sections, involves the cabling of the super-conductor and a drawing procedure in a small bend radius. This two process could affect the super-conductor performance if the amount of stress and strain reaches high levels (that depend on each superconductor). There are different test to evaluate the integrity of the superconductor at different development process, including optical inspection, SEM analysis of the wires and $J_C$ measurement.

To perform the $J_C$ measurement, the CIC is prepared, two types of strands are studied: 1.- Strands taken from a straight CIC, and 2.-Strands taken from bend samples at different bend radius. First, the CIC must be prepared, and dissected without damaging the superconductor. This procedure is done
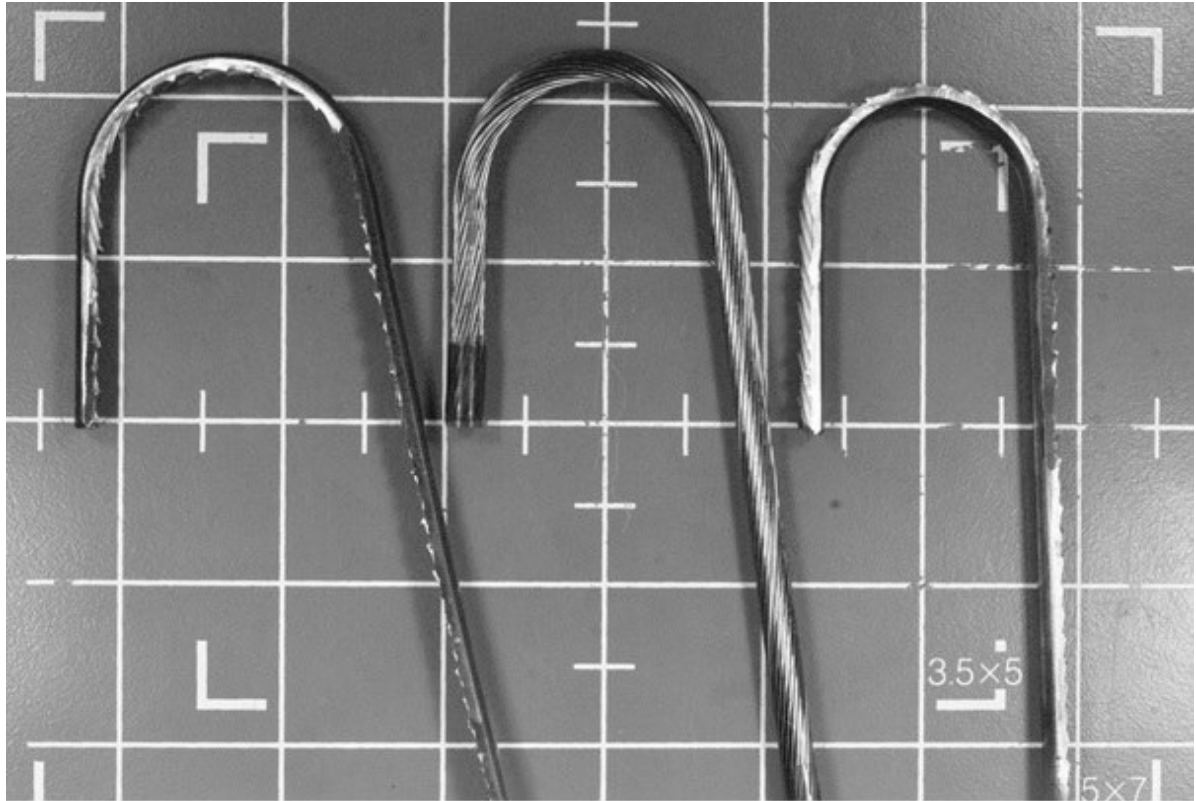
Figure 2.44: Dissection of a CIC to extract cabled strands of the superconductor.
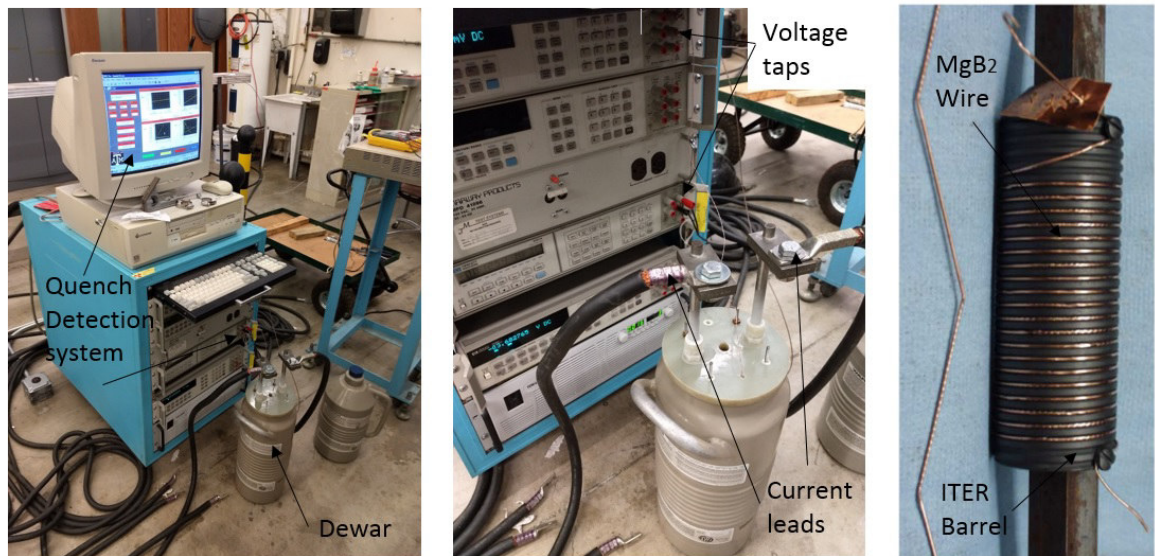


Figure 2.45: Experimental measurement of current degradation. At left, the quench detection system containing the HP Vee program, designed to recognize small levels of voltage developed during an Ic test. The photograph also shows the multimeters, power leads, voltage taps, and the Dewar. At center, the power leads connected to the ITER barrel containing a superconductor wound around. The Dewar is filled with coolant, and a current is sent to the wire. When the current reaches the critical current, a quench is developed, rising voltage across the wire.

manually with a high-speed dremel tool. The abrasive disc slowly brakes into the outer tube, exposing the wires, see figure 2.44. Then, the strands are carefully removed, and wound into an ITER barrel, as the one shown at right of in figure 2.45. The quench detection system is composed of a computer that operates and controls the power supply and the volt meters through an HP Vee program, the power supply, the current leads, the dewar, the coolant, and the ITER barrel.

The superconducting wires are then wound and solder into the ITER barrel and Voltage taps are connected along the wire. The barrel is inserted into the dewar and filled with coolant. Once the system is in thermal equilibrium with the temperature of the coolant, the power supply sends current in increments until reach the critical current. Most of the dewars incorporate a background field, which is also increased until achieve the critical values. The voltage tapas are recording the voltage, when the superconductor reaches the non-superconducting state, it becomes normal conducting, and a voltage is developed. When this happens the current is redirected into a dump resistor to avoid melting the superconductor. The curve $J_C$ vs B is known as the current degradation curve, it purpose is to compare virgin strands with others that are being subjected to deformations, in our case, the manufacturing procedure.

### Current degradation measurements on extracted $MgB_2$ and $Nb_3Sn$ CIC

To test the integrity of the $MgB_2$ and $Nb_3Sn$ CIC. Several wires were extracted, after the cables were bend, as depicted on figure 2.44. Figure 2.46, shows several current degradation test, nevertheless, samples labeled as 3489, represent measurements of virgin (orange squares) vs extracted (orange circle) strands. Notice that there is a substantial shift in the current, reveling some degree of degradation.
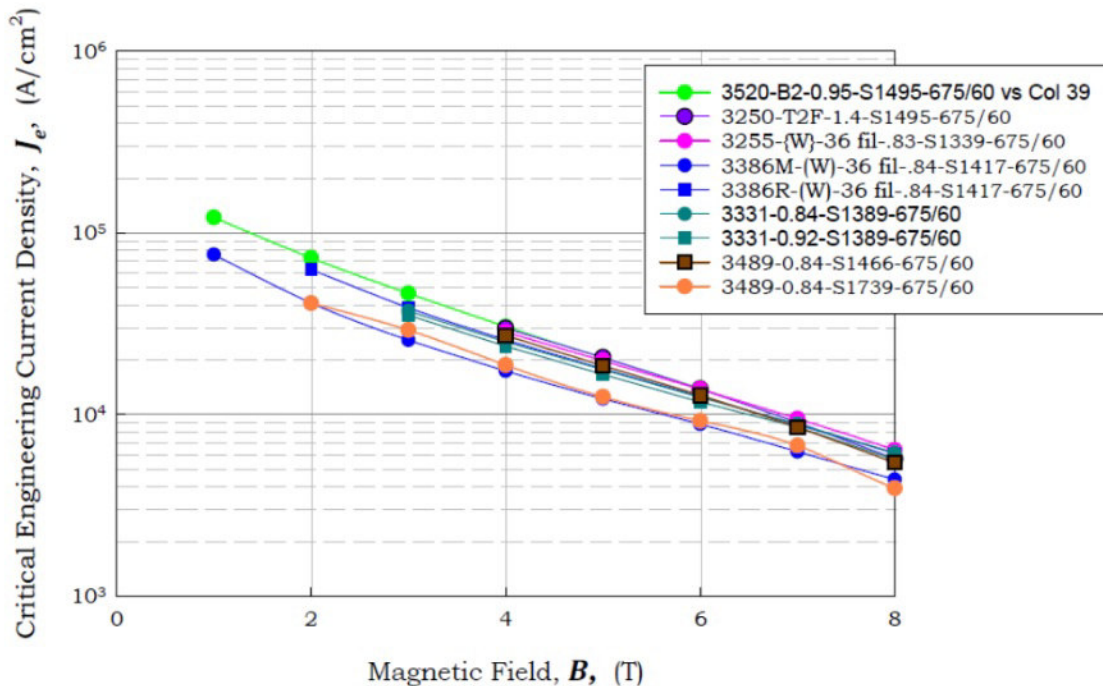


Figure 2.46: Current degradation on $MgB_2$ wires, extracted from a 1" bend CIC.

In this test, the extracted strands belong to a very small bend radius, less tan 25 mm, in which the twist-pitch of the wires did not meet the half-twist pitch requirement, as a consequence, the wires

experienced strain, which lead the samples to yield and degraded. As a comparison, figure 2.47, shows the current degradation measurement from a sample with proper twist-pitch. As, it can be seen on the measurements labeled as 3580-S137, there is practically no current degradation, the red prism and the green triangle, match at all points. The experiment was done at Ohio State University by Dr. Mike Sumption team.
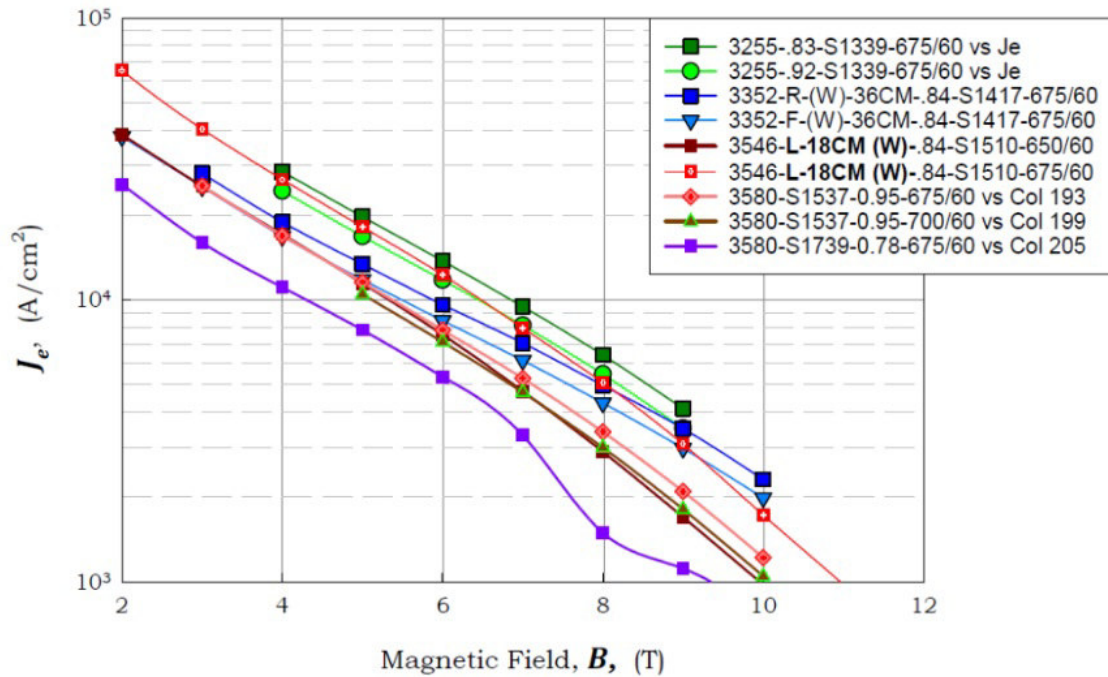


Figure 2.47: Current degradation on Glidcop sheathing-$MgB_2$ wires, extracted from a 1" bend CIC.

## 2.9   In-House Ic test: Experiment design

The wind-and-react CIC, made of $MgB_2$ and/or $Nb_3Sn$ wires, has a wide range of applications. Each application demands a costume-made CIC, with specific characteristics, specially the twist-pitch. For the proposed dipoles and quadrupoles of the interaction region of the future JLEIC, the CIC requires 18 wires, cabled with small twist-pitch. The development of this technology requires $J_c$ testing. The test time, for small samples normally takes from a couples of weeks to a month or two, usually the testing labs tent to be busy and the testing may get delayed. In the following subsection, a design for a holster for testing superconducting strands inside the CIC is presented. The design takes into account the restrictions and limitation on spacing into order to be used in the small-bore Dewar at TAMU. The experiments foresees to use one single superconducting wire, fully contained in the CIC, while having the remaining 17 as a dummy strands, or non-superconducting material. The strongest limitation for in-house testing is the available space in the Dewar bore, which is 50 mm. Luckily, the target bend radius for the $MgB_2$ CIC is 25 mm.

Figure above describes in detail the assembly. Two main components make possible the experiment. The first is a simple G11 machined sandwich (green) that clamps the CIC U-bend and supports the two splice joints from the CIC to the NbTi Rutherford current lead. The second, is the splice joint.
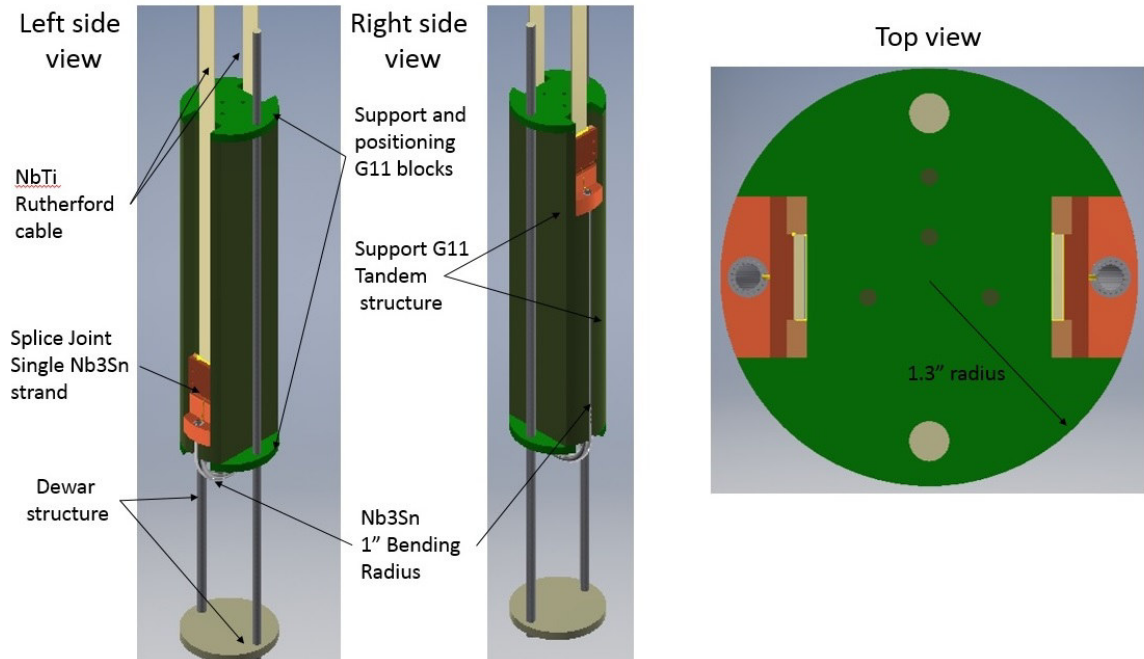
Figure 2.48: Schematics of a small profile U-bend CIC holster for LN$_2$ current degradation at Texas A&M University.

## Experiment preparation

To perform the J$_C$ measurement, the CIC (Wind-and-react) must be bend into the proper U-bend, and a both straight section at the end of the bend must be peeled, the single-superconducting wire must be exposed. The CIC is inserted into the splice joint and secured by tighten a set screw. The single-wire must be secured to the channel in the copper joint. Once both ends of the CIC are prepared, the CIC is taken to a inert atmosphere furnace and heat treated at 675 C for 1 hour in the case of MgB$_2$, the procedure for the Nb$_3$Sn is similar, but the soaking time is longer. Once the superconductor is reacted, the assemble is inserted into the G11 structure and secure, as depicted in figure 2.48, and figure 2.49. The voltage signal will be detected by antennas or hall probes, connected at the surface of the CIC. Once the sample is prepared, is then inserted into the Dewar and the cooling stages begin. First, a one-day cooling using LN$_2$ gas, then two days on LHe. A 1000 A power supply is proposed.

For the preparation procedure, cryogenic solder must be use. After the single-strand is reacted, the splice joint is opened and the NbTi Rutherford cable is inserted and secured. A thin layer of cryogenic solder must be used to properly connect the single-wire to the NbTi cable. The proposed solder is a eutectic 64Sn37Pb. A thermal model was done to estimate the power required to heat the cryogenic solder relatively fast, keeping within the 1 min boundary, where Sn-Copper diffusion has been reported [chamberlain], which can change the resistivity of the splice joint which could compromise the integrity of the experiment.

The simulation was done using the finite element analysis software COMSOL multiphysics, along with the thermal module. Two achieve the melting temperature, 183°C, four 250 W heat cartridges are installed within the splice joint. Figure 2.50 shows the splice joint, and the FEA model, at the right of the figure, a purple rectangle corresponds to the NbTi Rutherford area, which is soldered with the single strand. The eutectic temperature is achieved in 28 seconds, immediately after, a set of

NbTi Rutherford Cable

G11 support Tandem
(Half)

Splice Joint
assembly

Single Nb3Sn
strand

Nb3Sn CIC
1" Bending radius
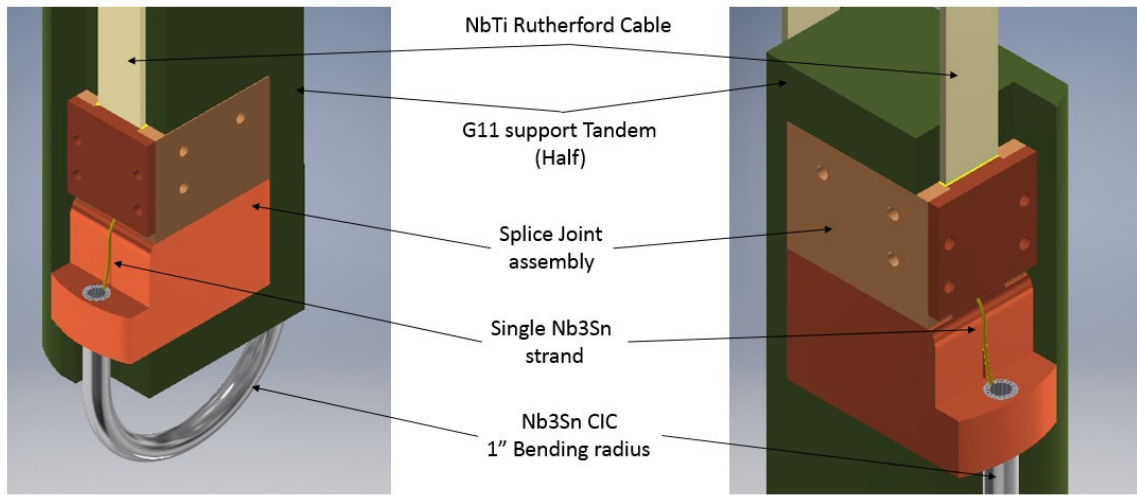
Zoom of the Splice Joints for both legs of the Nb3Sn CIC. Picture shows the NbTi Rutherford Cable, a single
Nb3Sn Strand sticking out of the CIC, and a half G11 Support tandem.

Figure 2.49: Close up of the detachable self-contained CIC single-wire testing unit.
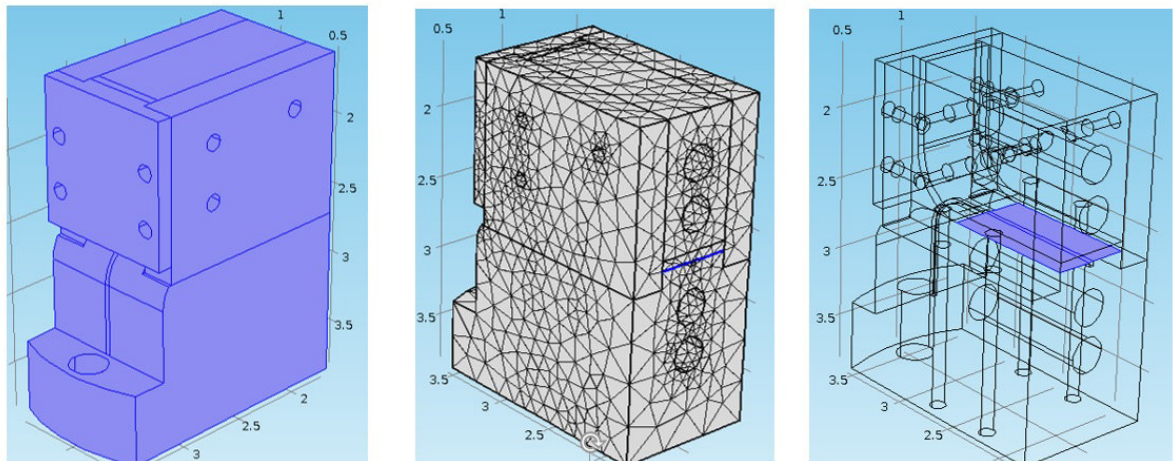


Figure 2.50: Thermal simulation on the single-wire testing unit, to determine the power required to achieve the eutectic point of the cryogenic solder without compromising the superconductor performance.

copper pipes inserted into the splice joint, cool down the system. This concept will be tested shortly, it offers the possibility to understand the actual impact on cabled superconductors at different fields.

## 2.10   2-layer CIC development

The EIC review panel has changed us to consider option of energy doubler [103]. The magnetic design for the 6 T dipole, is based on the 3 T superferric dipole, having the same structure but 5 layers instead of 3, and a 2-layer CIC instead of a single layer, figure 2.51 [104]. The strong and reliable design of the 3 T dipole [105], allow us to extrapolate the cost for the 6 T, on this, it was found that the magnet cost is proportional to the number of turns and the size flux return. On this basis, the 6 T dipole would cost 2.25 the cost of the 3 T. If compared with the usual Cos$\theta$, the price is proportional to the square of the magnetic field (B$^2$). The main element of this design is a 2-layer CIC, in the following section, the short-sample development is described, and a plan for future developments is proposed.
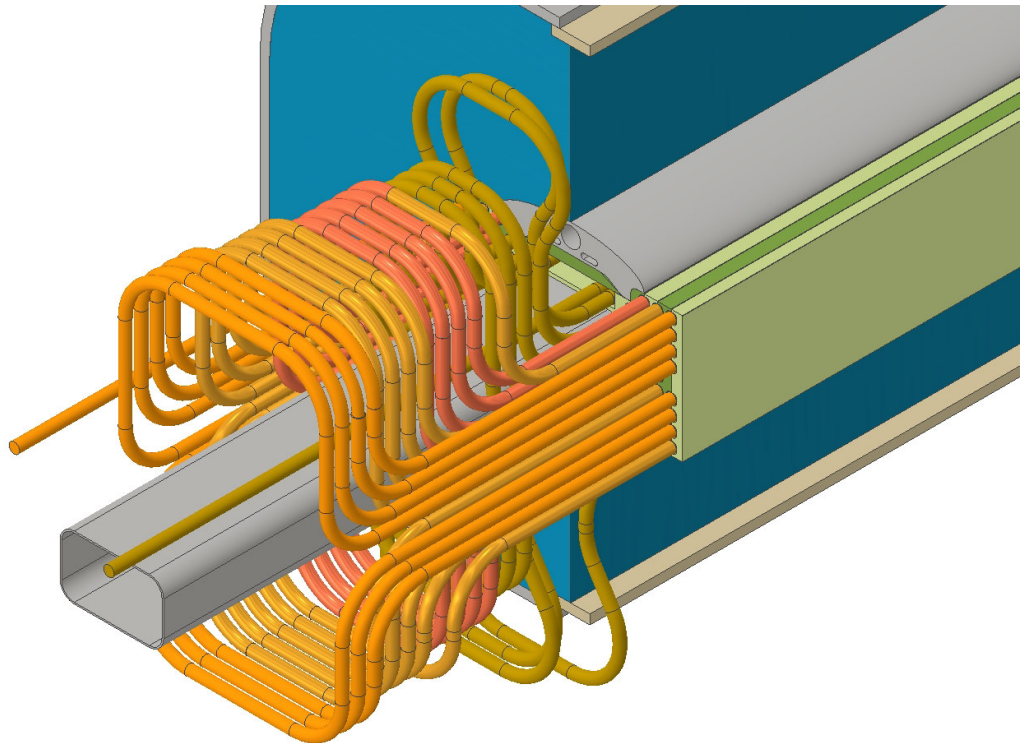


Figure 2.51: Schematics of the 6T dipole for the Future JLEIC

### 2.10.1   Short-sample development

Several issues concern the development of a two-layer CIC. In this cable, different effects takes place, the fact that there is a second layer, affects the way the wires redistribute both at drawing and at bending. There are a couple of things that the design must satisfy:

- The manufacturing procedure should not deform at any point the wires
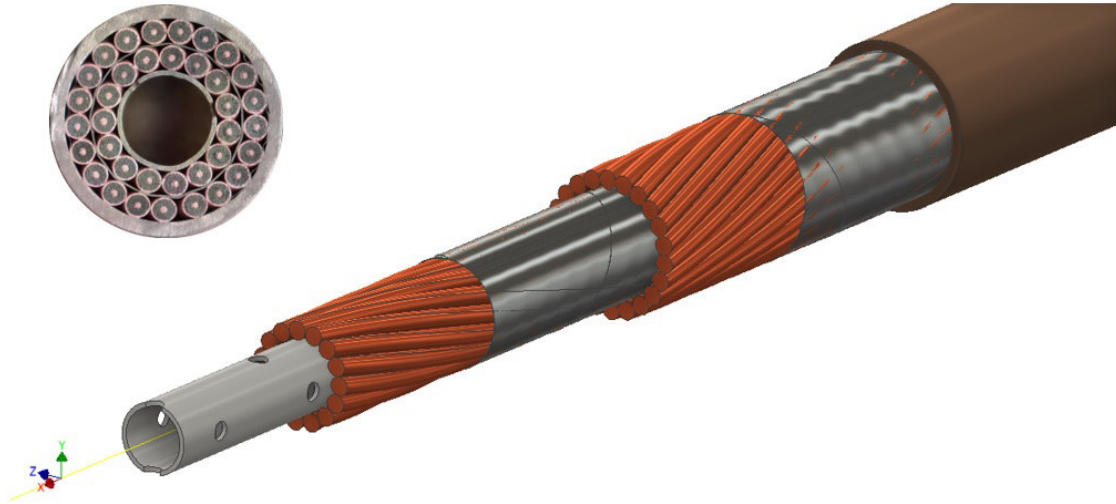
Figure 2.52: Schematic and cross-section of a 2-Layer CIC for the 6T dipole of the future JLEIC.

- The CIC must allow short bend radius. The bend radius used in the dipole is 2.351". Provisions must be taken to foresee over-bend requirements.

- The thickness of the outer tube must be considered in case of excessive strains could be developed.

- The first layer must remain open, to allow the LN2 to flow to the second layer, otherwise the cooling mechanism will be by conduction instead of contact.

A conceptual design and a cross-section of the 2-layer CIC is presented in figure 2.52. The design consist of a high-strength perforated tube, a first layer of NbTi superconducting wires, cabled with a twist-pitch of 2.351", which will leave a small azimuthal gap between the elliptical wires of about 0.5 mil. A high-strength, 0.1 mm thick, perforated stainless-steel foil is wrapped around without overlap, to provide a uniform surface for the second layer to be cabled around. The second layer is cabled in opposite direction to the first one. The assemble is inserted into a thicker outer tube, 0.0635 mm CuNi 90/10.

## 2.10.2   Mechanical characterization

The short-lenght development process, considered several options to determine the proper set of parameters to fulfill the requirements.

The drawing factor proved to be decisive to determine the performance of conductor. Large compunction factors affect in proportion the integrity of the wires. A compaction factor of .410" causes too much indentation in the wires, specially at the bends, see figure 2.53.

If individual strands are extracted, the damage caused in the strands is shaped elliptically. This small flat deformations propagate at every intersection point between the wires of the two layers. This flat regions cause discrete regions of friction, the global effect of all the deformation affect the spring back properties of the cable, and the overall mechanical behavior. The different bend test performed on the samples described in table 2.9.
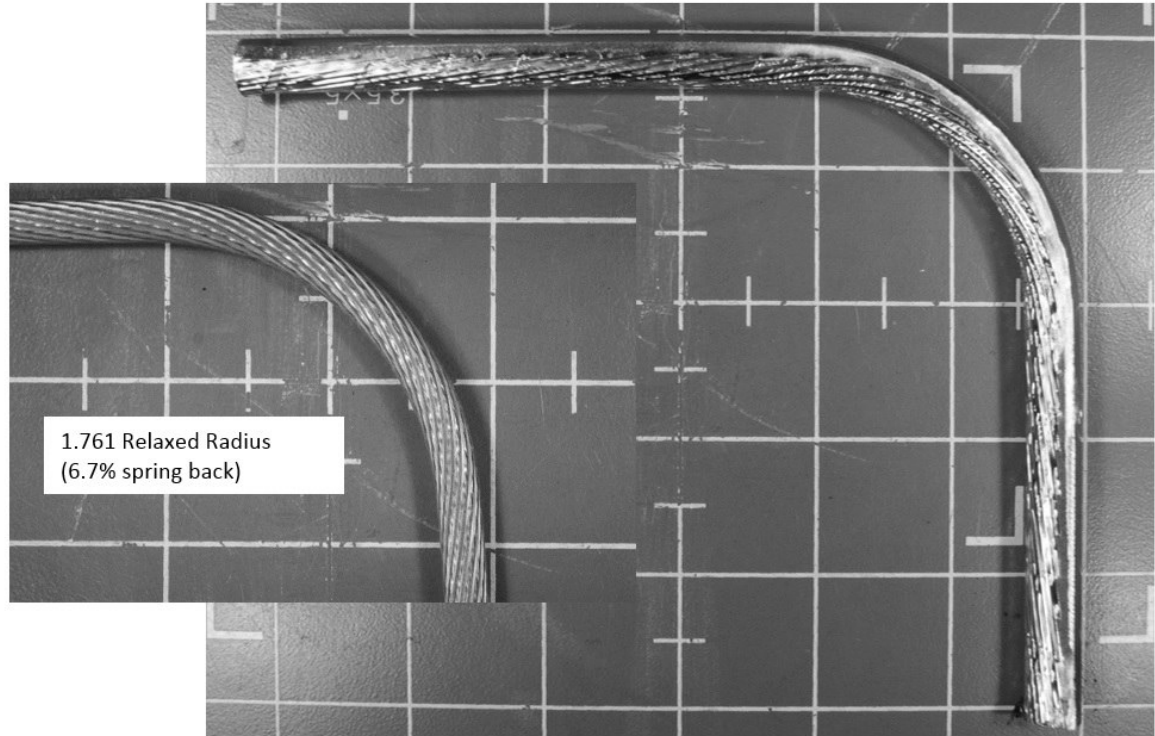
Figure 2.53: Short-sample development of 2-Layer CIC. Picture shows deformation on the strands that becomes more evident at the bend.
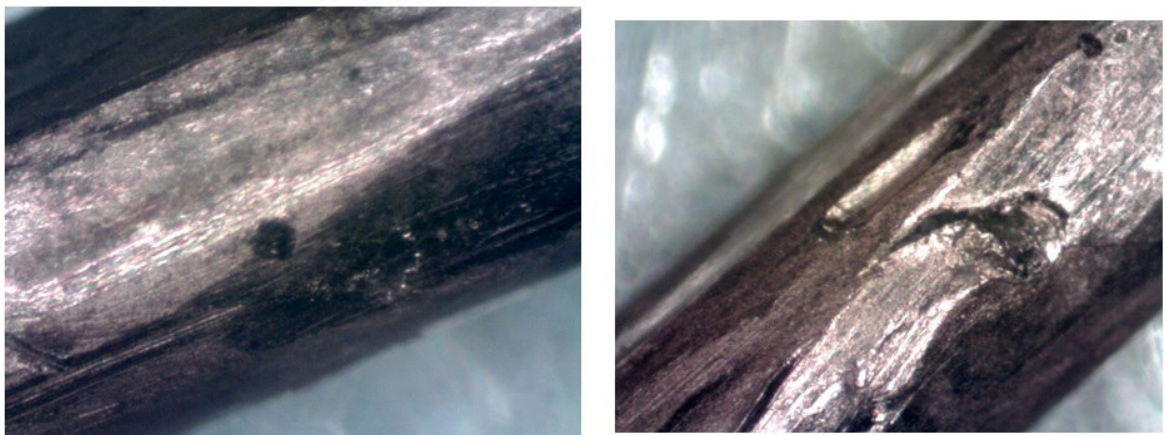


Figure 2.54: Local deformation due to manufacture process, the samples experiences excessive stress during drawing process.

| Layers orientation | Foil (in) | Outer Diameter | Wires x layer | Results |
|---|---|---|---|---|
| same | 0.001 SS | .410" | 15+21 | Excessive indentation wires-to-wire |
| opposite | 0.003 SS | .425" | 15+22 | Less indentation wire-to-wire |
| same | 0.002 Cu  0.004 SS | 0.432" | 15+22 | No indentation |
| same | 0.006 SS | 0.432" | 15+22 | No indentation |
| same | 0.004 ss | 0.432" | 15+22 | Azimuthal gap layers |
| same | 0.004 ss | 0.435" | 15+22 | Azimuthal gap layers |
| opposite | 0.004 ss | 0.432" | 15+22 | Azimuthal gap layers |
| opposite | 0.004 ss | 0.435" | 15+22 | Azimuthal gap layers |

Table 2.9: Candidate materials for the inner and outer tube of CIC conductors

As it can be seen on the figure 2.55, the larger the compaction factor, the larger the torque needed to bend the cables, this is a defining factor needed to understand the mechanical need for the robotic benders. The larger the drawing factor, the larger the local deformation on the wires between layers, this deformation proved to act as a locking effect between wires, impeding their natural movements during bend test, and not only that, but the accumulative friction could be large enough to tear the strands and deform the outer sheath.

## 2.10.3 Work in progress

The information obtained in the test described at table 2.9, provide a great starting point for developing a reliable 2-layer CIC. This results show that the development of a 2-layer CIC is more complex than the development of a single layer CIC. To determine the proper set of parameter needed to provide enough compaction and no deformation between wires, a analytical model is needed. The model described in section 1, is applied and a parametric sweep is performed over the main defining parameters: The radius of the inner tube, the radius of the wires-the elliptical shape is computed in the model, and depends on the bend radius-, the bend radius and the thickness of the foils in between the layers. This model shows that is not possible to produce a 2-layer CIC if the following parameters are fixed:

- An inner tube of diameter 0.1875".

- Superconducting wires of diameter 0.0472"

- Stainless Steel tape of 0.004" thickness

- An azimuthal gap between wires.
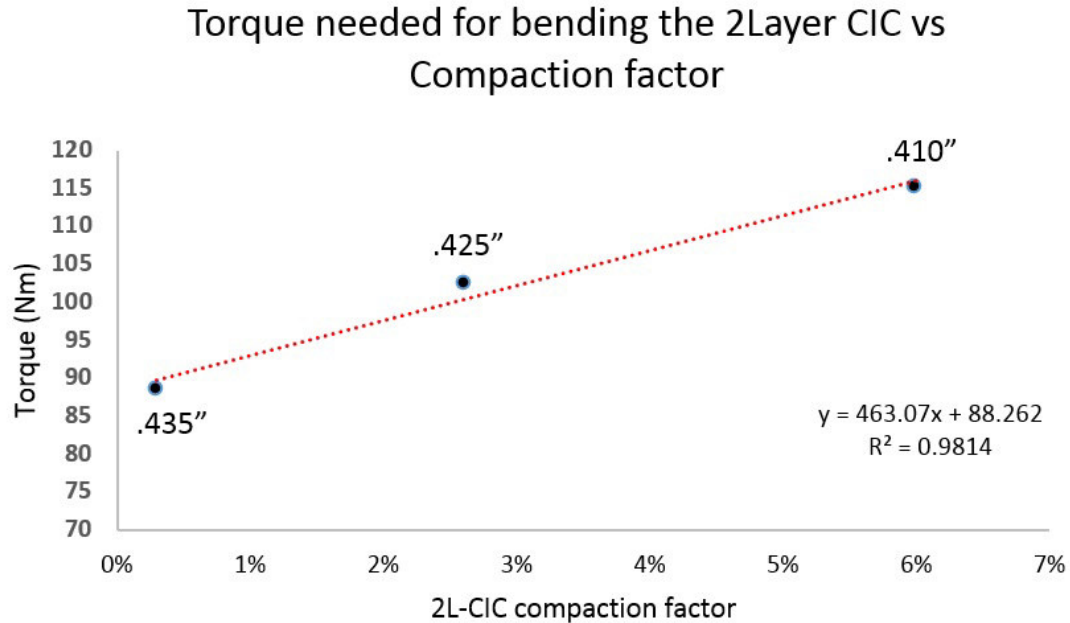
Figure 2.55: Torque vs compaction factor for a 2-Layer CIC.

Nevertheless, if two of the parameters are varied, one can produce an optimum 2-layer CIC conductor. The two parameters are: 1.-The inner tube, which will be slightly drawn (.1%), from .1875" to .1858", and 2- A small reduction of the diameter of the superconducting wires for the second layer, from 0.0472" to 0.0462", which represents a 2.1% reduction. If both modifications are applied, as shown in figure 2.56, a deformation-free 2-layer CIC can be produced, see figure 2.56 a). This cable is design to be used in the 6 T superferric dipole for the JLEIC upgrade. In this configuration, a bending radius of 2.351" used. The corresponding twist-pitch is 3.692". If the analytical model described in this chapter is applied, one can estimate the major axis for the ellipses for each layer. The wires in the first layer would have a mayor axis of $2x0.0239004$ inches, while for the second layer, the mayor axis is $2x0.0237551$ inches.

In this design, a small azimuthal gap between the wires of the first layer is allowed. The gap serves a cooling path for the helium to flow to the second layer. This opens an interesting question. That happens if one of the superconducting wires at the layer 1 quenches. The fact that there is an azimuthal gap, avoids the shoulder-to-shoulder current sharing. To determine if the amount of heat generated by the current flowing from the wire to the SS-foil, could comprise the CIC integrity, the overlap section has to be determined. An experimental measurement of such distance was taken from a 2-layer NbTi CIC. Metrology determine that the average arc length is 0.0165", as shown in figure 2.57 b).

To estimate the power dissipated, we will assume that once the wire quenches, the current flowing through the wire (I=1000 A), will be shared along the 22 contact regions, one for every wire at the second layer. This regions, can be modeled as squares of side 0.0165" of length and 0.004" of thickness. A current of 45 A flowing through this region produces 1.1 W of power. This is computed based on the resistivity of stainless steel (0.00000074 $\Omega$ m), and the geometry of the region. To determine the increase of temperature, the heat conduction equation, for the time dependent case, is used [106].
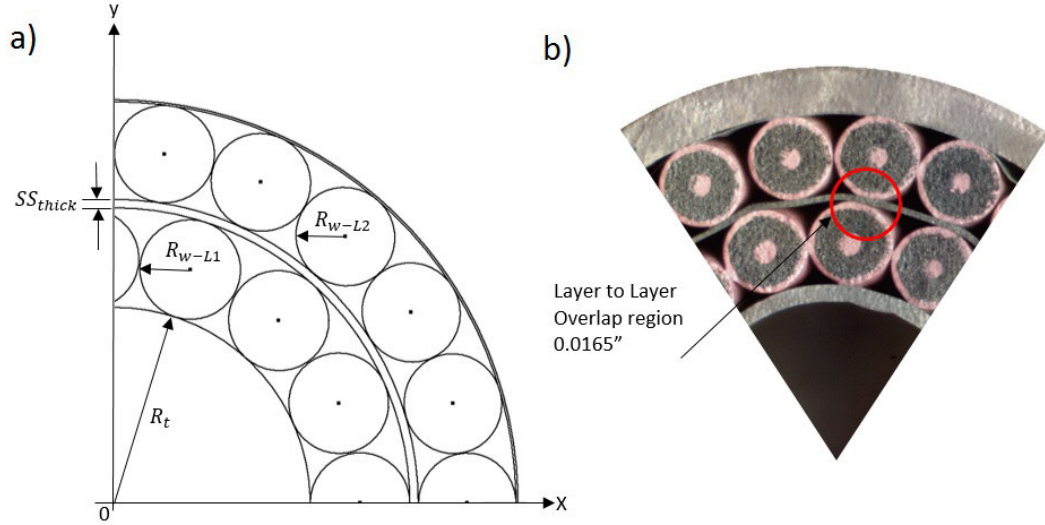
Figure 2.56: Quarter section of a 2-layer CIC conductor. On figure a), a schematic of a 2-layer CIC with superconducting wires of different diameters for each layer. On b), a triangular cut for a cross-section of a NbTi 2-layer CIC. A metrology software was used to determine the portion of the surface being in contact between the first layer and the SS foil. The measurement shows that a contact arc of 0.0165".

$$\rho C_p \frac{\partial T}{\partial t} = \nabla \cdot (k\kappa T) + Q \tag{2.23}$$

where $\rho$ is the mass density, $\kappa(T)$ is the thermal conductivity, $C_p(T)$ is the heat capacity, and $Q$ is the power source.

To do this, a single wire must be modeled. The superconducting strand is a complex structure. In its 1.2 mm diameter, houses 7400 filaments, 9 $\mu$m each. The Copper to NbTi superconductor ratio is 1.5. While the ratio in the superconductor is 53.5% for Nb and 46.5% for Ti. This proportions were considered for the thermal model. The temperature increment for the 1.1 W of power is neglectable, a .2 K rise was computed. The quench characteristic time, defined as:

$$t = 2\frac{C_p(T)}{\kappa(T)}R_w \tag{2.24}$$

computed in the range from 5 to 8 K, is less than $t = 6\mu$s. After this time, the quench is fully recovered. This statement validates the use of a azimuthal gap between the strands of the first layer of superconductor. The design described at the beginning of the section, will be developed and spring-back calculations will determine the required over-bend compensation. After that, a quench degradation test must be performed prior long-length production. The latter will be done in a two-step process. In the first, the 15 strands (1.2 mm OD) will be cabled around the perforated inner tube (.1858"). Then, the stranding machine will cable the second layer, using the reduced superconductor (1.1784 mm OD). The Cable will be drawn, and will be ready to be cabled at the 6 T dipole mandrel.
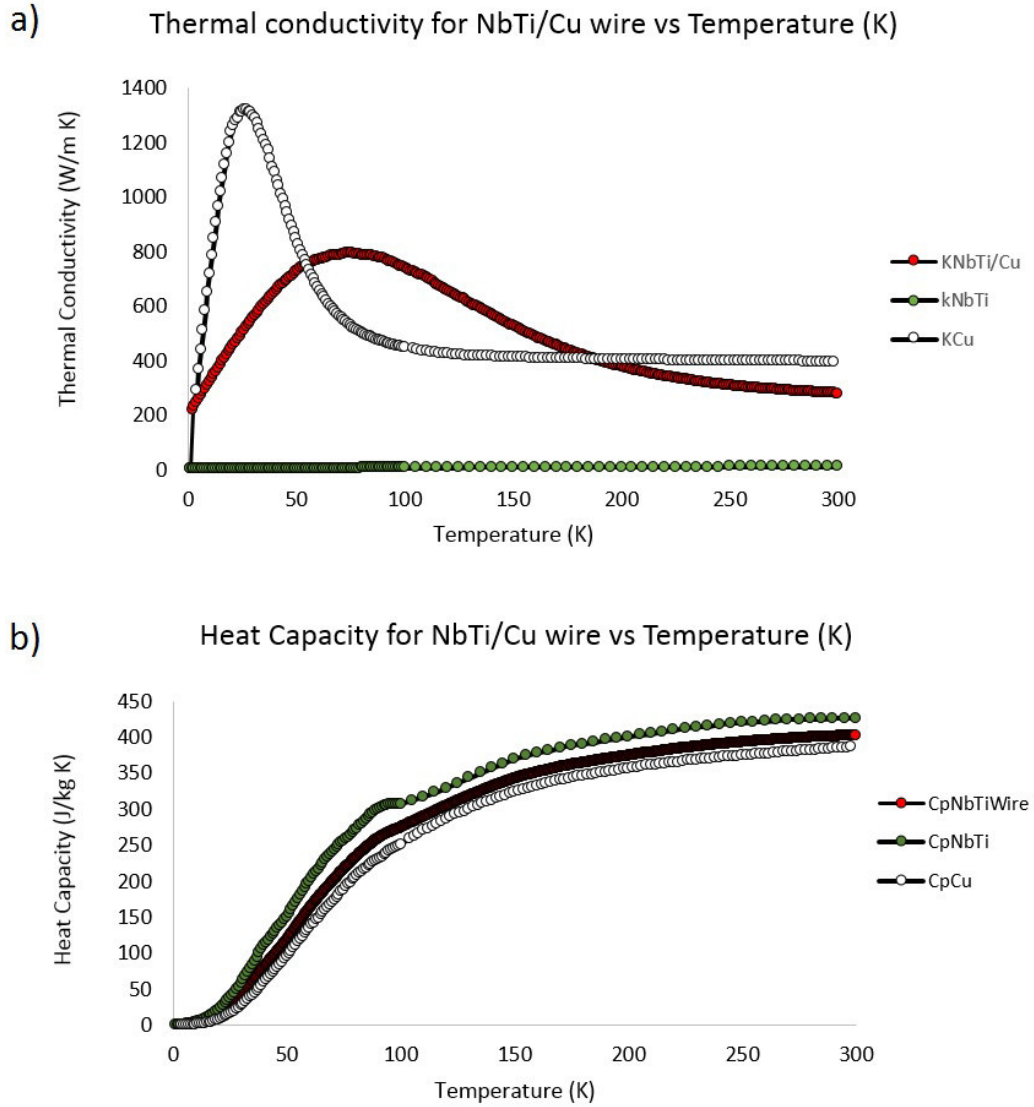
Figure 2.57: Computed thermal properties for NbTi/Cu superconducting wire at cryogenic temperatures. On a) the thermal conductivity vs Temperature (K) for the wire and its components: NbTi and Cu with a ratio Cu/Sc=1.5. On b), the heat capacity vs Temperature (K) for the wire and its components: NbTi and Cu with a ratio Cu/Sc=1.5.

## 2.11   Echo-Breaking-Detection System (Patent in tramit)

The development of CIC conductor is a well mature procedure. This process incorporates a three-step comprehensive quality control methodology:

- he first, is a detailed inspection of the CIC components and its cross-section. The inspection make use of both, a standard microscope and Scanning electron microscope. The inspection assess the integrity of superconductor and validates the uniformity of the twist-pitch.

- The second, is a chemical etching procedure, in which $FeCl_3$ solution is applied on extracted strands, to remove the copper and expose the superconducting filaments. Once the copper is removed, the broken strands are quantify. In normal conditions there is zero broken strands, the amount of broken filaments is intimately related with the current degradation on the wires.

- The third, is the experimental determination of the current degradation on extracted strands, where the $J_c$ of virgin strands is compare to that of extracted strands. A reliable conductor is that at which the current degradation due to manufacture is kept within 2%, in our case, the CIC technology and manufacturing procedure we developed, produces zero current degradation.

These quality control procedure, guarantee a damage-free procedure for manufacturing CIC conductors. Nevertheless, these procedures do not provide a quality control monitoring system to assess the performance of the conductor while its been formed into complex bends. A lot of thing can happen during the forming process of the CIC conductors. At this point, we are at the mercy of the performance and conditions of the materials. The materials may have imperfections that could led to damage of either the superconductor, or the other CIC components, and we may not notice until the magnet it fully ensemble and tested. This usually takes somewhere between 6 and 9 months, and about 100 K USD.

I have developed, model and implemented a real-time monitoring system, capable of recognizing deformations on the CIC conductor as the conductor is being form into bends, see figure 2.58. The system is specially design to isolate the environment noise and to increase the sound signature of different phenomenons developed during cable formation. The Sound spectrum is recorded as the CIC is being formed into complex bends, isolating background noises including the buzz from the stepper motors and slighting motion of metals. Different elements conform the sound spectrum. Each phenomenon has its own sound fingerprint with a specific decay constant. The possible deformation that could be detected are: displacement and rearrangement, breakage of filaments and wires, breakage of inner or outer tubes.

Its worth to mention that, every superconducting wire has its own fingerprint sound. The goal of this detection system is to monitor and identify breakage of superconductor during bends. To do so, we have developed a recognition system capable of isolating sound fingerprints, allowing the characterization of their decay constant.

There are four different types of damped signal, strong damping, critically damped, un-damped and under-damped, this signals are characterized by the decay constant. The signal detected when a superconducting wire brakes, is associated with an under-damping behavior. To determine the decay constant, the coefficient of the exponential fit must be estimated. This is done by computing the peaks on the sound fingerprint, and applying a costumed made exponential fitting, this computation is done in Wolfram Mathematica 2017. A patent has been submitted for the development of the Echo Breaking Detection System and its use in CIC forming. This technique represents a very powerful and useful
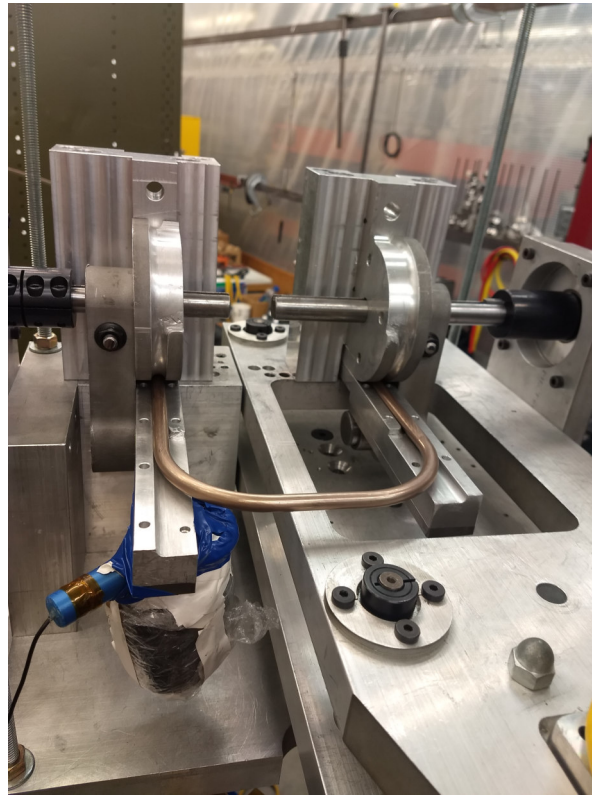
Figure 2.58: Echo Breaking Detection System applied as a quality control to assess the integrity of the CIC at every bend on the 3 T CIC dipole.

tool to preserve the integrity of the conductor, not only allow to identify on real-time the deformation of the superconductors, but it allow to precisely identify spatially where the deformation occurred. The development of the CIC technology is well understood and provision have been made to avoid filament breakage, nevertheless, a monitoring system add value to the winding process.

# Chapter 3

# JLEIC CIC Superferric dipole

## 3.1 JLEIC 3T dipole: Superconducting vs superferric designs

Several design considerations were evaluated in arriving at the two designs that are present-ed for review. First, the dipole could be built using either $\cos\theta$ or superferric coil geometry. A cost model for dipoles for JEIC requirements was prepared using the methodology developed by Willen [107], and used to compare the costs of $\cos\theta$ (figure 3.1 a)) vs superferric designs (3.1 b)) [108]. The model estimates that, for good-field aperture of $10x6cm^2$, a 3 T $\cos\theta$ di-pole would cost   twice as much as a 3 T superferric dipole. A second consideration is the cable design for the dipole. We developed superferric designs using two options for the cable: a Rutherford cable similar to that used in LHC (Figure 24b), and a cable-in-conduit (CIC) conductor similar to that used recently in GSIs dipoles for SIS-100 [109].



a)
b)

11 T dipole using Nb$_3$Sn
Rutherford cable
"Cos θ geometry"

3 T dipole using NbTi
CIC conductor
"Window-frame geometry"
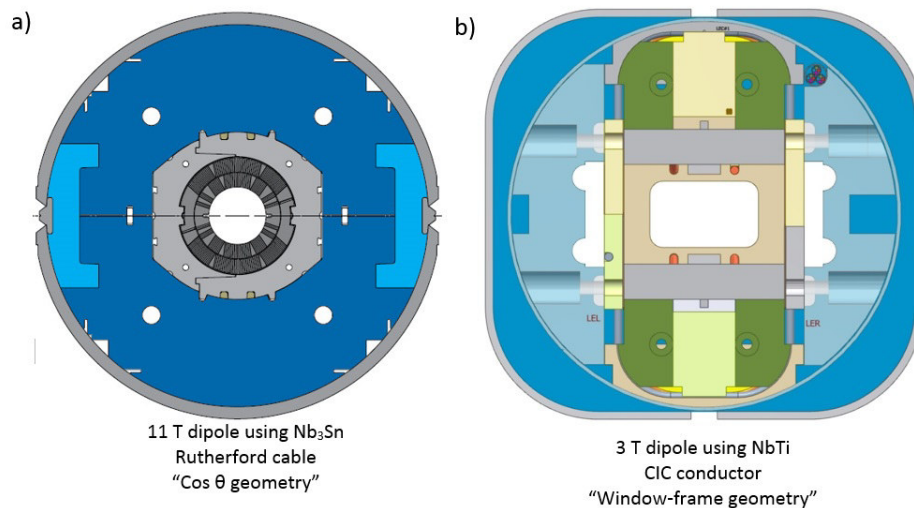
Figure 3.1: Cos $\theta$ dipole vs window frame dipole. Source: Figure a) was taken from Hill et al. [110].

Third, the dipole could be built with a straight body or on a curve (to eliminate sagitta as in the

SIS-100 dipoles). Curved-body construction would reduce the aperture requirement by 1 cm, but it would add significantly to the cost. We concluded that the potential savings from reduced horizontal aperture would be overwhelmed by the complexity of building the magnet on a curve.

## 3.2    Rutherford vs Cable-In-Conduit

For the 3 T JLEIC dipole two designs were prepared following superferric coil geometry, one based upon Rutherford cable and one based upon CIC. Both designs shared several common features: homogeneity at low-field was readily achieved by appropriate coil geometry and saturation multi-poles were nulled at the maximum field by judicious placement of holes. One big challenge for Rutherford design was the complicated winding sequence and the awkward topology for supporting Lorentz forces in the flared ends. A second challenge was to achieve precise location of each turn of winding in the body of the dipole. The robustness of the CIC allowed us to use robotic benders and perform precise and reproducible bends [111]. The flared ends were supported on NC-machined G11 blocks mounted on the structural beam, channels in the support blocks defined the curving path of each turn of CIC conductor.
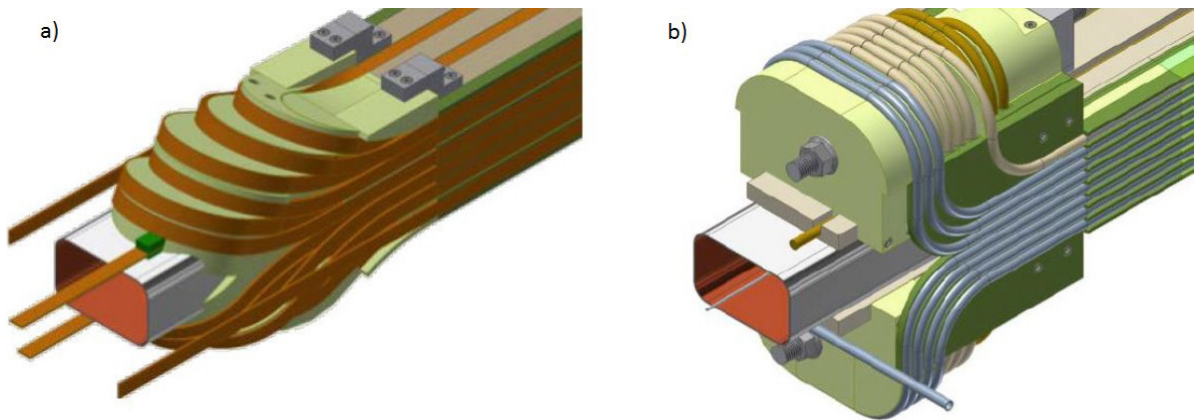


Figure 3.2: Two proposed designs of a 3 T dipole for the future Jefferson Lab Electron Ion Collider. Figure a) shows a block-coil design of a 3T superconducting dipole using NbTi Rutherford cable. Figure b) shows a design of a 3 T superferric dipole using a NbTi CIC conductor.

## 3.3    JLEIC 3T Superferric dipole

The Accelerator Research Laboratory at Texas A&M University is developing a 3 Tesla Superferric Cable-in-Conduit (CIC) dipole for the Ion Ring of Jefferson Labs proposed Electron-Ion Collider (JLEIC). JLEIC is a proposed colliding beam facility in which highly polarized beams of ions and electrons would collide at energies up to 100 GeV/u for ions and 20 GeV for electrons [18]. The Ion Ring has a figure-8 configuration with two 260°arcs connected by two long straight sections. Each arc lattice contains 32 half-cells, and each half-cell contains two 4 m long dipoles, a quadrupole and an instrumentation and correction package. The arc dipoles have a bore field of 3 T at full design energy. A short sextupole is located between the two dipoles to locally correct the effects of the (small) body sextupole in the dipole field distribution [112]. The required magnet aperture seen by the
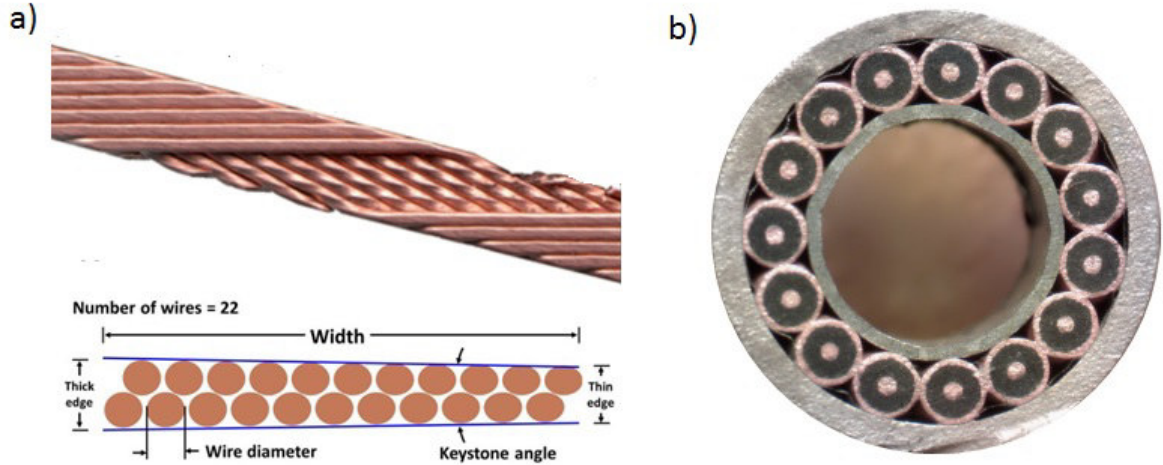
Figure 3.3: NbTi Rutherford cable vs NbTi CIC conductor.

beam is 10 cm horizontal x 6 cm vertical. Such a wide-aspect-ratio aperture represents a challenge for dipole homogeneity and dynamic range. The JLEIC dipole could be built using either *Cosθ* or superferric coil geometry. A cost model for such dipoles for JLEIC requirements was prepared using the methodology developed by Willen [113] and cost data from development of 3 T superferric dipoles and used to compare the cost of both designs. The cost model estimates that a dipole meeting the above requirements would cost twice as much using cos winding than using a rectangular winding. We developed superferric designs using two options for cable: a Rutherford cable similar to that used in Momentum Spectrometer at Jefferson Lab [114] and cable-in-conduit (CIC) conductor, similar to that used recently in GSI's dipoles for SIS-100. Both designs assume use of LHC-type NbTi/Cu superconducting strand that is currently manufactured by Supercon [115]: 7200 filaments, Cu:SC = 1.5. After evaluating both designs and considering the technical requirements, the CIC-based design was chosen in view of several unique benefits, discussed below
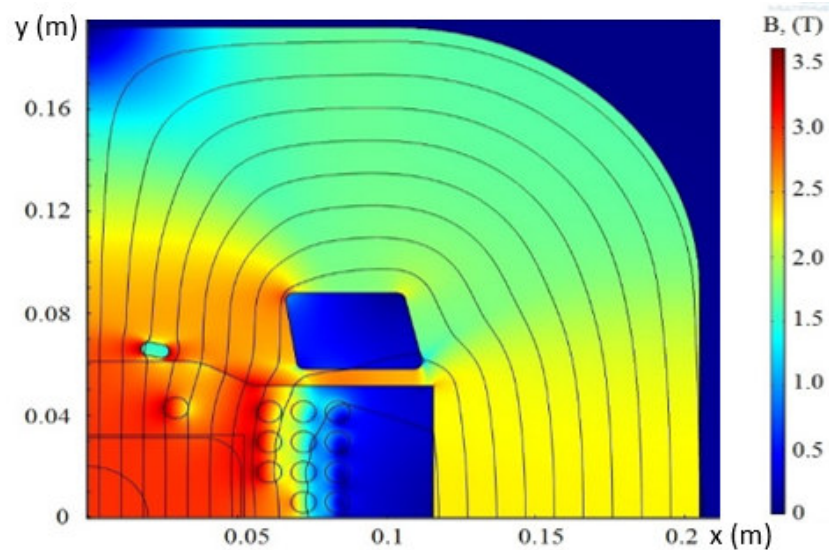


Figure 3.4: Quarter cross-section of the JLEIC CIC dipole at 3 T bore field.

### 3.3.1    Dipole design

Figure 3.4 shows a quarter cross-section of the JLEIC dipole.  A total of 24 turns of CIC cable are wound onto a central structural beam containing a 10x6 $cm^2$ stainless steel beam tube are shown and contours of the magnetic flux density B and isolines of vector potential Az are plotted for the case of full excitation.  The cables are wound in three equally spaced layers, eight equally spaced turns per layer.  To correct high field sextupole, one inner turn is removed near the the mid-plane of the dipole and relocated to the location (x,y)  (3 cm, 4 cm) as shown in figure 3.4.
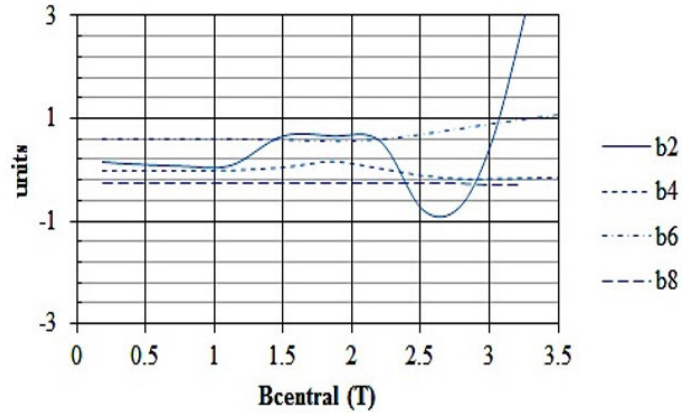
Figure 3.5: Systematic multipoles calculated in a 2cm reference radius.

The inner boundaries of the laminated steel flux return are contoured and holes are located as shown to control saturation over the dynamic range from 0.1 T to 3 T. Table 3.1 summarizes the main parameters of the dipole. We chose a large operating current (14 kA) to minimize the number of turns.  The lattice design requires that systematic multipoles be controlled to a tolerance $< 10^{-4}$ (expressed in dimensionless units, normalized to 2/3 of the magnet aperture radius).  This criterion must be maintained over the field range from 0.1 T, where the steel is completely unsaturated, to 3 T, where the inner regions of steel are strongly saturated.

Figure 3.5 shows the field dependence of the leading dimensionless multipoles over the full operating range, extracted from a 2D COMSOL [116] model and verified using Opera2D [117]. The bipolar excursion over the field range 1.5 to 2.8 T arises from the progressive saturation of the inner region of the flux return steel as field is increased.  The multipoles are expressed in dimensionless units of $< 10^{-4}$, normalized on a 2 cm radius reference circle.  All multipoles are kept to $< 10^{-4}$ over the entire dynamic range.  We also calculated the integrated multipoles taking into account the curved trajectory of an ion in the straight body of a 4 m long dipole. The curvature produced non-zero odd-order multipoles due to a curved path, but all multipoles were still less <0.6 units.

A 2D model was used to form multipole response matrix to small displacements of each turn of the cable (independently in each quadrant). The matrix was used to estimate manufacturing tolerances of support parts, errors in multipoles due to coil positioning during winding

### 3.3.2    NbTi CIC conductor

We have developed a true CIC conductor.  A single-layer of NbTi wires is cabled around a perforated thin-wall center tube.  The cable is pulled through a sheath tube and the sheath is drawn down to

| | | |
|---|---|---|
| Cable current at 3 T bore field, $I_{op}$ | 13.73 | kA |
| Stored Energy at $I_{op}$ | 64.1 | kJ/m |
| Inductance | 0.68 | mH/m |
| Max coil field at $I_{op}$ | 3.5 | T |
| Operating temperature, $T_{op}$ | 4.2 | K |
| Max Operating temperature | 6 | K |
| Short sample current, $I_{SSL}$ | 17.6 | kA |
| Max coil field at $I_{SSL}$ | 4.3 | T |
| Bore field at $I_{SSL}$ | 3.65 | T |
| Number of turns per bore | 2x12 | |
| Number of strands in CIC cable | 15 | |
| Diameter of strand | 1.2 | mm |
| Cu/Sc | 1.5 | |
| $J_C$ at 4.2 K | 3510 | A/mm$^2$ |

Table 3.1: Technical specification for the superferric cable-in-conduit dipole.

compress the strands against the center tube and immobilize them.  Liquid helium flows within the center tube and bathes all strands to provide stability against microquenches.  The sheath provides stress management at the cable level, so accumulation of Lorentz stress cannot cause degradation of superconducting performance.  It preserves the benefits of interior helium flow, so that the overall magnet is not a He vessel.  It also provides a bathing contact of liquid helium to all surfaces of the NbTi strands, which provides important thermal stabilization against microquench.  The CIC has 15 Cu-NbTi wires, 1.2 mm OD, containing 7400 filaments.  Copper to superconductor ratio is 1.5 and it is close to LHC wire parameters [118].  An important target of our development was to develop the ability to bend the cable on a relatively small radius of curvature: 5 cm radius bend for a cable with 1 cm overall diameter.  The confinement of the strands between the center tube and sheath tube permits the strands to shift in the bend as the inner and outer regions of the bend form different catenary lengths.  Several elements of that strategy proved to be crucial to success.  First, we controlled the twist pitch of the cable to be one half the overall path length for the $180°$U-bend that is required for the ends of the dipole.  With that choice, the catenary lengths of all 15 strands around the U-bend are equal and no tension or compression is propagated into the straight body segments.  This resolved a problem that was encountered in earlier development by the INTAS project [119].  Second, after cabling was completed, a thin (25 $\mu$ m) foil of stainless steel was spiral-wrapped around the cable to provide a slip plane to facilitate local re-arrangement of the strands during bending.  The assembly is then sheathed into a high strength Monel outer jacket and drawn to compress the strands against the center tube.  Third, the diameters of the center tube and the strands are chosen so that, when the cable is drawn down, the neighboring strands are compressed laterally against one another just as the strands are compressed radially between the tubes.  This matching compression provides for current-sharing between neighboring strands within the cable.  Fourth, after drawing, each wire leaves a groove-shape indentation in the center tube, which contributes to immobilizing each strand against Lorentz forces at high field.  Fifth, a bending die was developed that supports the sides of the cable sheath during bending.  This limits the ovalling that would otherwise occur, so that even in a 5-cm radius bend the cable remains round with very little ovalling.  With all those provisions, we were able to perfect the cable-forming and bending processes and validate by sectioning that the interior configuration remains stable and well-immobilized all around a U-bend.  We have fabricated and tested numerous 2 m-long samples, which have been tested for damage/deformation while drawing and bending: part of extracted from CIC strands were tested for current degradation at the Superconducting Magnet Division at Brookhaven National Laboratory, the remainder were etched to check for broken filaments.  No current degradation was observed in either analysis due to the CIC fabrication and subsequent bending process.

## Quench simulation

A set of 80 $\mu$m thick stainless-steel quench heaters are installed at each end of the dipole.  At this point, the sheath tube of each CIC turn is in direct contact with a quench heater, so that quench is driven in all 24 turns, as shown in figure 3.6.

To evaluate the quench diffusion time after quench heaters are fired, 2D and 3D COMSOL models were created.  A simple 3D heat transfer model with Joule heating was used to simulate quench propagation in the CIC cable.  The model make use of micrographs of actual samples of CIC cable to measure the contact surface between neighboring strands to be 6% of total strand circumference, and between strand and center and sheath tubes to be 18% of strand circumference, see figure 3.7.
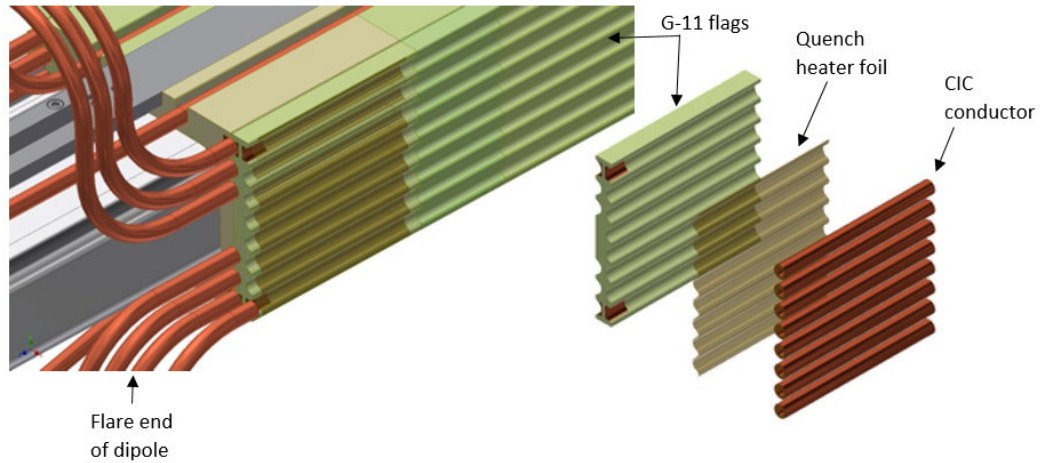
Figure 3.6: Stainless steel quench heaters at the end of the dipole.
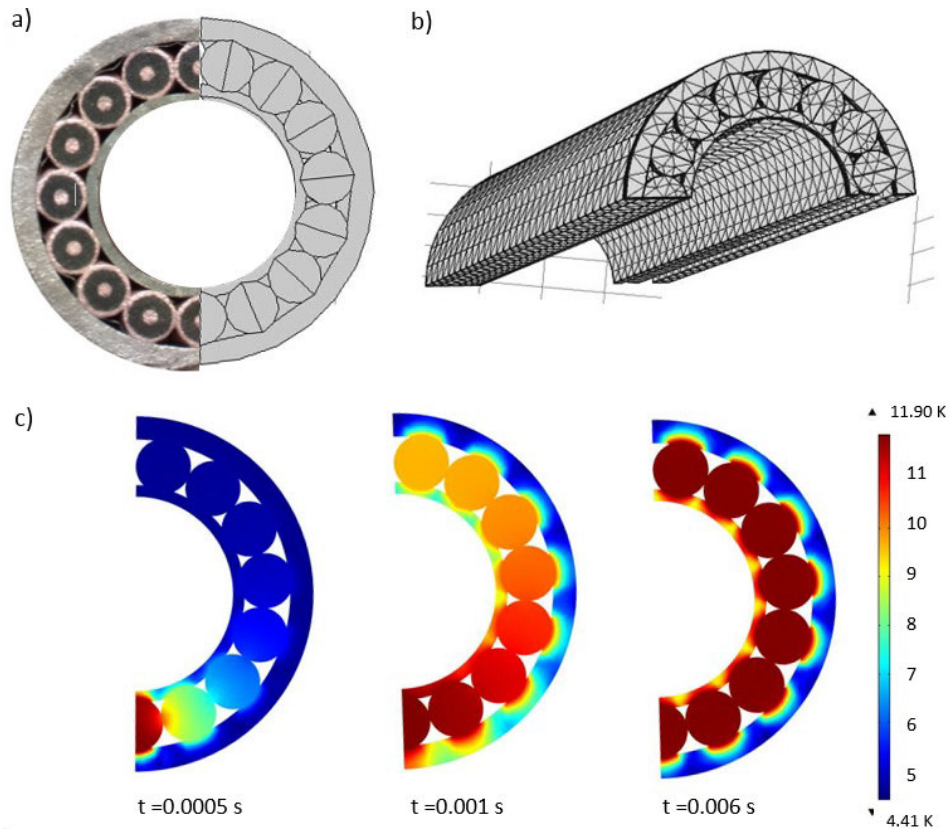


Figure 3.7: A Gaussian pulse induced in a single wire, induces a quench that propagates along neighboring strands. On a), a half-cut of a NbTi CIC is used to model the geometry on Comsol Multiphysics. On b), symmetry is used to model a 1 m section of CIC conductor. On C), the heat produced by the Gaussian pulse, exceeds the critical temperatures for the NbTi superconductor, and travels through the CIC cross-section in 6 ms.

It this model we assumed that each strand carries a superconducting current $I_s$ $(T_i,$B$)$ equal to the critical current at its particular value of temperature $T_i$ and magnetic field B, and that the balance of current is carried resistively, with current sharing among the copper regions of all strands.

To initiate the quench, a parametrized (Q, $\sigma$,$t_0$) Gaussian heat pulse is applied externally to a small volume $\Delta V$ of a strand:

$$Gaussian \quad pulse = \frac{Q}{\Delta V} \frac{1}{(\sigma\sqrt{2\pi})} e^{\left(\frac{-[(t-t_0)]^2}{\sigma\sqrt{2\pi}}\right)} \tag{3.1}$$

With this, we developed a criterion for the Minimum Propagation Zone (MPZ), which has the transverse dimension of the strand and a length of 1 cm, as is typical of composite NbTi strands [119]. The parameters for the Gaussian pulse are $\sigma = 40$ $\mu$s and $t_0 = 10$ $\mu$s, and Q is the point disturbance energy and is a parameter of the model [120].

Three cases were considered:

- liquid helium occupies all free space inside CIC (Full)

- only the center tube is filled with liquid helium (Center)

- no helium present in CIC (Dry)

The value of Q was varied to find the relaxation time for quench initiation, the minimum quench energy, and quench propagation velocity for each case, as summarized in Table 3.2.

| Case study | Full of LHe | LHe in center | Empty | units |
|---|---|---|---|---|
| Relaxation time | 2.0 | 5.4 | 9.0 | ms |
| Minimum quench heat | 4.4 | 4.0 | 3.6 | mJ |
| Quench velocity | 45 | 45 | 45 | m/s |

Table 3.2: Technical specification for the superferric cable-in-conduit dipole.

To model the case in which heat is transferred to the helium, we requite to make use of the Dittus-Boelter equation, which worth to be described.

### Dittus-Boelter equation

Heat transfer to the liquid helium was modeled using the Dittus-Boelter equation for turbulent flow in ducts [32, 121] [a]:

$$N_u = 0.0259 R_e^{0.8} P_r^{0.4} \left(\frac{\Theta}{\theta}\right)^{-0.716} \tag{3.2}$$

where $N_u$, $R_e$ and $P_r$ are the Nusselt, Reynolds and Prandtl dimensionless numbers of fluid flow. As we are interested in transferring the heat produced by the superconductor to the liquid helium, then the coefficient for the Prandtl number should be 0.4, and 0.3 for the opposite case, [121]. This coefficients are defined as:

---

[a]"the equation is for heating of the fluid, for cooling the power of the Prandtl number should be 0.3 instead of 0.4". R. H. S. WINTERTON.

$$R_e = \frac{\gamma \nu D_H}{\mu}$$

$$P_r = \frac{C_p \mu}{\kappa} \tag{3.3}$$

$$N_u = \frac{hL}{\kappa}$$

where the following parameters are for the coolant (helium): $\nu$ is the flow velocity, $\gamma$ is the fluid density, $\kappa$ is the thermal conductivity, $C_p$ is the heat capacity, $\mu$ is the viscosity, $\theta$ is the temperature of the coolant, $\Theta$ is the temperature of the inner tube, and $h$ is the heat transfer coefficient. The parameter $L$ is the characteristic length, and for the case of flow cooling in channels, is the hydraulic diameter $D_H$ of the CIC inner tube, which is defined as:

$$D_H = \frac{4 * Helium \quad cross - section}{heated \quad perimeter} \tag{3.4}$$

If the coefficients given in equation 3.3 are substituted in equation 3.2, one obtains the heat transfer coefficient:

$$h = 0.0259 D_H^{-0.2} \nu^{0.8} \gamma^{0.8} \kappa^{0.6} C_p^0 .4 \mu^{-0.4} \left( \frac{\theta}{\Theta} \right)^{0.716} \tag{3.5}$$

One can combine the parameter relating the physical properties of the coolant, and form a temperature dependent function $F(\theta)$, as suggested by M.N. Wilson [32]:

$$F(\theta) = 0.0259 \gamma(\theta)^{0.8} \kappa(\theta)^{0.6} C_p(\theta)^{0.4} \mu(\theta)^{-0.4} \tag{3.6}$$

with this simplification, and using the of the heat flux $q[W/m^2]$ definition:

$$q = \frac{h}{\Delta T} \tag{3.7}$$

we can compute the heat flux to the coolant, as:

$$h(\theta - \theta) = D_H^{-0.2} \nu^{0.8} F(\theta) \left( \frac{\theta}{\Theta} \right)^{0.716} (\Theta - \theta) \tag{3.8}$$

To use this equation, we require the physical properties of supercritial helium at 2.5 atm as a function of the temperature. The properties are taken from the software cryocomp v.5.2 [122].
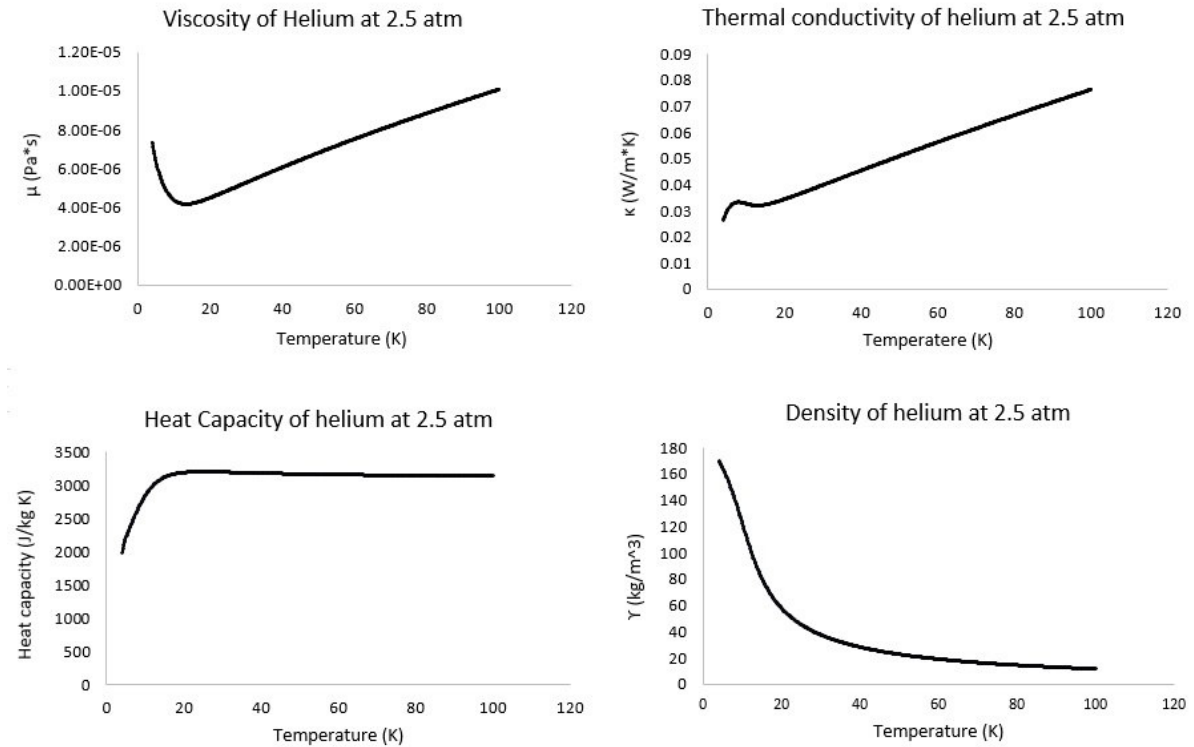
Figure 3.8: Physical properties of helium at cryogenic temperatures and low pressures: Supercritical helium. Source: Data taken from software CryoComp [122].

### Case study: CIC full of helium

Figure 3.9 shows dynamics of a quench in the Full case after a heat pulse of 4.4 mJ/cm is delivered into a single strand within the CIC cable, either as a spontaneous quench or as an external heat pulse delivered by a quench heater to drive quench in all cable turns [123] . If a smaller heat pulse is delivered, it does not produce a quench  the temperature excursion decays away. Curves 1, 2 and 3 show the temperatures at a given longitudinal coordinate, in the strands at the three locations indicated on the inset micrograph of the CIC: point 1 is the strand in which the heat originates; point 2 is a strand 90° around the cable; point 3 is a strand on the opposite side of the cable. Comparing those three T(t) curves enables us to characterize the transverse propagation among strands in the CIC cable.

Markers P1, P2 and P3 give the temperatures at 3 points 1 cm apart along the strand in which quench initiated. The curves are shifted from one another by  0.25 ms, corresponding to a quench velocity of  40 m/s. That value is comparable to the initial quench velocity of 31 m/s estimated by QUENCH, indicating that the adiabatic approximation is appropriate.

The relaxation time is 4.5 times faster in the Full case (an important help in microquench stabilization) but the quench heat and quench velocity are comparable in all cases. Two scenarios of protection for a 4 m long dipole were modeled and are shown in Figure 3 c. If the quench heaters are fired at both ends, the maximum coil temperature is Tmax = 136 K; if quench heaters are fired at only one end of the dipole, Tmax = 167 K. Thus the two-ended protection scenario provides a degree of failure tolerance. Figure 3.9 a) shows that a 60 A pulse of 10 ms duration is more than enough to quench the cable in less than 6 ms. We therefore assume an overall delay of 10 ms between the detection of a quench and the initiation of the induced quench in all turns at the ends of the dipole.
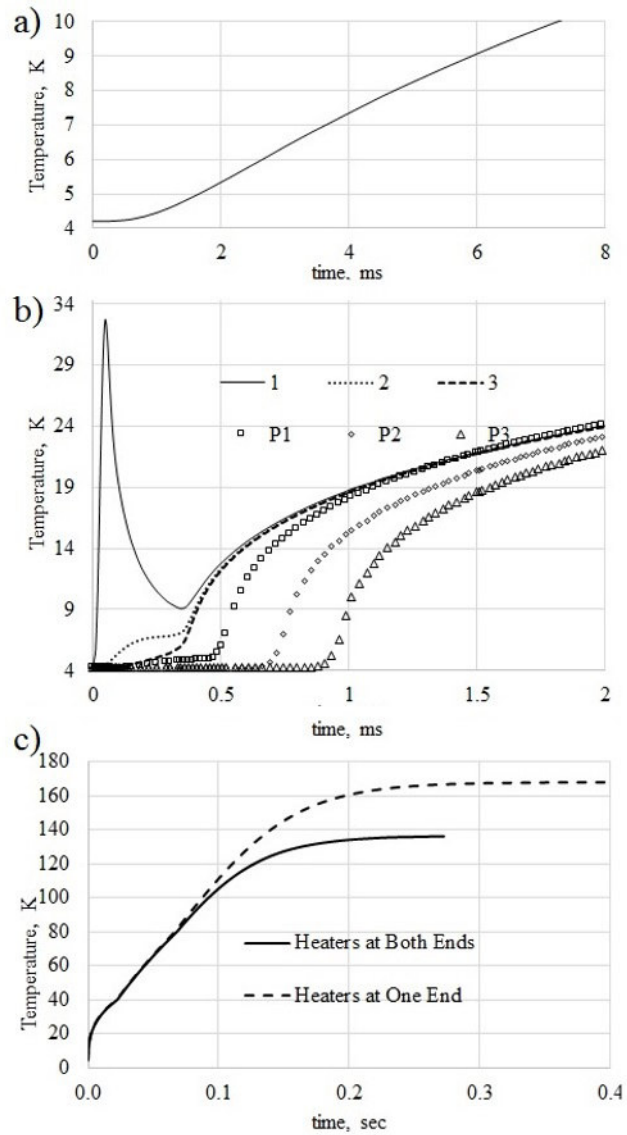
Figure 3.9: A Gaussian pulse induced in a single wire, induces a quench that propagates along neighboring strands. On a), a half-cut of a NbTi CIC is used to model the geometry on Comsol Multiphysics. On b), symmetry is used to model a 1 m section of CIC conductor. On C), the heat produced by the Gaussian pulse, exceeds the critical temperatures for the NbTi superconductor, and travels through the CIC cross-section in 6 $\mu$s.

# Chapter 4

# Winding and assembly

## 4.1    JLEIC 3T dipole: 3D schematics

The coil structure consists of a central composite beam which is epoxy-impregnated to the stainless steel beam tube. The beam is assembled as a stack of G-11 window-frame-geometry segments, each one machined from a 10-cm-thick slab of G-11 fiber-reinforced polymer. That approach is required to provide dimensional stability through cool-down. G-11 has an integrated coefficient of expansion that closely matches stainless that of steel in the plane of the reinforcing S-glass fabric, but its coefficient is 3x larger perpendicular to that plane. It is therefore necessary to orient the slab G-11 material from which the segments are machined so that the fabric plane is perpendicular to the beam axis, and to assemble the segments face-to-face using a bonding agent that provides a weak link that can separate on cool-down to relieve longitudinal strain. The structural beam is shown in figure 4.1. Each window-frame segment was machined by NC-milling the G-11 slab segment to make the central aperture clear for the beam tube and the pattern of channels that position all turns of the inner layer of CIC cable. The segments were assembled in a stack on the stainless steel beam tube, the pattern of channels was co-registered by inserting sheath tube segments into four corner channels. The entire assembly was then clamped and epoxy-impregnated to bond the segments to the beam tube. A pair of rectangular stainless steel bars were then bonded into channels on the top and bottom of the beam. They provide a stiff-modulus beam to directly transfer the support of axial forces from one end of the dipole to the other.

## 4.2    CIC Winding Strategy

The successful of a superconducting magnet is directly related to the quality of the winding procedure and its ability to confine the movement of the superconducting wires. In the case of the Rutherford cables, a major issue for the winding procedure are the instabilities that arise during close bends, as has been shown in picture 2.9. This type of instabilities are known to affect the field quality, and in worst case scenario, causing quenches. Fortunately, the CIC conductors possess a unique built-in feature, proper of its manufacturing process, that locks the superconductors and confines them into narrow channels around the inner tube.

For the case of the 3 T superferric dipole, the geometry of the magnet is known as window frame
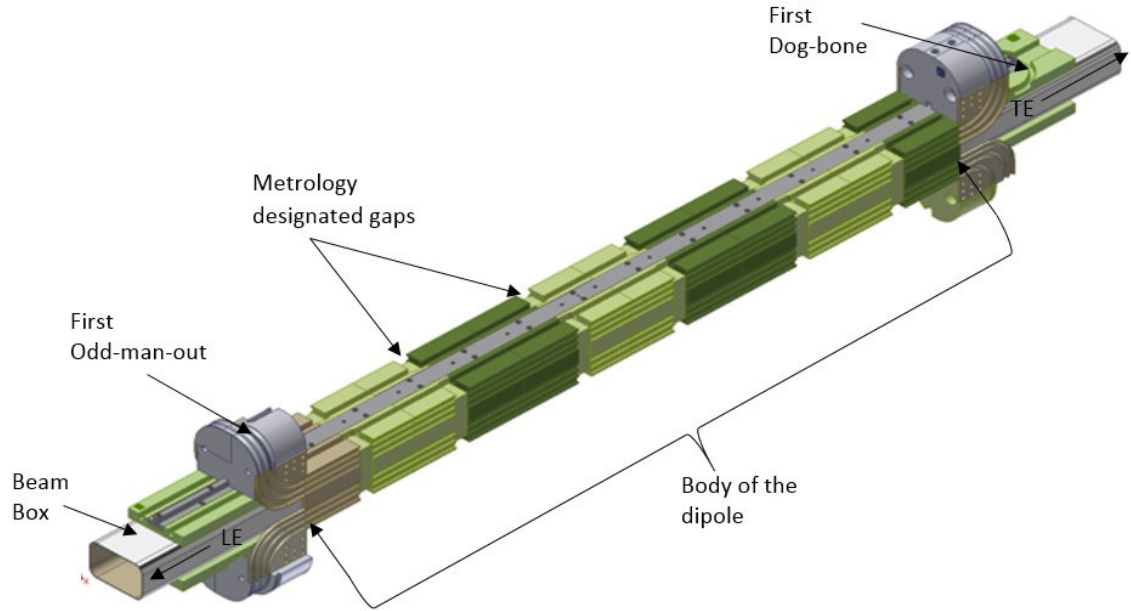
Figure 4.1: Systematic multipoles calculated in a 2 cm reference radius.

[124], also known as block-coil. Besides the natural benefits of this geometry, such as providing a direct path for stress-management of the Lorentz forces [125], the geometry also allows a simpler winding strategy, as compared with the Cos $\theta$ dipole geometry.
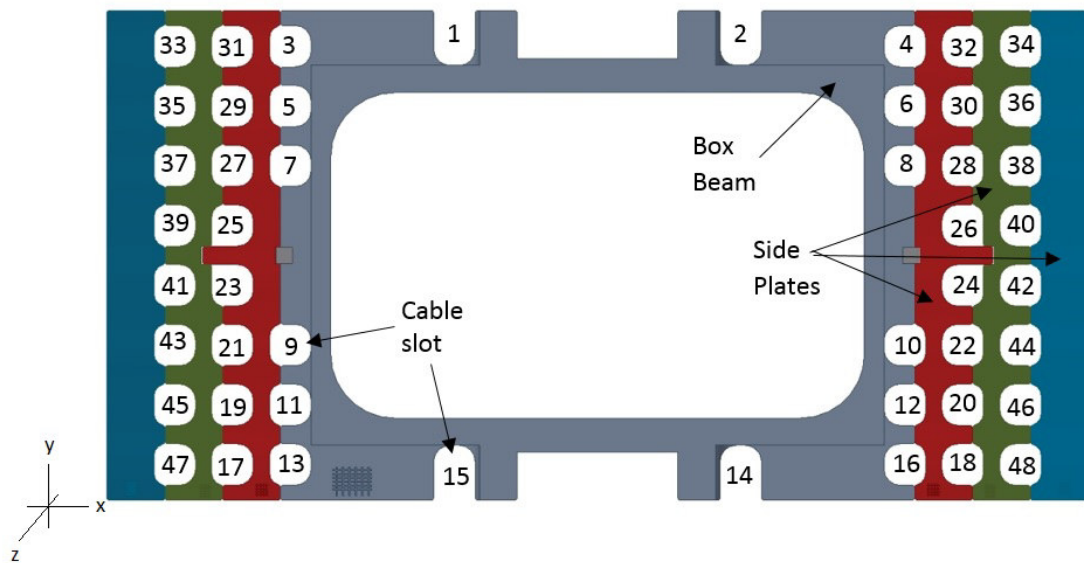


Figure 4.2: Cross-section of a window frame 3 T superferric dipole.

Figure 4.2 shows a cross-section of the body of the 3 T superferric dipole. Two components are described:

1. The central mandrel, containing the rectangular beam box and the grubs for the first layer of

windings.

2. The external flags, that acts as a boundary between layer of windings, providing guidance and confinement for CIC conductors.

The barrel-winding [126] procedure is characterized by consecutively winding the CIC conductor layer-by-layer, top-to-bottom, for the first layer, bottom-to-top, for the second layer, and so on.

For reference, the lead-end of the dipole is pointing in the -Z direction, according to the cross-section shown in figure 4.2. The lead-end (LE), is characterized by having a transition between windings on the same layer i.e., the return CIC is not in the same plane as the exiting cable, as it can be seen in windings from position 4 to 5, 6 to 7, 8 to 9 and so on. On the other hand, the tail-end (TE), which is facing in the +Z direction according to figure 4.2, is characterized by having no transition between the exiting and returning CIC. This can be seen in position 3 to 4, 5 to 6, 7 to 8 and so on.

Three types of bends are required for the winding process, and they will be enumerated according to order of appearance:

- The first bend is called "dog bone". Its characterized by being a 300°planar bend. This close-bend requires the use of a dedicated robotic bender. Only two of this bends are required in the whole magnet. The first is at the TE, going from grub 1 to 2. While the second is at LE, going from grubs 14 to 15.

- The second bend is called "odd-man-out". And its characterized by making a short-transition between the so called sextupole coils. A coil characterized for its relation with the sextupole components of the magnetic field, and by being located at the center of the beam box (grubs 1,2,14 and 15). This is a flared-bend. Two robotic benders are required, the first performs a 180°bend, while the second "flares" the planar bend 90°. Three of this bends are require in the whole magnet. The first is located at the LE, providing a transition for coils 2 to 3. While the other two, are located at the TE, for transitioning between coils 13 to 14, and 15 to 16.

- The third type of bend, is called "flare-bend", and is practically the same has the "odd-man-out", in fact, the same two benders are required. The only difference is that the bends make a larger transition, connecting all but the sextupole coils. This type of bend is the most common, and is the most used in the whole magnet. There are two versions of this bend. In the first, the legs of the "flare" are coplanar (TE side of the magnet), for instance, coils 3 to 4. While in the other type, the legs are shifted down one CIC diameter, as is coils 4 to 5.

The winding process is a complex, tedious and challenging task that requires a large number of especial tooling, software, hardware, and procedures specially developed for this task. This developments will be addressed in the following sections. For now, we will take care of the winding procedure previously described.

To wind the dipole, two main components are needed. First, a large spool (to avoid CIC ovalling deformation) containing 140 m of CIC conductor is required. The spool must be standing in a proper mount, that allow a free spin and self-leveling, see figure 4.3 a). The second component is a self-paced winding table, in which the dipole mandrel will be attached, see figure 4.3 b).

To begin the winding process, both the mandrel and the spool of superconductor must be aligned. A straight section of CIC conductor must be placed on grub 1, passing through TE and heading to LE. A half-meter section of CIC must stick out of the mandrel, this will be used for the splice-joint. Once the CIC is kept in the high tolerance grub, the winding table rotates 180 °, and the first dog bone must
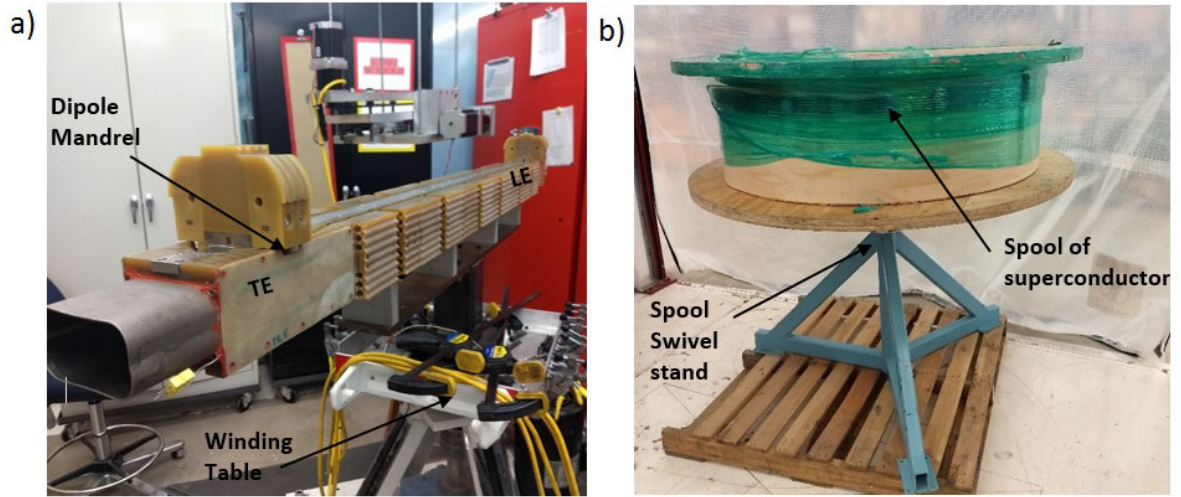
Figure 4.3: Winding table and spool of NbTi CIC conductor. On figure a), both, the Lead-End (LE) and Tail-End (TE) are show on the mandrel.

be formed and position into the channel. The winding naturally continuous thought the first layer until reaching mid-section, where coil 7 to 8 is the last. To perform the transition from coil 8 to 9, the mandrel and the spool must be rotated 180°, this will allows us to continue the winding procedure and to complete the first layer.
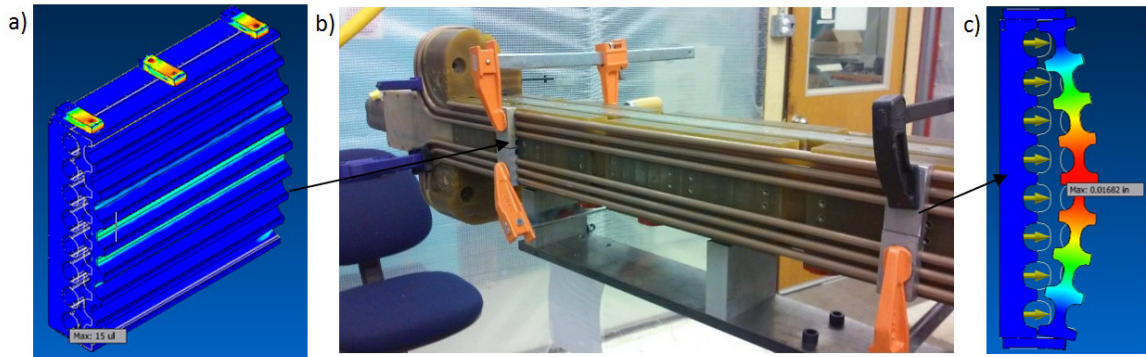


Figure 4.4: Mandrel and simulation of flags. On a), a proposed design for a .125" Stainless-Steel pins embed into the G-11 flags, designs to hold the CIC conductor into the grubs of the flags. A failure case is modeled to determine the maximum displacement of the flags due to a lateral force. On b), the measured displacement at the caused at the maximum force. The mechanical properties of the pins exceeds the expectations, the displacement represent an unrealistic scenario.

After the lateral CIC are placed on the flags, the flags are positioned. Clamps are used in the winding process to secure the conductor. On figure 4.4, a proposed design for securing pins is presented. The pins, are meant to be inserted into the thickness of the flag, penetrating .125" deep. The 316L Stainless-steel material used in the pins, is a magnetically compatible alloy, that support large outward forces (200N).

**Precision winding**

The G-11 fiber glass epoxy composite, used in the flags and mandrel, is machine with high-tolerances to restrict the motion of the CIC in the grub. In fact, the grubs are machined with a tolerance of $\pm$ 38 $\mu$m, to allow any fluctuation on the CIC diameter after manufacture. The machining and design of the flags, takes in consideration the non-isotropic thermal expansion of the epoxy resin: $0.72x10^{-5}$ in/in/°F in the lengthwise direction, and $0.83x10^{-5}$ in/in°F in the crosswise direction [127, 128]. This must be consider to decrease the friction between the CIC conductor and the flags, when reaching cryogenic temperatures.

Two parameters are key for maintain the high-precision in the winding, the first is to accurately measure and mark the lenght of the CIC conductor to perform the bends in the right place. A precision of 0.010" is maintained in this process thanks to a set of fiducials, see figure 4.5. The second, is relating with holding high precision tolerance in the bend, both azimuthal and radially. The bend achieved with the robotic bender, is capable of holding $\pm$ 0.5°for both cases, 90 and 180°bend. The radial tolerance is 0.03". This will be discussed in Robotic Bender section.
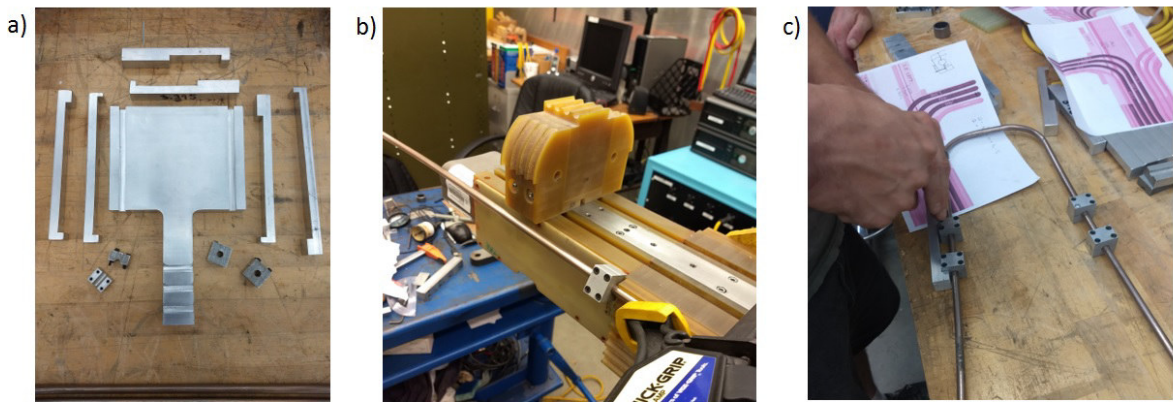


Figure 4.5: Set of fiducials used in the winding process. On figure a), a set of high-precision fiducials for transferring the proper length, previous the bends. On b), a fiducial clamped at the end of the straight section of the magnet, to perform the first 90°bend. On c), two fiducials are used to measure the length required for the flare bend.

## 4.2.1   Issues during winding: Knot

The winding strategy developed for completing the 3 T dipole is characterized by being composed of flare bends, and straight sections. The flares produce a symmetrical pattern at both ends of the dipole, while the straight sections produce a uniform pattern of parallel CIC conductors at the body of the dipole.

Designing the coil supports for the flare bends at the end of the dipole, require a vivid 3D image, the cumbersome 3D coil structure caused a drawback in the design, leading to a knot, this is depicted in figure 4.6 a) and b). We face this problem during winding strategy of the dummy trial, in which hollow conductor was used.

To correct this, a re-design of the support pieces for the flares was needed. Two corrections were applied, the first involve rotating the order of the four bends 180°, in which the odd-man-out
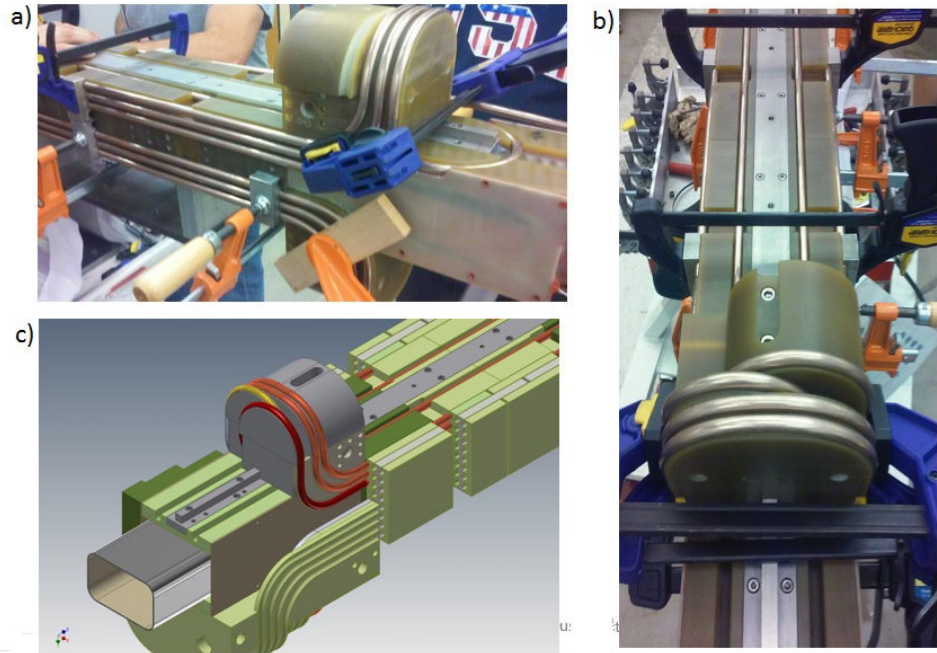
Figure 4.6: Knot in the design. On figure a), the dummy-trial in the winding process face the knot.

is switched from front to back. The second, is switching the order of the wining, now the winding goes from back to front, starting at with the odd-man-out. A radical mid-term solution was applied during the mock-up winding, in which hollow tube was used as a substitute of the CIC conductor. To avoid the knot, the spool of superconductor was inserted under the dog-bone bend, this wouldn't be possible if real CIC conductor were use. The G-11 pieces were re-machined and the winding strategy was validated, a drawing of the new pieces is shown in figure 4.6 c).

## 4.2.2   Robotic Benders

The robustness of the CIC conductor make it suitable for a wide number of applications, as has been described in previous chapters. This property represents a challenge as far as coil forming, the complexity of the spring-back and the requirement for an over-bend compensation, demand the use of a high-precision bending machine. Two components characterize the robotic benders. The first, is the costumed-made bending dies, especially design to reproduce the bends after their natural spring back. The second, is the software used to control the stepper motors.

Figure 4.8 shows the three robotic benders required to perform the three types of bends, previously describe in the winding strategy. The stepper motor used in the benders meets the experimental requirements for the torque needed to bend the CIC conductor. The motor is operated by a computer program, that will be described shortly.

## 4.2.3   LINUX CNC for robotic benders

Linux CNC [129, 130] is an open source software design to control and operate stepper motors, commonly used in milling machines, 3d-printers, etc, we use this program to operate and program the 3d bends on CIC conductor. The software make use of G-code, the most widely use numerical control
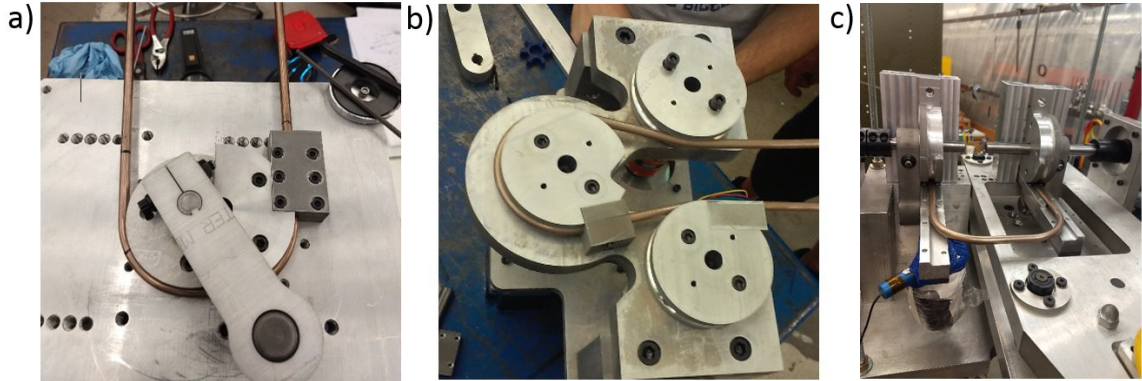
Figure 4.7: Set of robotic benders and their characteristic bends on CIC conductor.

programming language. The communication from the computer to the motors is made via LPT 1 port, as described in figure 4.8.

In the following subsections, the code use for forming the CIC bends is presented for the benders. The code incorporates provisions for adjusting the characteristics of the stepper motors.

## G-code for operating bender 1 and 3

```
/******** Accelerator  Research  Lab**************
/# This  first  part  of  the  program  makes  the  first  half  bend  on  bender
/# one .
/# Both  the  bender  1  and  the  winding  table  turn  in  a  synchronized  way
/# and  both  stops  at  the  90  bend ,  allowing  you  to  shift  the  motor  to
/# its  new  location .
/# When  you  run  the  program ,  make  sure  that  you  click  on:  Execute  next
/# line ,  in  order  to  run  the  program  in  steps ,
/# otherwise  it  will  complete  the  whole  cycle  without  stops .
/*************************************************************
G20  G64
M3  S1000
G92  X0.0  Y0.0
G00  x0.15
G01  x1.25  Y1.25  F10.0
G01  x1.388  F5.0
G01  x1.25
/*************************************************************
/# Now,  I  will  reestablish  the  zero  for  bender  one ,  with  the  G92  code .
/# In  this  step  you  should  shift  the  motor  to  position  number  2.
/# Its  important  to  mention  that  Winding  motor  is  still  running  under
/# the  same  considerations .
/# Whenever  you  re  ready  to  continue  with  the  second  half  of  the  bend ,
/# the  program  will  turn  both  motors  in  a  synchronize  way .
```

```
/*********************************************************************
G92 X0.0
G01 X1.25 Y2.5 F10 ; Turns 90 degrees, you must add the shift
/*********************************************************************
/# Add 0.2777 for 20 degrees, 0.1388 for 10 and 0.0694 for 5
/*********************************************************************
G01 X1.388 F5.0; 10 degrees over-bend
G01 X1.25; Return to 90
M02
```
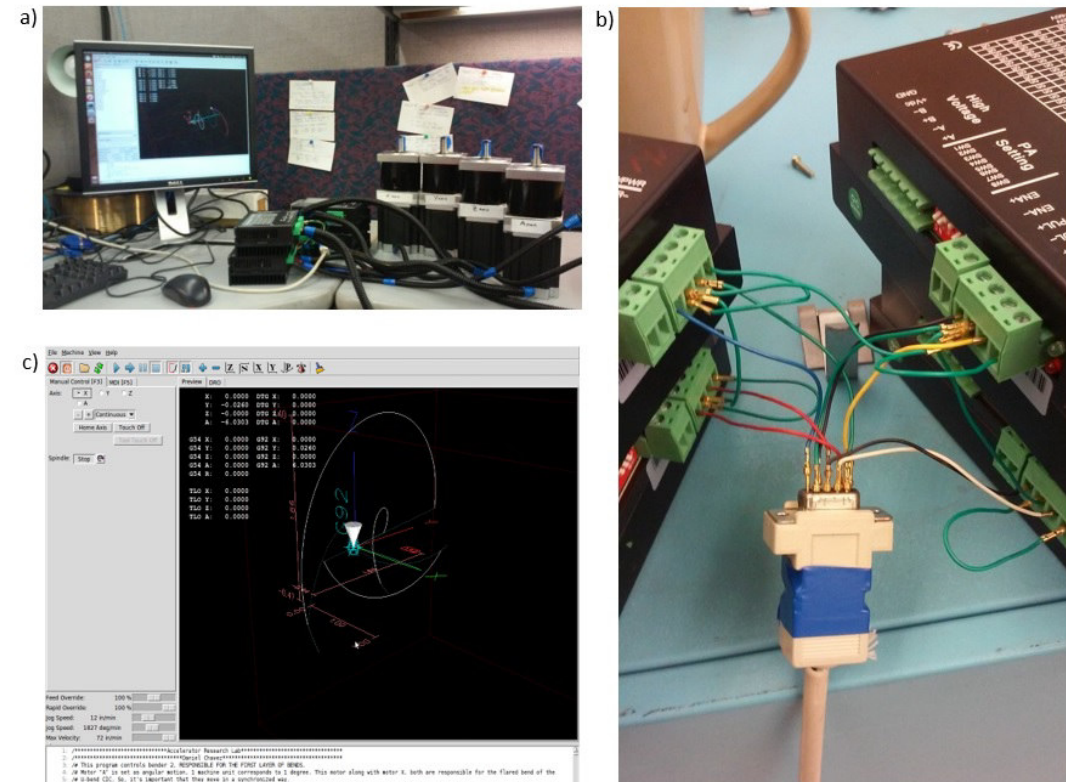


Figure 4.8: Linux CNC and the robotic benders. On a), four motors are connected to the controller through the PS+ and PS- signal wires. On b), the communication from the controller to the computer is made via serial port. On c), a typical path programmed in LINUX CNC, for a flare bend of a coil.

## G-code for operating bender 2

```
/*******Accelerator Research Lab*********
/***********Daniel Chavez**************
/# This program controls bender 2, responsible for making flared ends.
/# Motor "A" is set as angular motion, 1 machine unit corresponds to 1
/# degree. This motor along with motor X, both are responsible for the
/# flared bend of the U-bend CIC. So, it's important that they move
/# in a synchronized way.
```

```
/# Motor "X" is lineal, and .01 machine unit is 1 degrees. 3.6 units
/# is 360 degrees.
/# Motor "Y" controls the Y displacement, 1 machine unit corresponds to
/#1 inch of displacement.
/# It's of vital importance to do not change the zero of the Y axis.
/# Motor "Z" controls the Z displacement, 1 machine unit corresponds
/#to 1 inch in displacement.
/# It's of vital importance to do not change the zero of this axis.
/# When you run the program, make sure that you click on: Execute next
/#line, in order to run the program in steps,
/# otherwise it will complete the whole cycle without stops.
/***********************************************************************
/
#<FlushZ1>=1.0
#<FlushZ2>=0.466
#<FlushZ3>=1.398
/
/***********************************************************************
/# First bend. 180 bend.
G20 G64
G00 X.0 Y0.0 Z0.0 A0.0
G92 X0.0 Y0.0 Z0.0 A0.0
G0 A90.0 X0.9 F10
G0 A100.0 X1.0 F5
G0 A90.0 X0.9
/# Time to remove the bend, and take bender to zero position
G00 A0.0 x0.0 F5
/***********************************************************************
/# Second bend will be the same as bend 1.
G00 X.0 Y0.0 Z0.0 A0.0
G0 A90.0 X0.9 F10
G0 A100.0 X1.0 F5
G0 A90.0 X0.9
G00 X.0 Y0.0 Z0.0 A0.0
/#*********************************************************************
/# Get ready for 3th Bend.
G0 Y[-#<FlushZ2>] Z0.0 F5
/#Hoock up the CIC in dye 2.
G19 G03 Y0.0 Z[-#<FlushZ2>] R[#<FlushZ2>] A90.0 X0.9   F30
/# Unlock next line for a 10 degree over-bend.
G00 A100 X1.0 F5
/# Unlock next line for a 15 degree over-bend.
/ G00 A105 X1.05 F5
/# Unlock next line for a 20 degree over-bend.
/G00 A110 X1.10 F5
```

```
/# Unlock next line for a 25 degree over−bend.
/G00 A115 X1.15 F5
/# After the 90 deg bend is done, is time to pause de code and release
/# the CIC, then lets take the machine to zero.
G00 A90 X0.9 F5
G00 Y0.0 Z0.0 A0.0 X0.0 F5
/#*********************************************************************
/# For bend 4th, Change the dye to next position. ********************
G0 A90.0 X0.9 F10
G0 A100.0 X1.0 F5
G0 A90.0 X0.9
G00 X.0 Y0.0 Z0.0 A0.0
/#*********************************************************************
/# For 5th bend is the same as 3th bend.
G0 Y[−#<FlushZ2>] Z0.0 F5
G19 G03 Y0.0 Z[−#<FlushZ2>] R[#<FlushZ2>] A90.0 X0.9   F30
/# Unlock next line for a 10 degree over−bend.
G00 A100 X1.0 F5
/# Unlock next line for a 15 degree over−bend.
/ G00 A105 X1.05 F5
/# Unlock next line for a 20 degree over−bend.
/G00 A110 X1.10 F5
/# Unlock next line for a 25 degree over−bend.
/G00 A115 X1.15 F5
/# After the 90 deg bend is done, is time to pause de code and release
/# the CIC, then lets take the machine to zero.
G00 A90 X0.9 F5
G00 Y0.0 Z0.0 A0.0 X0.0 F30
/#*********************************************************************
/# For 6th bend, is the same as bend 2 or 4.
G0 A90.0 X0.9 F10
G0 A100.0 X1.0 F5
G0 A90.0 X0.9
G00 X.0 Y0.0 Z0.0 A0.0
/#*********************************************************************
/# 7th bend is the only large one, it must perform a 1.398 radius arc.
G0 Y[−#<FlushZ3>] Z0.0 F5
/# Hoock up the CIC in dye 2.
G19 G03 Y0.0 Z[−#<FlushZ3>] R[#<FlushZ3>] A90.0 X0.9   F30
/# Unlock next line for a 10 degree over−bend.
G00 A100 X1.0 F5
/# Unlock next line for a 15 degree over−bend.
/ G00 A105 X1.05 F5
/# Unlock next line for a 20 degree over−bend.
/G00 A110 X1.10 F5
```

```
/# Unlock next line for a 25 degree over−bend .
/G00 A115 X1.15 F5
/# After the 90 deg bend is done , is time to pause de code and release
/# the CIC , then lets take the machine to zero .
G00 A90 X0.9 F5
G00 Y0.0 Z0.0 A0.0 X0.0 F5
/#∗∗∗∗∗∗∗∗∗∗∗∗∗∗∗∗∗∗∗∗∗∗∗∗∗∗∗∗∗∗∗∗∗∗∗∗∗∗∗∗∗∗∗∗∗∗∗∗∗∗∗∗∗∗∗∗∗∗∗∗∗∗∗∗∗∗∗∗∗
M02
```
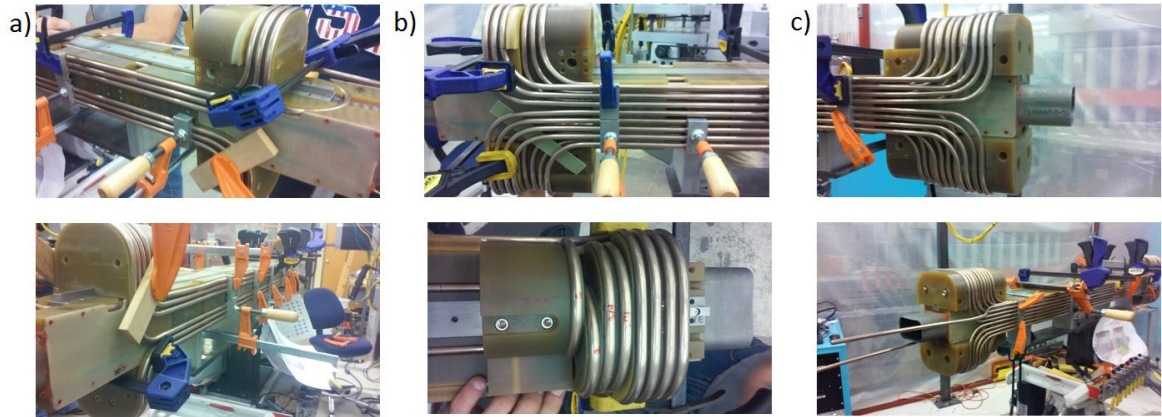


Figure 4.9: Metrology system used for measuring the position of cables for the three layers of 3 T dipole winding. On a), the dipole rest on a Starrett granite table, and a Mitutoyo coordinate measurement machine is used to determine the position of the cables. On b), the micrometer measures the position for the cables on the third layer.

## 4.3 Metrology of Muck-up winding

Figure 4.9 shows the three layers of CIC conductor wound into the G-11 mandrel.

Once the muck-up winding was complete, a precise measurement of the position (X,Y) of the CIC conductors was performed, to compare the actual position of each cable with respect to the position on the magnetic design. Two high-precision equipment's were used for this endeavour, a starrett flat granite table[a], and a Mitutoyo coordinate measurement machine (CMM) [132].

The body of the dipole posses a pattern of slot apertures, specially designed to accommodate X and Y measurements of each cable position. A 2 cm gap is provided in between each of the window-frame segments and side plates at 6 locations along the body, as described in figure 4.10 a), so that there was a local space for the CMM probe to contact the top and side surfaces of each cable. We were able to make measurements of the x and y positions of each cable with respect to a global reference frame, to a reproducible precision of $\pm.001$ in.

The location of each cable is defined according to its relative position in its quadrant, as described in figure 4.10 c). The data is presented for all 6 slots along the body of the dipole.

To relate the errors in the cable position, for all quadrants at the six locations, to its impact on the multipole content, the following considerations are needed:

---

[a]Laboratory Grade AA = (40 + diagonal squared/25) x .000001 in (unilateral)[131]
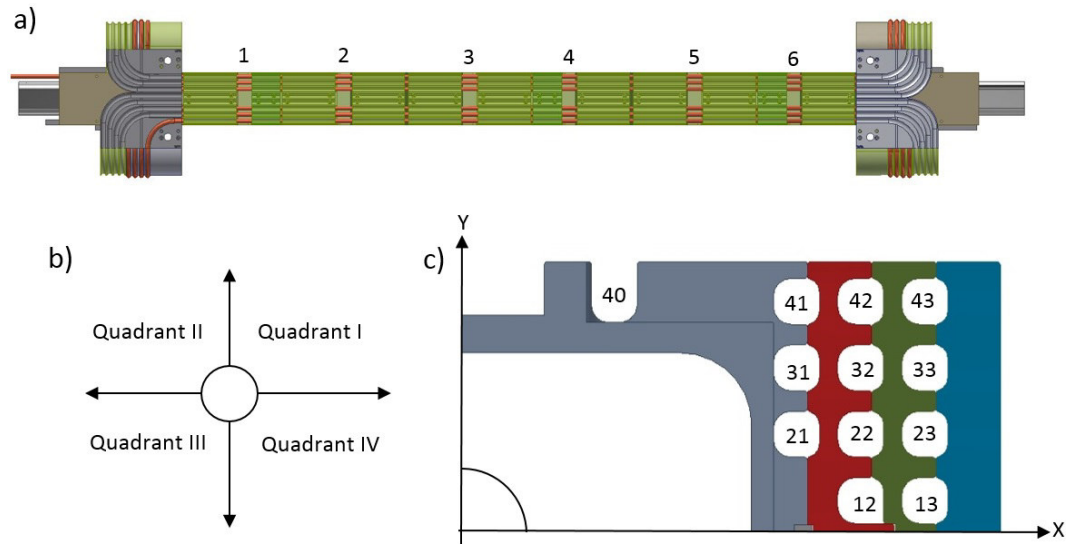
Figure 4.10: Reference system for the metrology of the complete winding. On a), a side-view of the 3 T dipole and the location for the measurements points along the body of the magnet. On b), the coordinate system of the cross-section. On c), the first quadrant of the dipole shows the numbering system for the cables. From left to right, the layers are numbered starting from zero, From bottom to top, the rows are numbered.

1. The errors in the cable positions are small, in this range, small displacements on the cables show a linear behavior of its multipole content.

2. The X and Y errors in the displacements for all the cables, measured at the six locations (as shown in figure 4.10), will be averaged for each quadrant.

3. A multipole matrix was computed for determining the effect of 0.001" cable displacements, for both X and Y directions, relative to its original position in the magnet design.

4. Both, the error matrix and the multipole matrix, were used to estimate actual multipole content produced by cable displacements in both, X and Y direction, this is presented in tables 4.1, 4.2, 4.3 and 4.4.

5. Table 4.5, shows the multipoles produced by the cables in each quadrant. This considers the combined contribution from both X and Y displacement, averaged along the 6 measuring points along the dipole.

6. Table 4.6, shows the multipoles produced by all cables of each layer; multipoles from all cables together.

Systematic multipoles are all within tolerance for the preliminary requirements of the JLEIC design, except for two skew multipoles (highlighted in red) that are driven by a particular offset that arose from a fabrication error that can be remedied. After inspection of the multipole content we have determined that more than half of all variability in cable positions arises from several details of the fabrication of the window-frame segments and the assembly and impregnation of the structural beam.

| Layer | Error | Db0 | Db1 | Db2 | Db3 | Db4 | Db5 | Db6 | Db7 | Db8 | Db9 | Db10 | Da1 | Da2 | Da3 |
|---|---|---|---|---|---|---|---|---|---|---|---|---|---|---|---|
| L1 | err40x | 1.03E-05 | -4.76E-02 | -1.90E-02 | 2.62E-03 | 6.38E-03 | 2.85E-03 | 1.04E-04 | -5.46E-04 | -2.97E-04 | -3.95E-05 | 3.72E-05 | 7.08E-03 | -1.97E-02 | -1.40E-02 |
| | err40y | 3.91E-06 | -3.15E-03 | 4.74E-03 | 3.80E-03 | 8.15E-04 | -4.71E-04 | -4.19E-04 | -1.14E-04 | 2.76E-05 | 3.61E-05 | 1.22E-05 | -1.11E-02 | -5.37E-03 | 5.48E-04 |
| | err41x | 7.54E-08 | 3.67E-04 | 3.13E-04 | 1.39E-04 | 4.09E-05 | 6.85E-06 | -5.46E-07 | -9.67E-07 | -4.33E-07 | -1.22E-07 | -2.35E-08 | -9.34E-04 | -2.43E-04 | -1.08E-05 |
| | err41y | -2.98E-06 | 8.20E-03 | 2.82E-03 | 3.83E-04 | -1.48E-04 | -1.20E-04 | -4.77E-05 | -1.14E-05 | -9.30E-07 | 3.91E-07 | 3.28E-07 | -7.29E-04 | 1.96E-03 | 1.24E-03 |
| | err31x | -4.31E-06 | 1.29E-03 | -2.79E-03 | -2.40E-03 | -1.23E-03 | -4.74E-04 | -1.47E-04 | -3.26E-05 | -2.84E-06 | 1.57E-06 | 1.32E-06 | 2.08E-02 | 8.77E-03 | 2.69E-03 |
| | err31y | -8.00E-06 | 2.53E-02 | 1.17E-02 | 3.69E-03 | 7.08E-04 | -2.71E-05 | -1.04E-04 | -5.70E-05 | -2.17E-05 | -7.22E-06 | -1.73E-06 | -1.01E-02 | 1.99E-03 | 2.95E-03 |
| | err21x | -7.16E-07 | 1.32E-03 | 4.49E-04 | 7.08E-05 | -2.56E-05 | -2.95E-05 | -1.76E-05 | -8.03E-06 | -3.19E-06 | -1.21E-06 | -3.99E-07 | 1.86E-03 | 1.04E-03 | 4.77E-04 |
| | err21y | -1.56E-06 | 5.68E-03 | 3.30E-03 | 1.51E-03 | 5.87E-04 | 2.02E-04 | 6.09E-05 | 1.58E-05 | 3.10E-06 | -2.60E-08 | -3.60E-07 | -5.88E-03 | -1.61E-03 | -2.00E-04 |
| L2 | err42x | -9.36E-06 | -9.65E-03 | -9.95E-03 | -4.50E-03 | -1.36E-03 | -2.96E-04 | -4.20E-05 | 4.05E-06 | 5.33E-06 | 1.61E-06 | 5.34E-07 | 4.36E-02 | 1.21E-02 | 1.65E-03 |
| | err42y | -8.99E-06 | 2.50E-02 | 8.79E-03 | 1.85E-03 | 7.37E-05 | -1.14E-04 | -6.30E-05 | -1.89E-05 | -3.36E-06 | -7.53E-07 | 2.72E-08 | -8.03E-03 | 2.84E-03 | 2.41E-03 |
| | err32x | 4.94E-07 | -2.83E-04 | 8.33E-05 | 9.94E-05 | 5.13E-05 | 1.94E-05 | 6.39E-06 | 1.67E-06 | 3.24E-07 | 6.67E-08 | 3.35E-12 | -1.66E-03 | -6.43E-04 | -1.93E-04 |
| | err32y | -2.34E-05 | 7.54E-02 | 3.30E-02 | 1.07E-02 | 2.60E-03 | 4.32E-04 | -7.86E-06 | -3.44E-05 | -1.57E-05 | -7.00E-06 | -1.99E-06 | -5.15E-02 | -3.78E-03 | 3.90E-03 |
| | err22x | -1.33E-05 | 2.14E-02 | 7.35E-03 | 1.75E-03 | 2.07E-04 | -6.75E-05 | -6.94E-05 | -3.13E-05 | -1.11E-05 | -4.61E-06 | -1.40E-06 | 2.60E-02 | 1.26E-02 | 5.04E-03 |
| | err22y | -2.29E-05 | 9.14E-02 | 4.67E-02 | 1.92E-02 | 6.73E-03 | 2.14E-03 | 6.16E-04 | 1.70E-04 | 4.42E-05 | 8.54E-06 | 1.43E-06 | -1.28E-01 | -3.56E-02 | -7.06E-03 |
| | err12x | -4.04E-05 | 7.85E-02 | 3.56E-02 | 1.33E-02 | 4.52E-03 | 1.43E-03 | 4.20E-04 | 1.31E-04 | 4.21E-05 | 1.02E-05 | 3.07E-06 | 2.38E-02 | 1.27E-02 | 5.80E-03 |
| | err12y | -2.28E-06 | 2.25E-02 | 1.24E-02 | 5.77E-03 | 2.31E-03 | 8.79E-04 | 3.15E-04 | 1.10E-04 | 3.76E-05 | 1.23E-05 | 3.96E-06 | -1.04E-01 | -3.80E-02 | -1.28E-02 |
| L3 | err43x | -3.55E-07 | -1.42E-04 | -1.71E-04 | -7.82E-05 | -2.28E-05 | -5.11E-06 | -1.08E-06 | -1.08E-07 | 4.66E-08 | 7.48E-09 | 5.55E-09 | 1.04E-03 | 2.86E-04 | 4.72E-05 |
| | err43y | 2.44E-06 | -5.16E-03 | -1.53E-03 | -3.33E-04 | -4.32E-05 | 1.30E-06 | 4.16E-06 | 1.21E-06 | 1.18E-07 | 1.23E-07 | 8.37E-09 | 1.64E-03 | -3.44E-04 | -3.00E-04 |
| | err33x | -7.20E-06 | 4.52E-03 | -2.70E-04 | -6.57E-04 | -3.26E-04 | -1.16E-04 | -3.94E-05 | -9.83E-06 | -1.63E-06 | -5.86E-07 | -6.08E-08 | 1.99E-02 | 7.02E-03 | 1.96E-03 |
| | err33y | -1.40E-05 | 3.94E-02 | 1.55E-02 | 4.88E-03 | 1.23E-03 | 2.60E-04 | 3.52E-05 | 3.25E-06 | 3.60E-07 | -9.12E-07 | -2.36E-07 | -3.53E-02 | -5.20E-03 | 4.24E-04 |
| | err23x | -3.01E-08 | 4.01E-05 | 1.32E-05 | 3.27E-06 | 6.45E-07 | 7.71E-08 | -2.61E-08 | -1.25E-08 | -2.37E-09 | -2.29E-09 | -5.10E-10 | 4.74E-05 | 1.94E-05 | 6.88E-06 |
| | err23y | -5.59E-06 | 1.97E-02 | 8.84E-03 | 3.31E-03 | 1.05E-03 | 3.06E-04 | 7.96E-05 | 2.10E-05 | 5.74E-06 | 1.12E-06 | 2.62E-07 | -3.56E-02 | -9.28E-03 | -1.95E-03 |
| | err13x | -2.39E-06 | 4.00E-03 | 1.63E-03 | 5.51E-04 | 1.68E-04 | 4.80E-05 | 1.21E-05 | 3.55E-06 | 1.18E-06 | 2.08E-07 | 6.74E-08 | 1.23E-03 | 5.40E-04 | 2.21E-04 |
| | err13y | 1.45E-06 | 1.70E-02 | 7.72E-03 | 3.29E-03 | 1.13E-03 | 3.80E-04 | 1.17E-04 | 3.50E-05 | 1.02E-05 | 3.00E-06 | 8.14E-07 | -9.67E-02 | -3.06E-02 | -8.76E-03 |

Table 4.1: Multipole matrix for Quadrant I: error multipoles in units ($x10^{-4}$) produced by a .001 displacement of each cable (X,Y), and scaling it to the measured cable displacement.

| | | Db0 | Db1 | Db2 | Db3 | Db4 | Db5 | Db6 | Db7 | Db8 | Db9 | Db10 | Da1 | Da2 | Da3 |
|---|---|---|---|---|---|---|---|---|---|---|---|---|---|---|---|
| L1 | err40x | -2.62E-05 | -1.42E-01 | 5.57E-02 | 8.74E-03 | -1.95E-02 | 8.48E-03 | -1.58E-04 | -1.71E-03 | 8.92E-04 | -1.02E-04 | -1.21E-04 | -2.00E-02 | -5.99E-02 | 4.20E-02 |
| | err40y | 5.36E-07 | 4.55E-04 | 6.80E-04 | -5.43E-04 | 1.16E-04 | 6.72E-05 | -5.99E-05 | 1.63E-05 | 3.94E-06 | -5.16E-06 | 1.74E-06 | -1.58E-03 | 7.68E-04 | 7.85E-05 |
| | err41x | 8.77E-06 | -1.72E-02 | 1.43E-02 | -6.45E-03 | 1.86E-03 | -3.08E-04 | -2.57E-05 | 4.56E-05 | -2.11E-05 | 5.79E-06 | -1.14E-06 | -4.37E-02 | 1.11E-02 | -4.26E-04 |
| | err41y | 1.26E-05 | 3.76E-02 | -1.28E-02 | 1.75E-03 | 6.83E-04 | -5.49E-04 | 2.15E-04 | -5.12E-05 | 4.36E-06 | 1.72E-06 | -1.47E-06 | 3.66E-03 | 8.99E-03 | -5.63E-03 |
| | err31x | 9.85E-06 | 1.81E-03 | 4.39E-03 | -3.88E-03 | 1.97E-03 | -7.65E-04 | 2.38E-04 | -5.24E-05 | 3.82E-06 | 2.79E-06 | -2.25E-06 | -3.38E-02 | 1.40E-02 | -4.28E-03 |
| | err31y | 7.23E-06 | 2.51E-02 | -1.16E-02 | 3.66E-03 | -6.97E-04 | -2.78E-05 | 1.03E-04 | -5.63E-05 | 2.16E-05 | -7.16E-06 | 1.73E-06 | 1.00E-02 | 1.97E-03 | -2.93E-03 |
| | err21x | -3.72E-06 | -5.40E-03 | 1.87E-03 | -2.81E-04 | -1.07E-04 | 1.24E-04 | -7.43E-05 | 3.38E-05 | -1.33E-05 | 5.07E-06 | -1.67E-06 | 7.65E-03 | -4.26E-03 | 1.96E-03 |
| | err21y | 2.41E-06 | 1.00E-02 | -5.80E-03 | 2.65E-03 | -1.03E-03 | 3.56E-04 | -1.07E-04 | 2.80E-05 | -5.41E-06 | -5.50E-08 | 6.40E-07 | 1.03E-02 | -2.82E-03 | 3.45E-04 |
| L2 | err42x | -2.07E-05 | 1.47E-02 | -1.47E-02 | 6.77E-03 | -2.01E-03 | 4.40E-04 | -6.56E-05 | -5.99E-06 | 8.96E-06 | -2.56E-06 | 8.99E-07 | 6.65E-02 | -1.79E-02 | 2.45E-03 |
| | err42y | 6.49E-06 | 1.72E-02 | -6.05E-03 | 1.27E-03 | -5.74E-05 | -8.05E-05 | 4.37E-05 | -1.26E-05 | 2.28E-06 | -5.50E-07 | -2.42E-08 | 5.39E-03 | 1.97E-03 | -1.67E-03 |
| | err32x | -5.13E-06 | -2.17E-03 | -6.10E-04 | 7.74E-04 | -3.87E-04 | 1.50E-04 | -5.04E-05 | 1.30E-05 | -2.35E-06 | 5.03E-07 | 2.08E-08 | 1.29E-02 | -4.90E-03 | 1.47E-03 |
| | err32y | 1.65E-05 | 5.64E-02 | -2.45E-02 | 8.01E-03 | -1.93E-03 | 3.17E-04 | 5.81E-06 | -2.51E-05 | 1.17E-05 | -5.24E-06 | 1.50E-06 | 3.82E-02 | -2.76E-03 | -2.89E-03 |
| | err22x | -2.14E-06 | -2.61E-03 | 9.18E-04 | -2.13E-04 | 2.68E-05 | 8.38E-06 | -9.00E-06 | 3.99E-06 | -1.34E-06 | 5.74E-07 | -1.72E-07 | 3.24E-03 | -1.52E-03 | 6.15E-04 |
| | err22y | -6.04E-06 | -2.20E-02 | 1.14E-02 | -4.65E-03 | 1.63E-03 | -5.17E-04 | 1.49E-04 | -4.12E-05 | 1.07E-05 | -2.05E-06 | 3.42E-07 | -3.08E-02 | 8.64E-03 | -1.70E-03 |
| | err12x | 4.77E-07 | 7.45E-04 | -3.44E-04 | 1.27E-04 | -4.36E-05 | 1.38E-05 | -4.00E-06 | 1.26E-06 | -4.18E-07 | 9.94E-08 | -3.05E-08 | -2.39E-04 | 1.21E-04 | -5.56E-05 |
| | err12y | -1.72E-06 | -1.19E-02 | 6.69E-03 | -3.03E-03 | 1.22E-03 | -4.60E-04 | 1.66E-04 | -5.84E-05 | 1.99E-05 | -6.42E-06 | 2.08E-06 | -5.44E-02 | 2.01E-02 | -6.68E-03 |
| L3 | err43x | 4.75E-06 | -1.45E-03 | 1.73E-03 | -8.05E-04 | 2.26E-04 | -5.26E-05 | 1.18E-05 | -1.07E-06 | -6.10E-07 | 7.85E-08 | -7.26E-08 | -1.09E-02 | 2.90E-03 | -4.89E-04 |
| | err43y | 3.03E-06 | 6.67E-03 | -1.98E-03 | 4.35E-04 | -5.55E-05 | -9.66E-07 | 5.42E-06 | -1.73E-06 | 1.65E-07 | -1.42E-07 | 1.27E-08 | 2.13E-03 | 4.76E-04 | -3.86E-04 |
| | err33x | 9.73E-06 | 4.08E-03 | 1.04E-04 | -6.08E-04 | 2.84E-04 | -1.08E-04 | 3.80E-05 | -8.89E-06 | 1.14E-06 | -5.56E-07 | 2.49E-08 | -1.88E-02 | 6.45E-03 | -1.77E-03 |
| | err33y | -2.93E-06 | -9.32E-03 | 3.65E-03 | -1.15E-03 | 2.89E-04 | -6.13E-05 | 8.52E-06 | -7.29E-07 | 3.09E-08 | 2.09E-07 | -5.82E-08 | -8.25E-03 | 1.24E-03 | 1.05E-04 |
| | err23x | -6.67E-06 | -6.15E-03 | 2.12E-03 | -5.05E-04 | 1.09E-04 | -1.25E-05 | -5.43E-06 | 2.17E-06 | -1.52E-07 | 3.49E-07 | -6.23E-08 | 7.47E-03 | -2.98E-03 | 1.06E-03 |
| | err23y | -1.93E-06 | -8.23E-03 | 3.65E-03 | -1.36E-03 | 4.28E-04 | -1.25E-04 | 3.33E-05 | -8.76E-06 | 2.33E-06 | -4.60E-07 | 1.03E-07 | -1.45E-02 | 3.79E-03 | -8.05E-04 |
| | err13x | -1.38E-05 | -1.63E-02 | 6.88E-03 | -2.25E-03 | 7.05E-04 | -2.00E-04 | 4.79E-05 | -1.43E-05 | 5.34E-06 | -8.95E-07 | 3.14E-07 | 5.17E-03 | -2.18E-03 | 8.73E-04 |
| | err13y | 1.03E-08 | -1.83E-03 | 8.78E-04 | -3.53E-04 | 1.21E-04 | -3.98E-05 | 1.27E-05 | -3.89E-06 | 1.13E-06 | -3.15E-07 | 8.64E-08 | -1.03E-02 | 3.31E-03 | -9.37E-04 |

Table 4.2: Multipole matrix for Quadrant II: error multipoles in units ($x10^{-4}$) produced by a .001 displacement of each cable (X,Y), and scaling it to the measured cable displacement.

| | | Db0 | Db1 | Db2 | Db3 | Db4 | Db5 | Db6 | Db7 | Db8 | Db9 | Db10 | Da1 | Da2 | Da3 |
|---|---|---|---|---|---|---|---|---|---|---|---|---|---|---|---|
| L1 | err40x | 3.17E-06 | 4.31E-02 | -1.69E-02 | -2.64E-03 | 5.89E-03 | -2.57E-03 | 4.95E-05 | 5.19E-04 | -2.54E-04 | 3.17E-05 | 4.46E-05 | -6.07E-03 | -1.81E-02 | 1.27E-02 |
| | err40y | 1.82E-05 | 1.06E-02 | 1.54E-02 | -1.26E-02 | 2.80E-03 | 1.52E-03 | -1.40E-03 | 3.95E-04 | 7.00E-05 | -1.22E-04 | 3.50E-05 | 3.63E-02 | -1.78E-02 | -1.66E-03 |
| | err41x | 2.17E-05 | -1.72E-02 | 1.42E-02 | -6.39E-03 | 1.85E-03 | -2.99E-04 | -3.14E-05 | 4.16E-05 | -6.85E-05 | 3.35E-06 | -2.50E-05 | 4.28E-02 | -1.10E-02 | 4.07E-04 |
| | err41y | -1.17E-05 | -1.45E-02 | 5.08E-03 | -7.08E-04 | -2.55E-04 | 2.10E-04 | -8.32E-05 | 2.20E-05 | 1.62E-05 | 2.35E-07 | 9.58E-06 | 1.37E-03 | 3.44E-03 | -2.18E-03 |
| | err31x | 5.93E-06 | 6.00E-04 | 1.43E-03 | -1.26E-03 | 6.42E-04 | -2.47E-04 | 7.57E-05 | -1.76E-05 | -8.65E-06 | 4.07E-07 | -5.69E-06 | 1.08E-02 | -4.57E-03 | 1.39E-03 |
| | err31y | -3.00E-06 | -4.56E-03 | 2.15E-03 | -6.81E-04 | 1.35E-04 | 1.71E-06 | -1.78E-05 | 1.06E-05 | 3.73E-07 | 1.55E-06 | 1.84E-06 | 1.86E-03 | 3.34E-04 | -5.27E-04 |
| | err21x | -3.78E-05 | -3.45E-02 | 1.19E-02 | -1.80E-03 | -6.97E-04 | 7.87E-04 | -4.70E-04 | 2.20E-04 | -3.69E-05 | 3.48E-05 | 1.36E-05 | -4.91E-02 | 2.74E-02 | -1.26E-02 |
| | err21y | -2.27E-05 | -3.57E-02 | 2.11E-02 | -9.60E-03 | 3.76E-03 | -1.32E-03 | 4.05E-04 | -1.04E-04 | 5.88E-05 | 8.39E-07 | 1.62E-05 | 3.76E-02 | -1.05E-02 | 1.47E-03 |
| L2 | err42x | -3.93E-05 | 1.28E-02 | -1.25E-02 | 5.70E-03 | -1.71E-03 | 3.61E-04 | -4.62E-05 | 4.53E-07 | 8.32E-05 | 1.58E-06 | 3.87E-05 | -5.49E-02 | 1.52E-02 | -2.08E-03 |
| | err42y | 3.69E-05 | 3.59E-02 | -1.28E-02 | 2.71E-03 | -1.38E-04 | -1.50E-04 | 8.64E-05 | -3.22E-05 | -5.82E-05 | -4.18E-06 | -3.15E-05 | -1.19E-02 | -4.11E-03 | 3.45E-03 |
| | err32x | 5.93E-06 | 1.20E-03 | 3.51E-04 | -4.39E-04 | 2.21E-04 | -8.31E-05 | 2.73E-05 | -8.15E-06 | -8.89E-06 | -7.82E-07 | -5.14E-06 | 7.23E-03 | -2.79E-03 | 8.32E-04 |
| | err32y | 3.47E-05 | 3.85E-02 | -1.73E-02 | 5.55E-03 | -1.36E-03 | 2.42E-04 | -5.14E-06 | -2.08E-05 | -5.27E-05 | -6.48E-06 | -2.91E-05 | -2.64E-02 | 2.21E-03 | 1.93E-03 |
| | err22x | -1.47E-06 | -9.97E-04 | 3.52E-04 | -8.18E-05 | 9.99E-06 | 2.92E-06 | -3.19E-06 | 1.68E-06 | 1.68E-06 | 3.26E-07 | 1.03E-06 | -1.22E-03 | 5.88E-04 | -2.36E-04 |
| | err22y | 3.78E-05 | 3.92E-02 | -2.07E-02 | 8.34E-03 | -2.93E-03 | 9.56E-04 | -2.80E-04 | 7.00E-05 | -9.43E-05 | 5.17E-07 | -3.77E-05 | -5.60E-02 | 1.58E-02 | -3.24E-03 |
| | err12x | -5.89E-05 | -5.58E-02 | 2.58E-02 | -9.55E-03 | 3.25E-03 | -1.05E-03 | 3.10E-04 | -8.87E-05 | 1.11E-04 | -3.65E-06 | 4.21E-05 | -1.75E-02 | 9.33E-03 | -4.19E-03 |
| | err12y | 6.55E-06 | 3.32E-03 | -1.93E-03 | 8.75E-04 | -3.55E-04 | 1.37E-04 | -4.92E-05 | 1.55E-05 | -2.23E-05 | 1.10E-06 | -8.82E-06 | -1.64E-02 | 6.06E-03 | -2.03E-03 |
| L3 | err43x | -3.37E-05 | 5.01E-03 | -5.61E-03 | 2.56E-03 | -7.55E-04 | 1.60E-04 | -2.82E-05 | 8.19E-06 | 6.79E-05 | 2.99E-06 | 3.34E-05 | -3.42E-02 | 9.38E-03 | -1.55E-03 |
| | err43y | -8.55E-06 | -5.68E-03 | 1.76E-03 | -3.77E-04 | 5.18E-05 | -1.45E-06 | -3.43E-06 | 2.44E-06 | 1.50E-05 | 8.66E-07 | 7.52E-06 | 1.83E-03 | 3.35E-04 | -3.31E-04 |
| | err33x | -1.11E-05 | -1.98E-03 | -4.06E-05 | 3.04E-04 | -1.50E-04 | 5.16E-05 | -1.66E-05 | 5.97E-06 | 1.97E-05 | 1.27E-06 | 1.02E-05 | -9.14E-03 | 3.24E-03 | -8.98E-04 |
| | err33y | 4.98E-06 | 3.78E-03 | -1.55E-03 | 4.79E-04 | -1.22E-04 | 2.74E-05 | -4.41E-06 | -3.73E-07 | -9.68E-06 | -5.43E-07 | -4.77E-06 | -3.45E-03 | 5.45E-04 | 3.16E-05 |
| | err23x | 8.80E-06 | 4.10E-03 | -1.43E-03 | 3.40E-04 | -6.62E-05 | 9.83E-06 | 1.56E-06 | -2.39E-06 | -1.46E-05 | -9.59E-07 | -7.33E-06 | 4.87E-03 | -2.03E-03 | 7.09E-04 |
| | err23y | 1.98E-05 | 1.30E-02 | -6.07E-03 | 2.21E-03 | -7.06E-04 | 2.13E-04 | -5.76E-05 | 1.11E-05 | -4.66E-05 | -1.25E-06 | -2.14E-05 | -2.35E-02 | 6.46E-03 | -1.36E-03 |
| | err13x | -3.39E-05 | -2.14E-02 | 9.03E-03 | -3.00E-03 | 9.27E-04 | -2.73E-04 | 6.98E-05 | -1.51E-05 | 6.09E-05 | 1.43E-06 | 2.74E-05 | -6.61E-03 | 3.03E-03 | -1.13E-03 |
| | err13y | -2.66E-06 | -7.69E-04 | 3.99E-04 | -1.54E-04 | 5.29E-05 | -1.88E-05 | 6.08E-06 | -1.15E-06 | 7.37E-06 | 1.90E-07 | 3.46E-06 | 4.68E-03 | -1.51E-03 | 4.31E-04 |

Table 4.3: Multipole matrix for Quadrant III: error multipoles in units ($x10^{-4}$) produced by a .001 displacement of each cable (X,Y), and scaling it to the measured cable displacement.

| | | Db0 | Db1 | Db2 | Db3 | Db4 | Db5 | Db6 | Db7 | Db8 | Db9 | Db10 | Da1 | Da2 | Da3 |
|---|---|---|---|---|---|---|---|---|---|---|---|---|---|---|---|
| L1 | err40x | -3.27E-05 | 1.52E-01 | 6.06E-02 | -8.35E-03 | -2.03E-02 | -9.10E-03 | -3.31E-04 | 1.74E-03 | 9.46E-04 | 1.26E-04 | -1.19E-04 | 2.32E-02 | -6.26E-02 | -4.47E-02 |
| | err40y | 1.83E-05 | -1.38E-02 | 1.99E-02 | 1.63E-02 | 3.61E-03 | -1.97E-03 | -1.81E-03 | -5.12E-04 | 1.10E-04 | 1.57E-04 | 5.52E-05 | 4.70E-02 | 2.31E-02 | -2.14E-03 |
| | err41x | 3.02E-06 | 1.55E-02 | 1.32E-02 | 5.87E-03 | 1.72E-03 | 2.87E-04 | -2.31E-05 | -4.04E-05 | -1.82E-05 | -5.17E-06 | -9.92E-07 | 4.00E-02 | 1.03E-02 | 4.70E-04 |
| | err41y | 7.53E-06 | -1.70E-02 | -5.93E-03 | -8.25E-04 | 2.89E-04 | 2.48E-04 | 9.96E-05 | 2.40E-05 | 2.01E-06 | -7.24E-07 | -6.78E-07 | -1.81E-03 | 3.97E-03 | 2.55E-03 |
| | err31x | 5.11E-06 | -1.57E-03 | 3.57E-03 | 3.07E-03 | 1.56E-03 | 6.05E-04 | 1.87E-04 | 4.15E-05 | 3.66E-06 | -2.00E-06 | -1.68E-06 | 2.70E-02 | 1.12E-02 | 3.44E-03 |
| | err31y | -2.67E-06 | 6.76E-03 | 3.19E-03 | 1.00E-03 | 2.00E-04 | -3.70E-06 | -2.70E-05 | -1.51E-05 | -5.79E-06 | -1.98E-06 | -4.86E-07 | 2.79E-03 | -4.81E-04 | -7.77E-04 |
| | err21x | -7.33E-07 | 1.33E-03 | 4.49E-04 | 7.02E-05 | -2.51E-05 | -2.95E-05 | -1.76E-05 | -8.02E-06 | -3.19E-06 | -1.21E-06 | -3.99E-07 | -1.88E-03 | -1.04E-03 | -4.78E-04 |
| | err21y | 9.81E-07 | -2.72E-03 | -1.59E-03 | -7.25E-04 | -2.85E-04 | -9.90E-05 | -3.02E-05 | -8.11E-06 | -1.72E-06 | -6.33E-08 | 1.45E-07 | -2.86E-03 | -7.99E-04 | -1.10E-04 |
| L2 | err42x | -5.06E-06 | -5.34E-03 | -5.58E-03 | -2.52E-03 | -7.59E-04 | -1.65E-04 | -2.32E-05 | 2.28E-06 | 2.93E-06 | 9.02E-07 | 3.01E-07 | -2.48E-02 | -6.74E-03 | -9.56E-04 |
| | err42y | 3.42E-05 | -6.57E-02 | -2.37E-02 | -4.97E-03 | -2.91E-04 | 2.95E-04 | 1.72E-04 | 5.02E-05 | 7.89E-06 | 2.09E-06 | -1.48E-07 | -2.19E-02 | 7.26E-03 | 6.31E-03 |
| | err32x | 9.85E-06 | -5.82E-03 | 1.78E-03 | 2.03E-03 | 1.03E-03 | 3.94E-04 | 1.30E-04 | 3.40E-05 | 6.63E-06 | 1.36E-06 | -7.72E-09 | 3.44E-02 | 1.33E-02 | 3.92E-03 |
| | err32y | 7.25E-05 | -1.58E-01 | -7.10E-02 | -2.27E-02 | -5.65E-03 | -9.43E-04 | 1.01E-05 | 6.64E-05 | 2.90E-05 | 1.48E-05 | 4.05E-06 | -1.07E-01 | -8.73E-03 | 7.92E-03 |
| | err22x | -1.19E-05 | 1.82E-02 | 6.25E-03 | 1.48E-03 | 1.81E-04 | -5.74E-05 | -5.89E-05 | -2.64E-05 | -9.37E-06 | -3.91E-06 | -1.18E-06 | -2.25E-02 | -1.07E-02 | -4.27E-03 |
| | err22y | 4.00E-05 | -8.92E-02 | -4.69E-02 | -1.89E-02 | -6.69E-03 | -2.12E-03 | -6.10E-04 | -1.72E-04 | -4.75E-05 | -9.12E-06 | -1.78E-06 | -1.29E-01 | -3.58E-02 | -7.25E-03 |
| | err12x | -8.83E-06 | 1.71E-02 | 7.77E-03 | 2.90E-03 | 9.83E-04 | 3.12E-04 | 9.17E-05 | 2.85E-05 | 9.19E-06 | 2.22E-06 | 6.67E-07 | -5.54E-03 | -2.84E-03 | -1.28E-03 |
| | err12y | 2.61E-05 | -4.24E-02 | -2.46E-02 | -1.08E-02 | -4.39E-03 | -1.64E-03 | -5.85E-04 | -2.09E-04 | -7.37E-05 | -2.32E-05 | -7.71E-06 | -2.03E-01 | -7.48E-02 | -2.50E-02 |
| L3 | err43x | -4.34E-06 | -2.15E-03 | -2.92E-03 | -1.28E-03 | -3.78E-04 | -8.60E-05 | -1.71E-05 | -1.46E-06 | 5.65E-07 | 9.63E-08 | 8.15E-08 | -1.73E-02 | -4.69E-03 | -7.95E-04 |
| | err43y | 1.50E-05 | -1.98E-02 | -6.17E-03 | -1.30E-03 | -2.02E-04 | 2.61E-06 | 1.88E-05 | 4.69E-06 | -2.53E-07 | 4.65E-07 | -1.71E-08 | -6.94E-03 | 1.15E-03 | 1.13E-03 |
| | err33x | -4.27E-06 | 2.86E-03 | -1.94E-04 | -4.30E-04 | -2.15E-04 | -7.59E-05 | -2.51E-05 | -6.37E-06 | -1.13E-06 | -3.81E-07 | -4.36E-08 | -1.31E-02 | -4.62E-03 | -1.26E-03 |
| | err33y | 1.99E-05 | -3.30E-02 | -1.35E-02 | -4.08E-03 | -1.07E-03 | -2.21E-04 | -2.76E-05 | -3.19E-06 | -1.39E-06 | 7.23E-07 | 1.12E-07 | -3.00E-02 | -4.55E-03 | 2.72E-04 |
| | err23x | 5.75E-06 | -6.82E-03 | -2.30E-03 | -5.64E-04 | -1.12E-04 | -1.40E-05 | 4.68E-06 | 2.28E-06 | 3.22E-07 | 3.70E-07 | 8.22E-08 | 8.33E-03 | 3.31E-03 | 1.17E-03 |
| | err23y | 2.55E-05 | -4.21E-02 | -1.97E-02 | -7.00E-03 | -2.25E-03 | -6.47E-04 | -1.66E-04 | -4.60E-05 | -1.41E-05 | -2.44E-06 | -6.99E-07 | -7.61E-02 | -2.04E-02 | -4.25E-03 |
| | err13x | 1.02E-05 | -1.59E-02 | -6.56E-03 | -2.17E-03 | -6.60E-04 | -1.90E-04 | -4.80E-05 | -1.40E-05 | -4.73E-06 | -8.17E-07 | -2.68E-07 | 5.28E-03 | 2.26E-03 | 8.42E-04 |
| | err13y | 9.34E-06 | -1.21E-02 | -6.12E-03 | -2.28E-03 | -8.16E-04 | -2.61E-04 | -7.76E-05 | -2.49E-05 | -8.47E-06 | -2.09E-06 | -6.57E-07 | -6.97E-02 | -2.24E-02 | -6.36E-03 |

Table 4.4: Multipole matrix for Quadrant IV: error multipoles in units ($x10^{-4}$) produced by a .001 displacement of each cable (X,Y), and scaling it to the measured cable displacement

| | Db0 | Db1 | Db2 | Db3 | Db4 | Db5 | Db6 | Db7 | Db8 | Db9 | Db10 | Da1 | Da2 | Da3 |
|---|---|---|---|---|---|---|---|---|---|---|---|---|---|---|
| err40 | 0.000 | -0.001 | 0.121 | 0.007 | -0.020 | -0.001 | -0.004 | 0.000 | 0.001 | 0.000 | 0.000 | 0.075 | -0.160 | -0.007 |
| err41 | 0.000 | -0.004 | 0.031 | -0.006 | 0.006 | -0.001 | 0.000 | 0.000 | 0.000 | 0.000 | 0.000 | 0.041 | 0.028 | -0.004 |
| err31 | 0.000 | 0.055 | 0.012 | 0.003 | 0.003 | -0.001 | 0.000 | 0.000 | 0.000 | 0.000 | 0.000 | 0.029 | 0.033 | 0.002 |
| err21 | 0.000 | -0.060 | 0.032 | -0.008 | 0.002 | 0.000 | 0.000 | 0.000 | 0.000 | 0.000 | 0.000 | -0.002 | 0.007 | -0.009 |
| err42 | 0.000 | 0.025 | -0.076 | 0.006 | -0.006 | 0.000 | 0.000 | 0.000 | 0.000 | 0.000 | 0.000 | -0.006 | 0.011 | 0.012 |
| err32 | 0.000 | 0.005 | -0.078 | 0.004 | -0.005 | 0.001 | 0.000 | 0.000 | 0.000 | 0.000 | 0.000 | -0.094 | -0.008 | 0.017 |
| err22 | 0.000 | 0.055 | 0.006 | 0.007 | -0.001 | 0.000 | 0.000 | 0.000 | 0.000 | 0.000 | 0.000 | -0.338 | -0.046 | -0.018 |
| err12 | 0.000 | 0.012 | 0.061 | 0.000 | 0.007 | 0.000 | 0.001 | 0.000 | 0.000 | 0.000 | 0.000 | -0.378 | -0.067 | -0.046 |
| err43 | 0.000 | -0.023 | -0.015 | -0.001 | -0.001 | 0.000 | 0.000 | 0.000 | 0.000 | 0.000 | 0.000 | -0.063 | 0.009 | -0.003 |
| err33 | 0.000 | 0.010 | 0.004 | -0.001 | 0.000 | 0.000 | 0.000 | 0.000 | 0.000 | 0.000 | 0.000 | -0.098 | 0.004 | -0.001 |
| err23 | 0.000 | -0.027 | -0.015 | -0.004 | -0.002 | 0.000 | 0.000 | 0.000 | 0.000 | 0.000 | 0.000 | -0.129 | -0.021 | -0.005 |
| err13 | 0.000 | -0.047 | 0.014 | -0.006 | 0.002 | -0.001 | 0.000 | 0.000 | 0.000 | 0.000 | 0.000 | -0.167 | -0.048 | -0.015 |

Table 4.5: Multipole matrix for Quadrant IV: error multipoles in units ($x10^{-4}$) produced by a .001 displacement of each cable (X,Y), and scaling it to the measured cable displacement.

| | Db0 | Db1 | Db2 | Db3 | Db4 | Db5 | Db6 | Db7 | Db8 | Db9 | Db10 | Da1 | Da2 | Da3 |
|---|---|---|---|---|---|---|---|---|---|---|---|---|---|---|
| Layer 1 | 0.000 | -0.011 | 0.196 | -0.004 | -0.009 | -0.003 | -0.004 | 0.000 | 0.001 | 0.000 | 0.000 | 0.142 | -0.090 | -0.018 |
| Layer 2 | 0.000 | 0.097 | -0.088 | 0.017 | -0.005 | 0.001 | 0.001 | 0.000 | 0.000 | 0.000 | 0.000 | **-0.816** | **-0.111** | -0.036 |
| Layer3 | 0.000 | -0.086 | -0.012 | -0.012 | -0.001 | -0.001 | 0.000 | 0.000 | 0.000 | 0.000 | 0.000 | **-0.457** | **-0.055** | -0.024 |
| All Layers | 0.000 | 0.000 | 0.096 | 0.001 | -0.015 | -0.003 | -0.003 | 0.000 | 0.002 | 0.000 | 0.000 | **-1.131** | **-0.256** | -0.078 |

Table 4.6: Multipoles produced by all cables of each layer; multipoles from all cables together.

**Shimming strategy: Correction of the multipoles**

An important element of design strategy for any collider dipole is to develop a shimming strategy by which multipoles that may be produced by construction or assembly tolerances can be corrected by shimming. The strategy starts by identifying multipoles that are particularly sensitive in the beam dynamics requirements, identifying multipoles that can arise from placement errors, and then seeking an orthogonal shimming strategy by which displacing a single turn of cable that is accessible in the completed winding tunes each such multipole without affecting others.

The two multipoles that we identify from the above criteria are sextupole (from beam dynamics) and skew quadrupole (from the above-discussed placement errors). We identified the y position of the dog-bone turn 40 as controlling a1 (see red values in Table 1b), and the x position of the outer turn 13 as controlling b2, as shown in Figure 10. The effect of example displacements of those two turns to suppress the problematically large a1 is shown in Table 1c.

This strategy can translate into a very nice procedure for manufacture of full-length dipoles for JLEIC. A coil assembly is completed, assembled into the flux return, and align the coil assembly vertically and preload the coil assembly horizontally. Current is passed through the coil at room temperature and the multipoles are measured. If there are unacceptable multipoles, the coil assembly is removed from the flux return and the above turns are shimmed as appropriate to correct the multipoles. The magnet is then completed and ready for cold testing. An important objective of building and testing a model dipole is to evaluate whether this strategy can yield agreement between warm and cold multipoles.

| | Db0 | Db1 | Db2 | Db3 | Db4 | Db5 | Db6 | Db7 | Db8 | Db9 | Db10 | Da1 | Da2 | Da3 |
|---|---|---|---|---|---|---|---|---|---|---|---|---|---|---|
| Layer 1 | 0.000 | -0.011 | 0.468 | -0.004 | 0.041 | -0.003 | -0.029 | 0.000 | 0.003 | 0.000 | 0.001 | 0.783 | -0.090 | -0.047 |
| Layer 2 | 0.000 | 0.097 | -0.088 | 0.017 | -0.005 | 0.001 | 0.001 | 0.000 | 0.000 | 0.000 | 0.000 | -0.816 | -0.111 | -0.036 |
| Layer3 | 0.001 | -0.106 | -0.170 | -0.022 | -0.017 | -0.002 | -0.001 | 0.000 | -0.001 | 0.000 | 0.000 | -0.314 | -0.093 | -0.018 |
| All Layers | 0.001 | -0.020 | 0.211 | -0.009 | 0.019 | -0.003 | -0.029 | 0.000 | 0.002 | 0.000 | 0.000 | -0.348 | -0.295 | -0.101 |

Table 4.7: Multipoles after shimming of cables 40 by +.005" in y to correct a1, and cables 13 by -.010" in x to suppress b2.

# Chapter 5

# Research and Development of Normal Conducting Magnets for Mexican projects

The research work described in this chapter is partly based on the following papers :

- Chavez, D. et al. "Status Report on the R&D of a 5 T/m Normal Conducting Quadrupole Magnet for the 10-MeV Beam Line of the Electron Linac of the Mexican Particle Accelerator Community". In Journal of Physics: Conference Series (Vol. 912, No. 1, p. 012038). IOP Publishing.

- Chavez, D., et al. "Field and Cost Optimization of a 5 T/m Normal Conducting quadrupole for the 10-MeV Beam Line of the Electron Linac of the Mexican Particle Accelerator Community." Journal of Physics: Conference Series. Vol. 1067. No. 8. IOP Publishing, 2018.

- Valerio-Lizarraga, C. A., Yee-Rendon, B., Duarte-Galvan, C., Guillermo Cantn, G., Medina, L., Chavez Valenzuela, D., & Maury Cuna, G. H. I. (2018). "Study of the first Mexican RF linear accelerator". Rev. Mex. Fis., 64, 116.

## 5.1    Introduction

Mexico interest in experimental particle physics started in early 1980's, when Leon Lederman, former director of FERMILAB and nobel prize of physics (1988), initiated a program to encourage experimental high-energy physics in Latin America [11]. From this, a successful first generation of Mexican experimental particle-physicist was born. This, inspired Mexican Universities for the continuous formation of human resources. After three decades, research groups in experimental high energy physics have been consolidated at eight Mexican Universities. This groups actively collaborate with international institutes, developing experimental high-energy physics [12]. Nevertheless, it worth to clarify, that the this collaborations are not targeting in-house development of particle accelerators. The first attempt to develop accelerator science and technology in Mexico, was conceived at the Institute of Physics of Universidad de Guanajuato in 1986, as a joint collaboration with FERMILAB. Unfortunately, this project did not succeed, in 1992 the accelerator project was closed and new groups working on other topics started a new era of this institute [13].

In early 2006, with the proposition of developing the first national synchrotron radiation facility in Mexico, a new era began, boosting the formation of human resources in different areas of particle accelerator physics.

With this in mind, the institute of physics of Universidad de Guanajuato, has been the largest group committed to form specialized PhD. students, targeting key areas required for developing accelerator technology.

After a decade, the Universidad de Guanajuato has consolidated a small, but efficient group of specialized PhD. students, trained in key topics for developing the first 6 MeV electron linear accelerator, for research purposes in Mexico [133]. This project represents a major challenge and a big opportunity, for me to contribute to the development of accelerator technology in Mexico, through the design, modeling and development of the low-gradient normal conducting quadrupoles, required by the eLINAC.

In the following sections, an analytic model that blends beam requirements, such field uniformity, with geometric requirements, such magnet aperture, is presented. This model is design to optimize: in-house production cost and field quality is has the potential to be extrapolated to higher order magnets, such sextupoles. The model is complemented with a series of studies such magnetic, mechanical and thermal models. Furthermore, a study of the fringe fields is presented, as well as a strategy of winding and characterizing a first prototype. In addition, the effects of wire misalignment, that could be produced during winding operation, and its relation with field quality are studied. From this, the allowed tolerance range to maintain the field quality within one unit $(10^{-4})$ of the multipole content are determined.

## 5.2 Analytic model: Parametric study

The development of accelerator technology represents a challenge, on one hand the technological and on the other hand economical perspectives [134, 135, 136]. To merge both concepts, a comprehensive design of a normal conducting quadrupole must consider a large number of parameters to fulfill beam requirements, and it should provide a feedback of how this affect the total production and operation cost. A schematic model of one quarter of the "standard type" quadrupole geometry is shown in figure 5.1, that relates the field requirement with the geometry parameters, providing a direct path for field and cost optimization.



Figure 5.1: Geometry parameters for a quarter section of a standard type geometry of normal conducting quadrupole.

The main parameters that defines the geometry of a quadrupole are: $R$ the aperture radius, $W$ the width of the hyperbola pole-profile, and $A$, the latter defined as in terms of the minimum pole distance [137]. This last parameter has a strongly influence of the field quality at the good region of the aperture. By geometric construction one can express the width of the pole as:

$$W = \sqrt{2}A \left| 1 - \frac{R^2}{2A^2} \right| \tag{5.1}$$

On the other hand, the length of the pole can be expressed in terms of the number of wires $N_p$, laying on the pole face of a block-coil distribution, which depends on the conductor radius $R_w$. The thickness of the flux return $B_t$, depends on the field saturation, and can be defined on the magnetic relaxation model. This model provides a correlation between the main geometric parameters and the beam requirements, and it could be easy extended to Collins and Panofsky geometries [138], or to higher order normal conducting electromagnets.

## 5.2.1 Cost optimization model for normal conducting quadrupoles

To produce an optimized quadrupole, in terms of minimum production, operation cost, and optimum field performance, we have merged the latter parametrization model,with the cost optimization procedure given by Brianti and Gabriel [139], and extended to normal conducting quadrupoles.

The total cost is divided into two main components: the equipment cost $M_e$, and the running cost, $M_r$. The first takes into account the cost of the power supply and associated equipment $M_1$, cost of finish coil mounted on the yoke $M_2$, cost of the finished yoke $M_3$, cost of a.c. and d.c. distribution $M_4$ and cost of cooling $M_5$, shown in Eq. (2). The latter, considers the operation cost for a given running time and involves the cost of electricity for the power supply.

$$M_{tot} = M_r + \sum_{i=1}^{5} M_i \tag{5.2}$$

We have chosen to normalize the cost components $M_i$i with respect to power supply cost, to avoid fluctuations in cost and economy. This normalization relates the cost between different components and leaves undetermined the actual money. The values and the functional dependence of the $M_i$ coefficients with the main parameters are given on Table 5.1.

Table 5.1: CMAP quadrupole parameters and values

| Parameter | Symbol | Value |
|---|---|---|
| *Field Gradient* | $K$ | 3.2 T/m |
| *Aperture radius* | $R$ | 0.025 m |
| *Field at pole tip* | $B_{tip}$ | 0.080 T |
| *Minimum pole distance*[a] | $A$ | 0.0074 m |
| *Flux return thickness* | $B_t$ | 0.013 m |
| *Wires along pole* | $N_p$ | *18* |
| *Wires along base* | $N_b$ | *6* |
| *Total Wires/pole* | $N = N_b N_p$ | *108* |
| *Conductor radius* | $R_w$ | 0.002 m |
| $M_1$ | $M_1 = M_{01} + m_1(\alpha P)$ | |
| *Power Supply & Equip.* | $M_{01}$ | *1.5161* |
| *Power cost/kW* | $m_1$ | $1.22x10^{-5}$ |
| *Power factor* | $\alpha$ | *0.99* |
| $M_2$ | $M_2 = m_2 V_c$ | |
| *Conductor cost/$m^3$* | $m_2$ | *114.744* |
| *Volume of finished coil* | $V_c$ | |
| $M_3$ | $M_3 = m_3 V_y$ | |
| *Cost of finished yoke/$m^3$* | $m_3$ | *5.458* |
| *Volume of finished yoke* | $V_y$ | |
| $M_4$ | $M_4 = m_4 P$ | |
| *a.c. distribution/kW* | $m_4$ | *0.3058* |
| $M_5$ | $M_5 = m5$ | |
| *Cost of cooling/kW* | $m_5$ | *0.002* |
| $M_r$ | $M_r = m_6 T(\beta P)$ | |
| *Running time* | $T$ | *36500*h |
| *Cost of electricity/kWh* | $m_6$ | $1.22x10^{-5}$ |
| *Power Correction factor* | $\beta$ | *0.5* |

## Main parameters

Both components of the capital cost, $M_e$ and $M_r$ depends on the active power, the volume of the conductor and the volume of the yoke, as described in [139]. The power P, defined by the Joule-Lenz law [140], can be express in terms of the main beam requirements: field gradient $K$, current density $S_f$, magnet length $L$, aperture radius $R$ and the field quality (A), setting the magnet length and the current density as the two scaling parameters. To determine the power $P$, we define the number of wires per pole in terms of the field gradient and aperture radius. The former is determined by the electrical excitation in the coils according to Amperes law [141]. If the integration path connecting the segments: P0P1, P1P2, P2P3 and P3P0 on figure 5.1 is used, one can estimate the field gradient in terms of the operational current $I_{op}$, as:

$$I_{op} = \frac{KR^2}{2\mu_0} \tag{5.3}$$

The number of wires per pole is obtained as the ratio between the operational current, and the total current per wire, in terms of the current density passing through a conductor of radius $R_w$:

$$N = \frac{KR^2}{2\mu_0(S_f \pi R_w^2)} \tag{5.4}$$

If a conductor of radius $R_w$ and resistivity $\rho_c$ is used, the resistance is:

$$R = \frac{\rho_c L}{A} = \frac{\rho_c}{\pi R_w^2}[L + W]8N \tag{5.5}$$

The power $P$ defined by the length of the magnet, the resistance of the conductor and the current density, can be expressed as:

$$P = \frac{4K\rho_c S_f R^2}{\mu_0}\left(L + \sqrt{2}A\left|1 - \frac{R^2}{2A^2}\right|\right) \tag{5.6}$$

One can estimate the volume of conductor as:

$$V_c = \frac{4KR^2}{\mu_0 S_f}\left(L + \sqrt{2}A\left|1 - \frac{R^2}{2A^2}\right|\right) \tag{5.7}$$

From figure 5.1, The volume of the iron yoke is calculated as a function of the quadrupole length $L$. Assuming that the cross-sectional area of pole is approximately $2N_p R_W W$, one can write the volume of the yoke as given by:

$$V_y = L\left[8B_t N_p R_W + 4B_t W + 16B_t N_b R_w + \sqrt{2}B_t^2 + 8B_t\left(A + \sqrt{2}R_W\left(N_p - N_b\right)\right)\right] \tag{5.8}$$

From $N = N_p N_b$ one can express $N_b$ as:

$$N_b = \frac{KR^2}{2\mu_0\left(S_f \pi R_w^2\right)}\frac{1}{N_p} \tag{5.9}$$

## Case study: CMAP quadrupoles

The latter procedure is applied to case of the normal conducting quadrupoles using the values described on Table 1. For the optimization procedure, several candidate materials for the yoke were considered in terms of the availability and machinability. The steels: A-1010, A-1008, A-1006 and A-1018 are available and at low cost. A preliminary study of the multipole content, considering the latter materials [142], revealed negligible difference

between them in terms of performance. Steel A-1010 was selected for the iron yoke. As far as machinability, laser-cut milling offers a 10x cheaper production, while maintaining tolerances, in comparison with Computer Numerical Control (CNC) milling, for a laminated quadrupole design.As it can be seen on figure 5.2, the total cost has a minimum with respect to the current density at 1.8 A/mm$^2$., and a minimum with respect to the length at L= 0.1 m. A 1% fluctuation of the cost around the minimum allows to set a current density in the range from 1.2 to 2.4 A/mm$^2$. If the length of quadrupole increases to next value, 0.15 m, the total cost increases by 2:8%. A dissection of the total cost in terms of the power supply, the magnet, and the cost of electricity, reveals that for the low field gradient and small aperture requirements, the power supply represents the major expense. The magnet cost and the electricity cost merge at current densities of higher than 2 A/mm$^2$.
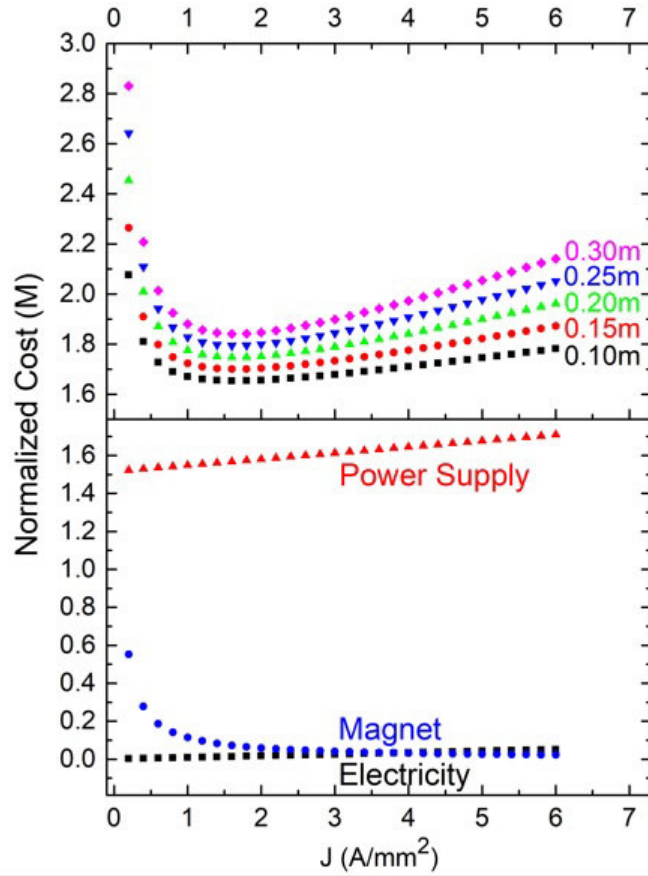


Figure 5.2: On top, cost optimization model applied to CMAP quadrupoles. On the bottom, the dissection of the total cost in terms of its main components.

## 5.2.2 Field optimization

The field quality of a quadrupole depends on a number variables such as, the positioning of the coils, the orientation of the poles, the tolerances on the machine parts, and the quality of the magnetic model. To evaluate the magnetic model alone, one can express the magnetic field inside the aperture, in terms of its components $B_x$ and $B_y$, which can be specified by the multipole expansion, Eq. 10, as described by [143]. Where $B_{ro}$ is the fundamental harmonic at the reference radius $R_r$ (1.8 cm for this calculations), $b_n$ and an are the normal and skew multipoles.

$$B_x + iB_y = 10^{-4} B_{ro} \sum_{n=1}^{\infty} (b_n + ia_n) \times [Cos(n\theta) + iSin(n\theta)] \left(\frac{r}{R_r}\right)^n \tag{5.10}$$

Applying the parametric model to the geometry shown in figure 5.1 and using Comsol Multiphysics [144] we performed a parametric sweep on the minimum pole distance $A$. For a 3.2 T/m gradient, the allowed higher order multipoles $b_5$, $b_9$ and $b_{13}$ [145] are kept within 1 unit when the minimum pole distance $A$ is 7.4 mm, if the pole width slightly increases beyond 7.6 mm, the multipoles rapidly grow, as shown at figure 5.3. This imposes a tolerance limit for machining parts. A tolerances of 76 $\mu$ m could readily be achieve by laser-cut milling [146], offering safe variation within 7:4 and 7.6 mm.
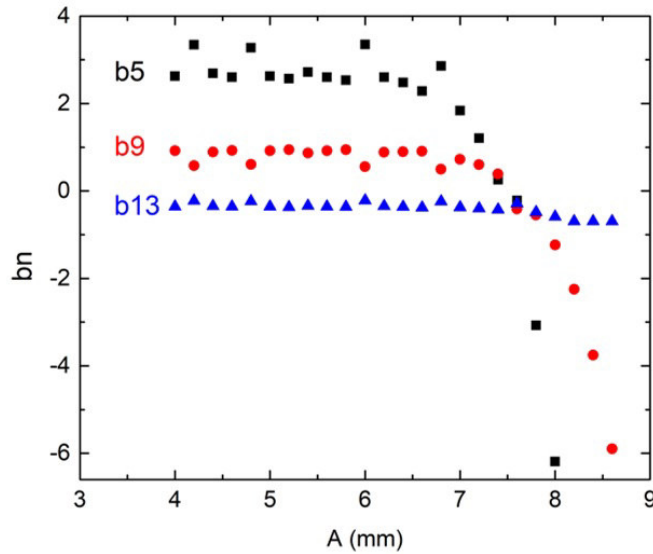


Figure 5.3: Multipole content as a function of the minimum pole distance $A$.

## 5.2.3 Mechanical design

If Lorentz forces are large, they could cause permanent damage or even affect magnet performance. The present magnetic requirements are small to produce large Lorentz forces. Although this statement is true, it must be validated. A finite element analysis study was performed to estimate the magnetic forced produced while energizing the quadrupole at full field. The model considers contributions from each turn at the pole, assuming no-ends effects, which in a first approximation is valid. In the 2D model, the wires are aligned parallel to beam direction. The estimated overall contribution along the total length of the quadrupole (0.1m) is 1.2 N toward the base of the pole. This amount of force gets redistributed along the iron yoke and does not represent a damage to the wires nor the mechanical structure of the quadrupole.
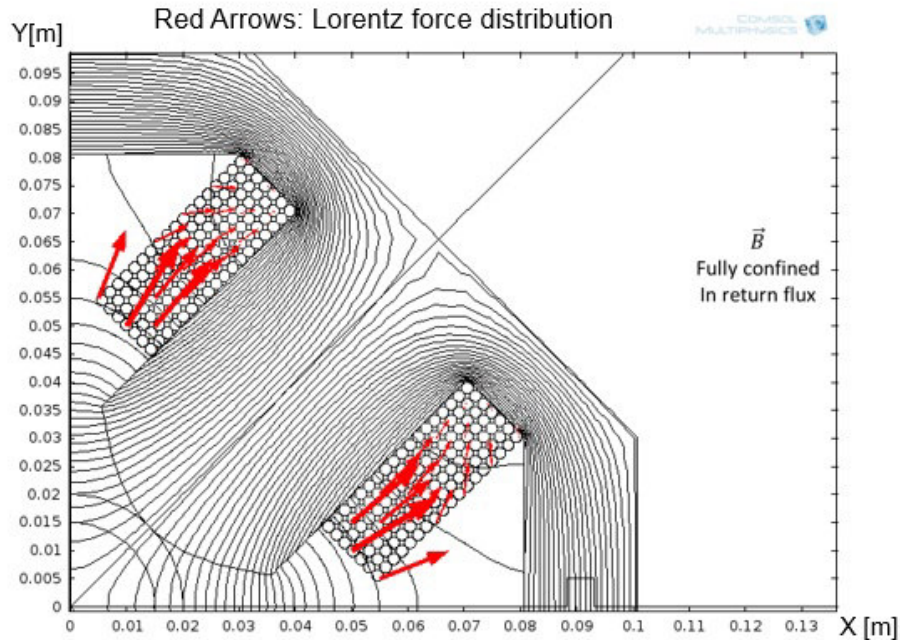
Figure 5.4: Lorentz force calculation for a 5 T/m normal conducting quadrupole.

**Materials for Iron Yoke and winding strategy**

Original field relaxation model assumed LHC type steel [5], which has an extended performance over the 2 T saturation limit. This is related to the carbon content in the alloy. For low field purposes, as in this case (0.09 T at pole tip), an evaluation of the multipole content must be study for candidate materials to determine how smaller magnetic permeabilities affect quadrupoles overall performance. A field relaxation study will be done varying different materials, i.e. changing the B-H curves at room temperature, see Figure 2. The study of the materials will consider the most common steel alloys that can be readily obtained in Mexico [6, 7]. The materials used were: Pure Iron, Pure Iron Annealed, Steel 1018, Steel 1020, Cast Iron, Cold drawn Low Carbon Steel. Hot Rolled Low Carbon Steel, MuMetal, Magnet Steel and LHC Steel. The goal of the study will be to preserve the field quality requirements (less than 1 unit for the allowed multipoles) at full field in both cases, the desired operation gradient and for future upgrades, in which the maximum recommended gradient will be 19 T/m. Analytic, thermal, mechanical and material studies confirm that, for the present field requirements, the current design satisfies the expectations. The next step is to develop a winding strategy for a model quadrupole. A barrel-winding procedure [8] will be used to wind the 18 layers (7 wires each) on each of the poles, starting inside-out of the base of the pole. Winding tables and special tooling is being developed for the first prototype.

## 5.2.4 Thermal design

Normal-conducting magnets use non-superconductor materials for windings, because of their characteristic non-vanishing resistivity ($\rho$=RA/L, resistivity $\Omega$m, $R$ electrical resistance $\Omega$, A crosssection are of conductor, and L the conductor length (m) the Joule-Lenz Law takes place, increasing the temperature of the system proportionally to the square of the current passing through the conductor. Considering standard copper wire AWG 12, the number of turns per pole, the length of the quadrupole and the resistivity of pure copper ($1.68x10^{-8}$ $\Omega$ m [4]), we estimated 31.8 W of dissipated power for a 4 T/m gradient. Bearing in mind thermal properties of pure iron as

the iron yoke material, and using heat equation, it is possible to estimate the increment in temperature produced by that amount of heat. The finite element analysis simulation estimates a temperature rise of 2 °C, assuming the quadrupole is in a 20 °C room. The gradient upgrade case was studied, the amount of current needed to produce a 19.27 T/m gradient is 19 $A$ per wire, which produces a 263 W power. For that case, the temperature increments 3.6 °C, which does not affect the actual air cooling method.
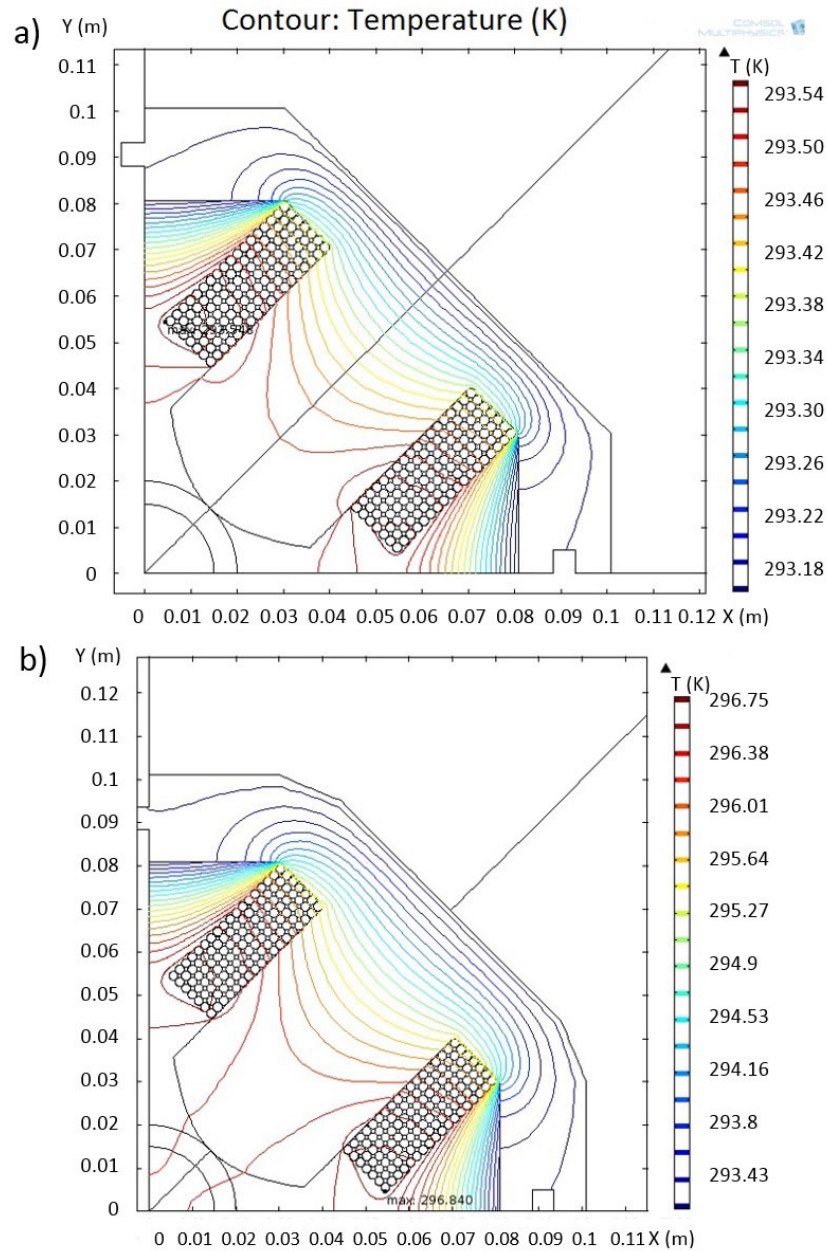


Figure 5.5: Thermal model. At left, a thermal model for estimating the increase in temperature of the quadrupole when the operational current is 6.6 A. At right, the model estimates the increase in temperature when the current at the copper wire triples its value.

## 5.2.5   Fringe field

Fringe field lines were computed on a 3D model at several magnetic flux density values, starting at 5 G (five times earths magnetic flux density field). Due to small field values and quadrupole geometry, the field at the body of the magnet is completely enclosed by the iron yoke. Naturally, the remaining component is at the ends of the magnet, in which there is no iron yoke. According to the International commission on non-ionizing radiation protection (ICNIRP, 2009) [9], prudent practice requires posting warnings at the 5 G line, and limit access to areas with more than 10 to 20 G to knowledgeable staff. The 5, 20, 50 and 100 G lines were computed, (see Figure 3). The estimated 5 G line is located at 0.14 m from the centre of the quadrupole while the 20 and 50 G lines are at 0.11 and 0.09 m respectively.



5 G @ .14 m Bo from center of quadrupole

20 G @ .11 m Bo from center of quadrupole

50 G @ .09 m Bo from center of quadrupole

100 G @ .08 m Bo from center of quadrupole
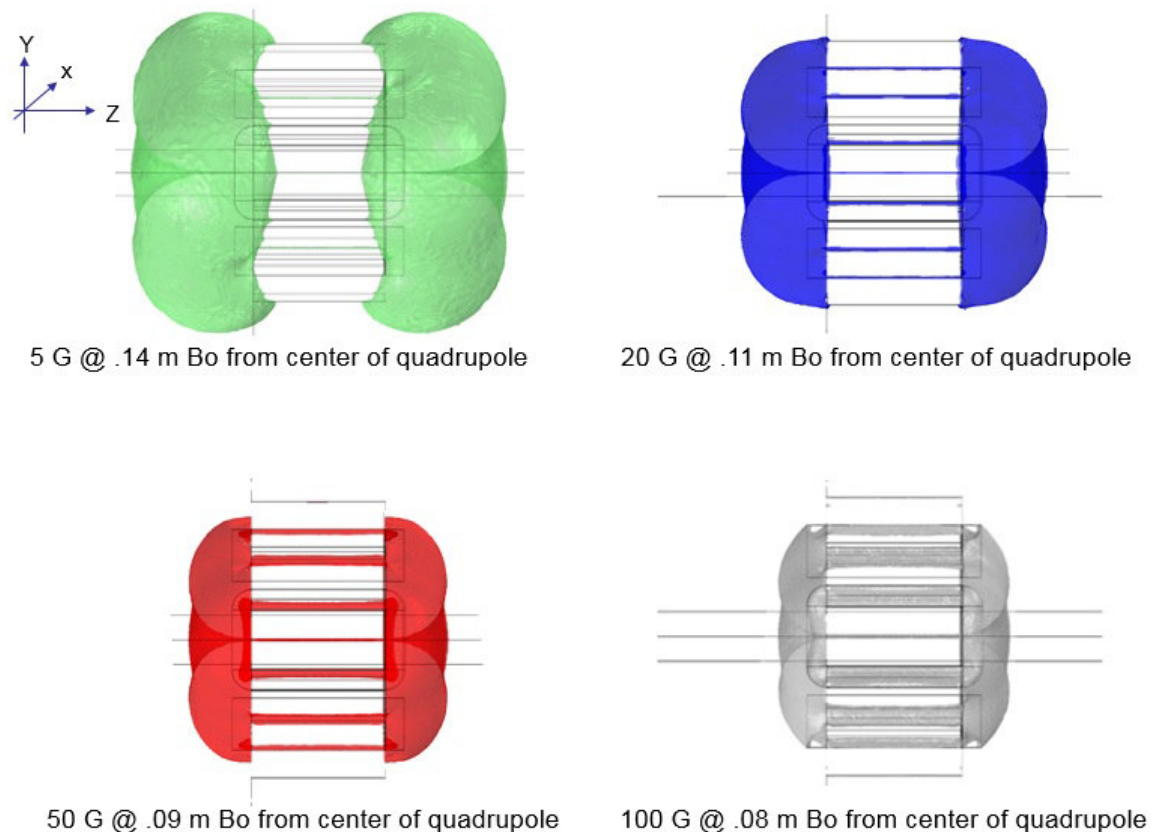
Figure 5.6: Determination of the fringe field 3D-surface for the case of 5, 20, 50 and 100 G.

## 5.2.6   Winding strategy

Winding operation is a complex procedure, tensions and alignment are the two major challenges. If the winding procedure is not accurate, the miss-positioning of the wires could compromise the field quality. Provision must be made to allow us a proper winding. Furthermore, the effects of the miss positions must be studied, and estimates must be computed to determine the allowed errors in the winding procedure. In the following, a design for a winding table is presented. In addition, a detailed study of the winding errors is given.

## winding table

As it has been described in chapter 3, the magnetic design set the upper boundary for optimum performance of the magnet. Reaching such boundary in real life, is the goal of the magnet designer and engineers. To satisfy this, the most important parameter is the proper location of the superconductors (or normal conducting) in their specific position, as stated in the magnet design. The winding procedure is challenging, and quality control must be done in a regular basis during the winding procedure.

For the normal conducting quadrupole, a winding table has been design, to aim a proper positioning of the wires on the poles. The winding table make use of a high precision, medium torque (60 Nm) stepper motor, see figure 5.7.
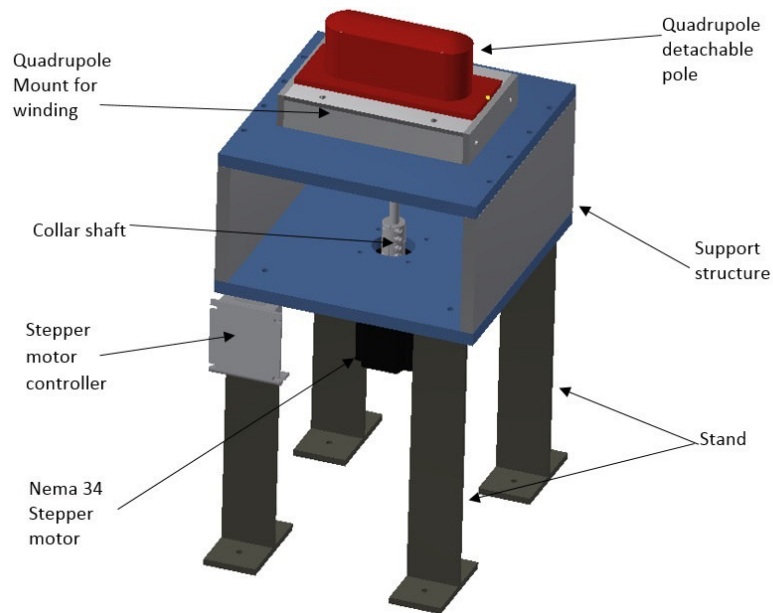


Figure 5.7: Design of a winding table for correct winding.

The stepper motor is control via a pedal that sends the signal to a controller, such that the winding operation can be control manually. Two main elements are necessary for winding operation:

- The first is the wire tensioner, that provides a costumed tension according to the wire physical parameters and recommended values i.e., for the AGW 12, the maximum pulling tension can be estimated based on the TANK formula [147], as described in equation 5.11. This formula make use of the cross-section area of the conductor $A$ (in units of circular mill), the number of conductors $N$ and a characteristic constant $K$ based on the mechanical properties of the material, for copper is 0.008:

$$T(lbs) = A(cmil)Nk \tag{5.11}$$

With this formula we can estimate a maximum pulling force of 231 N [147]. Using a proper tension helps to decrease irregularities during winding operation, and facilitated wire positioning. The tensiometer is located between the spool of wire and the winding table. Its composed of two symmetrical pieces containing a narrow leather channel especially designed to fit the diameter of the wire. The tension is adjusted by closing the two pieces by tighten the screws. To guarantee a reproducible tension, the torque applied to the screws is measured, as well as the tension on the wire.

- The second is the base on the winding table, to properly align and secure the pole without its based. This can be seen in figure 5.7.

This winding table has been designed, and its being built at Universidad de Guanajuato. It will be use for winding the quadrupoles required by the 6 MeV eLINAC of the Universidad de Guanajuato.

## Winding errors and field quality

As its mention in the previous section, a proper winding of the conductors is key for determining the proper performance of the conductor. In this section, a study of the foreseen errors in the winding is presented. These errors in the positioning are then inserted in the magnetic model to understand its impact on the field quality. Based on this, one can set boundaries for the highest allowed errors, in the multipole content.
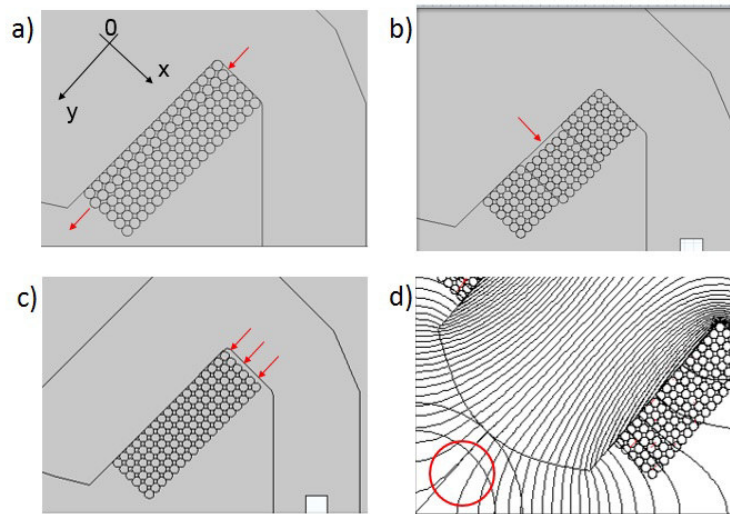


Figure 5.8: Design of a winding table for correct winding.

Figure 5.8 shows half a pole, and the positioning for the windings. Three types of possible miss-alignment are studied. In figure 5.8 a), the displacement of individual columns and its direct effect on the field quality is studied. Each column was shifted, one by one, with two different increments half wire diameter, and a quarter of the wire diameter. The greater effect happens when the closes column to the pole is shifted, as it can be seen on figure 5.9. In this study, it can be concluded that the maximum allowed displacement is half-wire diameter. The red line, labeled as "1", represents the displacement for column one.

On figure 5.8 b), a lateral displacement is studied. A block of 6 rows are displaced horizontally. The effect of this kind of displacements is less harmful than the vertical displacement. On figure 5.8 c), the case in which the whole coil is shifted vertically is studied.

In this case, due to the quadrupole symmetry, a displacement of half-wire diameter is less prejudicial than a quarter displacement, as far as field quality. As it can be seen in figure 5.10. The largest contribution comes from the multipole b5. A quarter displacement causes an increase of 2.5 units, while an displacement of half-diameter cases an increment of about one unit.

## Winding of a quarter-section: Winding errors

To practice the winding operation, a real scale 3D printed quarter-section of the quadrupole was used. At this time, the winding table was not ready, the winding procedure was done using a lathe. This process is a result
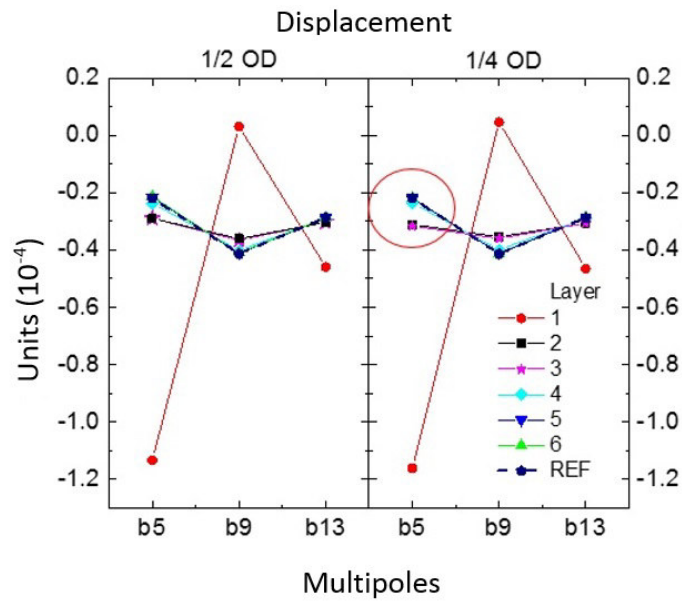
Figure 5.9: Experiment 1, coil displacements in the vertical direction, and its relationship with field quality.
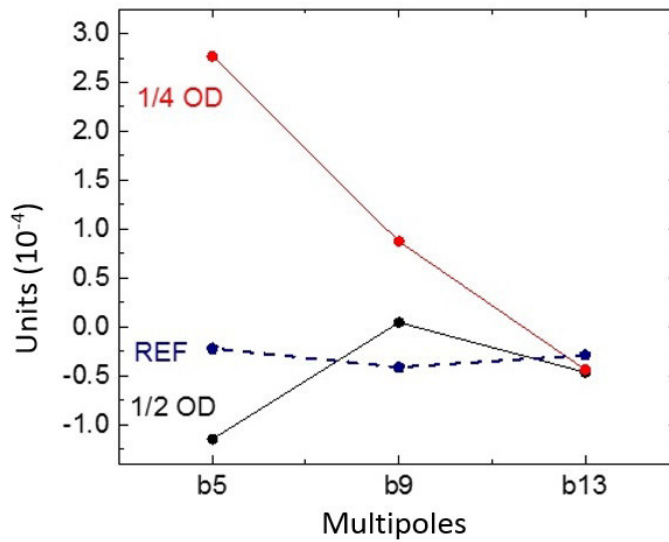


Figure 5.10: Experiment 3, all the winding is displacements in the vertical direction, and its relationship with field quality.

of a inter-institutional collaboration, called RIDTAP, for the development of magnet technology in Mexico. Details on the collaboration will be given at the end of the chapter. The 3D printing was done by Dr. Karla Cantun, at Universidad Autonoma de Yucatan. The winding operation was done by Dr. Max Rios, a professor at Universidad Tecnologica Metropolitana. The winding operation confirmed the need for a winding table. Figure 5.11, shows the quarter-section and the estimated multipoles produced by errors in the winding.
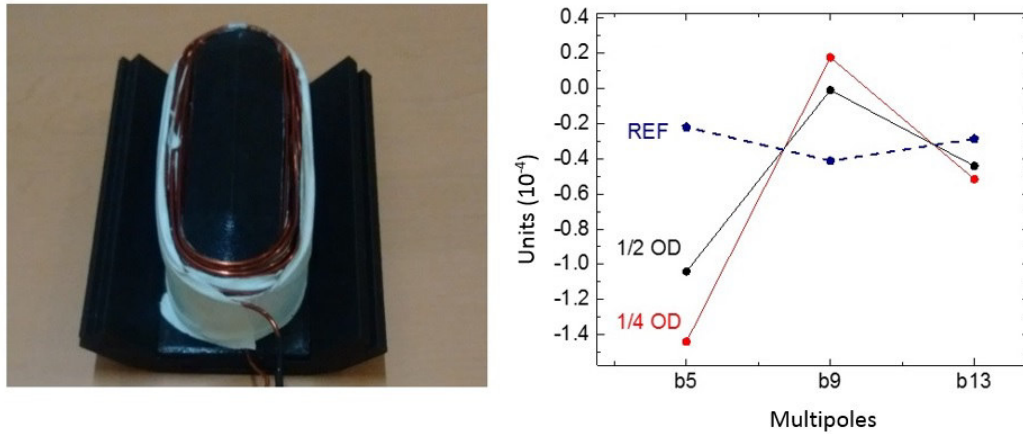


Figure 5.11: First muck-up winding on a 3D printed quarter-section of the normal conducting quadrupole.

# Chapter 6

# Conclusions and future work

## 6.1 Conclusions for CIC development for 3 T superferric dipoles

A novel approach to cable-in-conduit conductor has been developed for use in the arc dipoles of the future Electron-Ion Collider of the Thomas Jefferson National Laboratory. This technology proved to be a reliable and potential alternative for a wide range of applications requiring high current superconducting cables: MRI magnets, Power generators, D-shaped coils for nuclear reactors, Superconducting Magnetic Energy Storage machines, and high field accelerator magnets.

In this work, a complete study on the development of zero-current degradation CIC conductors is presented. The study includes a set of *analytical models* that provides the *selection rules* required to determine the feasibility, and the optimum parameters for tailoring a CIC for a given application. The model concludes that each application require defining the set of primal parameters $(R_w, R_t, R_b)$. An experimental development plan for producing short-lengths of CIC was undertaken, based on the parameters predicted by the analytical model. The experimental research helped us to understand the basics for developing CIC technology:

- It provided the manufacturing steps for producing reliable and reproducible segments of CIC conductor.

- It provided insight on the current degradation process. From this, a three step quality control was developed:

    - A method for physical inspection of superconducting filaments.

    - A method for determining the required compaction-factor, based on a specific application.

    - A method for Ic current-degradation measurement.

    - A method for inspection of integrity of the cryogenic vessel, based on small helium leaks.

    - A method for monitoring real-time breakage of superconducting filaments.

- It helped us to understand the spring-back effect, its cause and how to compensate it.

- It helped to determine the experimental ratio between the required drawing force and the optimum level of compaction.

- It helped to determine the relationship between the torque and the compaction factor on the CIC.

- The robustness of the CIC conductor served as a fast-feedback for developing costumed made robotic benders, and the program require to control their 3D bends.

The information obtained from the short-sample development was used to extrapolate the conditions for long-length production of CIC conductors. In this process, tooling and special technology was developed to incorporate in the manufacturing process, the possibility of varying a large number of values for the defining parameter of the CIC conductor. This allows us to produce and target many applications and design a CIC according to their needs.

A study on the development of exotic superconductors is presented, such the production in long-lengths of CIC conductors could be readily applied for non-NbTi conductors, which include $Nb_3Sn$, $MgB_2$ and Bi222. With this superconductors, high-field magnets up to 17 T could be produced, allowing more complex designs (as compared with Rutherford cable), while preserving full wire performance and internal cable registration. With this technology, the superconducting dipole can readily achieve excellent field homogeneity over a large aperture and dynamic range, as required by many accelerator machines.

Once the CIC technology was developed and understood, its was applied to produce a superferric dipole for the future Electron-Ion Collider for the JLAB. For this, magnetic, mechanical and thermal studies are presented, as well as a full description and characterization of the winding of a muck-up 1.2 m long dipole. The following, summarize the achievements obtained during the 3 T dipole designed and development for JLEIC. Three categories described:

- *Special tooling developed*: We have developed tooling and procedures that yield the required position tolerance and support for all turns of the winding needed to control random multipoles to ¡0.2 units. This first mock-up winding allowed us to test experimentally the capabilities and limitations of each of the benders, software, and fabrication tooling.

- *Quench studies*: A thermal study on the quench propagation shows that the CIC design provides thermal stability to the superconductor. Several thermal models were described and applied to predict the quench propagation velocities of the MPZ. The physical models shows that having a cryogenic flow of coolant thought the inner tube of the CIC, stabilizes the windings to tolerate significant beam loses. Quench propagation in the winding was simulated to take into consideration the internal strand geometry of the CIC, the distribution and flow provisions of liquid helium, and the heat transport from quench heater foils located at the ends of the each layer of winding. The quench velocity is 40 m/s, and a 4 m dipole is well-protected by end-located heaters with redundancy if one end heater fails. The relaxation time for micro-quench recovery is reduced by a factor of 4 by the direct contact of liquid helium in the CIC cable, which enhances stability for charging and discharging of the dipole. The above results establish that the CIC cable and dipole design provides the performance required for JLEIC requirements and establishes for the first time a method for precision winding of CIC conductor that is consistent with the field quality requirement for a large-dynamic-range collider.

- *splice joint development*: The CIC technology requires the development of a low-resistance demountable splice-joint system that allows testing, operate, and power magnets prior to and during operation in a its final installation. In particular, an easy-to-operate design of a splice joint for the CIC windings of the NbTi superferric magnets JLEIC was developed. Electrical simulation and thermal models predicts that the joint should support 13 kA current flow in the CIC splice with a resistance ¡ $2n\Omega$.

The development of both, the CIC technology and its corresponding splice joint, constitute a robust combination, suitable for a large number of applications. For example, the next leap in magnet design requires

exceptionally high magnetic fields ($\sim$ 17 T) to be produced in relatively large apertures; this represents an unrepresented challenge for the magnet design community, in particular, if the magnets are designed with Rutherford cable.

The robustness and high thermal stability of the CIC technology make it suitable for producing high-field magnets, or fast ramping magnets, as the dipoles and quadrupoles required at the interaction region of the JLEIC. Both applications required the use of wind-and-react superconductors Nb3Sn, MgB2, and Bi2212. These are reaction-bake superconductors, i.e., a special heat treatment is required to form the crystal structure which exhibits a superconducting phase when is taken to cryogenic temperatures. A drawback of this superconductors is that once the heat-treatment takes place, they become brittle making impossible formation of complex bends.

Adapting the CIC technology to embrace the reaction bake superconductors, represents a challenge. Two inherent problem arises, the CIC components must survive the heat treatment and maintain their mechanical properties. Typical heat treatment temperatures range from 650 to 820 C, an inert or oxygen-rich atmosphere depending on the superconductor. To extend the CIC technology for reaction bake superconductors, a full research plan was conducted, and the results are summarized in the following points:

1. *CIC for small bend radius, using $Nb_3Sn$ and $Mgb_2$ superconductors*: To evaluate the performance of reaction-bake CIC at small bend radius, as required by the dipoles and quadrupoles of the interaction region of the JLEIC, several samples were tested. The study revealed that 90% of the samples experienced wires breakage, or bottle-necking. Furthermore, the outer tube of the CIC tore in most of the test. The study concludes that the bending process induces excessive strains on the CIC components. To suppress the excessive strain, a thermal study on the CIC components was performed.

2. *Stress-relieve thermal process on CIC components*: to reduce the stress on the CuNi outer tube, and the Stainless-Steel inner tube, several heat treatments were explored:

   (a) Removing the peak stress

   (b) Stress Reliving between forming operations.

   In the first, the samples will be heat treated at 480 C in an air atmosphere, and then slow cooled; For the second, the sample will be stress relieved at 900 C, in an air atmosphere, and then slowly cooled. The soaking times for both procedures was determined based on the thickness of the tubes. CIC conductors were produce with various samples changing the soaking times and heat treatment temperatures. The samples then bent in the small radius and dissected. The study concludes that applying the first heat treatment (removing the peak stress) is not enough to soften the inner tube; therefore the strands are not able to rearrange and to indent deep enough into the inner tube, which leads to broken strands. On the other hand, if the second heat treatment is applied ( stress relieved between forming operations at a temperature of 900 C for 15 min), the inner tubes softens enough to allow the strands to indent and slightly deform the inner tube, avoiding the wires breakage and the deformation of the CIC components.

3. *Heat treatment characterization*: To understand and characterize the heat treatment process on the Stainless-steel inner tube, mechanical characterization test were perform on Stainless-steel samples. The test makes use of a nanoindenter; A device that performs compression load testing at the microscopic scale, and provides the elastoplastic characteristic curve for the material. The test concludes that the heat treatment must produce a reduction of 2 GPa is the hardness of the Stainless Steel inner tube, to produce optimum wind-and-react CIC conductors.

4. *Current degradation measurements on $Nb_3Sn$ and $Mgb_2$ CIC conductors*: To test the integrity of wind-and-react CIC. Several wires were extracted from CIC samples bent at the small bending radius. The

experiment measures the current degradation of virgin wires and it compares with the measurements of extracted wires. Notice that there is a substantial shift in the current, revealing some degree of degradation. The $Nb_3Sn$ measurements show less than 1% current degradation. The measurements for the case of $Mgb_2$ are not conclusive, the extracted strands were very small, and end-effects affected the measurement adding an error of 15%, with a current degradation of 10%. The test will be repeated with proper conditions. Based on the results extracted from the $Nb_3Sn$, we predict zero-current degradation.

The latter constitutes a major improvement on the CIC technology, open a real possibility for developing high-field dipoles.

To conclude, the basics for developing a 2 layer CIC conductor are presented. The CIC dipole was first developed for 3 T operation to operate JLEIC with 100 GeV/u ions. A closely similar 6 T CIC dipole, using 2-layer CIC conductor, has recently been explored by the JLAB committee. With this in mind, a preliminary development of the required cable is presented.

## 6.1.1  Future Work

So far, we have developed a reliable technology for producing long lengths of CIC conductor. Up to December 2018, a first 140+ meters of NbTi CIC conductor was produced. Furthermore, an extra 10 m section of NbTi CIC was manufactured and used for winding three layers on the G-11 mandrel. The lack of financial support from the Department of Energy of the U.S. has delayed the full winding. Nevertheless, we will carry-on. Starting January 2018, we will start the full winding process for the 1.2m long 3 T dipole. The winding will be done over the new G-11 mandrel, which incorporates the knot correction and a tighter tolerance. The new mandrel was manufactures as a single piece, contrary to the old mandrel, in which 6 sections were put together and epoxy impregnated[a]. A quality control measurements shows a +0.001" errors along the lenght of the dipole. The winding procedure its foreseen to be completed by late April 2018. Once the winding has been completed, a quality control metrology will be performed.

### Lamination

After competition of quality control, a shimming will be applied on specific coils if required. The iron-yoke will be manufacture using stamping procedure on low-carbon iron sheets of thickness 0.125". The stamping procedure is both, reliable and cost effective. Several stamping techniques offer cutting apertures in a sheet metal strip without producing stress-induced-distortion of the apertures after cut-off of the strip" [148, 149]. This is key element, for controlling the multipoles. The choice of solid or laminated cores has historically been associated with whether the magnetic field is time varying or steady state. Presently, many steady state magnets are assembled with laminated cores. The lamination technique is a natural path for machining long iron yokes, it would be almost impossible to machine a 1.2 m long solid piece of iron, and maintain the tight tolerances, specially at the apertures. Half of the laminations will be position and aligned such that it will provide a base, for sitting the magnet. The other half of the laminations will be inserted on-top. Then two pieces of rolled metal-sheath will enclose the laminations. The assembly will be preloaded, and both metal-sheaths will be welded providing compression load to the magnet. The final step of the dipole development, is to test its performance at cryogenic temperatures. In this process the magnet is *trained*. A process in which the magnet is cooled to the operational temperature and stepping current is applied. In this process, the magnet usually quenches from 6 to

---

[a]A small error in the alignment of the 6 pieces caused a bow on the body of the dipole as described in the quality control section, on chapter 3.

10 times, in every quench, a higher field is achieved until reaching stabilization i.e., until the operational current is maintained without quenching the magnet.

## 6.2 Conclusions: Magnet design for Mexican Projects

An optimized geometry and design for low gradient, normal conducting quadrupoles has been presented. The design is general, and its made to satisfy the magnet requirements for the two Mexican project for developing an electron LINAC: The 10-MeV LINAC of the Mexican Particle Accelerator Community, and the 6-MeV eLINAC of the Universidad de Guanajuato. With this in mind, a basic analytic model, based on general requirements and limitations, showed that a 637 A current must be applied to each pole to produce a 4.5 T/m gradient in a 0.02 m bore radius, as specified for both projects. The quadrupole is designed in such a way that allows future energy updates, ranging from 4 up to 19 T/m while preserving gradient uniformity. To improve field quality and keep gradient uniformity below 1%, the end of the hyperbolic poles was strategically shimmed. The mechanical model showed that a net force of 1.2 N is directed towards the base of each pole. The basic thermal model revealed that when a current at 6.6 A per wire is applied, the power dissipated barely increases the copper temperature by about a 2°C. The 19 A scenario was modelled, producing a temperature increment of 3.6 °C over the 6.6 A model. In both cases, the quadrupoles can be cooled using natural air convection. The iron yoke fully encloses the magnetic field at the body of the quadrupole, adding no contribution to the fringe field. At the end of the quadrupole, there is a small region in which the winding around the pole is not covered by the iron yoke. This region contributes to the fringe field that extends out of the quadrupole. According to the International Commission on Non-Ionizing Radiation (ICNIRP, 2009), prudent practice requires posting warnings at the 5 G line. The magnetic model computes the 5, 10 and 50 G lines, being the first at 0.14 m from the centre of the quadrupole. Special tooling is being designed and it will be developed shortly Thermal, mechanical and electromagnetic studies have shown that the quadrupole fulfill the requirements for the quadrupoles of eLINAC, low-cost production and air-cooled. In addition, thanks to the parametrized design only small modifications will be needed for the quadrupoles to be employed in the 60-MeV and 100-MeV beam lines. An optimization procedure, in terms of field quality, production, and operation cost, was applied to encourage the in-house development of the normal conducting quadrupoles in Mexico. The procedure merges a parametrization model with well known cost optimization procedure, and extended it to normal conducting quadrupoles. A 5 T/m quadrupole, was initially proposed, nevertheless, adjustments on the field requirements shifted the field gradient to a new value of 3.2 T/m. The cost optimization expressed in normalized units, considered several steels for iron yoke, being A-1010 the final candidate in terms of availability and low cost. For a 3.2 T/m field gradient, the total estimated cost is 1.66 the cost of the power supply at a current density of 2.2 $A/mm^2$.

### 6.2.1 Future work

By mid-march 2019, the winding table will be completely assembled and operational. The laminations for the low-gradient normal conducting quadruple, will be manufacture using laser-cut, at a local company at Guadalajara. An alignment base will be built for welding the laminations while preserving the tolerances. Once the poles are completed, a winding process will begin. An optical metrology will be used to record the position of the wires, layer by layer. A multipole analysis will use this data to understand the impact on the errors on the winding. Once the multipoles are controlled, the poles will be inserted and aligned. A secondary metrology process will be applied to determine the errors in the alignment of the poles. A thermal characterization will be done to compare the model vs experiment. Finally, an experimental determination of the multipole and the fringe fields will be done to validate the quality of the winding.

# Appendix A

# Appendix

## A.1 Physical properties of G-11 epoxy phenolic resin

| Property | Units | G-11 Glass/Epoxy Phenolic |
|---|---|---|
| **Physical** | | |
| Specific Gravity | - | 1.80 |
| Moisture Absorption (.062") | % | .20 |
| **Mechanical** | | |
| Rockwell Hardness (.062") | M Scale | 112 |
| Flexural Strength (.062") LW CW | psi psi | 80,000 70,000 |
| Flexural Modulus (.062") LW CW | psi psi | 3,000,000 2,700,000 |
| Tensile Strength (.125") LW CW | psi psi | 43,000 37,000 |
| Izod Impact Strength E-48/50 (.500") LW CW | ft-lb/in ft-lb/in | 12.0 9.0 |
| Compressive Strength flatwise (.500") | psi | 63,000 |
| Bond Strength (.500") | lbs | 2,200 |
| Shear Strength (perpendicular) (.062") | psi | 22,000 |
| **Thermal** | | |
| Maximum Operating Temperature | °F | 374 |
| Coefficient of Thermal Expansion (.062") X-axis Y-axis | in/in/°F in/in/°F | $7.2 \times 10^{-6}$ $8.3 \times 10^{-6}$ |
| Flammability Rating - U. L. 94 | | HB |
| **Electrical** | | |
| Permittivity (.062") Condition D-24/23 | - | 4.8 |
| Dissipation Factor (.062") Condition D-24/23 | - | .020 |
| Breakdown Voltage Condition - A (.062") D-48/50 | V | 60,000 55,000 |
| Electric Strength Condition - A (.062") D-48/50 | V/mil | 900 800 |
| Arc Resistance (.125") D-495 | sec | 120 |
| Comparative Tracking Index (.125") D3638 | - | 150 |
| Tg | °F | 365 |

Figure A.1: Physical properties of G-11 phenolic resin. Source: Pastics International [150]

## A.2   Physical properties of Kapton polyimide film

**Physical Properties of Kapton® MTB Polyimide Film vs. HN**

| Property | 300MTB | 500MTB | 500HN | Test Method |
|---|---|---|---|---|
| Thickness | 3-mil | 5-mil | 5-mil | — |
| Color | Black | Black | Amber | — |
| Thermal Conductivity, W/m·K | 0.45 | 0.45 | 0.15 | ASTM F-433-87 |
| Modulus, kpsi | 470 | 430 | 375 | ASTM D-882-91 |
| Dielectric Strength, AC V/mil (Min.) | 1,800 | 1,600 | 3,200 | ASTM D-149-94 |
| Approximate Yield, ft²/lb | 36 | 22 | 27 | — |
| Elongation, % MD and TD | | | | ASTM D-882-91 |
|   Maximum, % | 100 | 100 | 120 | |
|   Minimum, % | 50 | 50 | 60 | |
| Shrinkage, % MD and TD, Max. at 400°C (752°F) | 2.0 | 2.0 | 2.0 | IPC-TM-650 |
| Moisture Absorption, % | 3.0 | 3.0 | 3.0 | ASTM D-570-92 |
| Volume Resistivity, ohm·cm at 200°C (392°F) (Max.) | $10^{12}$ | $10^{12}$ | $10^{12}$ | ASTM D-257-93 |
| Dielectric Constant at 1 kHz (Max.) | 5.2 | 5.3 | 3.8 | ASTM D-150-94 |
| Dissipation Factor at 1 kHz (Max.) | 0.0025 | 0.0032 | 0.0035 | ASTM D-150-94 |
| Tensile Strength, psi at 23°C (73°F), MD and TD | | | | ASTM D-882-91 |
|   Maximum, psi | 25,000 | 25,000 | 39,000 | |
|   Minimum, psi | 15,000 | 15,000 | 24,000 | |
| MIT Fold Endurance, cycles | 27,000 | 5,000 | 1,500 | ASTM D-2176-89 |
| Cut-Through Resistance, lb | 85 | 105 | 95 | DuPont #PT-0025 |
| Initial Tear Strength, MD and TD, lb | 6 | 10 | 12 | ASTM D-1004-90 |

Figure A.2: Physical properties of Kapton polyimide film. Source: Dupont High performance materials [151]

## A.3 Thermal conductivity of materials at cryogenic temperatures



Figure A.3: Thermal conductivity at low temperatures for materials commonly used in superconducting magnets. Source: Helium Cryogenics, Van Sciver S.W. [152]

## A.4 Electrical resistance of materials at cryogenic temperatures
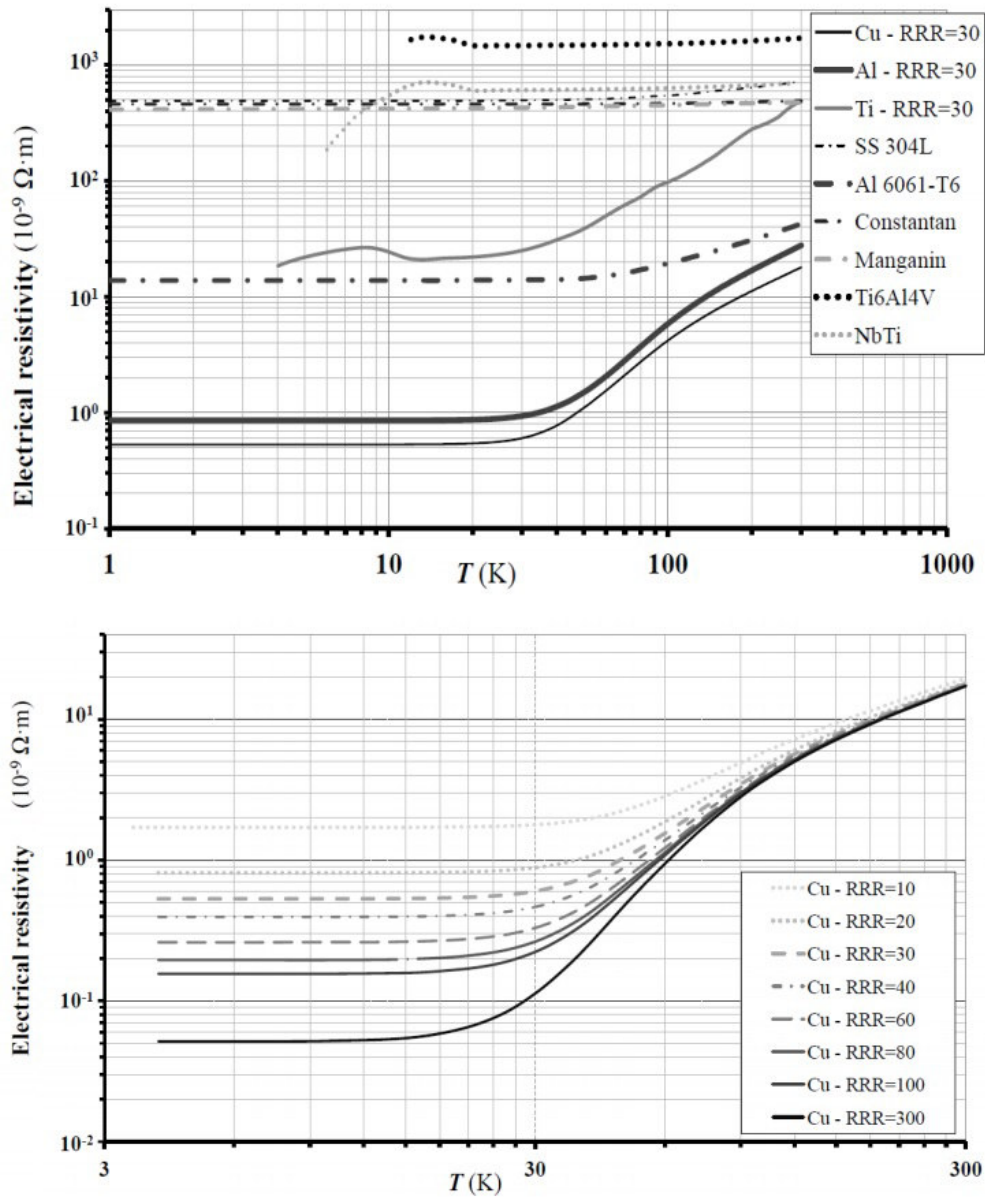


Figure A.4: Electrical resistance for some materials at cryogenic temperatures. Source: P. Duthil [153].

## A.5 Specific heat of some materials at cryogenic temperatures
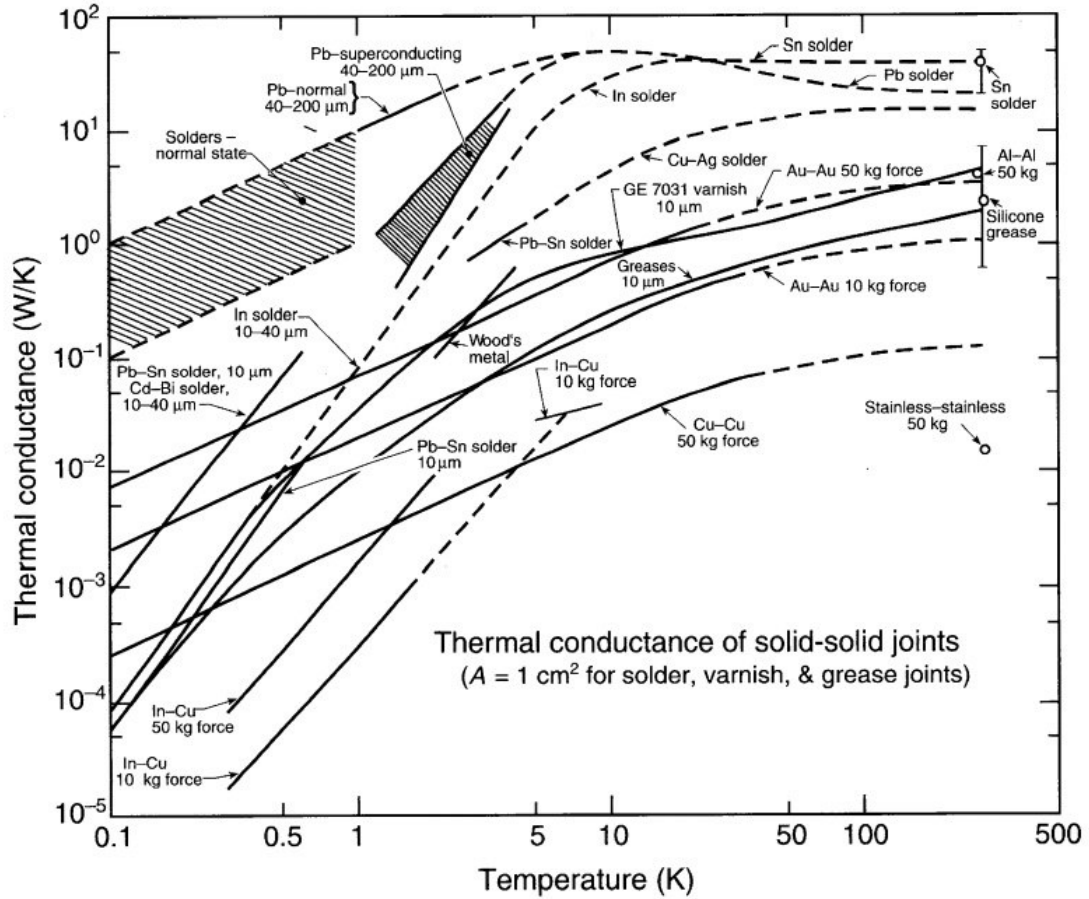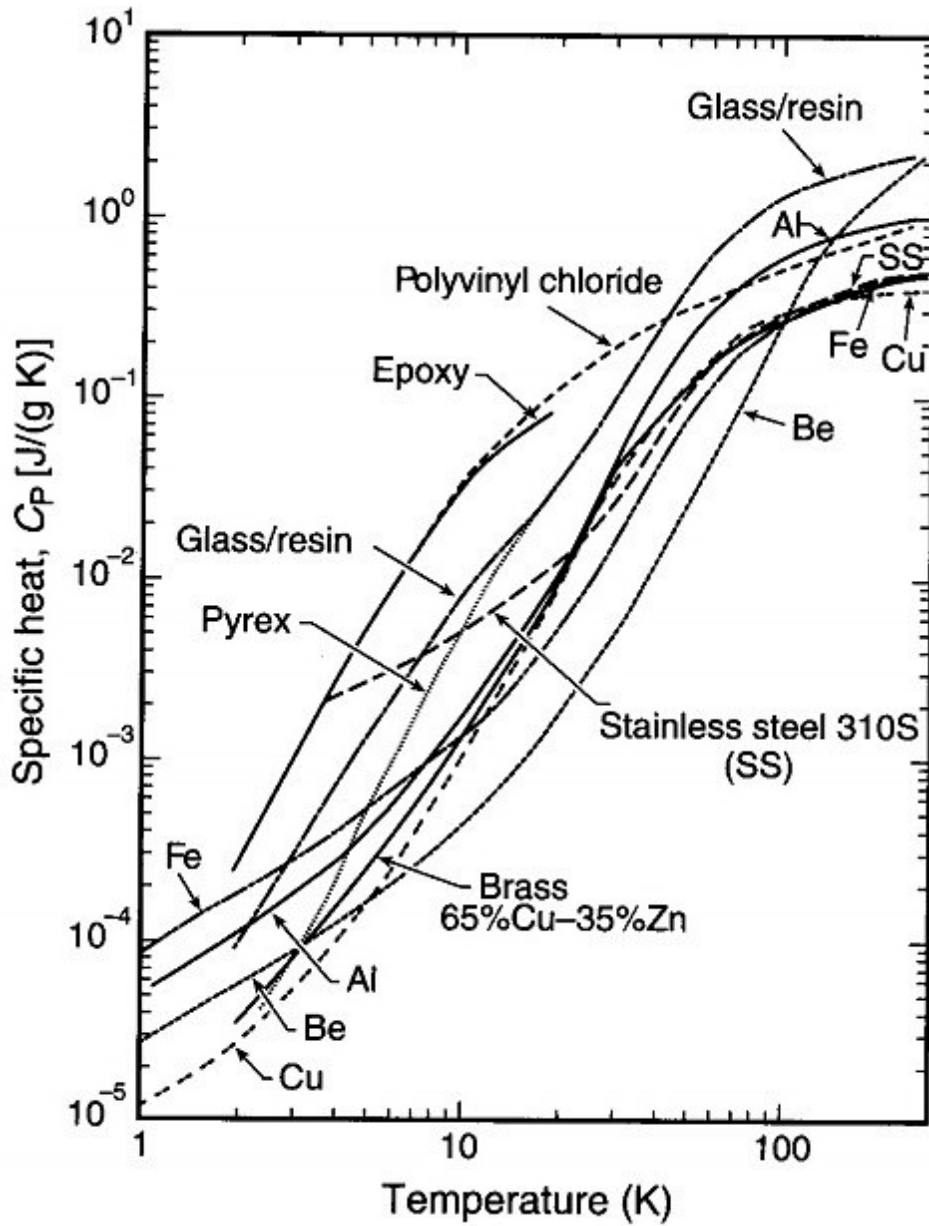


Figure A.5: Thermal conductivity at low temperatures for materials commonly used in superconducting magnets. Source: USPAS lectures on magnet technology [154].

## A.6 Thermal expansion of materials commonly used in cryogenics
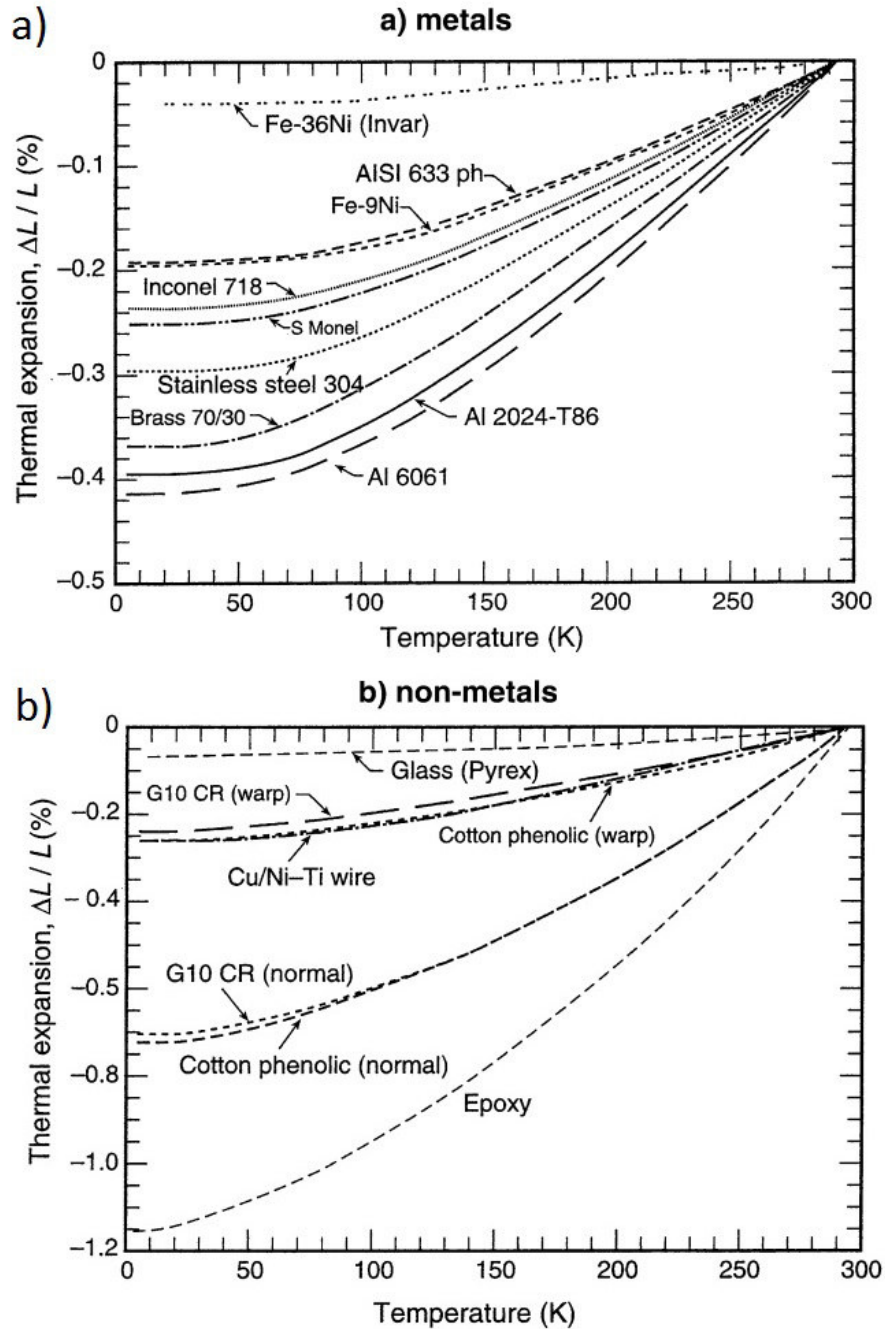


Figure A.6: Total thermal expansion/contraction for materials commonly used in cryogenics: (a) metals; (b) non-metals. Source: Van Sciver [152]

# Bibliography

[1] Frank Greenaway. *John Dalton and the atom*. London: Heinemann, 1966.

[2] Niels Bohr. I. on the constitution of atoms and molecules. *The London, Edinburgh, and Dublin Philosophical Magazine and Journal of Science*, 26(151):1–25, 1913.

[3] Julius Kuti and Victor F Weisskopf. Inelastic lepton-nucleon scattering and lepton pair production in the relativistic quark-parton model. *Physical Review D*, 4(11):3418, 1971.

[4] Walter Greiner, Stefan Schramm, and Eckart Stein. *Quantum chromodynamics*. Springer Science & Business Media, 2007.

[5] Gabriele Veneziano. Is there a qcd spin crisis? *Modern Physics Letters A*, 4(17):1605–1614, 1989.

[6] Mauro Anselmino, BL Ioffe, and E Leader. On possible resolutions of the spin crisis in the parton model. *Soviet Journal of Nuclear Physics (English Translation)*, 49(1):136–141, 1989.

[7] John Mulvey. The new frontier of particle physics. *Nature*, 278(5703):403, 1979.

[8] Rolf Ent, Thomas Ullrich, and Raju Venugopalan. The glue that binds us. *Scientific American*, 312(5):42–49, 2015.

[9] Elke-Caroline Aschenauer, Ian Balitsky, Leslie Bland, Stanley J Brodsky, Matthias Burkardt, Volker Burkert, Jian-Ping Chen, Abhay Deshpande, Markus Diehl, Leonard Gamberg, et al. Pre-town meeting on spin physics at an electron-ion collider. *The European Physical Journal A*, 53(4):71, 2017.

[10] 2007 long range plan: The frontiers of nuclear science. *URL:http://science.energy.gov/ /media/np/nsac/pdf/docs/NuclearScienceHighRes.pdf*, 2007.

[11] Roy Rubinstein. Two decades of mexican particle physics at fermilab. In *AIP Conference Proceedings*, volume 670, pages 352–353. AIP, 2003.

[12] Leah Hesla. 30 years of inter-american collaboration. https://www.symmetrymagazine.org/article/march-2014/30-years-of-inter-american-collaboration, 2014.

[13] JG Contreras and M Napsuciale. Creation of a group on particle accelerator science and technology in mexico. *arXiv preprint arXiv:1608.07456*, 2016.

[14] A. Accardi et al. Electron ion collider: The next qcd frontier - understanding the glue that binds us all. *arXiv:1212.1701*, 2012.

[15] V. Ptitsyn T. Roser O. Bruning, E. Ent. Electron-ion collider projects and their accelerator r&d needs. *Community Planing Study: Snowmass*, pages 1–6, 2013.

[16] S Abeyratne, D Barber, A Bogacz, P Brindza, Y Cai, A Camsonne, A Castilla, P Chevtsov, E Daly, YS Derbenev, et al. Meic design summary. *arXiv preprint arXiv:1504.07961*, 2015.

[17] Fanglei Lin, Pawel Nadel-Turonski, Peter Ostroumov, Robert Rimmer, David Douglas, Sumana Abeyratne, Yunhai Cai, Bela Erdelyi, Todd Satogata, Jiquan Guo, et al. Progress on the design of the polarized medium-energy electron ion collider at jlab. 2015.

[18] S. Abeyratne et al. Meic design summary. *https://arxiv.org/ftp/arxiv/papers/1504/1504.07961.pdf*.

[19] David Neuffer. A novel method for correcting the ssc multipole problem. Technical report, 1988.

[20] J Breitschopf, T Elliot, R Garrison, J Gerity, J Kellams, P McIntyre, A Sattarov, and D Chavez Univesidad de Guanajuato. Superferric ar booster of jleic.

[21] Jeffrey Breitschopf. Construction of next generation dipole magnets. *Bulletin of the American Physical Society*, 60, 2015.

[22] John B Pendry, David Schurig, and David R Smith. Controlling electromagnetic fields. *science*, 312(5781):1780–1782, 2006.

[23] Karl Hubert Mess and Peter Schmüser. Superconducting accelerator magnets. 1989.

[24] Jack T Tanabe. *Iron dominated electromagnets: design, fabrication, assembly and measurements*. World Scientific Publishing Company, 2005.

[25] G. E. Fischer. Iron dominated magnets. 1987.

[26] R. Gupta. Improving the design and analysis of superconducting magnets for particle accelerators. 1996.

[27] Animesh K Jain. Basic theory of magnets. 1998.

[28] Nathaniel J Pogue, Daniel Chavez, Joshua Kellams, Peter M McIntyre, and Akhdiyor I Sattarov. Strong focusing cyclotron and its applications. *IEEE Transactions on Applied Superconductivity*, 25(3):1–4, 2015.

[29] Jeffrey Breitschopf, Tim Elliot, Ray Garrison, James Gerity, Joshua Kellams, Peter McIntyre, A Sattarov, and Daniel Chavez. Sperferric arc dipoles for the ion ring and booster of of jleic. *Bulletin of the American Physical Society*, 61, 2016.

[30] Horst Rogalla and Peter H Kes. *100 years of superconductivity*. Taylor & Francis, 2011.

[31] H Kamerlingh Onnes. Further experiments with liquid helium g. on the electrical resistance of pure metals etc. vi. on the sudden change in the rate at which the resistance of mercury disappears. *Koninklijke Nederlandse Akademie van Weteschappen Proceedings Series B Physical Sciences*, 14:1911–1912, 1911.

[32] Martin N Wilson. Superconducting magnets. 1983.

[33] AK Geim, SV Dubonos, JJ Palacios, IV Grigorieva, M Henini, and JJ Schermer. Fine structure in magnetization of individual fluxoid states. *Physical review letters*, 85(7):1528, 2000.

[34] H Suhl, BT Matthias, and LR Walker. Bardeen-cooper-schrieffer theory of superconductivity in the case of overlapping bands. *Physical Review Letters*, 3(12):552, 1959.

[35] Manfred Sigrist and Kazuo Ueda. Phenomenological theory of unconventional superconductivity. *Reviews of Modern physics*, 63(2):239, 1991.

[36] John Robert Schrieffer and James S Brooks. *Handbook of high-temperature superconductivity: theory and experiment*. Springer New York, 2007.

[37] Joe Khachan and Stephen Bosi. The discovery of superconductors.

[38] John Bardeen. Theory of the meissner effect in superconductors. *Physical Review*, 97(6):1724, 1955.

[39] Chorng-Haur Sow, Ken Harada, Akira Tonomura, George Crabtree, and David G Grier. Measurement of the vortex pair interaction potential in a type-ii superconductor. *Physical Review Letters*, 80(12):2693, 1998.

[40] Hideo Hosono, Keiichi Tanabe, Eiji Takayama-Muromachi, Hiroshi Kageyama, Shoji Yamanaka, Hiroaki Kumakura, Minoru Nohara, Hidenori Hiramatsu, and Satoru Fujitsu. Exploration of new superconductors and functional materials, and fabrication of superconducting tapes and wires of iron pnictides. *Science and Technology of Advanced Materials*, 16(3):033503, 2015.

[41] KH Jürgen Buschow. *Concise encyclopedia of magnetic and superconducting materials*. Elsevier, 2005.

[42] David A Cardwell and David S Ginley. *Handbook of superconducting materials*. CRC Press, 2002.

[43] E Savitskii. *Superconducting materials*. Springer Science & Business Media, 2012.

[44] Critical current densities for practical superconductors, new data, april 2018. https://nationalmaglab.org/magnet-development/applied-superconductivity-center/plots. Accessed: 2018-11-12.

[45] H Kamerlingh Onnes. H. kamerlingh onnes, proc. k. ned. akad. wet. 16, 987 (1914). In *Proc. K. Ned. Akad. Wet.*, volume 16, page 987, 1914.

[46] Peter J Lee. *Engineering superconductivity*. Wiley-IEEE Press, 2001.

[47] J Jiang, WL Starch, M Hannion, F Kametani, UP Trociewitz, EE Hellstrom, and DC Larbalestier. Doubled critical current density in bi-2212 round wires by reduction of the residual bubble density. *Superconductor science and technology*, 24(8):082001, 2011.

[48] Hanping Miao, Kenneth R Marken, Maarten Meinesz, Boleslaw Czabaj, and Seung Hong. Development of round multifilament bi-2212/ag wires for high field magnet applications. *IEEE Transactions on applied superconductivity*, 15(2):2554–2557, 2005.

[49] A Matsumoto, H Kitaguchi, H Kumakura, J Nishioka, and T Hasegawa. Improvement of the microstructure and critical current densities of bi-2212 round wires with a precisely controlled heat treatment. *Superconductor Science and Technology*, 17(8):989, 2004.

[50] Philip W Anderson and YB Kim. Hard superconductivity: theory of the motion of abrikosov flux lines. *Reviews of Modern Physics*, 36(1):39, 1964.

[51] HF Hess, RB Robinson, RC Dynes, JM Valles Jr, and JV Waszczak. Scanning-tunneling-microscope observation of the abrikosov flux lattice and the density of states near and inside a fluxoid. *Physical review letters*, 62(2):214, 1989.

[52] M Cristina Marchetti and David R Nelson. Dislocation loops and bond-orientational order in the abrikosov flux-line lattice. *Physical Review B*, 41(4):1910, 1990.

[53] Kaname Matsumoto and Paolo Mele. Artificial pinning center technology to enhance vortex pinning in ybco coated conductors. *Superconductor Science and Technology*, 23(1):014001, 2009.

[54] Kaname Matsumoto, Tomoya Horide, Kozo Osamura, Masashi Mukaida, Yutaka Yoshida, Ataru Ichinose, and Shigeru Horii. Enhancement of critical current density of ybco films by introduction of artificial pinning centers due to the distributed nano-scaled y2o3 islands on substrates. *Physica C: Superconductivity*, 412:1267–1271, 2004.

[55] Tiziana Spina, Amalia Ballarino, Luca Bottura, Christian Scheuerlein, and Rene Flukiger. Artificial pinning in nb3sn wires. *IEEE Transactions on Applied Superconductivity*, 27(4), 2017.

[56] Gianni Blatter, Mikhail V Feigel'man, Vadim B Geshkenbein, Anatoly I Larkin, and Valerii M Vinokur. Vortices in high-temperature superconductors. *Reviews of Modern Physics*, 66(4):1125, 1994.

[57] Paul S Swartz and Carl H Rosner. Characteristics and a new application of high-field superconductors. *Journal of Applied Physics*, 33(7):2292–2300, 1962.

[58] F Ruggiero, O Bruning, R Ostojic, L Rossi, W Scandale, and T Taylor. Performance limits and ir design of a possible lhc luminosity upgrade based on nbti sc magnet technology. In *Proceedings of EPAC*, page 608, 2004.

[59] N Andreev, E Barzi, E Borissov, L Elementi, VS Kashikhin, V Lombardo, A Rusy, D Turrioni, R Yamada, and AV Zlobin. Development of rutherford-type cables for high field accelerator magnets at fermilab. *IEEE Transactions on Applied Superconductivity*, 17(2):1027–1030, 2007.

[60] P Bauer, G Ambrosio, N Andreev, E Barzi, D Dietderich, K Ewald, M Fratini, AK Ghosh, HC Higley, SW Kim, et al. Fabrication and testing of rutherford-type cables for react and wind accelerator magnets. *IEEE transactions on applied superconductivity*, 11(1):2457–2460, 2001.

[61] N Andreev, E Barzi, E Borissov, L Elementi, VS Kashikhin, V Lombardo, A Rusy, D Turrioni, R Yamada, and AV Zlobin. Development of rutherford-type cables for high field accelerator magnets at fermilab. *IEEE Transactions on Applied Superconductivity*, 17(2):1027–1030, 2007.

[62] Alex Chao, Herbert O Moser, and Zhentang Zhao. *Accelerator Physics, Technology, and Applications: Selected Lectures of OCPA International Accelerator School 2002, Singapore*. world scientific, 2004.

[63] G Celentano, G De Marzi, F Fabbri, L Muzzi, G Tomassetti, A Anemona, S Chiarelli, M Seri, A Bragagni, and A Della Corte. Design of an industrially feasible twisted-stack hts cable-in-conduit conductor for fusion application. *IEEE transactions on applied superconductivity*, 24(3):1–5, 2014.

[64] Jie He, Yuejin Tang, Jingdong Li, Li Ren, Jing Shi, Jin Wang, Ronghai Qu, Lushun Su, Xiaoyu Li, Ying Xu, et al. Conceptual design of the cryogenic system for a 12 mw superconducting wind turbine generator. *IEEE Transactions on Applied Superconductivity*, 24(3):1–5, 2014.

[65] S Hanawa, Y Wachi, K Shibayama, J Shibuya, S Mizumaki, T Yamamoto, K Nakamoto, T Kai, K Takahata, J Yamamoto, et al. Development of a superconducting joint technique between cic conductors for poloidal coil of large helical device (lhd). *IEEE Transactions on Applied Superconductivity*, 5(2):757–760, 1995.

[66] S Hanai, M Shimada, T Tsuchihashi, T Kurusu, M Ono, K Shimada, S Koso, K Tsutsumi, and S Nagaya. Design and test results of cic conductor for a cost reduced 100 mw/500 kwh smes. *IEEE transactions on applied superconductivity*, 13(2):1810–1813, 2003.

[67] K Kwasnitza, A Sultan, and S Al-Wakeel. Ac losses of a 10 ka nbti cable-in-conduit superconductor for smes applications. *Cryogenics*, 36(1):27–34, 1996.

[68] Saeed Assadi, Chase Collins, Peter McIntyre, James Gerity, Joshua Kellams, Thomas Mann, Christopher Mathewson, Nathaniel Pogue, Akhdiyor Sattarov, and Richard York. Higgs factory and 100 tev hadron collider: opportunity for a new world laboratory within a decade. *arXiv preprint arXiv:1402.5973*, 2014.

[69] Dariusz Pulikowski, Friedrich Lackner, Christian Scheuerlein, Dietmar Meinel, Frédéric Savary, Davide Tommasini, and Miroslaw Pajor. Testing mechanical behavior of nb 3 sn rutherford cable during coil winding. *IEEE Transactions on Applied Superconductivity*, 27(4):1–5, 2017.

[70] PM McIntyre, Saeed Assadi, Scott Bannert, Jeffrey Breitschopf, James Gerity, JN Kellams, Akhdiyor Sattarov, and Nathaniel Pogue. Collider in the sea: vision for a 500 tev world laboratory. In *North American Particle Accelerator Conf.(NAPAC'16), Chicago, IL, USA, October 9-14, 2016*, pages 13–16. JACOW, Geneva, Switzerland, 2017.

[71] Lawrence Dresner. Twenty years of cable-in-conduit conductors: 1975–1995. *Journal of Fusion Energy*, 14(1):3–12, 1995.

[72] Thomas Rummel, Konrad Ribe, Gunnar Ehrke, Kerstin Rummel, Andre John, Thomas Monnich, Klaus-Peter Buscher, Walter H Fietz, Reinhard Heller, Olaf Neubauer, et al. The superconducting magnet system of the stellarator wendelstein 7-x. *IEEE Transactions on Plasma Science*, 40(3):769–776, 2012.

[73] L Bottura, VE Sytnikov, M Wilson, G Moritz, VS Vysotsky, M Kauschke, E Fischer, and P Bruzzone. A cable-in-conduit superconductor for pulsed accelerator magnets. Technical report, 2005.

[74] A Stafiniak, C Schroeder, E Floch, P Schnizer, H Mueller, E Fisher, G Moritz, F Marzouki, F Walter, M Kauschke, et al. Cold testing of rapidly-cycling model magnets for sis 100 and sis 300-methods and results. *WAMSDO, May*, 2008.

[75] P Bruzzone, N Mitchell, H Katheder, E Salpietro, MR Chaplin, SS Shen, DS Slack, J Rauch, W Brehm, S Ceresara, et al. Test result of full size 40 ka net/iter conductor in the fenix test facility. *IEEE transactions on applied superconductivity*, 3(1):357–360, 1993.

[76] Kunihiro Matsui, Norikiyo Koizumi, Yoshihiro Nabara, Takaaki Isono, Yoshikazu Takahashi, and Kiyoshi Okuno. Evaluation of thermal strain caused by nb 3 sn reaction heat treatment for the iter cable-in-conduit conductors. *Teion Kogaku*, 42(9):311–316, 2007.

[77] Saeed Assadi, Jeff Breitschopf, Daniel Chavez, James Gerity, Joshua Kellams, Peter McIntyre, and Kyle Shores. Cable-in-conduit dipoles to enable a future hadron collider. *IEEE Transactions on Applied Superconductivity*, 27(4):1–5, 2017.

[78] Daniel Chavez and Peter McIntyre. A nbti cable-in-conduit conductor for the medium-energy electron-ion collider (meic) magnets and for ultimate-energy hadron colliders. *Bulletin of the American Physical Society*, 60, 2015.

[79] Peter M McIntyre, Jeff Breitschopf, Daniel Chavez, James Gerity, Joshua Kellams, Akhdiyor Sattarov, and Michael Tomsic. Stealth superconducting magnet technology for collider ir and injector requirements. *IEEE Transactions on Applied Superconductivity*, 28(3):1–6, 2018.

[80] Peter McIntyre, Saeed Assadi, Daniel Chavez, James Gerity, Nathaniel Pogue, Akhdiyor Sattarov, Michael Tomsic, and Thomas Mann. Magnet design and synchrotron damping considerations for a 100 tev hadron collider. Technical report, 2015.

[81] C Edeleanu and AJ Forty. Some observations on the stress-corrosion cracking of $\alpha$-brass and similar alloys. *Philosophical Magazine*, 5(58):1029–1040, 1960.

[82] JE Truman. The influence of chloride content, ph and temperature of test solution on the occurrence of stress corrosion cracking with austenitic stainless steel. *Corrosion Science*, 17(9):737–746, 1977.

[83] George Ellwood Dieter and David J Bacon. *Mechanical metallurgy*, volume 3. McGraw-hill New York, 1986.

[84] P Karnezis and DCJ Farrugia. Study of cold tube drawing by finite-element modelling. *Journal of materials processing technology*, 80:690–694, 1998.

[85] HW Swift. Lxxxi. stresses and strains in tube-drawing. *The London, Edinburgh, and Dublin Philosophical Magazine and Journal of Science*, 40(308):883–902, 1949.

[86] JW Ekin. Fatigue and stress effects in nbti and nb 3 sn multifilamentary superconductors. In *Advances in Cryogenic Engineering*, pages 306–316. Springer, 1978.

[87] I Tanakaa, F Oba, T Sekine, E Ito, A Kubo, K Tatsumi, H Adachi, and T Yamamoto. Hardness of cubic silicon nitride. *Journal of materials research*, 17(4):731–733, 2002.

[88] RI Schermer and BP Turck. Current sharing between insulated strands in a superconducting cable. In *Advances in Cryogenic Engineering Materials*, pages 599–607. Springer, 1980.

[89] JW Ekin. Strain scaling law and the prediction of uniaxial and bending strain effects in multifilamentary superconductors. In *Filamentary A15 superconductors*, pages 187–203. Springer, 1980.

[90] I Husek et al. Tensile stress applied to nbti, nb3sn,bi-2223 and mgb2 composite superconductors at room temperature. *IOP. Supercond. Sci. Technol.*, 17:14111414, 2004.

[91] Norman E Dowling. *Mechanical behavior of materials: engineering methods for deformation, fracture, and fatigue*. Pearson, 2012.

[92] JW Ekin. Fatigue and stress effects in nbti and nb 3 sn multifilamentary superconductors. In *Advances in Cryogenic Engineering*, pages 306–316. Springer, 1978.

[93] Jeff Breitschopf, D Chavez, R Albosta, T Elliot, R Garrison, J Kellams, P McIntyre, and A Sattarov. Fabrication of long-length cable-in-conduit for superconducting magnets. In *IOP Conference Series: Materials Science and Engineering*, volume 279, page 012036. IOP Publishing, 2017.

[94] J.N. Kellams P. McIntyre M. Rindfleish A. Sattarov D. Chavez, J. Breitschopt and M.Tomsic. Cable-in-conduit using mgb2, nb3sn and bi-2212 for wind-and-react coils. submitted.

[95] Superferric 3t cic dipole r&d 2016/17 project presentation. `https://www.jlab.org/indico/event/210/session/5/contribution/16/material/slides/0.pdf`. Accessed: 2018-12-05.

[96] Hypertech research inc. long length welded nbti cic superconducting cable for accelerators applications. `https://sbirsource.com/sbir/awards/166373-long-length-welded-nbti-cic-superconducting-cable-for-accelerators-appli` Accessed: 2018-12-05.

[97] Akhdiyor Sattarov, Peter McIntyre, Jeff Breitschopf, Daniel Chavez, James Gerity, and Joshua Kellams. New magnet technology for a 1.5 t open-mri breast imager. *IEEE Transactions on Applied Superconductivity*, 27(4):1–4, 2017.

[98] Ya E Shakhova, Zh Ch Yanushkevich, and AN Belyakov. Effect of cold rolling on the structure and mechanical properties of austenitic corrosion-resistant 10kh18n8d3br steel. *Russian Metallurgy (Metally)*, 2012(9):772–778, 2012.

[99] ASM Handbook. Volume 4: Heat treating. *ASM International*, 10, 1991.

[100] Harry Chandler. *Heat treater's guide: practices and procedures for irons and steels*. ASM international, 1994.

[101] In-suk Choi, Oliver Kraft, and Ruth Schwaiger. Validity of the reduced modulus concept to describe indentation loading response for elastoplastic materials with sharp indenters. *Journal of Materials Research*, 24(3):998–1006, 2009.

[102] Ti 950 triboindenter user manual, rev. 9.3.0314, pp. 115-134. hysitron incorporated. `https://engineering.unl.edu/downloads/files/UserManual-HystrionTriboIndenter-sm.pdf`. Accessed: 2018-12-05.

[103] P. McIntyre. Superferric 3t cic dipole r&d 2016-17 project report. *JLAB EIC annual collaboration*, pages 1–27, 2017.

[104] D. Chavez P. McIntyre and A. Sattarov. 6 t cable-in-conduit dipole to double the ion energy for jleic. Preparing for submission.

[105] Peter McIntyre, Jeff Breitschopf, Daniel Chavez, James Gerity, James Kellams, Akhdiyor Sattarov, and Michael Tomsic. Block-coil high-field dipoles using superconducting cable-in-conduit. *IEEE Transactions on Applied Superconductivity*, 28(3):1–7, 2018.

[106] Darrell W Pepper and Juan C Heinrich. *The Finite Element Method: Basic Concepts and Applications with MATLAB, MAPLE, and COMSOL.* CRC Press, 2017.

[107] Erich Willen, P Dahl, and J Herrera. Superconducting magnets. In *AIP Conference Proceedings*, volume 153, pages 1228–1276. AIP, 1987.

[108] Tamu meic team, cost estimates for meic dipole options, doe meic cost review, jan. 2015. `https://science.energy.gov/~/media/np/pdf/research/NP%20Accel%20RD%20PI%20Meeting/2016/Zhang_JLab_MEIC_RD_at_DOE-ONP-PI_Meeting_2016.pdf`. Accessed: 2018-11-26.

[109] Gunther Sikler, Claus Schroeder, Pierre Schnizer, Franz Walter, Egbert Fischer, Willi Gärtner, Dieter Krämer, Johann Macavei, Eric Floch, and Arnold Wessner. Fabrication of a prototype of a fast cycling superferric dipole-magnet. 2010.

[110] Christopher Hill, Craig Hogan, Steve Holmes, Young-Kee Kim, Joseph Lykken, Chris Quigg, and Katie Yurkewicz. Fermilab: A plan for discovery. Technical report, Fermi National Accelerator Lab.(FNAL), Batavia, IL (United States), 2011.

[111] Daniel Chavez Tim Elliott Raymond Garrison1 JamesGerity Joshua Kellams P. McIntyre, Jeff Breitschopf and Akhdiyor Sattarov. Cable in conduit dipoles for the ion ring of the jleic. submitted.

[112] P. McIntyre et al. Meic arc dipole conceptual design report. *http://arl.physics.tamu.edu/MEIC/task1*, 2015.

[113] D. Neuffer. A novel method for correcting the ssc multipole problem. *SSC-N-525. http://lss.fnal.gov/archive/other/ssc/ssc-n-525.pdf*, 1988.

[114] S.Chouhan et al. Design and fabrication of the superconducting horizontal bend magnet for the super high momentum spectrometer at jefferson lab. *IEEE Trans. Appl. Supercond.*, 25(3), 2015.

[115] Supercon inc. *http://www.supercon-wire.com*, 2015.

[116] Comsol multiphysics. *http://www.comsol.com*.

[117] Opera simulation software. *http://operafea.com/*.

[118] Z. Charifoulline et al. Residual resistivity ratio (rrr) measurements of lhc superconducting nbti cable strands. *IEEE Trans. Appl. Supercond.*, 16(2):1188–1191, 2006.

[119] V. E. Sytnikov et al. Development and test of a miniature novel cable-in-conduit conductor for sse in fast ramping accelerators with superconducting magnets. *IEEE Trans. Appl. Supercond.*, 16(2):1676–1679, 2006.

[120] T. Elliot R. Garrison J. Gerity J. Kellams P. McIntyre K. OQuinn D. Chavez, J. Breitschopf and A. Sattarov. 3 tesla superferric cable-in-conduit dipole for the ionring of the jleic collider. submitted.

[121] Richard HS Winterton. Where did the dittus and boelter equation come from? *International journal of heat and mass transfer*, 41(4-5):809–810, 1998.

[122] Cryocomp rapid cryogenic design. `http://www.eckelsengineering.com/`. Accessed: 2018-11-27.

[123] R. Fair S. Gopinath D. Kashy P. McIntyre T. Michalski R. Rajput-Ghoshal A. Sattarov. P. K. Ghoshal, D. Chavez. Quench protection study of 3t super-ferric boostermagnet using cicc for future electron-ion collider at jefferson laboratory. submitted.

[124] Alexander Kalimov, Gebhard Moritz, and Al Zeller. Design of a superferric dipole magnet with high field quality in the aperture. *IEEE transactions on applied superconductivity*, 14(2):271–274, 2004.

[125] N Diaczenko, T Elliott, A Jaisle, D Latypov, P McIntyre, P McJunkins, L Richards, W Shen, R Soika, D Wendt, et al. Stress management in high-field dipoles. In *Particle Accelerator Conference, 1997. Proceedings of the 1997*, volume 3, pages 3443–3445. IEEE, 1997.

[126] Waseem A Roshen. Fringing field formulas and winding loss due to an air gap. *IEEE Transactions on Magnetics*, 43(8):3387–3394, 2007.

[127] Technical data sheet, fiberglass laminates. `https://laminatedplastics.com/fiberglasslaminates.pdf`. Accessed: 2018-11-18.

[128] Gary R Hardin. Cryogenic materials properties reference list. *Cryogenics*, pages 230–235, 1962.

[129] Linux cnc. `http://linuxcnc.org/`. Accessed: 2018-11-18.

[130] Leonardo Romero Munoz, Moises Garcia Villanueva, and Mario Santana Gómez. Development of a computer numerically controlled router machine with 4 degrees of freedom using an open architecture. In *Power, Electronics and Computing (ROPEC), 2013 IEEE International Autumn Meeting on*, pages 1–6. IEEE, 2013.

[131] Starrett precision granite table. `http://www.starrett.com/metrology/metrology-products/precision-granite/precision-granite-faq`. Accessed: 2018-11-19.

[132] Mitutoyo coordinate measurement machine. `https://ecatalog.mitutoyo.com/Coordinate-Measuring-Machines-C101.aspx`. Accessed: 2018-11-19.

[133] Cristhian Valerio Lizarraga, Alejandro Castilla Loaeza, Gerardo Guillermo Cantón, Carlos Duarte, Daniel Chavez Valenzuela, Karim Hernández Chahín, Humberto Maury Cuna, Luis Medina Medrano, Juan Reyes Herrera, Salvador Sosa Güitrón, et al. Science and technology of accelerators. In *Journal of Physics: Conference Series*, volume 761, page 012005. IOP Publishing, 2016.

[134] Scott D.Watkins Caroline M. Sallee and Alex L. Rosaen. The economic impact of fermi national accelerator la-boratory. *Anders Economic Group, LLC.*, 2011.

[135] Lyndon R Evans. Lhc accelerator physics and technology challenges. In *Particle Accelerator Conference, 1999. Proceedings of the 1999*, volume 1, pages 21–25. IEEE, 1999.

[136] Massimo Florio, Andrea Bastianin, and Paolo Castelnovo. The socio-economic impact of a breakthrough in the particle accelerators technology: A research agenda. *Nuclear Instruments and Methods in Physics Research Section A: Accelerators, Spectrometers, Detectors and Associated Equipment*, 2018.

[137] Helmut Wiedemann. *Particle accelerator physics*. Springer, 2015.

[138] Th Zickler. Basic design and engineering of normal-conducting, iron-dominated electromagnets. *arXiv preprint arXiv:1103.1119*, 2011.

[139] G Brianti and M Gabriel. Basic expressions for evaluating iron core magnets-a possible procedure to minimize their cost. Technical report, 1970.

[140] SK Thangaraju and KM Munisamy. Electrical and joule heating relationship investigation using finite element method. In *IOP Conference Series: Materials Science and Engineering*, volume 88, page 012036. IOP Publishing, 2015.

[141] Thomas Weiland. On the numerical solution of maxwell's equations and applications in the field of accelerator physics. *Part. Accel.*, 15(DESY-84-006):245–292, 1984.

[142] D Chavez, GHI Maury, M Napsuciale, CB Ortiz, J Peña, C Galvan-Duarte, CA Valerio, and AI Sattarov. Status report on the r&d of a 5 t/m normal conducting quadrupole magnet for the 10-mev beam line of the electron linac of the mexican particle accelerator community. In *Journal of Physics: Conference Series*, volume 912, page 012038. IOP Publishing, 2017.

[143] CA Valerio-Lizarraga, B Yee-Rendon, C Duarte-Galvan, G Guillermo Cantón, L Medina, D Chavez Valenzuela, KG Hernández-Chahín, and GHI Maury Cuna. Study of the first mexican rf linear accelerator. *Rev. Mex. Fis.*, 64:116, 2018.

[144] COMSOL Multiphysics. software (2016) https://www. comsol. com, 2017.

[145] Jack T Tanabe. *Iron dominated electromagnets: design, fabrication, assembly and measurements*. World Scientific Publishing Company, 2005.

[146] D Chavez, GHI Maury Cuna, M Napsuciale, J Carlos Basilio, B Yee-Rendon, CA Valerio-Lizarraga, P McIntyre, and AI Sattarov. Field and cost optimization of a 5 t/m normal conducting quadrupole for the 10-mev beam line of the electron linac of the mexican particle accelerator community. In *Journal of Physics: Conference Series*, volume 1067, page 082014. IOP Publishing, 2018.

[147] Technical guide, superior essex, howpublished = `http://www. superioressexcommunications.com/uploadedfiles/docs/pdf/ technical-guidelines/tg10-copper-maxpulltension.pdf`, note = Accessed: 2018-11-25,.

[148] Glenn W Greenway. Metal stamping, November 30 1993. US Patent 5,265,320.

[149] S Kumar and R Singh. An intelligent system for selection of die-set of metal stamping press tool. *Journal of Materials Processing Technology*, 164:1395–1401, 2005.

[150] G-11 epoxy phenolic physical properties. `https://www.plasticsintl.com/datasheets/Phenolic_G11_Glass_Epoxy.pdf`. Accessed: 2018-11-24.

[151] Physical properties of Kapton polyimide film, howpublished = `vhttps://www.americandurafilm.com/data-sheets/kapton-mt.pdf`, note = Accessed: 2018-11-24,.

[152] Steven W Van Sciver. *Helium cryogenics*. Springer Science & Business Media, 2012.

[153] Patxi Duthil. Material properties at low temperature. *arXiv preprint arXiv:1501.07100*, 2015.

[154] Low temperature properties of materials. `http://uspas.fnal.gov/materials/10MIT/Lecture_1.2.pdf`. Accessed: 2018-11-25.

# Committe Members

León, Guanajuato, a 10 de diciembre de 2018
**Oficio Núm.** SAC-317-2018
**Asunto:** Asignación de Jurado

Dr. José Luis Lucio Martínez
Dr. Modesto Antonio Sosa Aquino
Dr. Peter McIntyre
Dr. Carlos Hernández García
Dr. Cristhian Alonso Valerio Lizarraga
Dr. Georfrey Humberto Israel Maury Cuna
Dr. Mauro Napsuciale Mendivil

**PRESENTES**

Por este conducto, en base al Artículo 68 del Estatuto Académico y en atención a la solicitud que presenta el Dr. Mauro Napsuciale Mendivil, Director para la defensa del trabajo de tesis que, bajo el título "Design and development of cable-in-conduit superconductor technology for the magnets of the future electron-ion collider" defenderá el **C. Daniel Chávez Valenzuela**, estudiante de Doctorado en Física de esta División, se hace la siguiente asignación de Jurado:

| | |
|---|---|
| Dr. José Luis Lucio Martínez | Presidente |
| Dr. Modesto Antonio Sosa Aquino | Secretario |
| Dr. Peter McIntyre | Vocal |
| Dr. Carlos Hernández García | Vocal |
| Dr. Cristhian Alonso Valerio Lizarraga | Vocal |

| | |
|---|---|
| Dr. Georfrey Humberto Israel Maury Cuna | Suplente |
| Dr. Mauro Napsuciale Mendivil | Suplente |

Sirva la presente para solicitar al estudiante entregar su documento de tesis a la brevedad posible al Jurado designado, para que dentro del plazo que marca el Artículo 68 del Estatuto Académico sus sinodales se pronuncien por escrito sobre la aprobación del documento.

Sin más por el momento, aprovecho la ocasión para enviarles un cordial saludo.

ATENTAMENTE
"LA VERDAD OS HARÁ LIBRES"

UNIVERSIDAD DE GUANAJUATO
CAMPUS LEÓN
DIVISIÓN DE CIENCIAS E INGENIERÍAS
**DR. DAVID YVES GHISLAIN DELEPINE**
**DIRECTOR DE LA DIVISIÓN DE CIENCIAS E INGENIERÍAS**

C. p. Archivo de Secretaría Académica

León Güanajuato, 13 de diciembre de 2018

Dr. David Delepine
Director
Div. de Ciencias e Ingenierías,
UG-Campus León
Presente

Por este conducto me permito informarle que he leído y analizado el trabajo titulado "Design and Development of Cable-in-Conduit superconductor technology for the Magnets of the Future ElectronIon Collider" que para obtener el grado de Doctor en Física ha desarrollado y somete para su consideración el M.F. Daniel Chávez Valenzuela. Al respecto manifiesto que considero que el trabajo es de alta calidad y que cumple con creces los estándares requeridos por nuestra institución para la obtención del doctorado por lo que expreso mi aval para que prosiga, conforme al procedimiento establecido, a la defensa de su tesis.

Atentamente

Dr. José Luis Lucio Martínez
Profesor titular C
Departamento de física, DCI
Universidad de Guanajuato

Campus León | División de Ciencias e Ingenierías

**León, Gto., 13 de Diciembre, 2018**

**DR. MIGUEL ÁNGEL VALLEJO HERNÁNDEZ**
**COORDINADOR DE POSGRADO**
**DIVISIÓN DE CIENCIAS E INGENIERÍAS**

**Estimado Dr. Vallejo Hernández:**

Por medio de la presente hago constar que he revisado la tesis titulada: "**Design and Development of Cable-in-Conduit Superconductor Technology for the Magnets of the Future Electron-Ion Collider**" que para obtener el grado de Doctor en Física presenta el **M.F. Daniel Chávez Valenzuela.**

El trabajo es interesante en su área pues constituye un desarrollo novedoso que servirá en un futuro como una de las partes fundamentales del colisionador electrón-ión.

Le comunico que he discutido cuidadosamente dicha tesis con el sustentante, a quien le he hecho llegar mis comentarios y correcciones. Le expreso además que en lo general me parece un buen trabajo por lo que avalo su presentación.

**Atentamente**

_____
**DR. MODESTO ANTONIO SOSA AQUINO**
**PROFESOR TIRULAR "C"**
**SINODAL**

Loma del Bosque 103
Lomas del Campestre, León, Gto.
Ap. Postal E-143     C.P. 37150
Tel. (477) 788-5100 ext. 8456
Fax. (477) 788-5100 ext. 8410
http://www.dci.ugto.mx

León, Guanajuato, 12 de Diciembre de 2018

Dr. David Delepine

Director DCI

Presente

Por este conducto le informo que he leído la tesis titulada *"Design and Development of Cable-in-Conduit superconductor technology for the Magnets of the Future Electron-Ion Collider"* que para obtener el grado de Doctor en Física ha formulado el M.F. Daniel Chávez Valenzuela.

En mi opinión, este trabajo reúne las características de calidad y forma para el grado al que se aspira, por lo cual, no tengo inconveniente en que se realice la defensa correspondiente.

Sin otro particular, reciba un cordial saludo.

Atentamente

Dr. Peter McIntyre

Texas A&M

Sinodal

## Jefferson Lab
Thomas Jefferson National Accelerator Facility
*Exploring the Nature of Matter*

Newport News, VA, USA, 12 de Diciembre, 2018

Dr. David Delepine

Director DCI

Presente

Por este conducto le informo que he leído la tesis titulada *"Design and Development of Cable-in-Conduit superconductor technology for the Magnets of the Future Electron-Ion Collider"* que para obtener el grado de Doctor en Física ha formulado el M.F. Daniel Chávez Valenzuela.

En mi opinión, este trabajo reúne las características de calidad y forma para el grado al que se aspira, por lo cual, no tengo inconveniente en que se realice la defensa correspondiente.

Sin otro particular, reciba un cordial saludo.

Atentamente

Dr. Carlos Hernandez Garcia
Center for Injectors and Sources
chgarcia@jlab.org
+1 (757)-269-6862

**Facultad de Ciencias Físico-Matemáticas**
Ciudad Universitaria, Culiacán Sinaloa.
Tel./Fax: (667) 16-11-54

Universidad Autónoma
de Sinaloa

León, Guanajuato, 12 de Diciembre de 2018

Dr. David Delepine
Director DCI
Presente

Por este conducto le informo que he leído la tesis titulada *"Design and Development of Cable-in-Conduit superconductor technology for the Magnets of the Future Electron-Ion Collider"* que para obtener el grado de Doctor en Física ha formulado el **M.F. Daniel Chávez Valenzuela**.

En mi opinión, este trabajo cumple con las características necesarias para obtener el grado al que se aspira, por lo cual, no tengo inconveniente en que se realice la defensa correspondiente.

Quedo pendiente a cualquier aclaración.

Atentamente

Dr. Cristhian Alfonso Valerio Lizarraga
Facultad de Ciencias Físico-Matemáticas.
Universidad Autónoma de Sinaloa.

UNIVERSIDAD DE
GUANAJUATO

León, Gto. a 12 de diciembre de 2018
**Asunto:** Visto bueno para defensa de tesis

**DR. DAVID YVES GHISLAIN DELEPINE**
**DIRECTOR**
**DIVISIÓN DE CIENCIAS E INGENIERÍAS**
**CAMPUS LEÓN**
**P R E S E N T E**

Por este medio le  informo que he leído la tesis titulada ***"Design and Development of Cable-in-Conduit superconductor technology for the Magnets of the Future Electron-Ion Collider"*** que para obtener el grado de **Doctor en Física** ha formulado el **M.F. Daniel Chávez Valenzuela**.

En mi opinión, **este trabajo reúne las características de calidad y forma para el grado al que se aspira**, por lo cual, no tengo inconveniente en que se realice la defensa correspondiente.

Sin más por el momento reciba un cordial saludo.

**Atentamente**
**"La Verdad Os Hará Libres"**

**Dr. Georfrey Humberto Israel Maury Cuna**
**Profesor Asociado C**
**Sinodal suplente**

Universidad de Guanajuato

León, Guanajuato, 12 de Diciembre de 2018

Dr. David Delepine

Director DCI

Presente

Por este conducto le informo que he leído la tesis titulada *"Design and Development of Cable-in-Conduit superconductor technology for the Magnets of the Future Electron-Ion Collider"* que para obtener el grado de Doctor en Física ha formulado el M.F. Daniel Chávez Valenzuela.

En mi opinión, este trabajo reúne las características de calidad y forma para el grado al que se aspira, por lo cual, no tengo inconveniente en que se realice la defensa correspondiente.

Sin otro particular, reciba un cordial saludo.

Atentamente

Dr. Mauro Napsuciale

Profesor Titular "C"

Sinodal suplente